STANFORD SYNCHROTRON RADIATION LABORATORY

1990 ACTIVITY REPORT

Stanford University • Stanford • California

1990 ACTIVITY REPORT

Arthur Bienenstock
Director

Herman Winick
Deputy Director

Katherine Cantwell
Editor

Stanford Synchrotron Radiation Laboratory
A National Users Facility

About the Stanford Synchrotron Radiation Laboratory

SSRL is a national facility supported primarily by the Department of Energy for the utilization of synchrotron radiation for basic and applied research in the natural sciences and engineering. It is a user-oriented facility that welcomes proposals for experiments from all researchers.

The synchrotron radiation is produced by the 3.5 GeV storage ring, SPEAR, located at the Stanford Linear Accelerator Center (SLAC). SPEAR has been dedicated to the production of synchrotron radiation during 50% of its operations time or about 4 months per year. Starting in the fall of 1990 SPEAR became fully dedicated to synchrotron radiation operation and is expected to operate 6–9 months each year starting in 1992.

SSRL currently has 23 experimental stations on the SPEAR storage ring. There are 133 active proposals for experimental work from 92 institutions involving approximately 374 scientists. There is normally no charge for use of beam time by experimenters.

Additional information for prospective users can be obtained from SSRL by writing or telephoning Katherine Cantwell at SSRL, SLAC Bin 69, P.O. Box 4349, Stanford, CA 94309-0210 — telephone (415) 926-3191.

This report summarizes the activity at SSRL for the period January 1, 1990, to December 31, 1990.

SSRL is operated by the Department of Energy, Office of Basic Energy Sciences, Division of Chemical Sciences. Support for research by SSRL staff is provided by the Office's Division of Material Science. The SSRL Biotechnology Program is supported by the NIH, Biomedical Resource Technology Program, Division of Research Resources.

Introduction

1990 was a year of major changes for SSRL and a harbinger of more changes in 1991 and 1992.

As discussed in last year's Activity Report, a fairly complete analysis of SPEAR problems was performed in concert with SLAC, and a major maintenance/improvement process was initiated in the spring of 1989. As a result, the SPEAR run of April, 1990, was one of the most successful in SSRL's history. This run made it apparent that SPEAR will remain a very useful and impressive synchrotron radiation storage ring for at least a decade, given a steady maintenance and improvement program. More details about SPEAR functioning during the run, as well as SPEAR improvements, are contained in Chapter I.

The formal SPEAR injector construction project was completed in November, 1990, on-time and on-budget. Although DOE was not able to provide anticipated FY90 commissioning funds due to Congressional appropriation actions, preliminary commissioning was performed and 2.3 GeV injection to SPEAR was demonstrated. (The upgrade of SPEAR injection components to permit injection at 3.0 GeV has not been completed as part of the injector construction project due to Gramm-Rudman-Hollings cuts in FY90.) A discussion of the Injector project is contained in Chapter II.

Commissioning of the injector and the injector/SPEAR complex is continuing in 1991 with Users participating during the May–September period. This user participation allowed normal experimentation, so that systems could be tested critically, but with the commissioning process having higher priority than data acquisition.

Another major event in 1990 was the full dedication of SPEAR to the synchrotron radiation program. Previously SPEAR was considered a high energy physics machine that was partially dedicated to synchrotron radiation. The full dedication means that the accelerator can be modified and improved for synchrotron radiation research.

Despite the heavy emphasis on completing the Injector, many beam line improvements were achieved, as described in Chapter IV. Among these was the optimization of stations 6-2 and 10-2, the provision of a considerably larger hutch for Station 1-5, which contains the area detector diffractometer, and the introduction of white light capability on 10-2. The latter achievement has made Laue analysis of protein (and other) structures possible at SSRL.

The provision of good beam during the month of April made an appreciable amount of experimentation possible. Some of the fruits of this and other runs are described in Chapter VI.

With the injector, the improved SPEAR, and the possibility of improving both machines even more, SSRL looks forward to providing its users with good beam during a large portion of the year. This has begun with the user-assistance, May–September portion of the injector commissioning run in 1991. We are optimistic that SSRL will receive sufficient funding and the DOE approvals required for considerably longer operation in 1992.

— A. Bienenstock
Director

Dedication

This 1990 Activity Report is dedicated
to long-time user Bill Parrish
who died in March 1991.

Contents

During the night shift on April 18, SPEAR achieved the highest integrated current for an 8-hour period in its history, an estimated 460 mA/hrs. Running conditions by mid-April led to delivered beam 94% of the time and average currents of 46 mA over each 24 hour period, with 90 mA of stored current at the top of the fill. Refills were occurring 22 hours later when the current had decayed to 35 mA.

On April 21, one of the two SPEAR klystrons failed. During the remaining 12 days of operation SPEAR was run with only one klystron, limiting the current at the top of the fill to 42 mA. Running at these lower currents produced an extremely stable beam with 35 hour lifetimes. Although some experiments were hurt by the loss of flux, others made good use of the stability and long lifetimes. SLAC agreed to a two day extension of the run to compensate for down time associated with this klystron failure. New klystrons have been purchased and installed in SPEAR.

PEP OPERATIONS

In contrast to SPEAR's limited but successful operation for synchrotron radiation, the 15 GeV storage ring, PEP, ran for six months (April 24-September 15) but delivery of synchrotron radiation light was disappointing.

Turning on PEP, which had been shutdown for the previous two years, and bringing it back into operation proved difficult. The main problem (in addition to specific hardware failure i.e., a klystron and RF window) was the inability to keep the stored beam for the long periods between available injections. This was attributed to the general unreliability of many components. Injection was limited due to concurrent operation of the SLAC Linear Collider. It is SLAC's policy that the storage rings not interfere with SLC running at more than the 20% level.

The first of the two SSRL beam lines on PEP was turned on in late August and the second in early September. Experiments were set up on both lines, resulting in a total of 10 shifts of delivered beam. Significant progress was made on the Mossbauer experiment in the limited time available. The second experiment was not able to take any data.

SPEAR IMPROVEMENTS

Following the successful April run it was decided to limit work on SPEAR, in order to minimize the uncertainties when restarting the machine from the new injector. Since it is no longer planned to store a counter-rotating positron beam, the positron injection line has been decommissioned. One of the positron kicker magnets was relocated to be used as a third electron kicker to facilitate injection into a low emittance lattice. In addition, some of the positron injection line magnets were removed for possible use in the future upgrade of the electron injection line from 2.3 to 3.0 GeV.

SPEAR and the injector together require three C.W. klystrons. This summer two new klystrons were built, and the third one, which had failed during the April run, refurbished. As of December 1990 SSRL had a total of four klystrons, giving backup capability.

Procedures for alignment of the storage ring, and the beam lines to the storage ring have never been clearly defined. SSRL began studies on the alignment process and did an extensive survey of the SPEAR monuments to provide a data baseline.

Another SSRL effort was in the development of an ongoing program to refurbish and tune the RF coupling loops.

Despite the limited 1990 budget, four new accelerator engineers were hired by SSRL. They will play a key role in undertaking SSRL's new responsibility for operation and maintenance of the SPEAR storage ring and injector complex. These staff bring expertise in RF systems, power supplies, VAX system programming, as well as instrumentation and control.

BEAM AND SPEAR USAGE TABLES

The following tables and graphs contain statistics on SPEAR running, experimental use and characteristics of SSRL stations. For earlier information, consult previous Activity Reports.

Table 1 and Figures 2 and 3 show the number of SPEAR shifts scheduled and delivered since dedicated running commenced in 1979.

Table 2 and Figure 4 show the use of beam at SSRL for experimental purposes. Table 3 lists the characteristics of the 23 SSRL SPEAR stations.

TABLE 1

BEAM TIME STATISTICS/DEDICATED TIME

DEDICATED RUN	SCHEDULE HOURS	DELIVERED HOURS	%DELIVERED
10/20-11/05/79	152	95.3	62
12/03-12/21/79	352	299.4	85
02/08-03/05/80	472	366.3	77
04/16-05/19/80	764	588.2	76
06/30-07/30/80	726	320.4	44
09/29-10/14/80	336	194.9	58
12/02-12/22/80	440	309	70
01/26-03/03/81	792	600.9	76
05/16-06/30/81	988	727	73
11/18-12/21/81	546	363.6	66
01/08/-02/22/82	748	612.5	81
03/09-04/26/82	995	830.9	83
10/15-11/05/82	473	316	66
12/27-02/22/83	1050	825.6	78
05/09-06/30/83	1195	960.3	80
11/07-12/23/83	857	662.8	77
03/21-04/30/84	835	674.3	80
01/10-02/21/85	905	606.6	67
03/15-07/22/85	1502	1056.5	70
10/14-11/11/85	416	203.7	48
04/11-06/30/86	1550	1106.5	71
11/17-12/24/86	752	527	70
01/02-02/07/87	696	522	75
03/18-05/02/87	1112	769	69
10/26-12/24/87	1360	801	59
01/23-03/17/89	1160	504	43
04/02-05/02/90	720	536	74

The history of dedicated time at SSRL/SPEAR since its inception in 1979 is shown. Until 1986 SSRL received one-half of the SPEAR operating time in a mode dedicated to synchrotron radiation while the other half was used for colliding beam physics. In the fall of 1990 SPEAR became a dedicated synchrotron radiation source. Dedicated shifts have been limited by SSRL budgetary considerations, SSRL and SLAC construction and the SLC schedule.

FIGURE 2

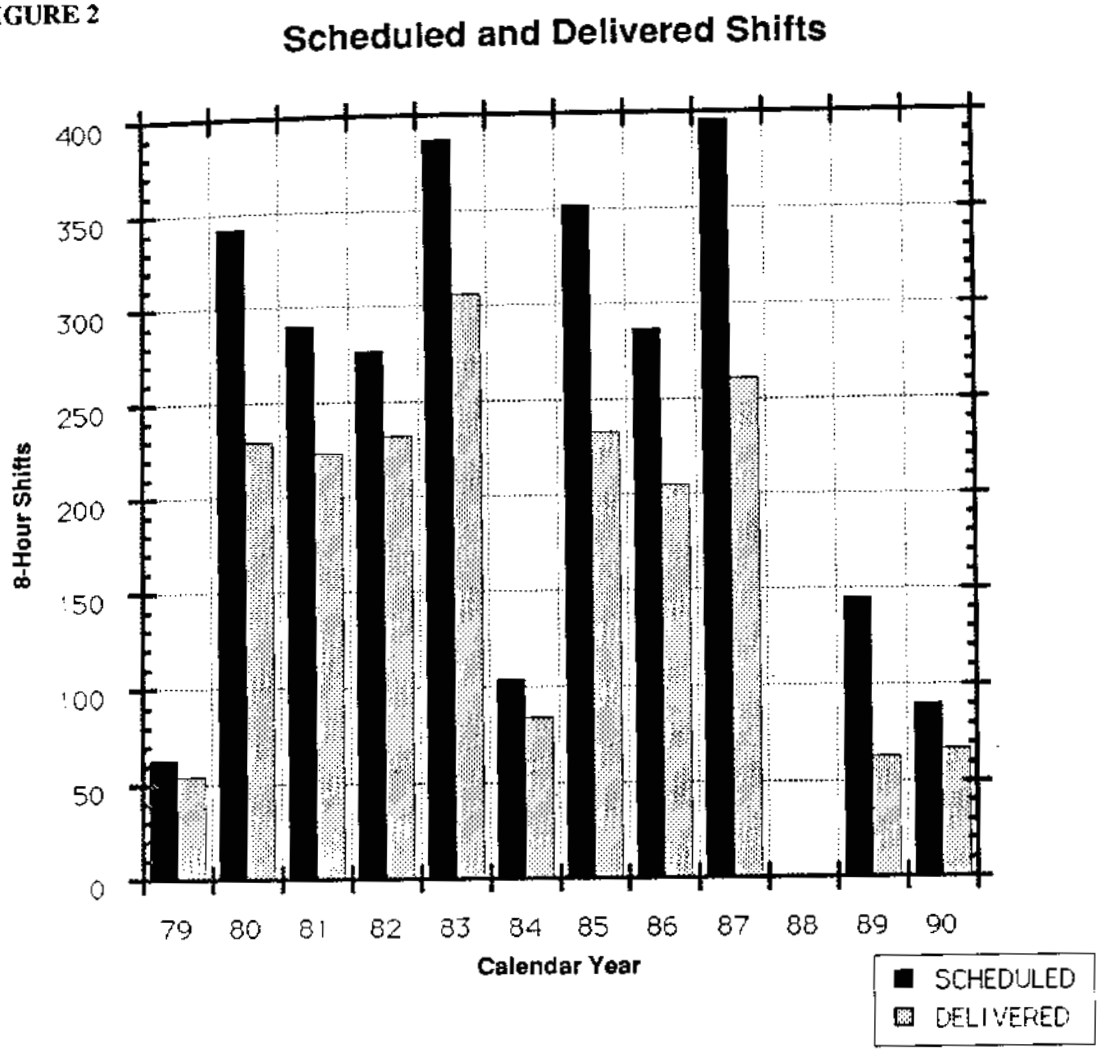

FIGURE 3

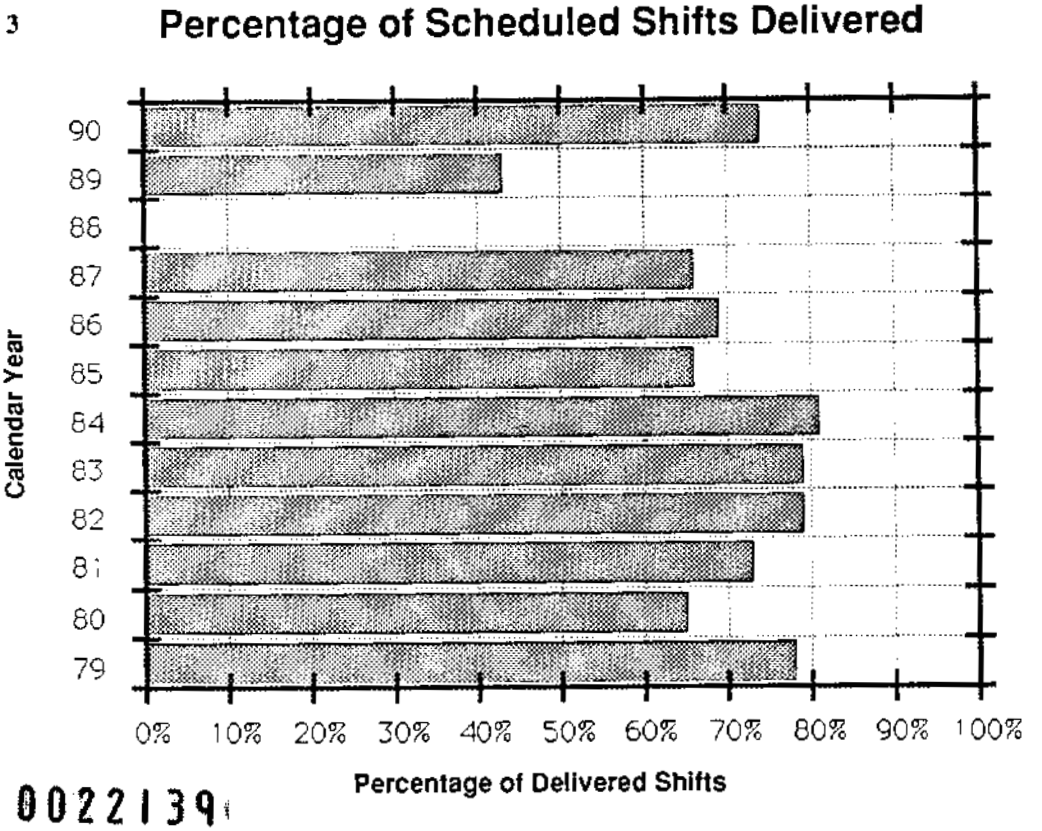

TABLE 2

USER SHIFTS BY EXPERIMENTAL STATION
Calendar 1990

Experimental Station	04/02/90 05/02/90	
Beam Line 1		
1-1	0*	
1-2	59	
1-4	33	
1-5	50	(9)**
Beam Line 2		
2-1	59	
2-2	59	
2-3	59	
Beam Line 3		
3-1	59	
3-2	49	(1)
3-3	59	
3-4	59	
Beam Line 4		
4-1	59	
4-2	58	
4-3	60	
Beam Line 5		
5-2	0	(59)
Beam Line 6		
6-1	0	(59)
6-2	59	
Beam Line 7		
7-1	59	
7-2	59	
7-3	58	
Beam Line 8		
8-1	59	
8-2	59	
Beam Line 10		
10-2	56	
PEP 1	9	
PEP 5	1	
TOTAL Shifts Used	**1269**	
Proposals Run	**62**	

** Station 1-1 was not operational during this run*
***( ) = facility characterization time*

In 1990, 1195 8-hour shifts were actually used by experimenters for data taking on SSRL's 23 SPEAR and two PEP stations. A total of 74 shifts were used by SSRL staff, PRT members and collaborators for characterization, upgrading and commissioning time. In 1990 both the new soft x-ray line on 6-1 and the multi-undulator on Beam Line 5 were being commissioned.

TABLE 3

CHARACTERISTICS OF SSRL EXPERIMENTAL STATIONS

SSRL presently has 23 experimental stations on SPEAR. 12 of these stations are based on insertion devices while the remainder use bending magnet radiation.

	Horizontal Angular Acceptance (Mrad)	*Mirror Cut Off (keV)*	*Monochromator*	*Energy Range (eV)*	*Resolution ΔE/E*	*Approximate Spot Size HgtxWdth (mm)*	*Dedicated Instrumentation*
INSERTION DEVICES STATIONS							
Wiggler Lines - X-ray							
End Stations							
4-2 (8-Pole)							
Focused	4.6	10.2	Double Crystal	2800-10200	~5×10^{-4}	2.0 x 6.0	
Unfocused	1.0		Double Crystal	2800-45000	~10^{-4}	2.0 x 20.0	
6-2 (54-Pole)							
Focused	2.3	22	Double Crystal	2800-21000	~5×10^{-4}	2.0 x 6.0	
Unfocused	1.0		Double Crystal	2800-45000	~10^{-4}	2.0 x 20.0	
7-2 (8-Pole)							6-circle Diffractometer
Focused	4.6	10.2	Double Crystal	2800-10200	~5×10^{-4}	2.0 x 6.0	
Unfocused	1.0		Double Crystal	2800-45000	~10^{-4}	2.0 x 20.0	
10-2 (31-Pole)							
Focused	2.3	22	Double Crystal	2800-21000	~5×10^{-4}	2.0 x 6.0	
Unfocused	1.0		Double Crystal	2800-45000	~10^{-4}	2.0 x 20.0	
Side Stations							
4-1	1.0		Double Crystal	2800-45000	~5×10^{-4}	2.0 x 20.0	
4-3							2-circle Diffractometer
Focused	1.0	Variable	Double Crystal	2800-20000	~10^{-4}	0.3 x 20	
Unfocused	1.0		Double Crystal	2800-45000	~10^{-4}	2.0 x 20.0	
7-1	1.0		Curved Crystal	6000-13000	~8×10^{-4}	0.6 x 3.0	Rotation Camera
7-3	1.0		Double Crystal	2800-45000	~10^{-4}	2.0 x 20.0	
Undulator Lines - VUV/Soft X-Ray							
5 undulators	1.5		Rowland Circle-Multiple Grating	10-1200	Δλ =.013-.13Å	6.0 x 8.0	
6-1			6m SGM	200-1000	~2×10^{-4}	≤1mm²	
BENDING MAGNET STATIONS							
X-Ray							
1-4	2.0		Curved Crystal	6700-10800	0.3×10^{-3}	0.25 x 0.5	SAS Detector
1-5	1.0		Double Crystal	2800-30000	~10^{-4}	3 x 20	Area Detector/CAD-4
2-1 (Focused)	4.8	8.9	Double Crystal	2800-8900	~5×10^{-4}	1 x 4	
2-2	1.0-6.1		None	3200-30000		4 x 22 - 4 x 134	
2-3	1.0		Double Crystal	2800-30000	~5×10^{-4}	3 x 20	
VUV/Soft X-Ray							
1-1	2.0		Grasshopper	64-1000	Δλ = .1-.2Å	1.0 x 1.0	
1-2	4.0		6m TGM	8-90	~2×10^{-3}	1.0 x 2.0	
3-1	2.0		Grasshopper	25-1000	Δλ = .05-2 Å	1.0 x 1.0	
3-2	4.0		Seya-Namioka	5-40	Δλ = .2-6 Å	2 x 7	
3-3	8-10	4.5	UHV Double Crystal (Jumbo)	800-4500	~5×10^{-4}	1.5 x 2.5	
3-4	0.6		Multilayer	0-3000	White or Δλ/λ = .6%	2 x 8	Vacuum Diffractometer/ Litho. Expo.Station
8-1	12		6m TGM	8-180	~9×10^{-3}	≤1mm²	Angle Resolved e⁻ Spectrometer
8-2	5.0		6m SGM	150-1000	~3×10^{-4}	≤1mm²	Angle Resolved e⁻ Spectrometer

FIRST BOOSTER BEAM
STORED IN SPEAR

NOVEMBER 21, 1990 10:55 P.M.

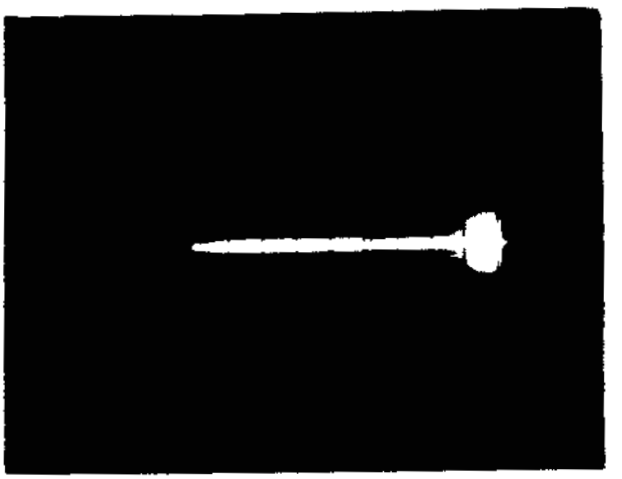

Nicole Sebek Heinz-Dieter Nuhn Helmut Wiedemann

Dave Hennegar R. Tighe

Jim Sebek

James Safranek

II. THE 3 GEV INJECTOR & ACCELERATOR PHYSICS RESEARCH

THE 3 GEV INJECTOR

Construction of the 3 GeV SPEAR injector ("booster") synchrotron was completed in 1990. Its commissioning and operation allows SSRL's physical independence from the SLAC linac. The parameters of the injector are shown in Table 4 and a description of the components follows the table.

Initial funding for this $14 million project was received in February 1988. The construction project was officially completed 33 months later, on November 29, 1990, within budget and within schedule. Most of the components were fabricated by the end of 1989 and the main effort in 1990 was completion of component installation, individual system tests and commissioning of the entire injector complex.

Commissioning of the Injector - By late March 1990 most of the major components were ready for systems tests, which were carried out through April and May. The linac preinjector was completed first. Beam tests began on the RF-gun and the first linac section while the last of the ring components were still being installed.

By the middle of May beam tests with the RF gun, alpha magnet and beam chopper (Figure 5) were advanced enough to start beam acceleration in the first linac section. On May 22 the first beam was accelerated to about 45 MeV, and shortly thereafter beam was accelerated down the complete linac. At this time only two of the three linac sections were powered and the total beam energy at the energy spectrometer was measured to be about 80 MeV. Intensity optimization soon led to reaching an intensity of 1.0×10^{10} electrons per second, surpassing the design intensity by 20%. By the first part of July all of the injection beam transport line and pulsed magnets were installed in the booster ring (Figure 6).

On July 19, 4000 turns were measured in the booster, on the first injection attempt. This significant step confirmed that many of the basic design objectives for the magnet, vacuum and power supply systems had been met.

During August the RF system was completed and tested. After initial regulation problems with the commercial main power supplies, the White Circuit was also completed and tested during August. The next step was beam acceleration and on September 7 the first beam was accelerated to 1.7 GeV.

While these tests were going on, the third linac modulator was completed, allowing acceleration of beam in the linac to a maximum of 137 MeV. The intensity was further increased to 1.5×10^{10} electrons/second. On September 24 beam was accelerated to 2.35 GeV, which is the present injection energy of SPEAR.

After observing the first synchrotron light from the booster on September 23, efforts were concentrated on improving the beam intensity at 2.35 GeV, which required delicate adjustments of the orbit and tunes during the energy ramping process. Ejection systems were completed during October, and the first beam was extracted from the booster on October 23. By November 13 beam had been sent down the beam transport line from the booster to SPEAR. These tests showed occasional radiation exceeding desirable limits. Shielding was added to the roof of the transport tunnel, bringing the radiation within required limits. After resumption of booster commissioning, first beam was stored in SPEAR from the new injector on November 21 at 10:55 p.m., or about 5 minutes before a two month site-wide shutdown of operations for utility upgrade work.

A week later, on November 29, the last DOE project review occurred and the construction project was accepted as complete.

TABLE 4

Design Parameters of the Injection System

Design Energy	3.0	GeV
Circumference	133.64	m
Particles	electrons	
Cycling Rate	10.0	Hz
Intensity	$>1.0 \times 10^{10}$	e-/sec
Number of Bunches	1	
Preinjector	linac	
Linac Frequency	2856	MHz
Energy of preinjector	>120	MeV
Storage Ring Filling Rate	>38.0	mA/min

Description of the Injector - The dedicated SPEAR injector system consists of a short linear accelerator with a beam energy of 120-150 MeV, a 3 GeV booster synchrotron and a beam transport line feeding the particles into the existing SPEAR injection line. At present the injector is limited to electrons, but the possibility of adding a future positron capability has not been excluded. The booster lattice is based on a simple FODO arrangement of the magnets with 20 equal FODO cells forming the total ring.

In collaboration with Varian Associates, a microwave gun was developed to produce a high brightness electron beam as the first step of the accelerator chain. Such an electron

FIGURE 5

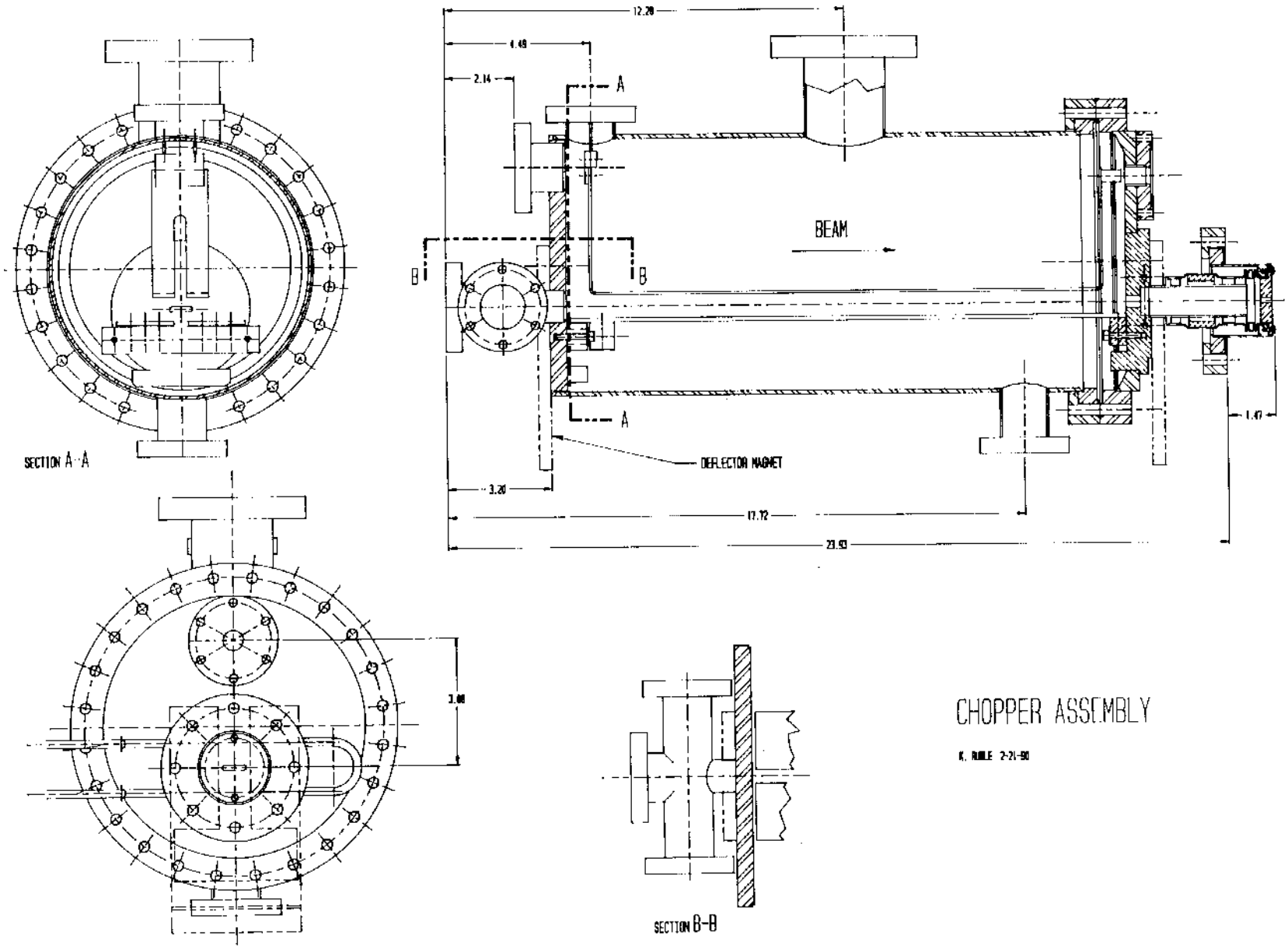

The Beam Chopper at the Electron Gun.
The chopper limits the number of S-Band bunches which can be accelerated per

FIGURE 6

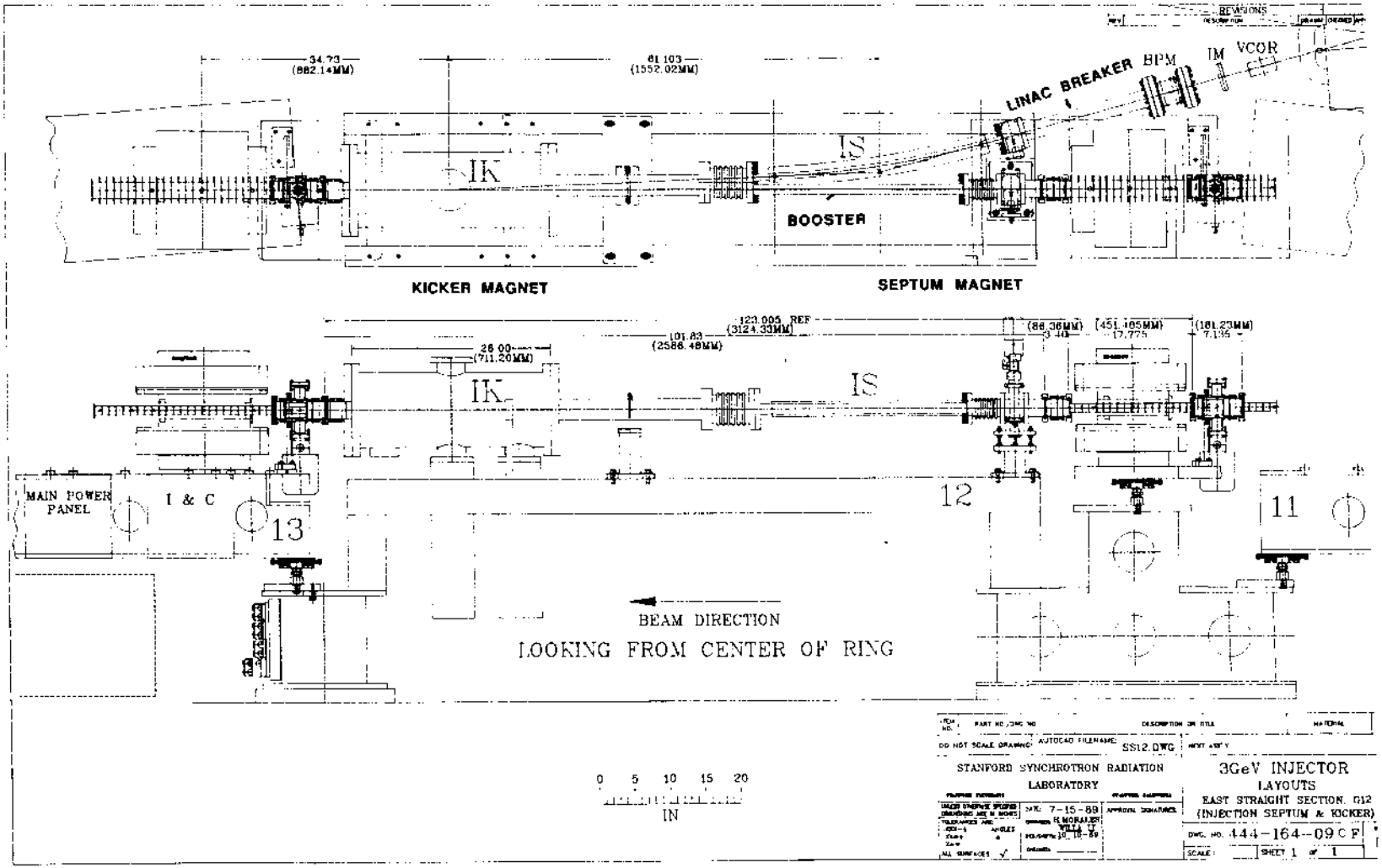

Beam Injection from the Linac into the Booster.

source consists of a cathode immersed into the electric field of an RF-cavity. Electrons emerging from the cathode through thermionic emission become accelerated immediately by a high RF electric field of the order of 75 MV/m and the repulsive electrostatic forces within the intense electron beam are compensated very quickly. As a consequence, the electron beam from a microwave gun has a much higher brightness than ordinary sources. The three linac modulator sections were constructed at SSRL, each driving one klystron connected to a ten foot long S-band accelerating section. The accelerator sections were manufactured at the High Energy Physics Laboratory in Beijing, Peoples Republic of China.

The 126 ring and transport line magnets were designed and manufactured at SSRL. In order to allow cycling the booster at 10 Hz, all ring magnet cores were constructed from laminations of magnetic steel. To minimize the interference of the booster with other sensitive facilities at the SLAC site, a White circuit was chosen to power the main magnets. In such a circuit the magnets are connected in parallel with capacitor banks to form a resonant circuit tuned to the operating frequency of the booster. The losses of this circuit are then compensated by energy pulses via magnetic chokes. All the magnets and the White circuit are designed for cycling up to 3.5 GeV at 10 to 15 Hz .

The vacuum chamber was also designed and fabricated at SSRL, using a technique pioneered by DESY in Hamburg, Germany. The vacuum chambers were constructed of 0.3 mm thick stainless steel tubes strengthened by external metallic ribs. In order to minimize maintenance complexity, a duplicate of the SPEAR RF system was used for the booster, and one of the original four accelerating cavities of SPEAR was reconditioned for the booster ring.

The injection and extraction transport systems were also designed and built at SSRL. The kicker magnets for injecting electrons into the booster and for extracting them out of the booster are ferrite picture frame magnets mounted inside the booster vacuum. The injection septum is a DC horizontal deflecting magnet. The extraction septum is a pulsed Lambertson type magnet which extracts the electrons vertically.

Figure 7 shows a number of the injector components. Figure 8 illustrates the booster control system.

Helmut Wiedemann, Director of the Injector Project, addressing the staff celebration of the first beam from the injector into SPEAR.

FIGURE 7

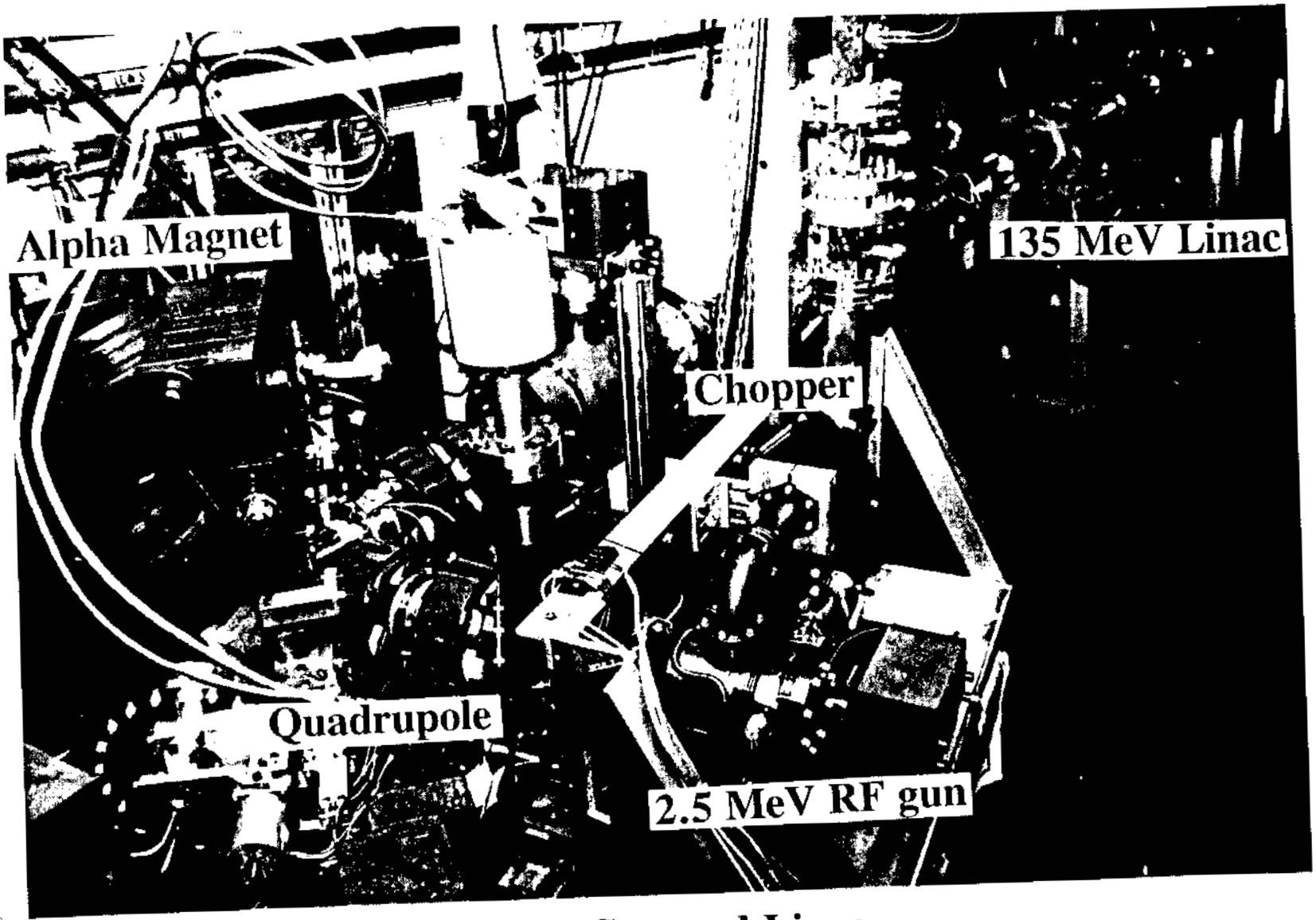

RF - Gun and Linac

FIGURE 8

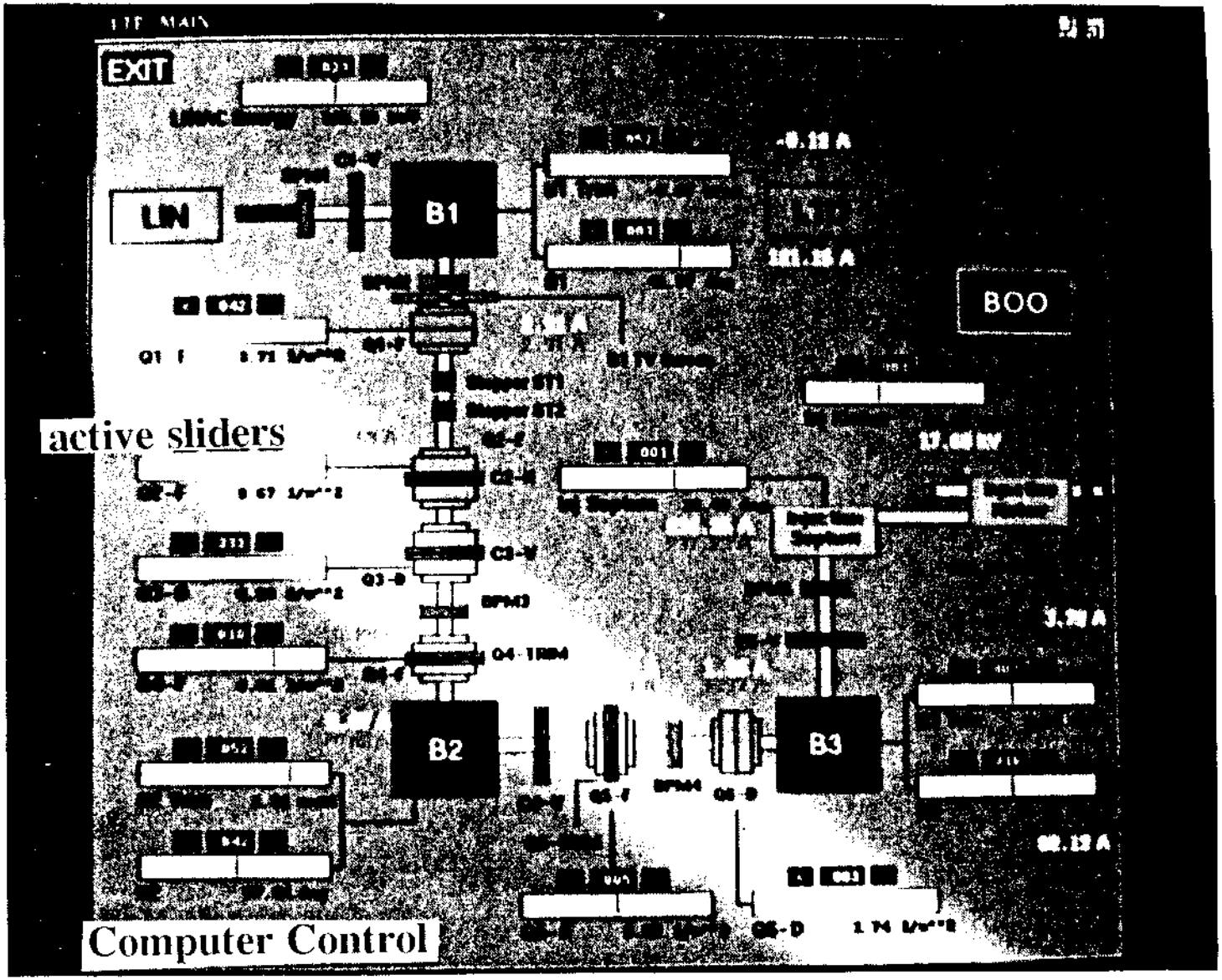

One of the Booster Control Panels showing the beam transport line from the linac to the booster.

ACCELERATOR PHYSICS RESEARCH

With the transition of SPEAR to a fully dedicated synchrotron radiation source with a fully dedicated injector, and with the announcement by SLAC that, due to a large budget reduction, PEP would not operate after the fall of 1990 for colliding beam physics, the emphasis on accelerator physics research and development has shifted to SPEAR.

SPEAR Studies - In collaboration with SLAC, a start-up program was carried out in March 1990 to characterize and understand the present SPEAR operational capabilities and identify its limitations. Specific studies included the calibration of the beam position monitor system using the circulating beam, a test of the SPEAR model, minimization of closed orbit deviation, optics corrections during the energy ramping, and photon beam steering.

This work indicated that the understanding of the SPEAR ring needs to be improved. The measurements of SPEAR optics parameters do not sufficiently agree with predictions made by the SPEAR model. Minimization of the closed orbit deviations could not be achieved down to the lowest desired values. The horizontal minimization process required retuning of the RF frequency to achieve low levels of closed orbit deviations, indicating misalignment problems.

The photon beam steering efforts showed that more work is needed to develop procedures and algorithms for independent control of each beam line. One of the reasons problems occur is that some of the beamline source points are located very close to each other.

Survey and Alignment - Work is in progress to evaluate survey data taken by the SLAC alignment crew of the SPEAR monuments. The goal is to understand the magnitude of SPEAR magnet misalignments and their impact on SPEAR operation. Measurements with the circulating beam will be carried out during the 1991 start-up to confirm the survey data and analysis. Results of these studies will be used to develop a plan to realign the SPEAR ring.

Revised Optics for Long Straight Sections - A study was carried out on modifications to the magnetic optics of the SPEAR long straight sections to accommodate longer insertion devices than is presently possible. In particular, an optics was developed to provide a free space of 5 meters for an undulator.

Ion Clearing - Following work done at CERN and at the UVSOR ring in Japan, equipment was assembled to clear positive ions, which sometimes are trapped in the circulating electron beam, by a resonant excitation technique, . Brief initial tests of this equipment with stored beam were carried out with inconclusive results.

Low Emittance Configurations for SPEAR - Implementation of a low emittance configuration in SPEAR has been precluded by the inability to inject into such a configuration. As part of the SPEAR Injector Project, a third kicker magnet was incorporated into the SPEAR injection system. This kicker was moved from its original position in the SPEAR positron injection line where it was no longer needed. This third kicker magnet, required to permit injection into the low emittance lattice, was installed in 1990. In parallel the details of a realistic low emittance configuration were worked out together with detailed studies of beam stability and the ability to accumulate beam. This work is the main part of a PhD thesis in accelerator physics by J. Safranek.

Other Accelerator Physics Research

Feedback Systems - In collaboration with scientists from SLAC and from Hiroshima University in Japan, design and construction of a longitudinal feedback system to increase the threshold for multi-bunch instabilities in PEP was initiated in 1989 and continued in 1990. The system is based on an existing 850 MHz cavity borrowed from SLAC. During 1990 modifications were completed to the cavity and waveguide system to broaden the bandwidth so feedback can be used to obtain longitudinal stability for up to 18 bunches. Following this, characterization tests of this system were carried out at low power level, and the cavity was installed in the PEP ring where it is now ready for tests with beam. Design and construction of the signal processing electronics continued through 1990. Following the shutdown of PEP by SLAC, work has been suspended. Efforts are now underway to use some of the equipment to study longitudinal instabilities in SPEAR.

FEL Studies - Exploration of the possibility that large circumference, high energy colliders such as PEP and TRISTAN can be used to produce very high levels of coherent power at short wavelengths by Self Amplified Spontaneous Emission (SASE). If successful, this approach would produce picosecond pulses of coherent, short wavelength (around 40Å) light with a peak power of several hundred megawatts and an average power up to about one watt. The wavelength around 40Å is particularly interesting because it is in the so-called "water window" between the carbon and oxygen absorption edges. This is the wavelength range most appropriate for biological imaging.

The SASE approach requires that low emittance, high peak current electron bunches with rather low energy spread radiate in a long (20-60 m) undulator. The interaction of the light and the electron beam travelling together through the undulator builds up a bunch density modulation in the electron beam at the desired optical wavelength in a single pass. When the bunch density modulation and the optical field intensity reach a high enough level, stimulated emis-

sion of coherent radiation grows exponentially in the last part of the undulator. The coherent power level ultimately saturates due to the energy spread induced in the electron beam.

The PEP ring has features which make it very suitable for this use. These include its large circumference (2.2 km), long straight sections (up to 117 m), and low bending magnet field (0.07 T at 3.5 GeV). The single pass approach to a short wavelength FEL eliminates the need for the optical cavity normally used in an FEL. It is the lack of availability of normal incidence reflectors that now sets the short wavelength limit of conventional FELs.

The necessary emittance (given by the wavelength/2 p) for wavelengths around 40Å can be reached by operating PEP at about 3-3.5 GeV, a fraction of its maximum energy (15 GeV), in a low emittance optics with extra emittance reduction provided by damping wigglers or the long FEL undulator itself. Study is needed to develop techniques for satisfying the other requirements; namely achieving high enough peak current with an acceptably small energy spread in the electron beam.

Super Low Emittance Damping Ring or Spatially Coherent X-ray Source - The minimum beam emittance in a storage ring is limited by aberrations caused from strong focusing. This aberration limits the beam stability and beam lifetime. The theoretical study concentrated on the fundamental limitations and an attempt to determine new nonlinear correction schemes to extend the minimum beam emittance achievable in storage rings down to the order of 10^{-11} rad-m. An electron beam of such a small emittance could provide a spatially coherent x-ray source or is required for future linear colliders to perform high energy physics experiments in the TeV regime. The fundamental contributions to aberrations have been studied in detail and compensatory schemes have been developed. As a test ring to apply nonlinear correction schemes a ring that would fit in the PEP tunnel has been chosen. With the developed correction methods applied to this ring a minimum beam emittance of 4×10^{-11} rad-m at 4 GeV could be achieved. This would be small enough to produce fully spatially coherent synchrotron light for wavelength down to about 4 Å and more than meets the requirements of future linear colliders. This work comprised the first Ph.D Thesis in Accelerator Physics at SSRL. *[L. Emery "A Wiggler Based Ultra Low Emittance Damping Ring Lattice and it's Chromatic Correction", Stanford University, August 1990].*

RF Electron Gun-Based Accelerator Physics

High Brightness Thermionic RF Electron Gun - High brightness electron beams can be extracted from RF guns. While such guns have been built for a long time little detailed theoretical work has been done to characterize this electron source and determine the parameters to obtain specific beam qualities. A thorough evaluation of high intensity beams in the accelerating RF field was conducted. Relationships between technical design characteristics and beam parameters were established and can now be used to construct RF guns optimized for desired beam characteristics. In this work such a gun was specified, designed, fabricated and installed as the electron source for the new SPEAR injector. Extensive experiments were conducted to correlate theory with observations. While such an RF gun with thermionic dispenser cathode proved to be a low cost, high intensity electron source for injectors and storage rings it also can be used to produce electron beams with a high peak current for FELs in the far infrared regime as well as very short particle and light pulses as short as 100 femtoseconds. This work has been conducted in collaboration with industry and SLAC and is the centerpiece of a PhD in accelerator physics *[M. Borland, "A High Brightness Thermionic Microwave Electron Gun", Stanford University, February 1991.]*

Spontaneous Coherent Synchrotron Radiation from 10 mm to 1 mm - Short electron bunches can be produced from the thermionic RF gun. For the particular gun design under study beam simulations show that intense bunches as short as 20 to 30 mm can be produced. Such short electron bunches emit spontaneous coherent radiation for wavelength of 20 to 30 mm and longer. The intensity of this coherent radiation is increased by a factor of N above the noncoherent radiation where N is the number of electrons in the bunch. The intensity of the bunches from the RF gun are of the order 10^9 electrons/bunch. A single RF gun together with an alpha magnet could thereby become an intense source of coherent synchrotron radiation in the far infrared regime with wavelength from tens of mm to 1 mm. Theoretical calculations were performed to evaluate and simulate the performance of such a source in more detail. In parallel, assembly of an experimental setup to produce such radiation has been started.

Generation of Femto Second Electron Pulses - The thermionic RF gun developed for the injector project exhibits interesting characteristics for other applications. Simulations show that it is possible to produce high intensity electron pulses of extremely short duration. Pulse durations as short as 100 femto seconds seem to be possible. After transforming such pulses into light equally short light pulses can be produced. Similar to ordinary synchrotron light these short light pulses also can be tuned by varying the field in the bending magnet or wiggler magnet. Theoretical and experimental investigation of the limits and causes for such limits on the pulse duration started in 1990.

III. CONFERENCES AND MEETINGS

During the first week in October, 1990 three events were held: a SPEARfest, celebrating twenty years of SPEAR's contributions to research and marking its new role as a fully dedicated synchrotron radiation source; the 17th annual Users Conference and a workshop to plan for a future 1-4 keV beam line.

1-4 keV Workshop - On Monday, October 1, a workshop devoted to the scientific opportunities of a proposed 1-4 keV beam line was held. This beam line is planned for the east long straight section of SPEAR which, with the dedication of SPEAR to synchrotron radiation, is now available for insertion devices. Among the talks at the workshop was a description of resonant magnetic x-ray scattering using 1-4 keV x-rays (D. Gibbs, BNL), EXAFS at the sulphur edge (G. George, EXXON) and x-ray microscopy using soft x-rays (C. Jacobsen, SUNY). A strong interest in circularly polarized light emerged. This interest led SSRL to change its plans for the the beam line to one incorporating a circularly polarized device.

17th Annual Users Meeting - The users meeting, chaired by Sean Brennan and Brad Pate, was held October 2nd and 3rd. The meeting focused on talks based on results from the April 1990 run. Highlights of the scientific talks included Z.X. Shen, Stanford University, describing a photoemission study of transition metal oxides; B. Clemens, Stanford University, describing diffraction work on relating the strains in sputtered metal multilayers to expitaxial growth stresses; R. Carr, SSRL, discussing a new design for an undulator device which changes the phase of the magnetic fields rather than the gap between the fields and T. Barbee, LLNL, describing EXAFS work of Cu deposited on W in a sputtering chamber mounted in the hutch on the beam line.

SPEARfest - The highlight of the week was the October 4, 1990, SPEARfest celebration. This event marked the transition of SPEAR to a dedicated synchrotron light source and commemorated the exciting physics of the past two decades. The morning scientific program included review talks by John Rees, Associate Director of SLAC, on the Genesis of SPEAR and Herman Winick, Deputy Director of SSRL, on the Genesis of SSRL. These talks were followed by two user reviews, one from Gerson Goldhaber, LBL, on the Great Particle Physics Discoveries at SPEAR and one from William Orme-Johnson, MIT, on The Role of SSRL in the Development of Synchrotron Science.

The afternoon festivities were kicked off by talks from Donald Kennedy, President of Stanford University, Robert Byer, Dean of Research, Donald Stevens, Department of Energy, Burton Richter, Director of SLAC and Arthur Bienenstock, Director of SSRL. The crowd then dispersed to a balloon-decorated SPEAR storage ring for refreshments and celebration.

Burton Richter addressing the SPEARfest gathering.

Burt Richter, Director of SLAC, handing the key to SPEAR to Arthur Bienenstock, Director of SSRL.

William Orme-Johnson, MIT, and Keith Hodgson, Associate Director of SSRL for Biotechnology.

Arthur Bienenstock,
Director of SSRL.

Donald Stevens addressing the SPEARfest gathering on behalf of the DOE.

Wolfgang Panofsky, SLAC Director Emeritus, and Boyce McDaniel, Cornell University.

Herman Winick (left), Deputy Director of SSRL and Arthur Bienenstock, Director.

George Brown, Associate Director SSRL (left) and Herman Winick, Deputy Director, SSRL.

Sebastian Doniach, first Director of SSRL, and David Moncton, Director of the Advanced Photon Source.

Burton Richter (above) and Wolfgang Panofsky (below) at the morning SPEARfest session.

SPEAR fest photographs by Tom Nakashima, SLAC

IV EXPERIMENTAL FACILITIES

Experimental stations at SSRL are of two types: general facility stations and participating research team (PRT) stations. General user stations have been funded by various government agencies, principally the DOE, NIH and NSF and are open to the user community on a competitive basis for most of their operating time. In addition to experimental stations there are facilities such as sample preparation laboratories, dark rooms and a machine shop available to users.

SSRL has three operational PRT's with a fourth in the final phases of constructing a beam line. All present PRT's are three part collaborations, with SSRL as one of the parties. The two outside institutions receive two-thirds of the available beam time while the other third is reserved for SSRL general users. The PRT arrangements are for a 3 year period. Renewal is based on review by an ad hoc committee, appointed by the Stanford University Dean of Research, which considers the quality of the research achievements, contributions to graduate student education and contributions to the SSRL user community.

Major beam line activity in late 1989 and 1990 was directed towards the March/April 1990 run. Beam line maintenance and upgrade activities were aimed at not only increasing capability but increasing reliability. This effort bore fruit in the March/April 1990 run and resulted in very reliable operation due to a very low incidence of accidental beam losses caused by beam line or equipment failure. A number of changes in user support policies were also tried during this run, in order to cope with a reduced beam line support staff. Experience during this run will serve as a guide for user support in future runs.

EXPERIMENTAL STATIONS

There are 13 x-ray stations located on six beam lines at SSRL. Two of these are PRT lines (wiggler lines 6 and 10). The other 11 are SSRL facility stations. Of the facility lines, two (Beam Lines 4 and 7) have wigglers as sources for six stations and the other two (Beam Lines 1 and 2), serving five stations, have bending magnet sources.

There are currently ten VUV or soft x-ray stations at SSRL. Four of these facilities were built by PRT's and the general user community has access to one-third of the time on these lines. The facilities being scheduled for users are: two TGM's (1-2 and 8-1), two grasshopper monochromators (1-1 and 3-1), a Seya-Namioka monochromator (3-2), an in-vacuum double crystal monochromator (3-3), a SGM (8-2) and the lithography/optics line (3-4). Two PRT lines, 6-1 and 5, are in the final stages of commissioning.

IMPROVEMENTS TO EXISTING STATIONS

Station 1-4 - The commercial version of the photodiode array for Station 1-4 and a modification of its detector to handle low temperature operation which were installed in 1989, were successfully used to collect small angle scattering data from polymer systems.

Station 1-5 - A new and more spacious hutch was constructed for the area detector diffractometer (Station 1-5 ES2). It allows improved access for sample crystal mounting and alignment, thereby making the system more convenient to use. This new enclosure replaces the portable hutch that had been in use since the area detector system was first built and allows the diffractometer to be bolted to the floor for greater stability. There is now enough space for an additional detector, which will greatly enhance the efficiency of data collection, and for a liquid-nitrogen cryostat. In many instances, cooling the sample crystals down to liquid nitrogen temperatures has dramatically reduced the radiation damage to the sample.

An x-ray polarimeter, to dynamically monitor the polarization of the incident x-ray beam, has been fabricated and is currently being installed. This will enable more accurate polarization corrections to be made to the data, which is important because the net diffracted intensity varies as a function of the polarization of the incident beam.

The software has also been modified to implement an improved dead-time correction that will permit measurement of sharp diffraction peaks with a higher degree of accuracy. Furthermore, semi-automatic crystal alignment software from the area detector manufacturer has been incorporated into the system. These improvements are clearly important since the success of the multi-wavelength anomalous scattering phasing technique depends on the collection of very accurate data.

Station 2-2 - Two precision double-axis goniometers for plane wave monochromatic topography, high resolution rocking curve measurements and other diffraction experiments have been installed on the white light station, 2-2. The new instruments will allow quantitative studies of defects, strains and thin films/interface characterization in Si, II-VI, and III-V materials technology as well as new materials.

Station 4-2 - Modifications have been made on Station 4-2 in order to implement a semidedicated small angle scattering (SAS) system in the end station hutch. This system is particularly effective for anomalous small-angle

scattering, as it couples well to the Brown/Hower variable photon energy monochromators on SSRL's standard x-ray beam lines.

Station 7-1 - A number of improvements were made to the Station 7-1 (rotation camera) monochromator. The liquid nitrogen cryostat built in 1989 was tested, and further low temperature tests were performed on protein samples. The cryostat has proved to be very stable over long running periods and is economical in the use of liquid nitrogen. This cryostat is available to users and was used by two groups in the April/May run.

Station 10-2 (National Laboratories/University of California/SSRL) - As described in the 1989 Activity Report, the beam line was modified to allow operation without the Be window module, thereby providing spectral coverage in the soft x-ray region. A differential pumping section was installed to serve as a transition from UHV to HV. Tests and characterization of the modifications were made during the spring run but were limited because the present monochromator cooling was insufficient to operate at full wiggler field.

In the April run, a quick-scan EXAFS capability was implemented. R. Frahm (HASYLAB) collaborated with J. Wong (LLNL) to install this new capability using a continuous motor drive and a software package developed at HASYLAB. This new tool was used successfully to perform a number of time-resolved experiments in the time domain of seconds and milliseconds. These included measurements of high temperature solid combustion processes and in-situ thin film growth of Cu on W using a glancing angle fluorescence collection geometry. With a photon flux of 10^{12} photons/s at the sample plane at full wiggler field of 1.45 T and SPEAR operating at 3.0 GeV and ~ 100 ma, Beam Line 10-2 is extremely suitable for performance of quick-scan EXAFS experiments.

Optimization of Stations 6-2 (EXXON/LBL/SSRL) and 10-2 - After extensive discussions between SSRL, LLNL and LBL, it was agreed that the users would be best served if Station 10-2 were reserved for hard x-ray use and Station 6-2 were modified for operation into the soft x-ray region. As a result, a new water-cooled, high vacuum monochromator has been designed for Station 6-2 and the 10-2 differential pumping system (described above) will be installed on Station 6-2. This will allow operation with a single thin Be window after the monochromator and will permit photon energies as low as 2.05 keV to be reached using Si(111) monochromator crystals, with about a two order of magnitude increase in flux at 2.3 keV. This low energy spectral region is particularly important since it covers the absorption edges of elements like P, S, and Cl.

White Light Capability on 10-2 - During the past year major progress has been made towards the development of a new white beam Laue diffraction facility on Station 10-2 at SSRL. This facility will enable time-resolved protein crystallographic experiments to be performed. The design and fabrication of the necessary beam line and hutch components to convert the high power 31-pole wiggler to have a white beam capability have been completed. This has involved the redesign of the beam line components to handle the very high intensity white x-ray beam and the design of the relevant personnel protection devices to permit the safe use of the beam. A Laue camera is also being designed and constructed at this time, which incor-

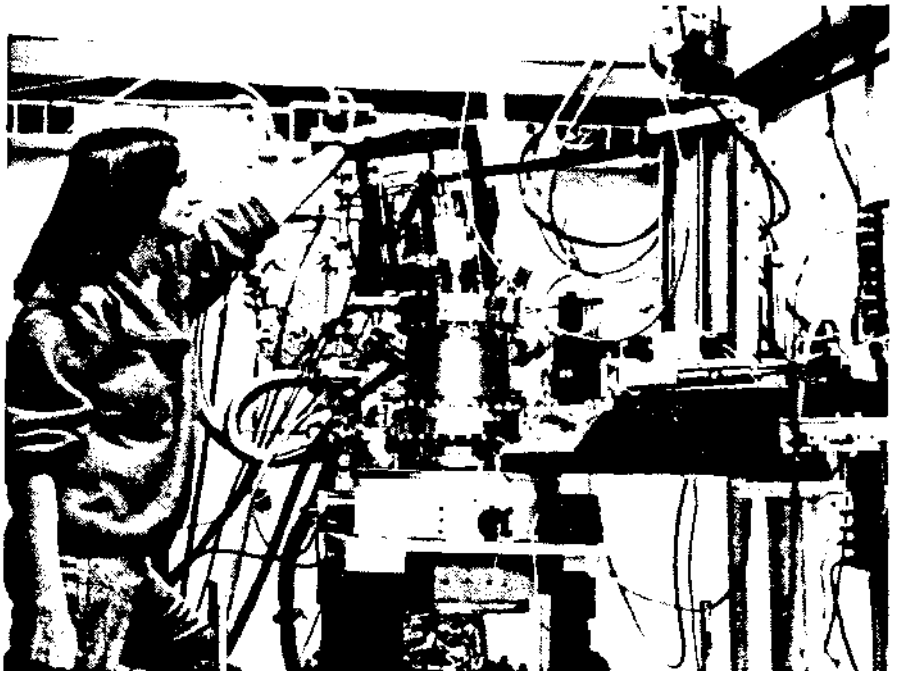

Stanford graduate student, Janet Kahn, with a ultra-high vacuum surface diffractometer used for studying disordered systems.

porates a water cooled collimator and a two-circle goniometer with motorized sample translation. When completed, this camera will be fully automated for convenient alignment to the x-ray beam.

New Mirrors - New mirrors have been installed in Stations 2-1 and 3-3. The mirror in Station 3-3 (JUMBO) has replaced the original mirror, which had been severely damaged by radiation after 10 years of use.

NEW EXPERIMENTAL STATIONS

Station 10-1 (IBM/Stanford University-Center for Materials Research/SSRL) - On Station 10-1, the new soft x-ray branch line, all major components were completed and readied for installation. These are: M0, branch line stoppers, M1 and the monochromator. Considerable difficulty was encountered in qualifying the commercially supplied M0 and M1 mirrors for ultrahigh vacuum use. The mirrors are fabricated from a technology new at SSRL which employs a silicon carbide coating on graphite. These mirrors have been successfully used at HASYLAB in Hamburg. The M0 was eventually qualified, but the M1 had to be returned to the manufacturer for further work. The M1 should be returned from the manufacturer early in 1991.

Beam Line 5 (Xerox/Stanford University-Stanford Electronics Lab/SSRL) - On Beam Line 5, the main activity during the April run was directed at getting performance data on the WUNDER monochromator in which three of the four gratings were tested. Results were obtained using the 2° grating on the carbon 1s core exciton peak in diamond with a resolution of approximately 0.15 eV (Figure 9). The ultimate resolution of the monochromator is 0.08 eV for this region and should be achieved with more operational experience. Using the 10° grating, the resolution at the aluminum 2p edge at 75 eV was found to be 0.055 eV. Aside from an alignment error that was found for the 4° grating, no major problems were encountered. In particular, the repairs to the cooling system made after the 1989 run seem to have been successful.

The fact that the resolutions are so close to the design goals at this stage of commissioning is very promising. The design

FIGURE 9

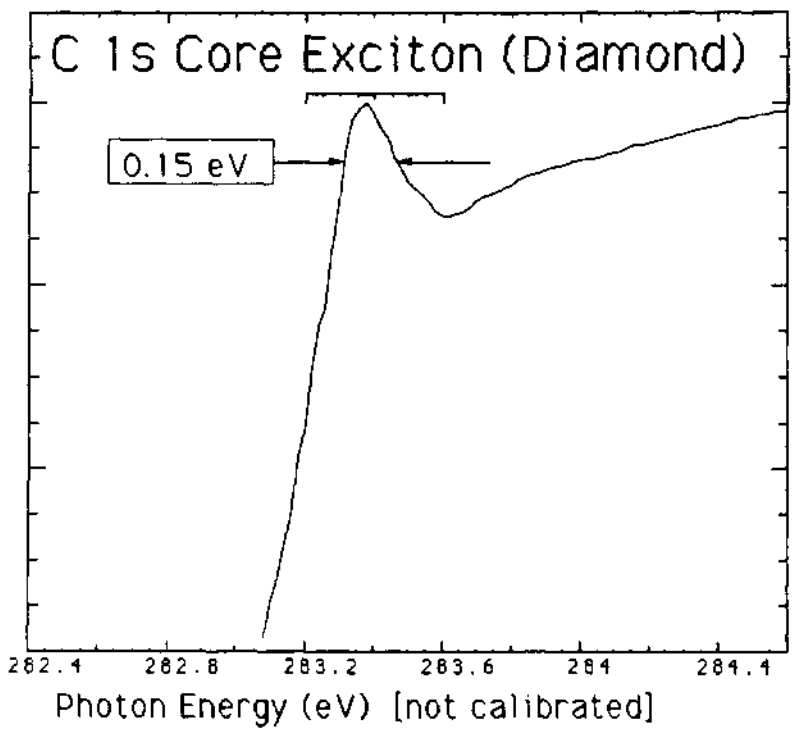

There was very limited time for experimental data taking during the April/May run, but the Stanford side station on Beam Line 5 was used by B. Pate and J. Wu to obtain total electron yield curves on diamond samples. Using the 2° grating, and 10 μ entrance and exit slits, they were able to resolve the carbon 1s core exciton peak near the carbon K edge of diamond, with a resolution of about 0.15 eV. The ultimate resolution of the monochromator is expected to be about 0.08 eV for this region, but this result already compares well with the 0.10 eV peak width measured with the Dragon monochromator at NSLS.

FIGURE 10

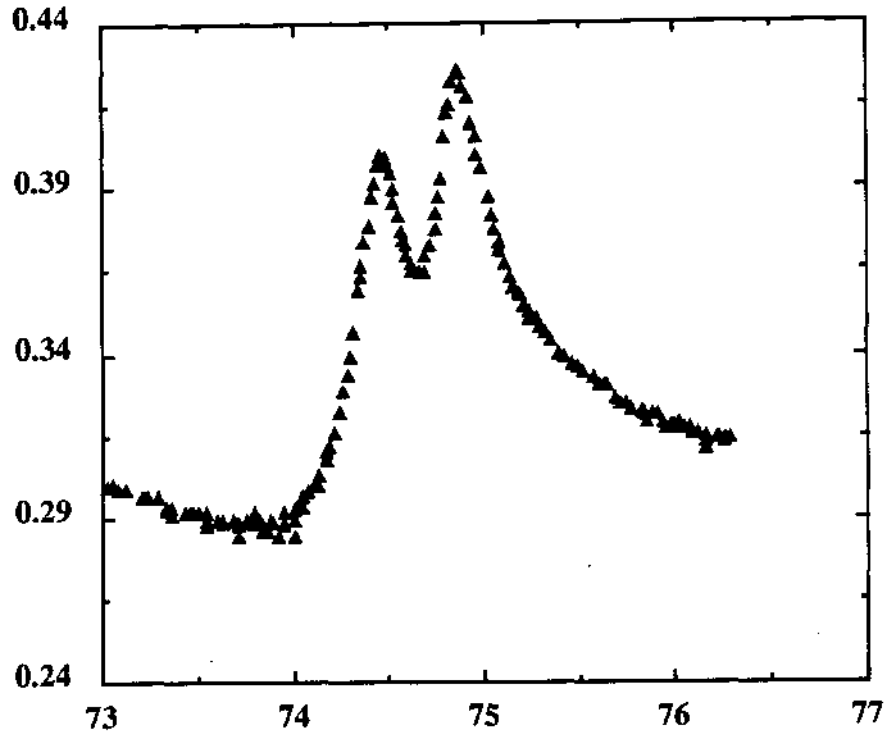

Jon Erickson (Naval Weapons Center, China Lake) obtained the total yield scans in Figure10 from the Al 2p levels on AlAs(100) using the 10^{O} grating and 10 m slits during the April/May run. The resolution obtained at 75 eV was 0.055 meV.

goals of this monochromator are to have high resolution and high throughput. The resolutions of 1000-2000 already achieved are comparable to the SX-700 and Extended Range Grasshopper (ERG) monochromators in this energy region. The design goals of the WUNDER monochromator performance are similar to that of the SX-700.

Design and development work on a novel specular/multilayer takeoff mirror for Beam Line 5 continued. Modeling studies for the spectral-angular distribution of 10 eV photons for a proposed high-intensity molecular-desorption experiment were concluded. Further studies were initiated on the use of the same mirror as a polarized-light reflector for polarized-light instrumentation development and science on the take-off line following the anticipated installation of a polarizing insertion device in the Beam Line 5 straight section. This project is led by R. Tatchyn.

SPECIAL PROJECTS

In December, 1990, a prototype silicon x-ray monochromator employing microchannel water cooling was tested by the SSRL x-ray group, led by J. Arthur, at the CHESS storage ring (Cornell University). The new CHESS wiggler beam line produces x-ray power levels which approach those expected from the APS, and which greatly exceed the capabilities of standard methods for crystal cooling. The microchannel cooling proved to be as effective as calculations had indicated, and adequate for the heat load presented by the CHESS beam line. The next goal is to perfect the microchannel manufacturing process and to produce a monochromator designed for extended service both at SSRL and CHESS. It is expected that microchannel cooling will be used in many future monochromators at APS and PEP beam lines.

Design Study of Adjustable Phase Insertion Devices as X-ray Sources - An insertion device, such as an undulator, consists of rows of magnets with alternating field directions; one row is placed above the electron beam of a storage ring, another below it. The conventional method of tuning the x-ray spectrum output is by changing the gap between the rows, which changes the vertical magnetic field between the rows. However, if the rows are shifted longitudinally with respect to each other, this will also change the vertical field over the same range as for an adjustable gap device. In a theoretical design study of the adjustable phase approach, it has been shown that the two devices produce very much the same x-ray spectrum, but that there are some significant design advantages with phase adjustability. An adjustable phase device produces a constant vertical tune shift in the storage ring, while the adjustable gap device's vertical tune shift varies as the square of the vertical field strength, which is in turn exponentially dependent on the gap. Thus an adjustable phase device should be much less difficult for storage ring operations, particularly if it is desired to tune the x-ray output dynamically while other users are running.

An adjustable phase device may also be built with a much simpler mechanical structure, just a simple rail on which one of the magnet rows slides by one half the period length. The change of field is not exponential with motion, but only sinusoidal, which should make motion control easier. An adjustable phase design might also be preferred for a very long insertion device, because it could be built with small enough cross section to allow quadrupole magnets to surround it, thus keeping the beta function low in a long beampipe; this is infeasible with an adjustable gap device. This project is led by R. Carr.

FIGURE 11

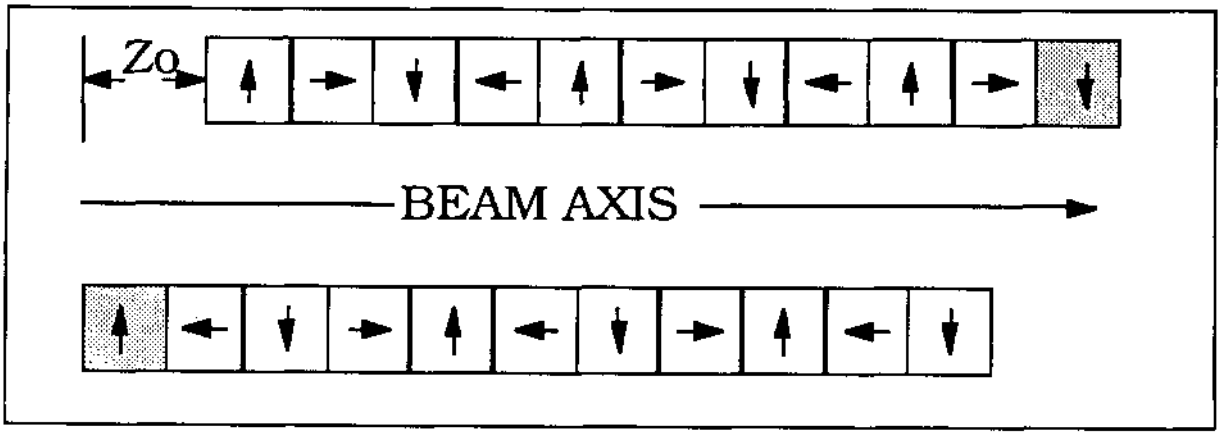

Figure 11 shows a side view of three periods of an adjustable phase insertion device, with arrows indicating the direction of the easy axis of magnetization for blocks of permanent magnet material. Zo indicates the relative phase shift of the two rows of magnets.

SUPPORT FACILITIES

Mirror Coating Facility - The SSRL mirror coating facility coated 22 mirrors in 1990. The facility continues to coat high quality thin film mirrors for laboratories such as NSLS, AT&T Bell Labs, SSRL and users at Colorado School of Mines. The mirror coating system is currently set up to evaporate platinum, nickel, rhodium, gold and chromium. The system was updated this year with a computer for systems control as well as a quadrupole mass analyzer.

Computer Systems - Major progress was made in 1990 in the development of new data acquisition software and installation of the VAXstations required to run it on the experimental stations. This effort required two stages. The first stage, that of development of low-level hardware control systems to communicate with the beam line components and graphics I/O subsystem interfacing is complete. Currently proceeding is the development of the high-level applications programs which understand the nuances of the individual experiments. The first such "incarnation" of the application program supports EXAFS data collection and was tested during the April, 1990 run at SSRL by several user groups. By June 1990, all but one of the PDP-11's had been retired and replaced with VAXstations.

Tony Cox demonstrates the new MIDAS program during the Users Conference

V. SSRL ORGANIZATION

SSRL is organized into three functional divisons: the Accelerator Research and Operations Division (AROD), the Photon Research and Operations Division (PROD) and the Computing and Administration Resources Division (CARD). The functions of the AROD Division are to operate, maintain and develop the booster and SPEAR as well as performing research on these and future machines. The functions of the PROD Division are beam line managment, beam line development, research using the synchrotron radiation and user support. The CARD group provides central computing services for scientific research, user data collection and administrative purposes as well as business services, contract management, personnel and facility administration.

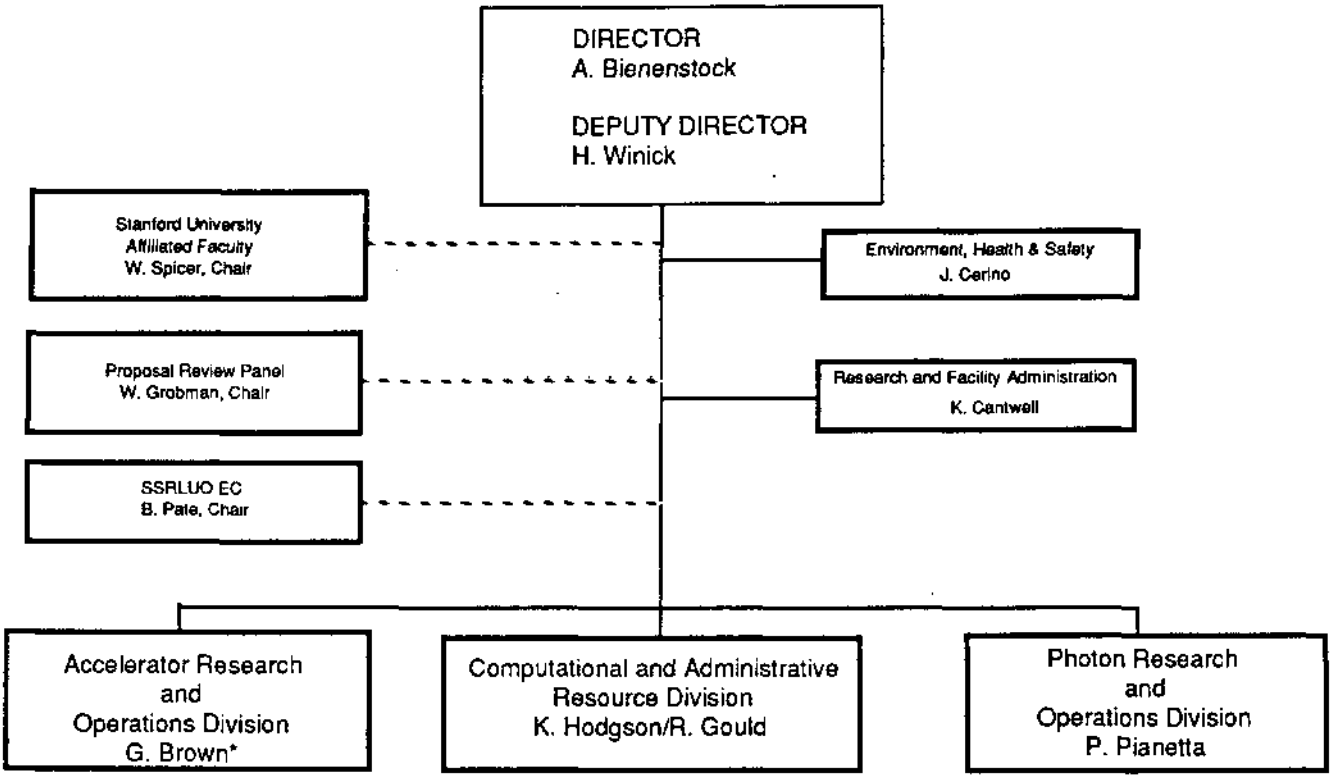

SSRL ORGANIZATION CHART

** Dr. George Brown served as head of the AROD division during 1990. On May 1, 1991 Dr. Max Cornacchia took over this position.*

SSRL EXPERIMENTAL STATIONS
RESPONSIBLE PERSONNEL

BRANCH LINE		RESPONSIBLE PERSON(S)
1-1	Grasshopper	F. Coffman
1-2	TGM	M. Rowen
1-4	SAS	H. Tompkins
1-5	Unfocused Bend Magnet	H. Tompkins
1-5 ES2	Area Detector	P. Phizackerley/H. Bellamy
2-1	Focused Bend Magnet	H. Tompkins
2-2	White Radiation	Z. Rek
2-3	Unfocused Bend Magnet	H. Tompkins
3-1	Grasshopper	F. Coffman
3-2	Seya - Soft X-ray	F. Coffman
3-3	Jumbo - Soft X-ray	M. Rowen
3-4	Lithography	P. Pianetta
4-1	8-Pole Wiggler	H. Tompkins
4-2	8-Pole Wiggler	H. Tompkins
4-3	8-Pole Wiggler (Materials Diffraction)	H. Tompkins
5	Mutli-Undulator	R. Carr/F. Coffman
6-1	54- Pole Wiggler - SGM	R. Tatchyn*(SSRL)*, P. Heimann *(LBL)*
6-2	54- Pole Wiggler	J. Arthur *(SSRL)*, G. George, *(EXXON)*, P. Ross *(LBL)*
7-1	8-Pole Wiggler (Rotation Camera)	P. Phizackerley/M. Soltis
7-2	8-Pole Wiggler (Scattering)	S. Brennan
7-3	8-Pole Wiggler	H. Tompkins
8-1	TGM	M. Rowen *(SSRL)*, J. Tobin *(LLNL)*, S. Williams *(UCLA)*
8-2	SGM	M. Rowen *(SSRL)*, G. Tirsell *(LLNL)*, J. Tobin *(LLNL)*
10-2	31- Pole Wiggler	S. Brennan *(SSRL)*, J. Wong *(LLNL)*, M. Nicol *(UCLA)*

INSTRUMENTATION/FACILITY RESPONSIBILITIES

MATERIALS DIFFRACTOMETER: S. Brennan, H. Tompkins
PERKIN-ELMER CHAMBER: M. Rowen
VG SAMPLE CHAMBER: M. Rowen
AREA DETECTOR: P. Phizackerley, H. Bellamy
ROTATION CAMERA: P. Phizackerley, M. Soltis
CAD-4 DIFFRACTOMETER: M. Soltis
COMPUTER SYSTEMS and SOFTWARE: T. Cox
7-2 SPECTROMETER: S. Brennan, H. Tompkins
SAMPLE PREPARATION LABORATORY: B. Hedman, R. Mayer
DARKROOMS: M. Soltis, Z. Rek
EXAFS EQUIPMENT: B. Hedman, R. Mayer
SAS CAMERA (BIOTECH): D. Eliezer
EXAFS CONSULTANT: B. Hedman
SCATTERING CONSULTANTS: S. Brennan. J. Arthur
TOPOGRAPHY EQUIPMENT: Z. Rek

SSRL ADVISORY BOARDS

PROPOSAL REVIEW PANEL

A main task of the Proposal Review Panel is the review and rating of scientific proposals to SSRL based largely on reports obtained from outside (non-panel) referees. During 1990 the panel met only once, on June 7-8 and rated the new proposals which had been received in September 1989 and March, 1990.

As of January 1, 1991 SSRL had received a total of 2133 proposals of which 133 are presently active.

The Proposal Review Panel meets twice yearly, generally in June and January. Deadlines for receipt of proposals for consideration at the next meeting are the first of September and the first of March each year.

The panel members in 1990 were:

Biology Sub-panel
Don Engelman, Yale University
Willaim Orme-Johnson, MIT
Douglas Rees, Cal Tech

Materials Sub-panel
Howard Birnbaum, University of Illinois
G. Slade Cargill, IBM
Russell Chianelli, EXXON
Peter Pershan, Harvard University

VUV Sub-panel
Warren Grobman, IBM *(Chair)*
Torgny Gustafsson, Rutgers University
Victor Henrich, Yale University

SCIENCE POLICY BOARD

The Science Policy Board reviews all aspects of SSRL operation, development and plans for the future. It reports to Stanford University President, Donald Kennedy. The Board met once during this reporting period, on May 4-5, 1990. Members of the 1990 Board were:

Craig Barrett, Intel Corporation
Praveen Chaudhari, IBM
Marvin Cohen, University of California
Edward Ginzton, Varian
Ed Knapp, Los Alamos National Laboratory
Walter Kohn, University of California
Boyce McDaniel, Cornell University *(Chair)*
Venkatesh Narayanamurti, Sandia National Laboratory
Yves Petroff, LURE
William Orme-Johnson, MIT
Mark Wrighton, MIT

SSRL USERS ORGANIZATION

Members of the Executive Commitee of the SSRLUO were appointed at the 17th Annual SSRL Users Group Meeting as follows:

C. Richard Brundle, IBM-Almaden
Stephen Cramer, UC Davis/LBL
Paul Fuoss, AT&T Bell Laboratories *(Vice Chair)*
Philip Heimann, LBL
Janet Kahn, Stanford University
Paul King, Stanford University
Stephen Laderman, Hewlett-Packard
Brad Pate, Washington State University, *(Chair)*
David Templeton, LBL
James Tobin, LLNL
Katherine Cantwell *(Secretary-SSRL Liaison)*

VI. EXPERIMENTAL PROGRESS REPORTS

MATERIALS PROPOSALS

VUV PROPOSALS

BIOLOGY PROPOSALS

X-RAY ABSORPTION STUDIES OF DISORDERED SYSTEMS

PROPOSAL NO. 100M

E.D. Crozier and D. Jiang
Physics Department, Simon Fraser University, Burnaby, B.C., Canada V5A 1S6

R.Ingalls and J. Freund
Physics Department, University of Washington, Seattle, WA, 98195, U.S.A.

Introduction

During our April 1990 run at beamline IV-1 we continued our study of the structure of ultrathin magnetic films only a few monolayers thick grown by molecular beam epitaxy. This class of films has unusal anisotropic properties, metastable structures which do not exist in nature and superlattices with unexpected exchange and electron transport properties. The details of the structure are central to an improved understanding of the films.

In the following we first discuss additional developments in the application of the glancing incidence EXAFS technique to the structure of buried films. We then indicate that 9 ML (monolayers) of Cu epitaxially grown on Ag(001) and buried beneath an epitaxially grown film of Au has a metastable body centered tetragonal structure.

Buried films: Glancing-incidence EXAFS

In applications of the glancing-incidence EXAFS technique it is normally stated that a buried film or substrate can only be studied at angles less than its critical angle for total reflection, θ_c, if the θ_c of the covering layer is smaller. But this is not valid for thin covering layers. Fig. 1 shows the electric field amplitudes, E, as a function of depth, z, of penetration of the evanescent wave from the Au surface of the Au(10ML)/Cu(9ML)/Ag/(001) system at an x-ray energy of 8985 eV. At this energy the θ_c for Au, Cu, and Ag, are 8.6, 5.6 and 6.9 mrad respectively for vacuum/solid interfaces. E_R and E_T are the reflected and transmitted amplitudes and $E_{Total} = E_R + E_T$. At the angle of incidence of the figure, $\theta = 5.6$ mrad, there is a clear enhancement of E_T in the buried Cu film. This also occurs at smaller and larger θ and at other energies. Our calculations indicate that experimentally useful penetration into the Cu layer will occur for covering films of Au up to 30 Å thick. With higher brilliance sources, measurements may be feasible for covering layers up to ~50 Å thick

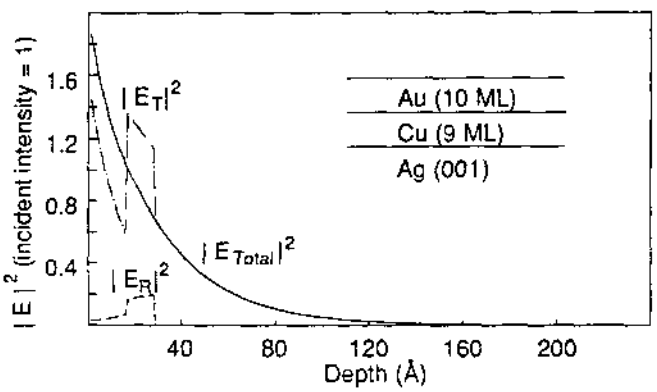

In applying the glancing-incidence EXAFS technique to probe the structure of a surface region, spurious EXAFS/XANES results can occur due to anomalous dispersion and the energy and angular dependence of the x-ray penetration depth. In the case of our 9 ML Cu film, in measuring the Cu K-edge spectra, the Cu itself is too thin to be affected by these effects. However, what we wish to emphasize here is that significant distortion of XANES spectra can still result from background contributions to the total signal measured in the three main detection methods: reflectivity, fluorescence, and total electron yield. For example, in the present study, surprisingly, the energy and angular dependence of the fluorescence and total electron yield of the Au and Ag background signal produce a large distortion. By appropriate filters, the fluorescent spectra can be made independent of anomalous background contributions. This was done for the Cu results summarized below.

The structure of Metastable Cu on Ag(001)

We have examined 9 monolayers (ML) of Cu epitaxially grown on Ag(001) and covered with 10 ML of Au. Using XPD, Egelhoff (J.Vac. Sci A8 (1990) 1582) found that Cu in the Cu/Ag(001) system forms a metastable nearly "bcc" structure rather than the normal fcc of bulk Cu. Our EXAFS shows that the Cu is body centered tetragonal with the c-axis (perpendicular to the substrate) being expanded 7% relative to the a-axis (Jiang, Crozier, Heinrich). This system is important in the context of the magnetic behaviour of Fe/Cu/Fe trilayers on Ag(001). Heinrich (Phys. Rev. Lett. 64 (1990) 673) has shown that the exchange coupling depends on the thickness of the Cu interlayer, changing from ferromagnetic to antiferromagnetic for greater than 8 Ml of Cu. Theoretical attempts to explain the antiferromagnetism assuming a pure bcc structure have failed. In further studies we will examine the Cu structure as a function of Cu thickness to see if there is a thickness-dependent tetragonal distortion which correlates with the ferromagnetic/antiferromagnetic behaviour.

The results for 9ML Cu are also relevant to the theory of XAS. Fcc Cu has been a traditional testing ground for first principle calculations of XANES spectra. The body centered tetragonal Cu spectrum will provide an important test of the calculation methods that have been developed. The XANES of 9 ML Cu is compared with spectra from bulk samples of fcc Cu and bcc Fe in Fig. 2.

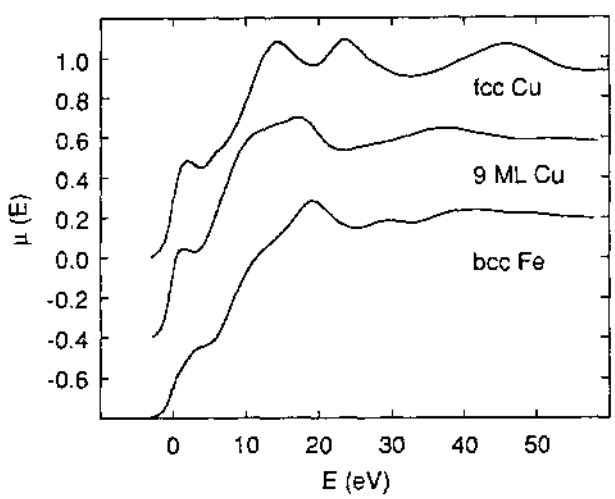

STRUCTURAL DETERMINATION OF IRON-BASED CATALYSTS IN ION-EXCHANGED COAL

M. Mehdi Taghiei, Frank E. Huggins, Naresh Shah and Gerald P. Huffman

University of Kentucky
233 Mining and Minerals Resources Building
Lexington, KY 40506

Introduction

The economical production of synthetic liquid fuels from coal depends upon the effective use of catalysts. Use of catalysts for coal liquefaction was first introduced in 1924, and has remained a topic of interest till this day.

The product of an ion-exchange process in which an ion such as calcium is exchanged for a catalytic ion like iron yields a highly dispersed catalytic species for coal liquefaction. In this study, an attempt has been made to determine the structural form of iron species in ion-exchanged coal by the means of x-ray absorption fine structure (XAFS) spectroscopy. In situ observation of the spectra was also made at elevated temperatures in appropriate atmosphere.

Experimental

Ion-Exchange Process:

Experiments were conducted with a lignite (PSOC 1482) from the Fort Union region in North Dakota. The coal was first ground to <200 mesh under a nitrogen atmosphere. In order to remove inorganic minerals like clays, quartz, pyrite, etc., the ground coal was floated in carbon tetrachloride ($\rho = 1.55$). A 1:10 mixture by wt. of coal and CCl_4 was left undisturbed in a separating funnel until two distinct layers formed. The floated coal was then filtered off and washed with 5N HCl for further demineralization of the coal and to exchange the metal cations bound to carboxyl groups with hydrogen cations. The coal was further washed with distilled water and air dried to constant weight.

Samples of demineralized coal were mixed with freshly made iron(II)acetate and iron(II)chloride solutions with pH values of 5.45 and 2.5, respectively. These mixtures were stirred at 40°C for 24 hours under a N_2 atmosphere. After the process was completed, the coal was filtered off. To remove the adhering salt from the ion-exchanged coal, the samples were repeatedly washed with distilled water until the pH value of the filtrate for two consecutive washes was constant.

XAFS Study:

XAFS spectra were obtained at beam line IV-3 at the Stanford Synchrotron Radiation Laboratory. Iron K-edge XAFS spectra of the ion-exchanged coal samples were taken both in transmission and fluorescent mode using a Si(111) double crystal monochromator. The energy was calibrated with respect to metallic iron foil by assigning 7112.0 eV to the inflection of the pre-edge peak on the absorption edge. Further XAFS measurements were conducted on iron-impregnated Wyodak coal samples provided by Dr. J. Shabtai of University of Utah.

Results and Discussion

Figure 1 compares the XANES spectra of α-FeOOH to the spectra of different coals treated with iron compounds. It is evident that the spectra are similar.

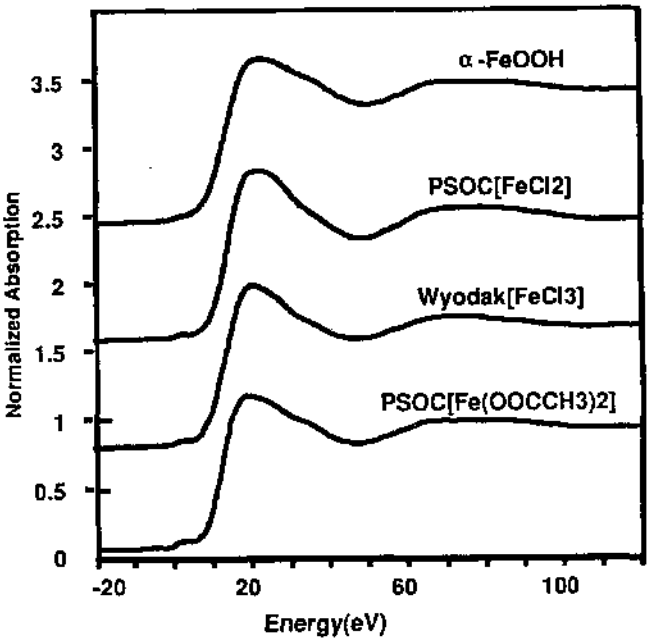

Figure 1. Comparison of XANES spectra of ion-exchanged coal samples with reference model compound.

The Fourier transform of the EXAFS or radial structure function (RSF) of several ion-exchanged coals are compared to those of standard compounds in Figures 2 and 3. Figure 2 compares the RSF of magnetite and ion-exchanged lignite treated with a 0.05M solution of iron(II)acetate. In Figure 3 the RSF of α-FeOOH is compared to that of lignite ion-exchanged in an 0.025M solution of $FeCl_2$ and an 0.025M solution of $Fe(OOCCH_3)_2$. It is seen that the RSF of the more concentrated ion-exchanged sample is similar to magnetite, while the less concentrated samples exhibited RSFs similar to goethite. However it is evident that the amplitude of the third and fourth iron nearest neighbor shells are reduced significantly relative to the bulk compounds. As discussed elsewhere[1], this occurs because the particle sizes are only a few nanometers in diameter, and a significant percentage of the iron does not have a full complement of third and fourth nearest neighbors.

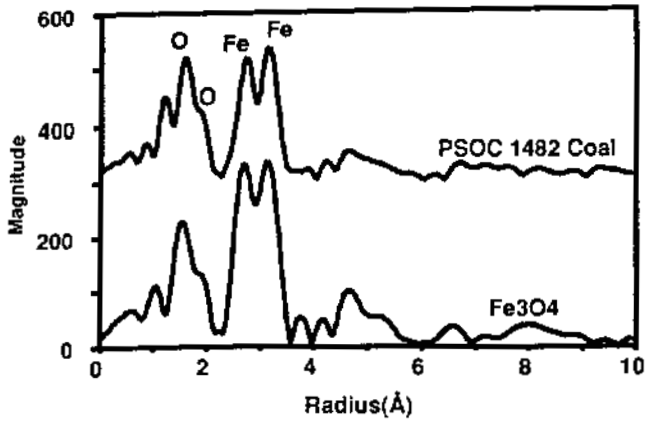

Figure 2. Comparison of RSF's between ion-exchanged PSOC 1482 coal treated with Fe(OOCCH3)2 and magnetite.

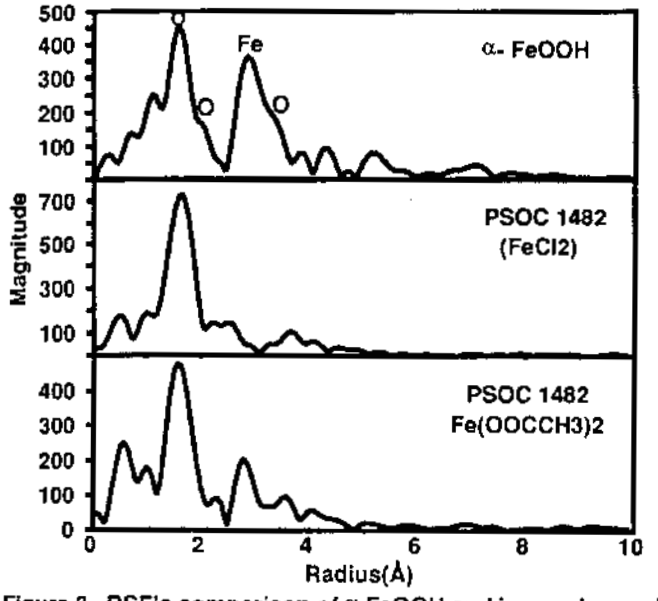

Figure 3. RSF's comparison of α-FeOOH and ion-exchanged lignite treated with FeCl2 anf Fe(CCOOH3)2.

In situ high temperature experiments under either helium or hydrogen at atmospheric pressure indicate no evidence of any significant change in the structure and electronic state of iron in ion-exchanged lignite at temperatures up to 450°C. Typical RSF's are shown in Figure 4. However, when sufficient sulfur is present, the iron is transformed to pyrrhotite ($Fe_{1-x}S$) under these conditions. This is illustrated by Figure 5, which shows in situ spectra obtained from the $FeCl_3$-impregnated Wyodak coal when 10% elemental sulfur is added to the sample. Similar reactions have been noticed under high pressure liquefaction conditions. For instance, Figure 6 shows the comparison of the RSF of pyrrhotite derived from ion-exchanged lignite during liquefaction in a microautoclave at 385°C and 427°C at 800psig H_2 atmosphere with that of pure pyrrhotite.

Further studies are in progress in order to reveal more clearly the nature of highly dispersed iron-based catalysts and their transformations in coal liquefaction.

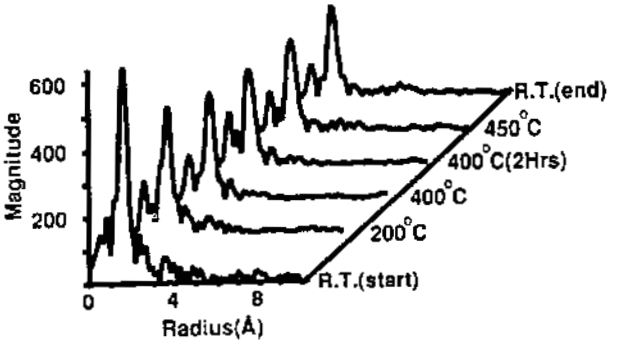

Figure 4. In situ treatment of ion-exchanged PSOC 1482 treated with FeCl2 under H2 atmosphere.

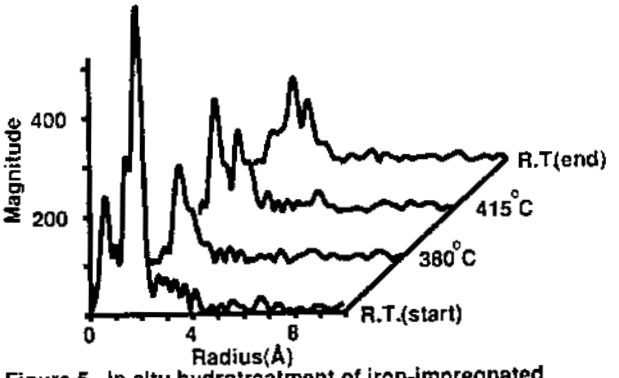

Figure 5. In situ hydrotreatment of iron-impregnated Wyodak with 10% elemental sulfur.

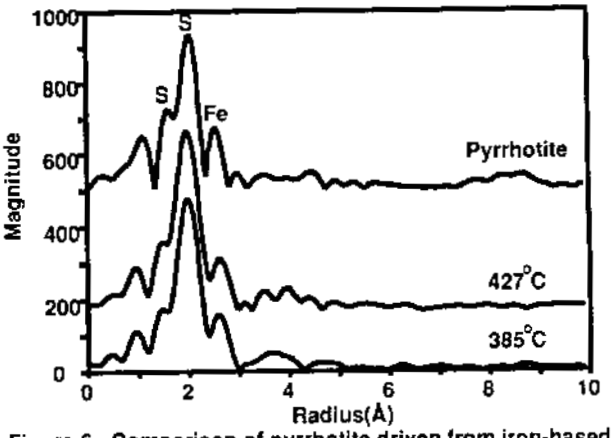

Figure 6. Comparison of pyrrhotite driven from iron-based catalyst during liquefaction with bulk pyrrhotite.

Reference:

(1) G. P. Huffman et al., "Structure and Dispersion of Iron-Based Direct Coal Liquefaction Catalysts", submitted to Energy & Fuels, (1991).

Acknowledgment: The authors acknowledge the Department of Energy for providing the support for this research through contract No. DE-FC22-89PC89851.

In-Situ High-Temperature X-ray Absorption Study of Ferrous Iron in Orthosilicate Crystals and Liquids

W.E. Jackson[1], G.E. Brown, Jr.[1], G.A. Waychunas[2], J. Mustre[3], S.D. Conradson[3], J.M. Combes[4]

[1]Department of Geology, Stanford University, Stanford, CA 94305 USA
[2]Center for Materials Research, Stanford University, Stanford, CA 94305 USA
[3]MEE-11, Los Alamos National Laboratory, Los Alamos, NM 87545 USA
[4]St. Gobain Recherche, 39, quai Lefranc, 93304 Aubervilliers, France

Introduction

The following paper was presented at the XAFS VI conference in York, England, in August of 1990, and has been published in XAFS VI, X-Ray Absorption Fine Structure VI, ed. S.S. Hasnain, Chishester, U.K., Ellis Horwood Ltd, Publishers.

An *in-situ* high-temperature EXAFS study has been conducted to clarify the structural role of ferrous iron in orthosilicate (i.e. Q^0) liquids of compositions Fe_2SiO_4 (fayalite), $CaFeSiO_4$ (kirschsteinite), and $Fe_3Al_2Si_3O_{12}$ (almandine). The high-temperature EXAFS data collected from the orthosilicate liquids were modeled with high-temperature Fe-EXAFS data collected from a crystalline model compound of composition $Ca_3Fe_2Si_3O_{12}$. The degree to which ferrous iron behaves as a network former or network modifier greatly affects certain bulk physical properties of Fe^{2+}-bearing silicate liquids, such as viscosity and density. Ultimately, structural information extracted from these very depolymerized crystals and liquids is required to interpret and model the propagation of seismic waves in the mantle and lower crust of the Earth where phases of these compositions predominate.

Most past structural information on Fe^{2+} in silicate 'liquids' has come from studies of glasses which may not necessarily have the same average structure as the corresponding liquid due to possible structural rearrangements during the quench. Low glass transition temperatures associated with highly depolymerized liquids suggest major structural rearrangement during glass formation and, hence, large differences between glass and liquid structure. Analogously, large contributions of configurational entropy to the entropy of fusion calculated for the melting of orthosilicates (relative to more polymerized silicates) [1] also suggests major structural differences between crystal and liquid which may be a consequence of both short-range (local coordination environment) and long-range reordering at fusion temperatures.

Experimental

Fe K-EXAFS data for the crystalline model compound $Ca_3Fe_2Si_3O_{12}$ and fluorescence Fe K-EXAFS data for the liquids were collected at NSLS on BL X19A and X23B and SSRL on BL 4-1 and 7-3. Each study used Si (111) monochromator crystals. High temperature data were collected with a Stern-Heald type detector and a water cooled, controlled-atmosphere (by use of a Mo/MoO buffer and N_2 atmosphere), resistive-type (Mo coils) furnace capable of sustaining temperatures up to 1750 K for several hours. The crystals and liquids were contained in isostatically pressed BN and BeO, respectively. Low temperature data were collected by means of a liquid N_2 dewar assembly. In each case the crucibles did not react with the samples and Mossbauer spectroscopic analyses of the quench crystals, following high-temperature data collection, indicated no more than 5 mol % of the iron was ferric.

Data Analysis

To correctly model high-temperature EXAFS data, anharmonic vibrations of the Fe-O pair must be considered (e.g. [2]). As a consequence, the harmonic potential associated with the Debye-Waller type factor, which implicitly generates a Gaussian distribution of bond distances, must be replaced with an asymmetric potential which correctly models the thermal expansion of the crystalline model compounds. This modeling yields a non-Gaussian distribution of bond distances and a component of the RDF at high R (asymmetric tail) which is otherwise lost due to the low-k data truncation. The RDF is derived directly from a model potential determined from a non-linear least squares fit between calculated and experimental EXAFS data. This approach permits the treatment of highly anharmonic motion that cannot be treated using series expansions of the Debye-Waller factor (cumulant expansions). The functional form of the model chi function taken as a thermal or time average is given by:

$$\langle\chi\rangle = \int dr\ g(r)\ \chi(k, r(x))$$

Where χ (k, r (x)) describes all the usual EXAFS modeling parameters except a Debye-Waller term, and $r = R + x$, where x denotes displacement relative to the average pair distance R. (For a more complete description, see [3]). The calculated and normalized RDF and the anharmonic potential for oxygen are given by:

$$g(r) = \frac{e^{\frac{-V(r)}{kT}}}{\int dr\ e^{\frac{-V(r)}{kT}}} \qquad V(r) = a\left\{\left[\frac{r_0}{r}\right]^{12} - 2\left[\frac{r_0}{r}\right]^{6}\right\}$$

In this potential well, 'a' is the depth of the well corresponding to the energy or temperature of uncorrelated pair motion (i.e., Einstein oscillators) and r_0 is related to the minimum of the well and the electronic structure of the Fe-O bond.

$Ca_3Fe_2Si_3O_{12}$ contains Fe^{3+} in a regular octahedral coordination environment and was chosen for its nominally zero static disorder (only thermal disorder) at low temperatures and the fact that Fe^{3+} in octahedral coordination is similar to the bond distance of Fe^{2+} in tetrahedral coordination with oxygen (at 300 K: $^{VI}Fe^{3+}$-O ~ 2.02 A, $^{IV}Fe^{2+}$-O ~ 2.00 A). Phase and amplitude information were extracted from the 90 K EXAFS data and held constant in all fits as a function of temperature. The phase shift was found to be ~ 0.50 A. In each case the coordination number of iron was fixed at six oxygens. The high-temperature Fe K-EXAFS data for $Ca_3Fe_2Si_3O_{12}$ were collected at 90 K, 300 K, 415 K, 670 K, 870 K, and 1070 K. A comparison of the Fourier transforms of the anharmonic fits to the Fourier filtered $k^3\chi(k)$ data including the calculated FT at 1575 K is given in Figure 1. Figure 2 illustrates the good agreement between anharmonic theory and the Fe-O bond distance taken from refinements of the crystal structure at high temperature [4]. Harmonic fits result in distances ~ 0.1 A too short at the maximum temperature. Figures 1 and 2 show that the apparent bond length contraction caused by truncating the low-k data is correctly modeled by the anharmonic theory.

Assuming that thermal disorder is much greater than static disorder at very high temperatures [5,6] and that the Fe-O bonds in the liquids may be adequately described with a 12-8 potential, we plot the experimental Fourier transforms for the liquids with respect to the high-temperature (1573 K) $Ca_3Fe_2Si_3O_{12}$ Fourier transform to establish the Fe-O distances in the liquids. Figure 3 plots the Fourier transforms for Fe_2SiO_4 liquid (1525 K), $CaFeSiO_4$ liquid (1525 K), and $Fe_3Al_2Si_3O_{12}$ liquid (1585 K) along with crystalline $Ca_3Fe_2Si_3O_{12}$ (1573 K). Taking the high temperature Fe-O pair in $Ca_3Fe_2Si_3O_{12}$ (2.07 A) as the model for estimating an anharmonic correction to the observed bond distances, the relative Fe-O bond distances in the liquids are 1.95

A (Fe_2SiO_4, compare with crystal: ^{VI}Fe-O, 2.16 A), 1.95 A ($CaFeSiO_4$, crystal: ^{VI}Fe-O, 2.16 A), and 2.10 A ($Fe_3Al_2Si_3O_{12}$, crystal ^{VIII}Fe-O, 2.30 A). When compared with values extracted from crystalline silicates and oxides, these bond distances are consistent with ferrous iron in 4-coordinated sites in Fe_2SiO_4 and $CaFeSiO_4$ liquids, and 6-coordinated in $Fe_3Al_2Si_3O_{12}$ liquid. This result indicates that the coordination number of Fe^{2+} is reduced on melting these crystalline phases. This is analogous to coordination number increases for ferrous iron across high-pressure first-order phase transitions. Static disorder effects will tend to increase these average bond distances on the order of several hundredths of an angstrom. XANES spectra for Fe_2SiO_4 crystal, $Fe_3Al_2Si_3O_{12}$ liquid, $CaFeSiO_4$ liquid, Fe_2SiO_4 liquid, Fe_2SiO_4 glass and crystalline $FeAl_2O_4$ (spinel, $^{IV}Fe^{2+}$ - O, 2.00 A) are illustrated in Figure 4. The 1s → 3d electronic transition intensity (arrow) suggests that Fe site distortion in the $CaFeSiO_4$ liquid, Fe_2SiO_4 liquid, and Fe_2SiO_4 glass are comparable to that in the tetrahedral site in $FeAl_2O_4$. The 1s → 3d transition in $Fe_3Al_2Si_3O_{12}$ liquid represents a more centrosymmetric coordination environment and is similar to the pre-edge feature for Fe^{2+} in the octahedral sites of Fe_2SiO_4. These observations are consistent with the EXAFS results.

The EXAFS suggestion of tetrahedrally coordinated Fe^{2+} in Fe_2SiO_4 liquid is similar to the EXAFS [7] and Raman [8] results for Fe_2SiO_4 glass. The presence of tetrahedrally coordinated Fe offers the possibility of a pressure-induced coordination change from 4 to 6 deep in the Earth. This coordination change may be a driving force for nucleation and subsequent growth of $(Mg,Fe)_2SiO_4$ crystals and may be related to delineation of the bottom of the mantle's low velocity zone which is considered a boundary between crystalline material and a region of liquid plus crystals. The pressure at this boundary (~ 10 GPa) is close to the pressure at which Fe_2SiO_4 crystallizes from its liquid at high temperature.

Acknowledgments

This work was supported by NSF grants EAR-8513488 and EAR-8917437. We acknowledge support of the SSRL and NSLS staffs.

References

[1] Jeanloz, R. (1985) In *Reviews in Mineralogy Vol. 14: Microscopic to Macroscopic*, Mineralogical Society of America 1985, 428p.

[2] Eisenberger, P., and Brown, G.S. (1979), Solid State Communications, 29, 481-484.

[3] Mustre, J., Conradson, S.D., Bishop, A.R., Batistic, I., Jackson, W.E., Brown, G.E., Jr., Waychunas, G.A. (this volume)

[4] Rakai, R.J. (1975), M.Sc thesis, Univ. British Columbia.

[5] Smyth, J.R. (1975) Am. Min., 60, 1092-1097.

[6] Waychunas, G.A., Brown, G.E., Jr., Jackson, W.E., and Ponader, C.W. (1988) Nature 332, 251-253.

[7] Jackson, W.E., Brown, G.E., Jr., Waychunas, G.A., and Cooney, T. (1990) (In preparation)

[8] Cooney T., and Sharma, S.K., (1990) J. Non-Crystalline Solids (In press)

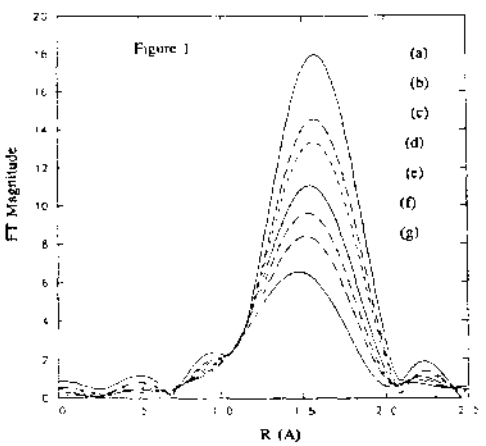

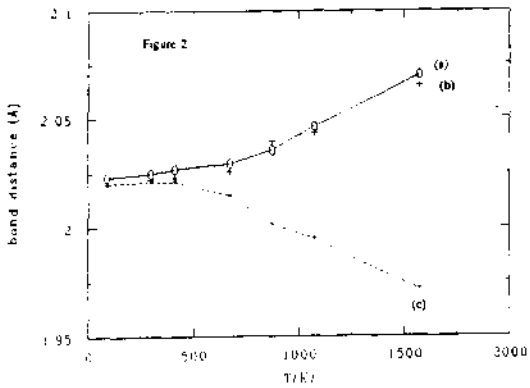

Figure 1. Fourier transforms of the anharmonic fits to the $Ca_3Fe_2Si_3O_{12}$ Fe K-EXAFS data at (a) 90 K, (b) 300 K, (c) 415 K, (d) 670 K, (e) 870 K, (f) 1070 K, (g) 1573 K. Phase shift ~ 0.50 A. Anharmonic correction ~ 0.10 A. $R_{1573\,K}$ ~ 1.46 A.

Figure 2. Fe-O bond distances as a function of temperature for (a) Ovals: Anharmonic theory fits to experimental Fe K-EXAFS data collected from $Ca_3Fe_2Si_3O_{12}$. (b) Pluses: Structure refinements [5]. (c) Stars: Harmonic fits illustrating loss of phase information due to low-k data truncation. Iron coordination number equals six in all fits.

Figure 3. Fourier transforms of $k^3\ \chi$ (k) silicate liquid data for (a) $CaFeSiO_4$ (1.95 A), (b) Fe_2SiO_4 (1.95 A), (c) $Fe_3Al_2Si_3O_{12}$ (2.10 A). Fe-O bond distances reported are corrected for phase shifts and anharmonic effects.

Figure 4. Fe K-XANES data for (a) Fe_2SiO_4 crystal, (b) $Fe_3Al_2Si_3O_{12}$ liquid (c) $CaFeSiO_4$ liquid (d) Fe_2SiO_4 liquid (e) Fe_2SiO_4 glass, and (f) $FeAl_2O_4$ crystal. The coordination environment of Fe^{2+} in liquids (c), (d) and (e) is tetrahedral while the coordination environment for Fe^{2+} in liquid (b) is octahedral. (E_0 fixed at 7111 eV).

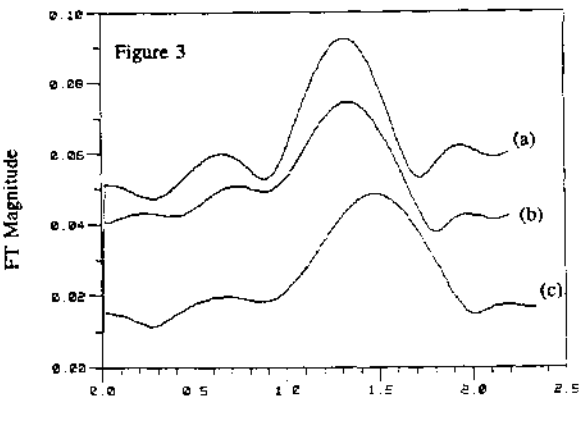

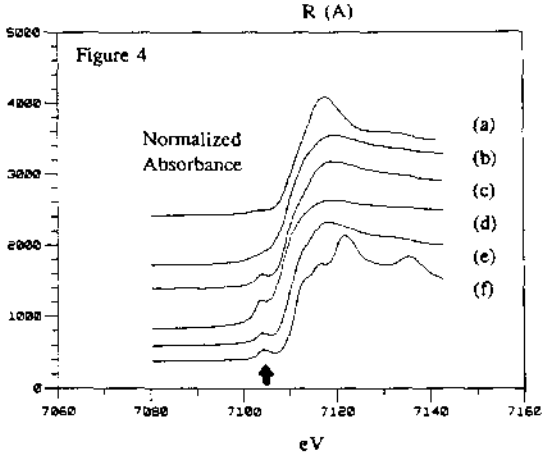

PROPOSAL NO. 995Mp

EXAFS STUDY OF AQUEOUS Co(II) SORPTION COMPLEXES ON KAOLINITE AND QUARTZ SURFACES

P. A. O'Day, G. E. Brown, Jr., and G. A. Parks
Surface and Aqueous Geochemistry Group, School of Earth Sciences,
Stanford University, Stanford CA., USA 94305

This article was presented at the 6th International Conference on X-ray Absorption Fine Structure, York, England, and will be published in the Conference Proceedings (ed. S.S. Hasnain) (Ellis-Horwood Publishers, in press).

INTRODUCTION

Uptake of metal ions from aqueous solutions by mineral substrates occurs through formation of surface precipitates or complexes whose molecular structures are not well known. Previous chemical and spectroscopic studies of sorption on oxides and kaolinite have suggested that, at low sorption densities (Γ), Co(II) sorbs as Co^{2+} or simple mononuclear hydroxo complexes such as $CoOH^+$ [1,2]. At high Γ, it is proposed that the sorption complex is a polymeric hydroxide-like species or a surface precipitate of $Co(OH)_2$, even in solutions undersaturated with respect to $Co(OH)_2$(s) [1,3]. Alternatively, James *et al.* [4] suggest that "low to high molecular weight polymeric hydrolysis products" form on the surface as intermediates between mononuclear sorption complexes and surface precipitates. X-ray absorption spectroscopy allows quantitative structural characterization of *in situ* sorption complexes which can be used to distinguish among types of surface species and, thus, to understand and predict the partitioning of metal ions in natural systems and industrial processes. In this study, EXAFS spectroscopy has been used to characterize the local coordination environment of aqueous Co(II) complexes sorbed to a natural clay, kaolinite, and ground quartz, α-SiO_2, in an effort to distinguish between adsorbed polymeric species and surface precipitates.

EXPERIMENTAL

Sorption samples were prepared using variable solution concentrations of Co(II) (0.6 - 18.5 x 10^{-3}M) and pH-adjusted to achieve $\geq$ 95% uptake of cobalt. In Co/kaolinite sample A and Co/quartz samples A and B, the solubility of both the thermodynamically stable, pink form of $Co(OH)_2$ (called "inactive", designated "i") and the metastable blue form (called "active" or "a") [5] was exceeded. For the other sorption samples, $Co(OH)_2$ saturation was not reached and surface coverages (Γ = 3 to 10 μmoles/m^2) represent about 25 to 50% of a surface layer of closest-packed oxygen-coordinated Co^{2+} ions. Final pH of the solutions ranged from 7.60 to 10.70. Cobalt K-edge (7720 eV) fluorescence-yield x-ray absorption spectra were collected at ambient conditions on wet sorption samples and an aqueous 12 mM $Co(NO_3)_2$ solution on wiggler beamlines at SSRL and NSLS; spectra for aged, solid $Co(OH)_2$(i) were collected in transmission mode. Data were analyzed using the plane-wave formalism and empirical phaseshift and amplitude parameters derived from several well-characterized model compounds [6] to determine distance (R), coordination number (CN), and relative Debye-Waller factor ($\Delta\sigma^2$) of first-, second-, and fourth-shell cobalt neighbors.

RESULTS

Normalized EXAFS of sorption samples and $Co(OH)_2$(i) show distinct beat patterns not found in the spectra of Co^{2+}(aq) (Figure 1). These beats suggest the presence of cobalt backscatterers in the second and greater coordination shells of sorbed cobalt, indicating clustering or precipitation. However, EXAFS spectra of sorption samples are not identical to that of solid $Co(OH)_2$(i). Best fits of the Fourier-filtered EXAFS spectra show that sorbed Co(II) is coordinated by 6 first-shell oxygens at 2.08 $\pm$ 0.02 Å on both kaolinite and quartz (Table 1). The average second-neighbor Co-Co distances in the sorption samples are slightly shorter (3.10 - 3.16 $\pm$ 0.02 Å) than in $Co(OH)_2$(i) (3.17 Å) (Table 1), and the number of second-neighbor cobalt atoms increases with increasing surface coverage. At the lowest surface coverages, the average number of second-shell cobalt atoms is higher on kaolinite (CN = 3.9) than on quartz (CN = 2.6), suggesting smaller clusters of cobalt atoms on quartz than on kaolinite at similar Γ. Fits of the second-shell EXAFS spectra at low surface coverages (Γ= 5 and 3 μmoles/m^2) are improved by including an atom from the solid, M_s = Al or Si, in the empirical fit. Best fits yield a Co-M_s distance of 3.26 $\pm$ 0.02 Å in both sorption samples which indicate direct bonding of cobalt complexes to oxygen atoms on the mineral surfaces [7]. At higher coverages, good fits are obtained with only Co included in the second shell. Small relative Debye-Waller factors for the sorption samples ($\Delta\sigma^2$ = -0.008 to 0.005 $Å^2$) suggest atomic disorder similar to that of the model compounds.

A peak at high R (5.2 - 5.8 Å) in the radial structure functions (RSF) of the sorption samples results from multiple scattering among colinear, equidistant cobalt atoms [8] in the fourth coordination shell around a central cobalt, as in the RSF of $Co(OH)_2$(i) (Figure 2). In the RSF of the sorption samples, this peak is at lower R than in $Co(OH)_2$(i) and shifts to still lower R as cobalt surface coverage decreases on quartz (Figure 2). Best fits of the sorption sample spectra using empirical parameters from $Co(OH)_2$(i) yield average distances which are shorter and coordination numbers which are smaller than those of $Co(OH)_2$(i) (Table 1). Futhermore, in sample solutions where the solubility of $Co(OH)_2$(i) and $Co(OH)_2$(a) was exceeded, distances are 0.15 Å shorter than in $Co(OH)_2$(i) and fourth-shell CN = 3 to 4, compared to CN = 6 in $Co(OH)_2$(i).

CONCLUSIONS

At very low Γ (<1 μmole/m^2), Chisholm-Brause et al. [7] used EXAFS to demonstrate that Co(II) forms mononuclear sorption complexes on γ-Al_2O_3. With increasing Γ (3 to 10 μmoles/m^2) on kaolinite and quartz, second- and fourth-shell cobalt CN increases, but Co-Co distances are shorter and the average number of cobalt neighbors is significantly less than in $Co(OH)_2$(i) (Table 1). Futhermore, the presence of atoms from the solid in the second shell at a distance of 3.26 Å suggests largely two-dimensional, multinuclear adsorption complexes bonded directly to oxygen atoms on the surface. Above $Co(OH)_2$(i) and $Co(OH)_2$(a) solubility, EXAFS analyses show that the surface species formed on kaolinite and quartz are not identical to $Co(OH)_2$(i), implying that they are not well-ordered, crystalline $Co(OH)_2$(i). An average of 6 second-shell cobalt neighbors and the lack of a significant contribution from M_s suggest a large (probably > 50 Co atoms), three-dimensional phase. However, fourth-shell distances shorter than in $Co(OH)_2$(i) and fourth-shell CN $\leq$ 4 suggests that the sorbed cobalt could be either (1) a more disordered phase of $Co(OH)_2$(i), (2) small particles of $Co(OH)_2$(i), or (3) a precipitate with a contracted $Co(OH)_2$(i)-like structure. The EXAFS spectrocopic results of this study and [7] are consistent with previous interpretations from solution chemistry [4] that surface hydrolysis and adsorption proceeds from mononuclear adsorption complexes, through multinuclear adsorption complexes of increasing size as the system approaches saturation, to precipitation of a three-dimensional hydroxide phase as the solubility of the solid hydroxide is exceeded.

ACKNOWLEDGEMENTS

This work is supported by U.S. National Science Foundation grant EAR-8805440. We thank the staffs of SSRL and NSLS, and C.J. Chisholm-Brause for valuable assistance.

REFERENCES

[1] James, R.O., and Healy, T.W., J. Colloid Int. Sci., **40**, 53 (1972).
[2] Dillard, J.G., and Koppelman, M.H., J. Colloid Int. Sci., **87**, 46 (1982).
[3] Tewari, P.H., and McIntyre, AIChE Symp. Ser., Sci., **71(150)**, 134 (1975).
[4] James, R.O., Stiglich, P.J., and Healy, T.W., Farad. Disc. Chemical Soc., **59**, 142 (1975).
[5] Fietknecht, W., and Hartmann, L., Chimia, **8**, 95 (1954).
[6] Chisholm-Brause, C.J., O'Day, P.A., Brown, G.E. Jr., and Parks, G.A., Nature, **348**, 528 (1990).
[7] Chisholm-Brause, C.J., Brown, G.E. Jr., and Parks, G.A., Proc. 6th Int. Conf. on X-ray Absorption Fine Structure (ed. S.S. Hasnain) (Ellis-Horwood Publishers, in press).
[8] Co, M.S., Hendrickson, W.A., Hodgson, K.O., and Doniach, S.J., J. Amer. Chem. Soc., **105**, 2748 (1978).
[9] Lotmar, V.W., and Feitknecht, W., Z. Kristallogr., (A)**93**, 368 (1936).

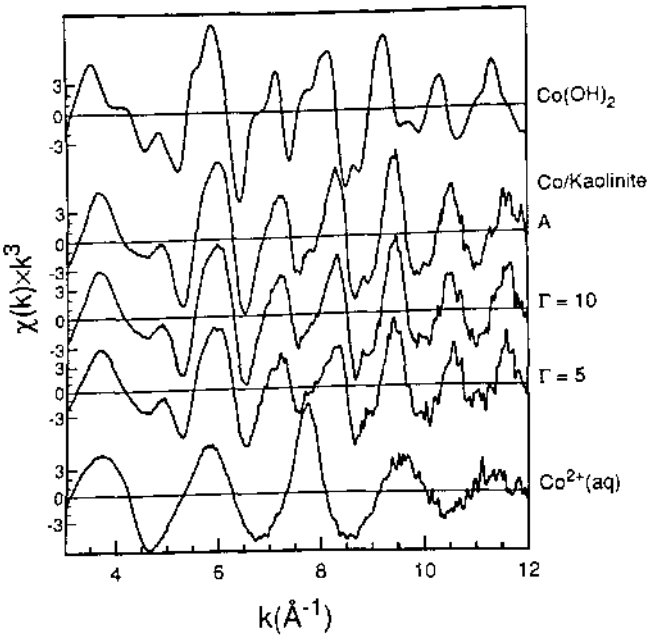

Figure 1. Normalized, background-subtracted EXAFS spectra for Co sorbed to kaolinite at the sorption densities (Γ) shown compared with spectra for $Co(OH)_2$(i) and aqueous 12 mM $Co(NO_3)_2$ solution.

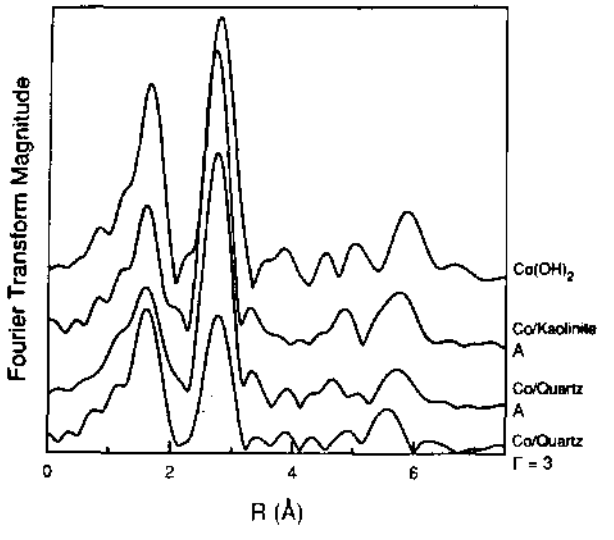

Figure 2. Radial structure functions (RSF), uncorrected for phase shift, for cobalt sorbed to kaolinite and quartz compared to the RSF for $Co(OH)_2$(i). Note the shift in the position of the peak at R = 5.2-5.8 to lower R with decreasing surface coverage (Γ).

Γ	1st SHELL: Co-O			2nd SHELL: Co-Co			2nd SHELL: Co-Ms[1]			4th SHELL: Co-Co		
(μmoles/m²)	R(Å)	CN	Δσ² (Å²)	R(Å)	CN	Δσ² (Å²)	R(Å)	CN	Δσ² (Å²)	R(Å)	CN	Δσ² (Å²)
Co/Kaolinite												
A[2]	2.08	5.6	0.004	3.10	5.8	0.0	--	--	--	6.21	4.2	-0.001
10	2.07	5.2	0.003	3.11	5.0	-0.001	--	--	--	6.20	3.4	-0.001
5	2.08	5.6	0.002	3.14	3.9	-0.001	3.26	2.2	0.0	6.20	2.3	-0.004
Co/Quartz												
A[2]	2.08	6.0	0.005	3.12	6.0	0.001	--	--	--	6.22	3.1	0.0
B[2]	2.06	6.0	0.003	3.13	6.1	0.0	--	--	--	6.23	3.3	0.0
3	2.08	5.3	0.002	3.16	2.6	0.002	3.26	0.7	0.001	6.09	0.8	-0.008
$Co(OH)_2$	2.10	6.0	--	3.17	6.0	--	--	--	--	6.35	6.0	--
Co^{2+}(aq)	2.10	6.6	-0.003	--	--	--	--	--	--	--	--	--

[1] Ms represents Al or Si for Co sorbed on kaolinite and Si for Co sorbed on quartz
[2] Thermodynamic solubility of $Co(OH)_2$(i) and $Co(OH)_2$(a) exceeded.

Table 1. Interatomic distance (R), coordination number (CN), and Debye-Waller factor ($\Delta\sigma^2$) for Co(II) sorbed to kaolinite and quartz at the surface coverages (Γ) shown compared with $Co(OH)_2$(i) and 12 mM $Co(NO_3)_2$(aq) solution. R, CN, and $\Delta\sigma^2$ for the sorption samples and solution were determined by least-squares fits of the Fourier back-transformed EXAFS functions of peaks in the radial structure functions shown in Figure 2. R and CN for $Co(OH)_2$(i) are from x-ray diffraction measurements [9]. $\Delta\sigma^2$ is the difference between the σ^2 parameter derived from fits of model compounds and σ^2 calculated from fits of the unknown samples.

INTERDIFFUSION IN Cu-Au AND Cu-Au-Ag

PROPOSAL NO. 1018Mp

E. S. K. Menon*, P. Huang*, M. Kraitchman*, J. J. Hoyt**,
P. Chow*** and D. de Fontaine*

* Department of Materials Science and Mineral Engineering, Berkeley, CA 94720.

** Department of Mechanical and Materials Engineering, Pullman, WA 99164.

*** Department of Physics, University of Houston, TX 77204.

INTRODUCTION

Interdiffusion studies have been carried out in binary Cu-16at%Au and ternary Cu-24.2at% Au-37.5at% Ag alloys using multilayered thin films. In the binary alloy, nonlinear diffusion effects have been determined and analysed. In the ternary alloy, by making use of the anomalous scattering effects near the absorption edges of Cu and Au, the ternary diffusion matrix and the diffusion path have been established. Results of these two experiments are discussed here.

EXPERIMENTAL

Synchrotron radiation experiments were carried out at experimental station of beamline VII-2 of SSRL. This station has an automated Huber diffractometer equipped for six circle operation. The intense white radiation from the storage ring was monochromatized by a Si (220) double crystal and the incident beam intensity was monitored by measuring the Compton scattering from a kapton tape placed in the path of the monochromatized x-rays by means of a NaI scintillation detector. Any effects of fluctuations in the incident beam intensity was minimized by collecting diffracted intensity for a constant number of monitor counts. The sample was always maintained in an evacuated shroud (provided with kapton windows for entry and exit of x-rays) so as to reduce air scattering. A high purity Ge solid state detector was used to measure the diffracted intensity and this detector allowed the discrimination of the fluorescent radiation.

RESULTS AND DISCUSSION

Non-linear diffusion in Cu-Au

A generalised theoretical treatment of diffusion in binary nonhomogeneous systems was carried out in 1969 by Cook, de Fontaine and Hilliard [2] by considering composition variations on a discrete lattice. Experimental studies on compositionally modulated binary films were conducted under the direction of Prof. Hilliard at Northwestern University for several years [3,4,5] In all these studies, covering a wide variety of binary alloy systems, the interdiffusion coefficient was assumed to be composition independent. In his doctoral dissertation submitted in 1967, de Fontaine[6] carried out a theoretical study of non-linear diffusion in binary systems and examined the influence of composition dependent diffusivity on the annealing behaviour of composition modulated films. It may be mentioned here that despite the availability of this detailed theoretical analysis for all these twenty-three years, a systematic experimental study of this nature has not been attempted as yet on metallic alloys! Interestingly, several researchers have observed nonlinear diffusion effects in multicomponent artificial superlattices made from amorphous[7] and crystalline semiconductor compounds[8,9]

In the present experiment, multilayered Cu-16 at% Au samples with a wavelength of 3.31 nm with [100] epitaxy were prepared and diffractograms were obtained with an incident beam energy of 8860 eV. The average composition of the alloy was chosen to be in the solid solution region of this ordering system. The intensity of the first three satellites on the low angle side and the first two on the high angle side were monitored as a function of annealing time at 515 K.

Fig. 1 shows diffractograms obtained from this sample at three different annealing times. The initial growth and subsequent decay of the second and third order satellite peaks is clear here. A semi-log plot of the satellite intensity normalised to that of the Bragg peak as a function of annealing time, shown in Fig. 2, summarises the data. As can be seen from this figure, the first order satellite decays exponentially as expected. However, the second and third order satellites (which decay very rapidly in the early stages of annealing) increase in intensity before an exponential decay at long annealing times. This behavior clearly indicates that the linear solution of the diffusion equation breaks down for this system. A simple analysis of the nonlinear diffusion process can be made by following the scheme proposed by de Fontaine[6], in combination with the approximate solution obtained by Tsakalakos[10] later. Here, following de Fontaine[6], the composition dependence of the interdiffusivity, $\tilde{D}$, is expressed as :

$$\tilde{D} = D_0 + D_1 u + D_2 u^2 \qquad (1)$$

with $u = c - c_0$ where c represents the at% Au and c_0 refers to the average composition of the sample. The function $\tilde{D}(u)$ were evaluated by Menon et al[11] to be:

$$D_0 = 9.17\times10^{-19} - 7.24\times10^{-19}u + 2.62\times10^{-20}u^2 \text{ cm}^2/\text{sec}. \qquad (2)$$

Tsakalakos[10] obtained expressions for the variation of the first three satellites with annealing time from an approximate solution of the nonlinear diffusion equation. The calculated results for Cu-16at% Au are shown in Fig. 3 and it can be seen that in spite of the simplifications that are involved in determining the parameters of the composition dependent diffusivity and the assumptions made in the approximate solution to the nonlinear diffusion equation, the results obtained are very satisfying.

Ternary Diffusion in Cu-24.2at% Au-37.5 at% Ag

X-ray diffraction experiments performed by Murakami et al [12,13] showed for the first time that from two sets of ternary modulated thin films one could determine the diffusion matrix and calculate the diffusion path. These results were extracted from measurements of intensity of satellites which can be expressed as [13] :

$$I(k,t) = [\,\Gamma_1(k,t)\,\Delta f_1 + \Gamma_2(k,t)\,\Delta f_2\,]^2 \qquad (3)$$

where $\Delta f_i = f_i - f_3$ (i = 1,2 ; 1,2 and 3 representing Cu, Ag and Au respectively in the present case) and $\Gamma_i(k,t)$ represent Fourier transforms of the two independent concentration deviations. From a linear kinetic theory for diffusion, Murakami et al [12] expressed the intensity (square of the amplitude) as:

$$\frac{I(k,t)}{I_0} = \left[\frac{R\,\exp(\alpha_1 t) + \exp(\alpha_2 t)}{1+R}\right]^2 \qquad (4)$$

where, α_1 and α_2 are the eigenvalues of the diffusion matrix and R, the amplification factor is expressed as:

$$\frac{R}{1+R} = \frac{(1+fT_1)(g-T_2)}{(1+fg)(T_1-T_2)} \qquad (5)$$

where T_1 and T_2 are the eigen vectors of the diffusion matrix and

$$f = \frac{\Delta f_1}{\Delta f_2} \text{ and } g = \frac{\Gamma_1^0}{\Gamma_2^0}$$

In the Murakami et al [12,13] experiments, the eigenvalues of the diffusion matrix were found from plots of log (I/I_0) versus time for a given sample. Murakami et al [12] used a second film with the same overall composition but a different modulation scheme i.e. a sample with a different value of R, and solved equation (5) to determine the eigenvectors T_1 and T_2. Once the eigenvalues and the eigenvectors were found, the diffusion matrix and the diffusion path in the composition space were computed.

We had adopted a somewhat different approach in the experiment carried out at SSRL. In general, the complex atomic scattering factor, f, is expressed as

$$f = f^0 + f' + if'' \qquad (6)$$

where f^0 is the value of the atomic scattering factor far from an absorption edge and f' and f'' are the real and imaginary part, respectively, of the anomalous scattering factor which become important as the x-ray energy approaches any absorption edge. In the present context, if one were to record satellite intensities using energies where the Δf_i's in expression (3) are sub-

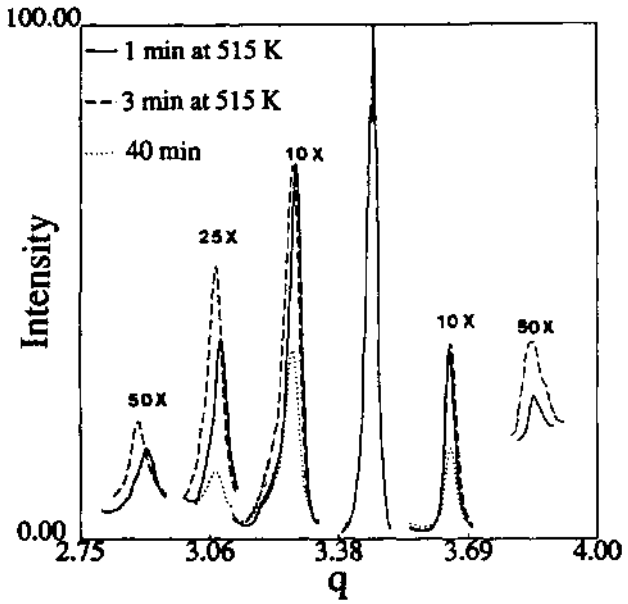

Fig. 1 : A series of satellite profiles obtained during different stages of the annealing treatment as indicated. Three orders of satellites on the low angle side and two on the high angle side shown here were obtained with 8500 eV sychrotron radiation. The reciprocal lattice vector $q = 4\pi\sin\theta/\lambda$ is plotted on the x-axis

stantially different, then the two unknown Γ_i's can be readily found. Thus the diffusion paths can actually be measured experimentally. Also, as can be readily observed from expression (5), different Δf_i's would result in different amplification factors, R and thus one can solve for the eigenvalues and eigenvectors [equations (4) and (5)] by choosing two synchrotron radiation wavelengths near absorption edges where the scattering factors are quite different. The major advantage of this approach lies in the fact that from a single ternary multilayered sample, one can determine the complete diffusion matrix and the diffusion path. Such an experiment has hitherto not been performed.

In the present experiment, we studied ternary diffusion in Cu-Au-Ag taking the above approach using synchrotron radiation and anomalous scattering. Fig. 4 shows the isothermal section of this ternary system at 515 K; the average composition of the multilayered thin film has been indicated by a star. The experiment was successfully completed during the last session that we were granted at SSRL. Diffractograms were recorded at three different beam energies near the Cu K-edge and at three energies in the vicinity of the L-edge of Au. In the Cu-24.2at% Au-37.5at% Ag samples, the ordered Cu_3Au phase was also found to be present. Since the (111) peak of this phase appears close to the satellite peak, a deconvolution algorithm was developed to separate the peaks, perform the various corrections and compute the integrated intensities. Fig. 5 shows the variation of the satellite intensities as a function of annealing time at different beam energies. Satellite intensity decreases as the energy of the incident radiation approaches that of the L-absorption edge of Au (11918 eV), while it decreases as the K-absorption edge of Cu (8979 eV) is approached. As can be noted from Fig. 5, the data obtained shows very little scatter and the data for different energies are well separated. Hence equations (4) and (5) can be solved accurately to obtain the diffusivity matrix. Equation (3) can be solved to obtain the Fourier amplitude $\Gamma_i(\mathbf{k},t)$ at all reciprocal space point $\mathbf{k}$, for each annealing time t. The two independent composition profile in the ternary sample are then obtained as the inverse Fourier transform of the $\Gamma_i(\mathbf{k},t)$ profiles. Subsequently, from these composition profiles, the average concentration in the two types of layers in the multilayered sample is calculated to trace the diffusion path in Gibbs' triangle.

The multilayered sample used in this study consisted of layers of Au alternating with layers containing Cu and Ag in equiatomic proportion, as represented by the vertical line in Fig. 4. One of the aims of this work is to observe the path in composition space chosen by the system while approaching the equilibrium tie line compositions, which are almost 90 degrees to the starting compositions imposed by the deposition technique in this sample. A plausible sequence of tie line rotation is indicated in Fig. 4 by the lines marked (a) to (e) and the resulting diffusion path traced out.

In addition to the above, the conducted experiment also provides solution to another very difficult problem. It is well known that, the anomalous scattering effect can be used to obtain the three independent partial structure functions (PSF) in a ternary system by inversion of a 3 × 3 matrix. Unfortunately, this matrix is typically ill-conditioned and the results according to various studies have been disappointing. In earlier work carried out in our group on the unmixing kinetics in Al-Zn-Ag system, the three PSF in one favourable case were determined. In the present work, where we have investigated at energies close to the K edge of Cu as well as the L edge of Au, the resulting intensity matrices are better-conditioned. Also, due to the large composition amplitudes associated with the multilayered samples, the diffracted intensities are very strong compared to the small angle scattering experiments. Finally, the initial phases of the composition amplitudes Γ_i are known from the deposition parameters.

CONCLUSIONS

The two experiments completed at SSRL provide examples of new areas of research that had so far remained largely unexplored : (a) nonlinear diffusion in a binary metallic system and (b) experimental determination of the diffusion path in a ternary alloy. The results on the ternary alloy also represent significant extensions of our previous work[1] , and which will constitute a completely new application of anomalous synchrotron radiation scattering, with application to the important practical problem of kinetics of ternary thin film diffusion.

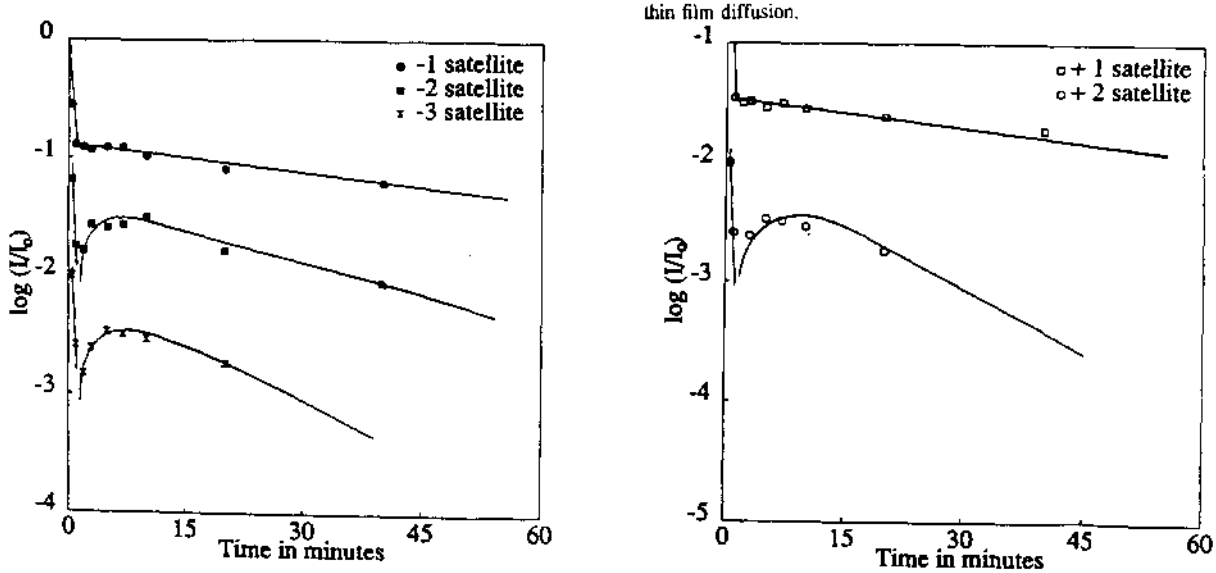

Fig. 2 : $\log(I/I_0)$ versus annealing time for all the satellites observed in a Cu-16at% Au specimen with wavelength of 3.31 nm annealed at 515 K. -n and +n refer to the low and high angle satellites respectively.

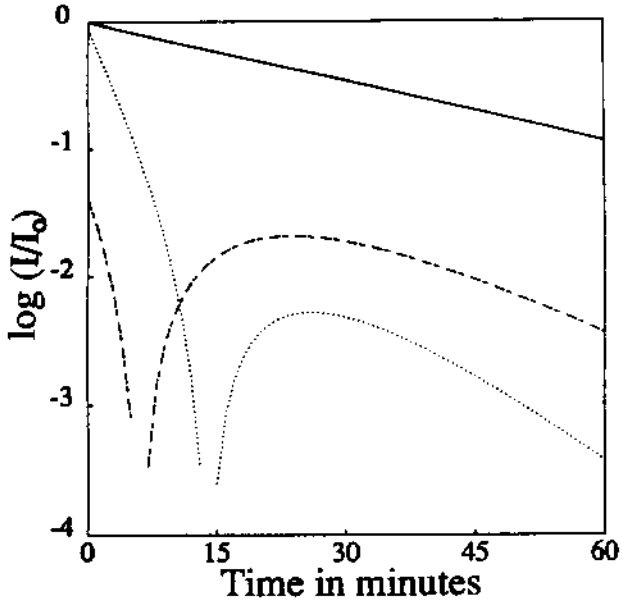

Fig. 3 : Calculated intensity versus annealing time for the first (full line), second (dashed line) and the third (dotted line) order satellites in modulated Cu-16at% Au. The initial composotion profile was assumed to be rectangular.

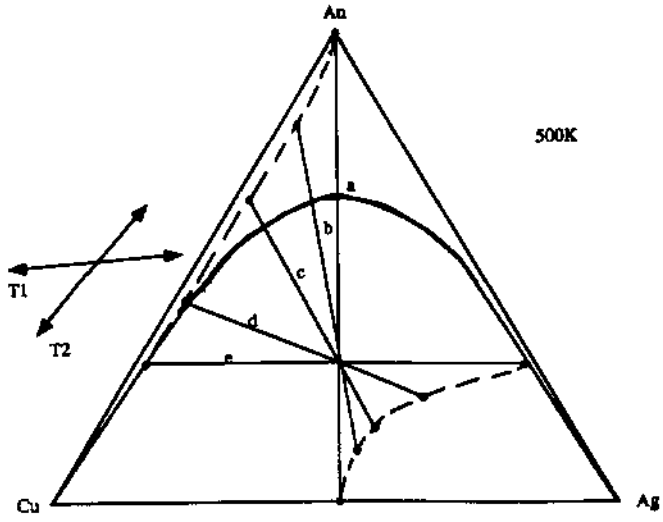

Fig. 4 : Schematic isothermal section of the Cu-Au-Ag system at 515K. The average composition of the multilayered sample is indicated by a star. A series of tie lines are indicated to show the diffusion path.

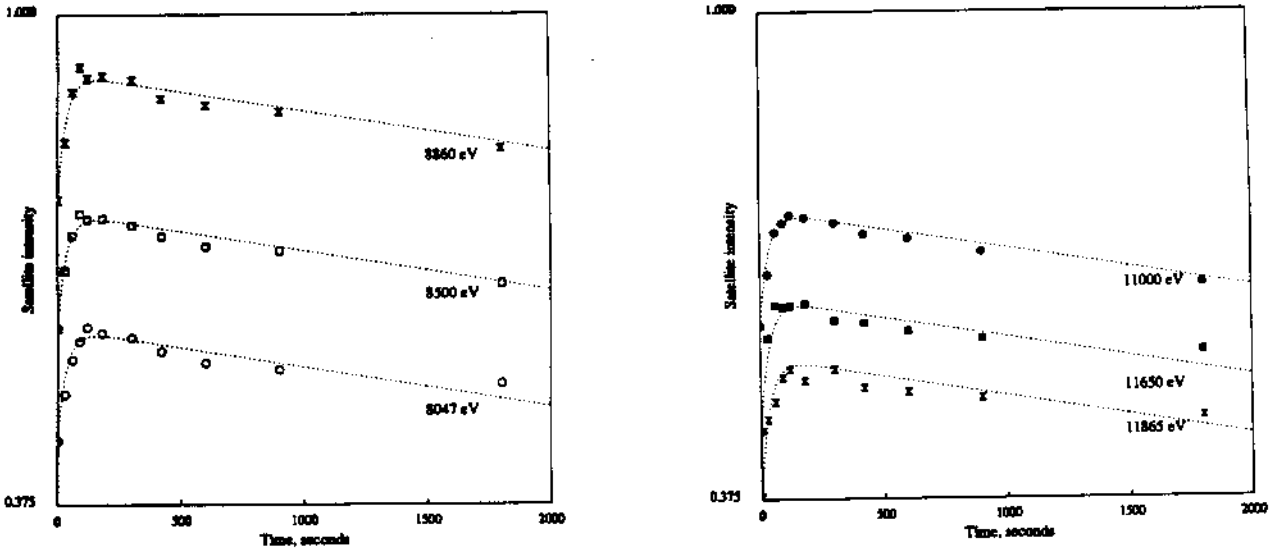

Fig. 5 : Cu-24.2at%Au-37.5at% Ag multilayered film; Semi-logarithmic plot of the intensity of the satellite as a function of aging time at 515 K at different synchrotron radiation energies.

References

1. M. Murakami, D. de Fontaine, J. M. Sanchez, and J. Fodor, *Thin Solid Films*, vol. 25, p. 465, 1975.
2. H. E. Cook, D. de Fontaine, and J. E. Hilliard, *Acta Metall.*, vol. 17, p. 765, 1969.
3. H. E. Cook and J. E. Hilliard, *J. Appl. Phys.*, vol. 40, p. 2191, 1969.
4. E. M. Philofsky and J. E. Hilliard, *J. Appl. Phys.*, vol. 40, p. 2198, 1969.
5. J. E. Hilliard, in *Modulated Structures - 1979, AIP Conference Proceedings*, ed. B. J. Wuensch, vol. 53, p. 407, AIP, New York, 1979.
6. D. de Fontaine, Ph. D Thesis, Northwestern University, 1967.
7. A. L. Greer, in *Modulated structure materials*, ed. T. Tsakalakos, p. 491, Martinus Nijhoff Publishers, The Netherlands, 1984.
8. R. M. Fleming, D. B. McWhan, A. C. Goussard, W. Wiegmann, and R.A. Logan, *J. Appl. Phys.*, vol. 51, p. 357, 1980.
9. A. L. Greer and F. Spaepen, in *Synthetic Modulated Structures*, p. 419, Academic press, New York, 1985.
10. T. Tsakalakos, Ph. D thesis, Northwestern University, 1977.
11. E. S. K. Menon, P. Huang, M. Kraitchman, J. J. Hoyt, P. Chow, and D. de Fontaine, in *Kinetics of phase Transformations*, MRS Proceedings, 1990.
12. M. Murakami, D. de Fontaine, J. M. Sanchez, and J. Fodor, *Acta Metall.*, vol. 22, p. 709, 1974.
13. D. de Fontaine, in *Local Atomic Arrangements studied by X-ray diffraction*, ed. J. E. Hilliard, vol. 36, p. 51, Gordon and Breach Science publishers, New York, 1966.

SYNCHROTRON X-RAY POLYCRYSTALLINE DIFFRACTOMETRY - VI.

W. Parrish[1], M. Hart[2], H. Toraya[3], and C. Erickson[1]

1. IBM Research Division, Almaden Research Center, San Jose, CA 95120-6099
2. Dept. of Physics, The University, Manchester M13 9PL, U. K.
3. Ceramic Engineering Research Laboratory, Nagoya Institute of Technology, Asahigaoka, Tajima 507, Japan

Introduction

During this period we had a two-week run in which we studied high resolution powder diffractometry, high precision lattice parameter determination, and crystal structure analysis. There was insufficient time to continue our grazing incidence reflectometry (3).

High Resolution Powder Diffractometry

The X-ray optics used in these studies is shown in Fig. 1 (4). Most of our crystal structure studies were done with the Soller collimator (SS) in the diffracted beam and the profile width (FWHM) was 0.05 to 0.06° at about 20° (2θ). This is sufficient for most powder studies except where there is extreme overlapping. Replacing the SS with a Si (111) channel monochromator (CM) reduced the FWHM to 0.02° which is about the same as obtained at Brookhaven NLS with a single crystal plate analyzer. The pair of Si (400) CMs reduced the width to about 0.015°, Fig. 2.

The pseudo-Voigt profile-fitting function gave an excellent match with the experimental data as shown in Fig. 3. The wavelength spread of the monochromators determine the profile widths. The widths increased with increasing 2θ when the SS or the Si (111) CM (in the nondispersive setting) were used. The Si (400) CMs were used in the dispersive setting and showed only a small increase in width, an important factor in profile shape studies and in profile fitting strongly overlapped reflections in the higher 2θ region.

The use of the second Si CM caused a large decrease of intensity, and the necessity of using smaller step increments greatly increased the experimental time. The time would have to be increased by a large factor to obtain data with the same statistical accuracy as with the SS. The intensity loss for the Si (400) CM was much larger.

High Precision Lattice Parameter

Precision of 3-6 p.p.m. was obtained for tungsten powder using the high precision Daresbury powder diffractometer (1). Studies at SSRL continued using our conventional diffractometer which was reworked to use a new portion of the main gear wheel and better balancing of the detector arm. The work was guided by immediate PC calculations. A Fourier series method was used to determine the gear correction and the method requires further study. We reached 10 p.p.m. on Si and W specimens. Other possible uncertainties include thermal expansion of the first monochromator, and orbit instability, both of which could change the wavelength. Another method was tried using the angular separation of a pair of high-angle reflections from each phase separated by no more than a few degrees; the data are being analyzed.

Crystal Structure

Crystal structure determinations using the SS collimator arrangement in previous runs were published during this period: $MnCrInS_4$ (6), $Na_2Al_2Ti_6O_{16}$ (5). The better resolution and line shape of the parallel beam SS method compared to conventional X-ray tube focusing provided a superior pattern of poly (p-hydrobenzoic acid) for interpreting the laboratory data (7). Data were collected for monoclinic ZrO_2 and the zeolite ZSM5 for an international round-robin on synchrotron powder diffraction.

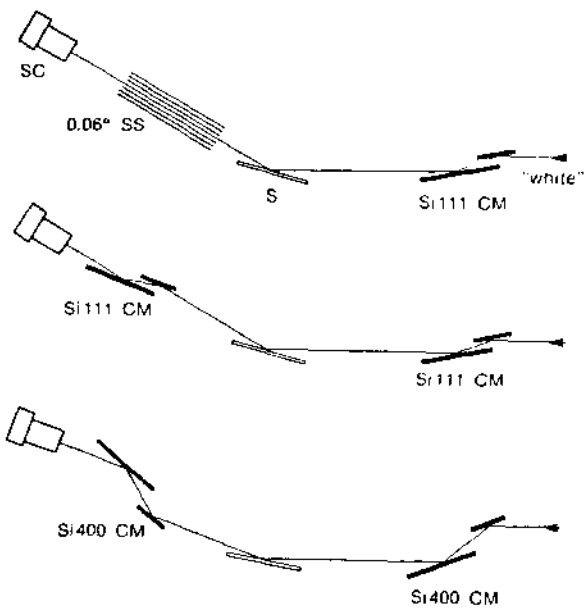

1. X-ray optics used for powder diffraction

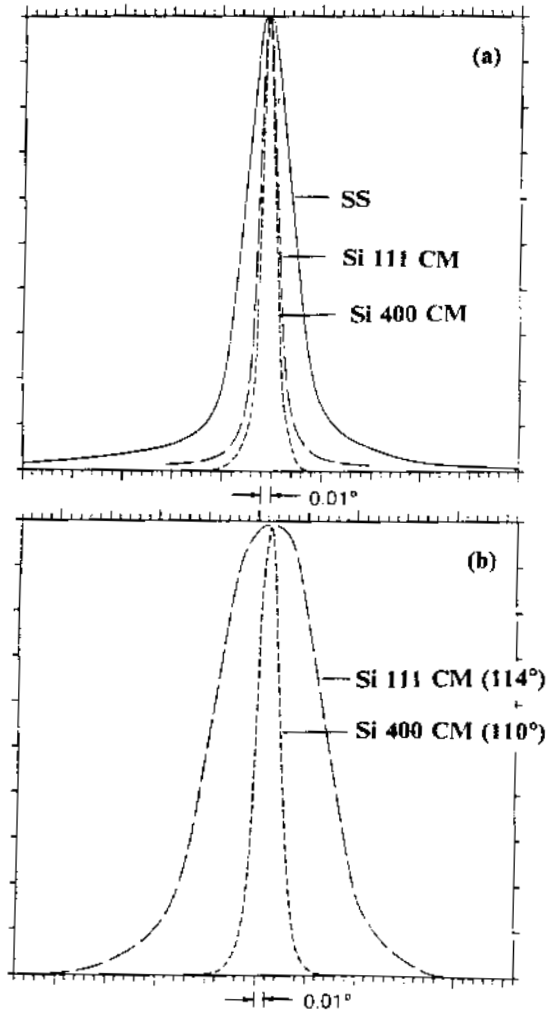

2. Si powder profiles. (a) 111, (b) 555

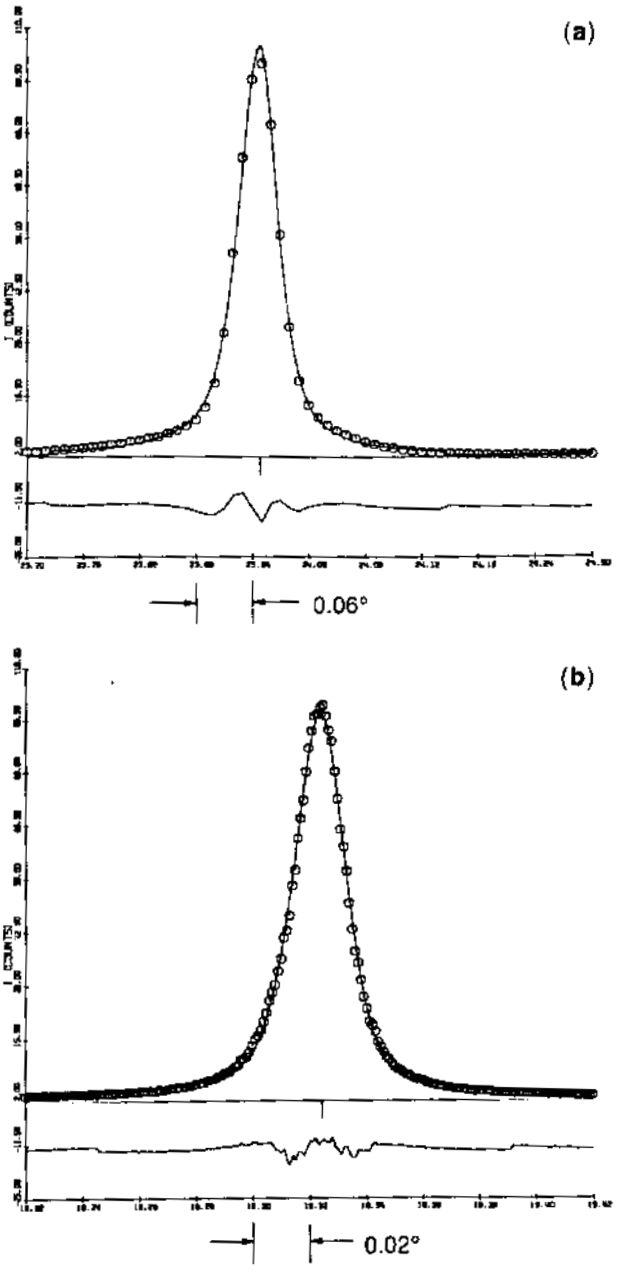

3. Pseudo-Voigt profile fitting function of Si 111 reflection obtained with SS (a) and 111 CM (b)

References

(1). M. Hart, R. J. Cernik, W. Parrish & H. Toraya, Lattice-Parameter Determination for Powders Using Synchrotron Radiation, J. Appl. Cryst., 23, 286-291, 1990.

(2). T. C. Huang, W. Parrish, N. Masciocchi & P. W. Wang, Derivation of d-Values from Digitized X-Ray and Synchrotron Diffraction Data, Adv. in X-Ray Anal., 33, 295-303, 1990.

(3). W. Parrish, M. Hart, B. Gilles, & C. Erickson, Instrumentation for Grazing Incidence X-Ray Relectometry, XV Int. Union Cryst., Acta Cryst. A46, C-375, 1990.

(4). W. Parrish, M. Hart, & H. Toraya, High Resolution Powder Diffractome Using Synchrotron Radiation, Powder Diffraction Satellite Meeting of XV Int. Union Cryst., 1990.

(5). H. Toraya, N. Masciocchi & W. Parrish, Rietveld Powder Structure Refinement of $Na_2Al_2Ti_6O_{16}$; Comparison of Synchrotron Radiation and Conventional X-Ray Tube Datasets, J. Mater. Res., 5, 1538-1543, 1990.

(6). G. Will, N. Masciocchi, W. Parrish & H. D. Lutz, Crystal Structure and Cation Distribution of $MnCrInS_4$ from Synchrotron Powder Diffraction Data, Zeit. f. Krist., 190, 277-285, 1990.

(7). D. Y. Yoon, N. Masciocchi, L. E. Depero, C. Viney & W. Parrish, High-Temperature Structures of Poly (p-hydrobenzoic acid). Macromolecules 23, 1793-1799, 1990.

GEOMETRY OF THE ADSORBED ARSENATE COMPLEX ON FERRIHYDRITE AND ON CRYSTALLINE FEOOH POLYMORPHS

G. A. Waychunas[1], J. A. Davis[2], C. C. Fuller[2] and B. A. Rea[2]

[1]Center for Materials Research, Stanford University, Stanford CA 94305
[2]U.S. Geological Survey, Water Resources Division, Menlo Park CA 94025

Introduction

Ferrihydrite is the mineral name identifying poorly crystalline to amorphous hydrous iron oxides with chemical formula near $5Fe_2O_3.9H_2O$. The mineral is the first product of the hydrolysis of dissolved iron in natural geologic systems, and is a globally distributed common product of surficial low-temperature geochemical processes.

The major controls on the dispersion of ore or associated trace elements in the weathering environment are reaction sites on the surfaces of minerals, especially the oxides of iron, manganese, aluminum, and silicon, as well as carbonates, secondary sulfides and organic matter. Iron oxides are particularly ubiquitous and are strong scavangers of metal ions. Frequent dissolution and reprecipitation tend to maintain iron oxides in a state of low crystallinity and small particle size, both of which facilitate the incorporation of foreign elements, especially metals, in these oxides.

Arsenate ion is a common environmental pollutant occurring in natural waters running through mine dumps, mine workings and associated metal deposits, and collecting in local streams and rivers. It is efficiently scavanged by ferrihydrite formed from iron from the same sources. The ultimate disposition of the adsorbed arsenate depends both on the ferrihydrite reactivity, and its tendency to transform into other more stable iron oxides.

In particular, the transformation of ferrihydrite into goethite is slowed by the adsorption of arsenate, presumably by a blocking of reactive surface sites. This blocking behavior affects the cycling of metals bound by ferrihydrite and other iron oxides in natural systems, and is an important factor in concentration processes. In order to predict the rate of metal transport in surficial geological environments an understanding of the atomistic-level processes is essential. However, no structural characterization of the surface and reactive sites of ferrihydrite has been performed. Similarly, the basic arsenate adsorption geometry has not been established, although it is believed to be similar to the phosphate case.

In the current investigation we focus on determining the geometry of the arsenate-iron oxide adsorbate complex, and any reconfiguration of the iron oxide surface as a result of adsorbate bonding, via EXAFS analysis on freshly prepared arsenated samples. Besides ferrihydrite, we also examine arsenate adsorption on FeOOH polymorphs of known structure.

Experimental Details

Ferrihydrite samples were prepared in two distinct forms: precipitated in the presence of arsenate ion (coprecipitated samples, CPT); and precipitated separately then exposed to arsenate solutions (adsorbed samples, ADS). Both types of samples were prepared with a wide range of arsenate loadings (from sample saturation to the detectability limit). Samples were made immediately before studies at SSRL and kept moist until data collection was completed.

FeOOH polymorphs goethite, lepidocrocite and akaganeite were prepared using standard recipes. Single phase synthesis was confirmed with x-ray diffraction. Only ADS samples were prepared.

As and Fe K-edge EXAFS and XANES spectra were collected on beam line 4-1 using Si (111) monochromator crystals. Detection was carried out in fluorescence and transmission modes simultaneously. Hematite (α-Fe_2O_3), sodium arsenate and scorodite ($FeAsO_4.4H_2O$) standards were used to acquire phase and amplitude functions for EXAFS analysis. Cu metal foil was used for energy calibration.

Results

A typical As absorption edge for adsorbed arsenate is shown in Figure 1. The main EXAFS oscillations are due to the oxygen nearest neighbors in the arsenate tetrahedron. However, the small secondary oscillations, visible as a flat top in the first peak at about 11950 eV, are due to As-Fe correlations. Fourier transforms of the As K-edge

EXAFS spectrum for representative samples are shown in Figure 2.

Scorodite has monodentate arsenate linkages where each oxygen in the AsO_4 group is shared with one distinct adjoining $Fe(O,OH)_6$ octahedron. It thus has four second neighbor Fe atoms about each As atom. In contrast, there are only about two second neighbor Fe atoms observed about arsenate on akaganeite (β-FeOOH) and the other FeOOH polymorphs. The As-Fe distance is also shorter (3.26 Å) than in scorodite (3.36 Å), and is consistent with a bidentate adsorption geometry: The arsenate group shares two apices with edge-joined $Fe(O,OH)_6$ octahedra on the FeOOH surface (Figure 3).

On ferrihydrite, the arsenate is more disordered but also shows the identical bidentate signature, as well as a smaller proportion of monodentate bonds. The latter have As-Fe distances of 3.58(3) Å, consistent with an As-O-Fe angle near 180°.

Analysis of the Fe EXAFS indicates that the Fe-Fe correlations in ferrihydrite are progressively

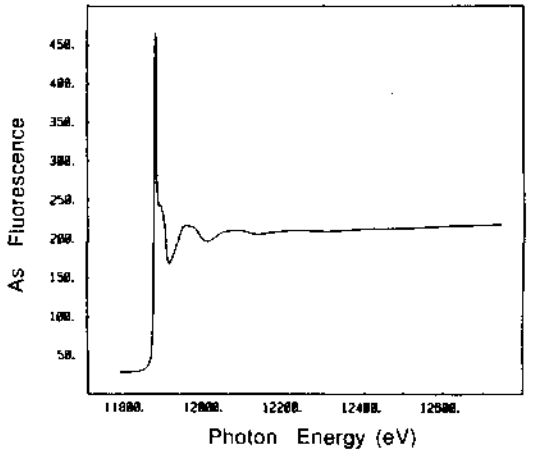

Fig. 1 EXAFS spectrum of AsO_4^{-3} adsorbed on ferrihydrite. As/Fe=0.01

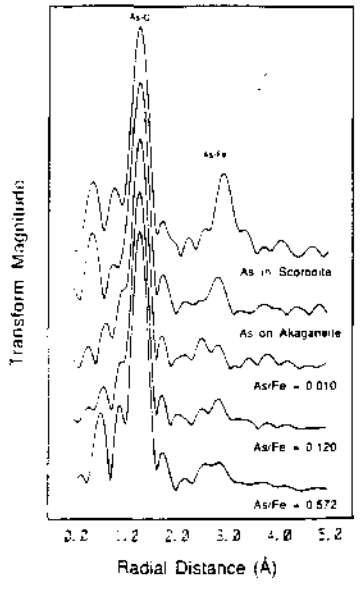

Fig. 2 Fourier Transforms of As K-edge EXAFS spectra for various arsenated samples and scorodite.

Fig. 3 Various geometries for arsenate ion attachment to $Fe(O,OH)_6$ polymers. Goethite (αFeOOH) Fe-O,OH distances assumed.

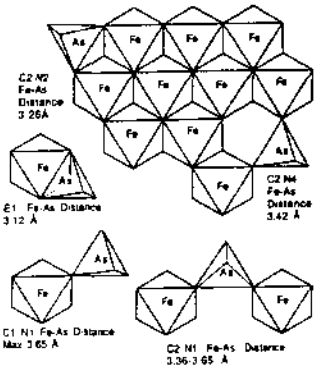

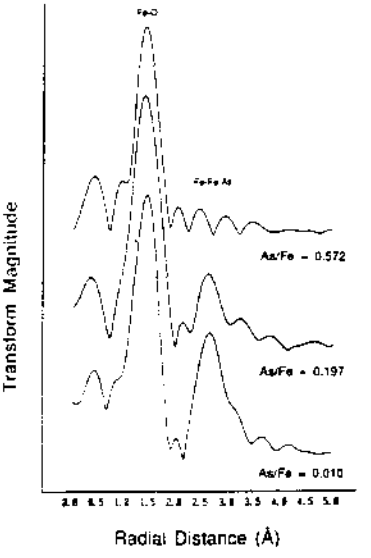

Fig. 4 Fourier transforms of Fe K-edge EXAFS spectra for ferrihydrite of varying As/Fe ratios.

disrupted as arsenate loading increases. This is shown in the Fourier transforms of Fe EXAFS from several ferrihydrite samples with differing As/Fe composition in Figure 4. The second peak is due mainly to two Fe-Fe and one Fe-As correlation. Detailed analysis shows that, as the arsenate content of the ferrihydrite increases, the number of longer Fe-Fe distances, associated with $Fe(O,OH)_6$ octahedra sharing corners, decreases linearly, while the shorter Fe-Fe distances, associated with edge-sharing $Fe(O,OH)_6$ octahedra, become progressively disordered but do not decrease in number. Hence increasing arsenate disrupts Fe octahedra polymerization.

This result agrees with the observation that CPT samples had larger As/Fe saturation levels (0.6) than ADS samples (0.2). During coprecipitation the surface-complexed arsenate blocks the proto-ferrihydrite particles from forming the longer Fe-Fe correlations. This reduces particle size, and results in more arsenate loading. In ADS samples the polymerization has already occurred, offering less sites for bidentate arsenate attachment. Surface-enhanced Mössbauer spectroscopy measurements and x-ray diffraction observations are also consistent with these results.

THE DETERMINATION OF NICKEL AND CHROMIUM SPECIES IN EMISSIONS FROM A WASTEWATER SLUDGE INCINERATOR USING XANES AND EXAFS

N.F. Mangelson*, L.B. Rees, J.E. Silk and M.W. Hill
Departments of Chemistry and Physics
Brigham Young University
Provo, Utah 84602

F.W. Lytle and R.B. Greegor
The Boeing Company
Seattle, Wasington 98124

INTRODUCTION

This study represents the third and final phase of a project to evaluate nickel and chromium species in emissions from municipal wastewater sludge incinerators. The cytotoxicity of these elements is dependent upon the chemical form of the elements [1,2]. The U.S.E.P.A. has drafted regulations proposing limits on the annual increase in ambient-air metal concentration estimated to result from incinerator emissions. The limits proposed are based upon assumptions about the chemical species of metals emitted. Determinations from this study will help form an experimental basis for the final emission regulations. Emphasis in this phase of the study is on the determination of nickel species but a few measurements of chromium XANES spectra were also made. These measurements determine the fraction of nickel and chromium in the chemical states of nickel subsulfide (Ni_3S_2) and Chromium(VI) respectively, as these species are suspected carcinogens.

EXPERIMENTAL

Bulk flyash samples from a municipal wastewater sludge incinerator, known as site 8, were collected at the inlet (in) to a venturi scrubber/tray scrubber. Particulate samples were also collected on quartz filters at a location (mid) between the venturi scrubber/tray scrubber equipment and a pilot-scale wet electrostatic precipitator.

Nickel and chromium K-edge XRA spectra were taken at SSRL. The electron beam energy was 3.0 GeV with 50 to 20 microamps of current. Most of the data was taken on beam line IV-1, an 8 Pole Wiggler Side Station with a parallel crystal monochromator using Silicon 220 crystals. The entrance slit was 1 mm in vertical height and 20 to 23 mm wide. Some data were taken on beam line IV-3, an 8 Pole Wiggler Side Station with a parallel crystal monochromator using Silicon 111 crystals. The entrance slit was 2 mm in vertical height and 20 to 23 mm wide.

Spectra for reference compounds were taken in the transmission mode or with a total-electron-yield detector and extended from -100 eV to 1000 eV relative to the metal absorption edge. Spectra for the samples were taken with a Lytle fluorescence detector and extended from -100 eV to 300 eV.

RESULTS

Representative spectra from this study are shown in Figures 1 to 4. The solid lines in Figure 1. are the K-edge XANES spectrum of nickel for a mixture of nickel subsulfide, Ni_3S_2, and nickel hydroxide, $Ni(OH)_2$, with 10.5% subsulfide nickel. Linear additions of pure subsulfide and pure hydroxide spectra are shown as dotted lines. The curve fitting for identification of subsulfide is most sensitive just as the absorption edge rises above the baseline into the steepest part of the edge in the region of 0 eV to 10 eV. In this region it is seen that the dotted curves for 0% and 5% subsulfide are below the solid line. The 15% dotted line is clearly above the solid line. The 10% line seems to be just on the high part of the solid line. This fit would suggest that nickel subsulfide in the mixture is 8 to 9%, which is in quite good agreement with the calculated value of 10.5%.

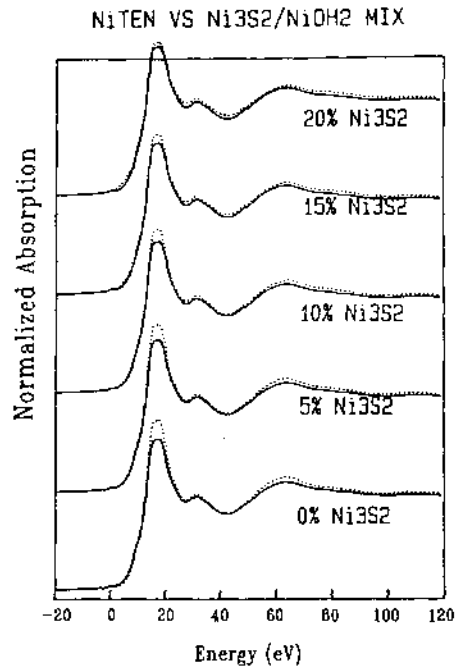

Figure 1. Solid lines are the nickel K-edge XANES spectrum of a mixture of $Ni(OH)_2$ and Ni_3S_2 with 10.5% subsulfide nickel. Dotted lines are constructed as a linear combination of the $Ni(OH)_2$ and Ni_3S_2 spectra. Each curve is labeled with the percent subsulfide nickel. Spectra were collected in electron yield mode.

In Figure 2. the fluorescence spectrum of sample 5C-MID-NI-F2 is compared to the absorption spectra of four reference compounds. The sample spectrum is the summation of 10 runs taken with the silicon 111 crystal. The increased X-ray intensity obtained with the 111 crystal was an advantage for this sample which contains nickel in the 100 ppm range. 5C-MID is certainly not primarily subsulfide. It is

seen that the sulfate is a near perfect match for the whole spectrum. The small, second maximum in the oxide compound seems to be out of phase with the sample spectrum.

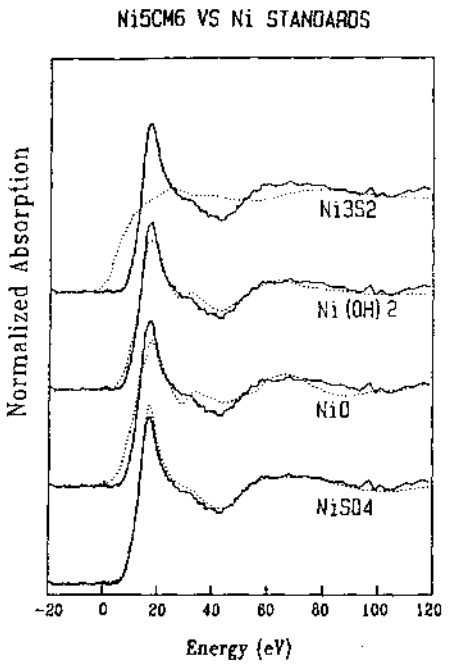

Figure 2. Solid lines are the nickel K-edge XANES spectrum for sample 5C-MID-Ni-F2. Dotted lines are spectra collected in the absorption mode for the several related compounds indicated.

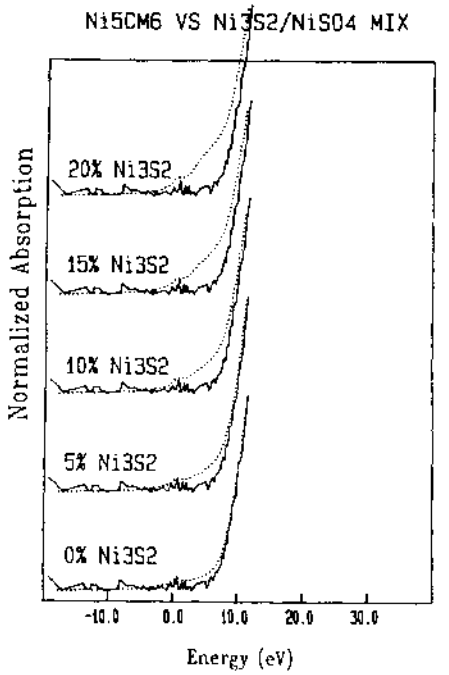

Figure 3. Solid lines are the nickel K-edge XANES spectrum for sample 5C-MID-Ni-F2. Dotted lines are linear combinations of $NiSO_4$ and Ni_3S_2 spectra shown in Figure 2. The scale has been expanded to show detail at the rise of the absorption edge.

In Figure 3. The sample spectrum is compared to an admixture of subsulfide and sulfate. The addition of subsulfide to the fitting spectrum is made more dramatic by expanding the scale. It is seen that even the pure sulfate spectrum seems to be a little higher than the sample spectrum which could be due to the background subtraction prior to spectrum normalization. The addition of 5% subsulfide raised the fitting curve clearly above the sample spectrum. From these data it can be concluded that the nickel subsulfide upper limit can be set at about 3% in this sample. It is interesting to note also that there is clear evidence in the reference compounds and the sample for a preedge feature near 2 eV.

In Figure 4. The spectrum for bulk sample 11C-IN-Ni taken with the 111 crystal pair is compared to admixtures of subsulfide and hydroxide reference compounds. In this case the hydroxide is a near perfect fit except for normalization. A 10% admixture of subsulfide is clearly raising the reference curve above the sample spectrum in the 0 to 10 eV region. An upper limit of about 5% subsulfide can be placed on this sample.

ACKNOWLEDGMENTS

We gratefully acknowledge the help given us at SSRL by the staff and crew. This work was supported in part by U.S.E.P.A. Contract No. 68-02-4442 and Contract 68-02-4462 through Entropy Environmentalists, Inc. JOB No. 3808.

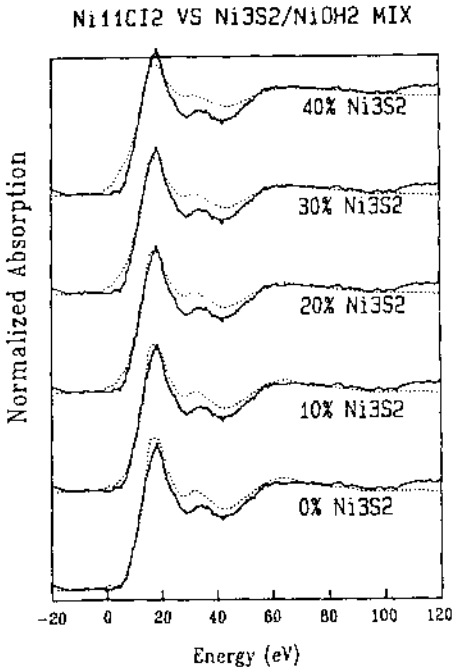

Figure 4. Solid lines are the nickel K-edge XANES spectrum for sample 11C-In-Ni. Dotted lines are linear combinations of $Ni(OH)_2$ and Ni_3S_2 spectra shown in Figure 2.

REFERENCES

1. L.D. Hansen, G.L. Fisher, C.E. Chrisp and D.J. Eatough. Proceedings of the Fifth International Symposium, Polynuclear Aromatic Hydrocarbons, M. Cooke and A.J. Dennis, eds., Battelle Press, Columbus, OH, (1981) 507-517.

2. C. Wei, M.A. Al Bayati, M.R. Culberston, L.S. Rosenblatt and L.D. Hansen. J. Toxicol. Environ. Health, **10** (1982) 673-687.

PROPOSAL NO. 1078M

EXAFS Studies of (100) III-V Semiconductors Treated with $[Ru^{II}(NH_3)_5H_2O]^{2+}$

S. R. Lunt, T. L. Longin, G. M. Miskelly, M. J. Sailor, and N. S. Lewis
Department of Chemistry and Chemical Engineering
California Institute of Technology
Pasadena, CA 91125

K. O. Hodgson

Department of Chemistry
Stanford University
Stanford, CA 94305-5080

We have continued our investigations of the interaction of $[Ru^{II}(NH_3)_5H_2O]^{2+}$ with semiconductor surfaces. The ammine ligands are substitutionally inert and so this compound is expected to react selectively with the GaAs surface via substitution of the aquo ligand. This species is of interest because, unlike cobalt complexes,[1] X-ray Photoelectron Spectroscopy (XPS) and Rutherford Backscattering (RBS) analysis showed that the coverage of GaAs (100) surfaces exposed to this complex was less than a half of a monolayer. The low coverage allows the investigation of the surface-metal bond and the determination of rather this complex binds directly to a substrate atom or through a surface oxygen bridge. While it is possible to distinguish between a Ga or As substrate atom and oxygen as a backscatterer in the surface EXAFS data because of the different behavior of the envelope functions with k, the individual Ga and As surface contributions can not be determined because they are very similar scatters. To separate out effects of Group III and Group V elements, InAs and GaP substrates were also studied.

Surface EXAFS experiments were conducted on GaAs, InAs, and GaP (100) surfaces. The $[Ru^{II}(NH_3)_5H_2O]^{2+}$ was synthesized by Zn reduction of $[Ru^{III}(NH_3)_5H_2O]Cl_3$ in water (deareated with Ar). The solution was then filtered and a 1" X 1" etched wafer of the semiconductor was exposed to the solution for 30 min. The exposure was done under Ar and the wafer was placed in a Kapton covered cell which was continually purged with Ar during the course of the SEXAFS data collection. XPS of the sample before the experiment showed no detectable surface oxides, though some oxidation was evident after the 24+ hours of SEXAFS data collection.

The Ru Kα fluorescence was detected by a solid state Ge detector at a low angle to the surface normal. The spectra were analyzed using $Ru^{II}(NH_3)_6Cl_2$ as a model compound to determine scatteirng amplitudes and phase factors. The raw data and fourier transforms of the model compound and the ruthenium exposed GaAs are shown in figures 1 and 2. Fits of the first shell with the model parameters do not fit well at higher k values, indicating the possibility that a heavier scatter, such as an As, may be present in the inner sphere of the ruthenium. A strong variation of background with time precluded the collection of enough spectra for the InAs and GaP samples to get the signal to noise ratio to a level where the EXAFS could be analyzed. The average of some of the spectra for GaP is shown in Figure 3. When further data collection becomes possible, a quantitative and qualitative comparison of the three surfaces can be made. The surface EXAFS of the InAs and GaAs surface should be different than that of the GaP surface if the Ru-As bond is the primary binding mode. If the primary binding mechanism is through an oxygen bridge than the bond lengths and EXAFS will be identical for three of these surfaces.

Acknowledgements
We wish to thank G. N. Ryba, G. A. Shreve, and B. Tsai of Caltech for help in this research and Dr. B. Hedman of SSRL for useful discussions. Material was kindly provided by T. Hasenberg of Hughes Research Laboratories (InAs) and Semia Corp. (GaP). We also thank Dr. J. Gordon of IBM Almaden for the use of equipment and helpful discussions.

References
1. B. J. Tufts, I. L. Abrahams, C. E. Caley, S. R. Lunt, G. M. Miskelly, M. J. Sailor, P. G. Santangelo, N. S. Lewis, B. M. Hedman, A. L. Roe, K. O. Hodgson, J. Am. Chem. Soc. **112**, 5123 (1990).

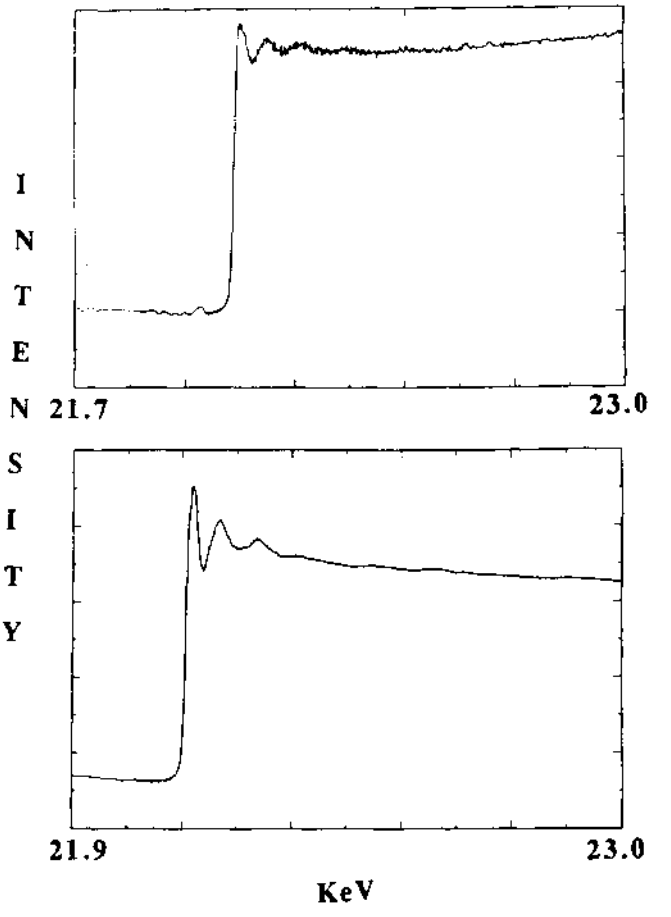

Figure 1. a) X-ray absorption data taken at room temperature for (100) GaAs which had been exposed to $[Ru^{II}(NH_3)_5H_2O]^{2+}$. The spectrum is an average of 25 scans and was collected in the fluorescence mode. b) X-ray absorption data taken at room temperature for $[Ru^{II}(NH_3)_6]Cl_2$. The data was collected in transmission mode.

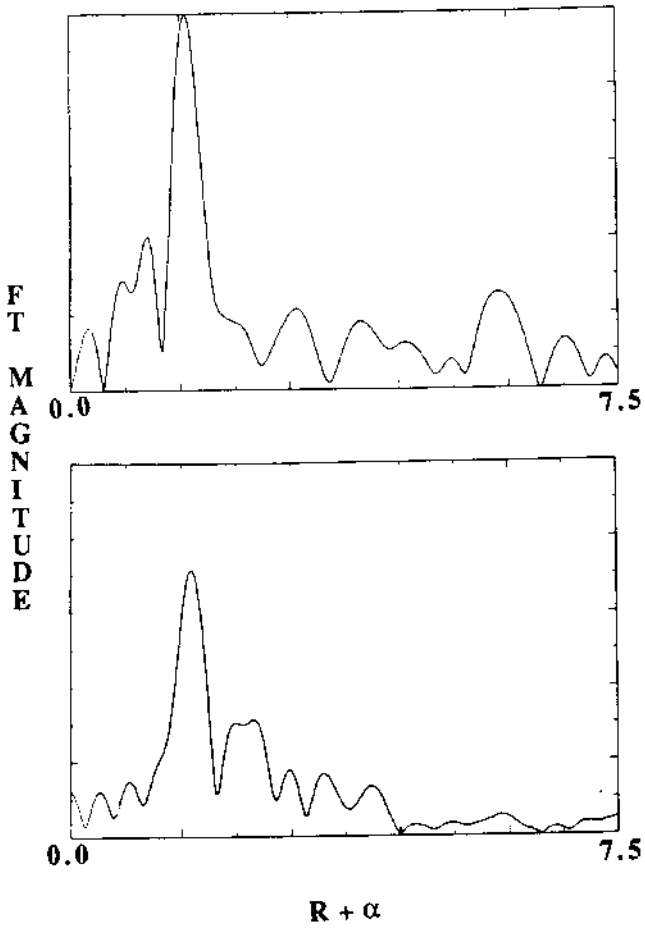

Figure 2. a) Fourier transform of EXAFS from data in figure 1a. b) Fourier transform of EXAFS from data in figure 1b.

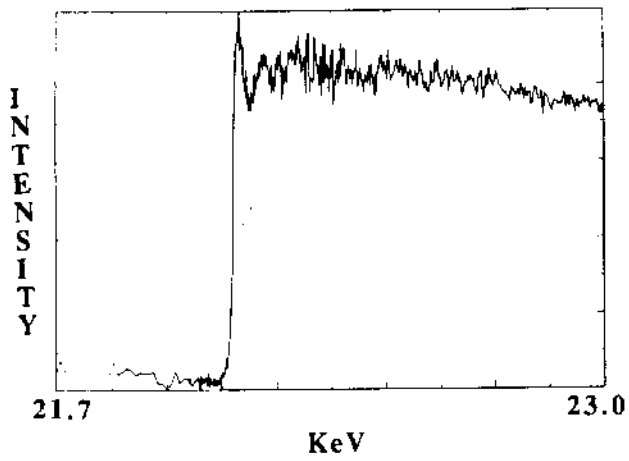

Figure 3. X-ray absorption data taken at room temperature for (100) GaP had been exposed to $[Ru^{II}(NH_3)_5H_2O]^{2+}$. The spectrum is an average of 8 scans and was collected in the fluorescence mode.

XAFS Studies of Perovskites as a Function of Pressure

R. Ingalls, B. Houser† and J. Freund‡

Physics Department, University of Washington, Seattle WA

E. D. Crozier

Physics Department, Simon Frazer University, Burnaby, B.C. Canada

Studies of Focussed Multiple Scattering

While XAFS spectroscopy is a well-established local structural probe, its development is not complete and there are still basic questions that need further study. The problems associated with determining the structural parameters of the first nearest neighbors are understood, the strengths and limitations defined. However, the reliability of second and higher shell information needs clarification which can be obtained through studies of focussed multiple scattering.

When there is an atom in between that which is photoexcited and that which is contributing to the backscattering there are multiple-scattering pathways and the interference is enhanced. This multiple scattering is termed the focussing effect. In the simple case of the three atom configuration, A-B-C, there are four paths involving C, the intervening atom B and the absorber, A. The precise structural specifications of C relative to A and B is complicated by difficulty in obtaining reference amplitudes and phase shifts for each path with a consequent reliance upon theoretical calculations for both their angular and radial dependence, uncertainty in inelastic effects, the loss of information associated with a finite values of k in the low k region, and significant contributions from anharmonicity and asymmetrical distribution functions. By application of pressure we have been able to vary the multiple scattering in a controlled way, providing data for a thorough theoretical study.

Perhaps the simplest example is that of rhenium trioxide, the structure of which is related to the general perovskite, ABO_3. In this case, however, the A site is vacant and the rhenium atom occupies the ocatahecral B site. At atmospheric pressure the rhenium-oxygen-rhenium atoms are collinear and the rhenium L-edge shows a strong focussed multiple scattering. However at 5 kbar ReO_3 undergoes a compressibility collapse in which the octahedra rotate, with the rhenium-oxygen-rhenium bond angle decreasing from 180° to less than 165° at 30 kbar. By systematically changing the pressure, and therefore the bond angle, we are able to control the multiple scattering.

We have performed a room temperature study as a function of pressure as well as an atmospheric pressure study as a function of temperature.[1] We find that the data can be adequately analyzed in terms of the spherical separable wave theory due to our collegue, J. Rehr, yielding bond angles consistent with neutron diffraction experiments. At the same time, however, it is necessary to make rather ad hoc assumpltions about the thermal and static atomic disorder. Therefore in order to sort out these contributions it will still be necesary to to extend this work to low temperatures. An improved cryogenic system has been developed for such work.

XAFS Studies of High T_c Superconductors

One of the new, refreshing and exciting areas of research involves the new classes of superconducting compounds based on copper oxide. The role of high pressure in this connection is to increase T_c and also provide information for testing theories. There have been many high pressure measurements in this field and many XAFS studies, but, to our knowledge, our work under this proposal is the only combined high pressure, low temperature XAFS work.

We have obtained preliminary data on the pressure dependence of the XAFS of both the 90K material, $YBa_2Cu_3O_7$, and 40K material, La_2CuO_4. For the former, our analysis strongly suggests that the oxygen bridges between copper atoms bend with pressure. Strong beating among the yittrium, barium and copper shells makes the analysis complex, and the evidence of chain bending is mainly from a reduction of the copper-oxygen-copper multiple scattering amplitude, much like in rhenium trioxide. On the other hand, the copper-oxygen bonds are relatively incompressible. In the case of the 40K material, the data is easier to unravel. Again we infer that pressure causes the copper-oxygen-copper bonds to bend, in this case from 180° to 164°± 10° at 90 kbar. In both cases this implies that with pressure the copper-oxygen octahedra rotate. Therefore the consequent change in the electronic structure should be addressed in any theoretical treatment. In addition, our XANES study of the temperature and pressure dependence of spectral features on the high energy side of the edge jump shows that they are not due to trivalent copper, in contrast to some published interpretations. Plans have been made to study in detail the 90K material with oxygen content, 6.9, to obtain more information on the nature of the bond buckling described above. Although dT_c/dP on these systems varies greatly with sample, in one instance it has been reported to remain positive to over 150 kbar, with Tc approaching 107K, a healthy increase. At the same time we shall study the non-high T_C material with an oxygen content of 6.1, as a control experiment.

Other Studies

We have continued to study the EXAFS of three alkali-metal halides (NaBr, KBr, RbCl) as a function of pressure with emphasis on determing the second and third cumulants. Monte Carlo simulations using various interatomic potentials such as the generalized Huggins-Mayer formalism, with optional three-body potential terms, have been carried out. The calculated cumulants turn out to be quite model dependent. While our method of calculation is still CPU-time intensive and not yet suited for parameter-fitting, proper, we find high pressure EXAFS data contain sensitive information on interatomic potentials and thus on elastic constants.[2].

References

1. Brian Houser, Ph.D. Thesis, University of Washington, 1990 (unpuplished); Phys. Rev. B (in preparation).
2. Jürgen Freund. Ph. D. Thesis, University of Washington, 1990 (unpublished); Phys. Rev. B (to be published).

Acknowledgements

This work was supported in part by the U. S. Department of Energy and the Natural Sciences and Engineering Research Council of Canada.

† Present address: Physics Department, Eastern Washington University, Cheney WA

‡ Present address: Physics Department, University of Paderborn, Paderborn FRG

PROPOSAL NO. 2033Mp

S And Cl K-Edge XAS Studies of Photographic Materials

Jane G. DeWitt,[1] Teresa A. Smith,[2] Britt Hedman,[3] and Keith O. Hodgson[1]

[1]Department of Chemistry, Stanford University, Stanford, CA 94305
[2]Eastman Kodak Co., Photographic Research Laboratory, Rochester, NY 14650
[3]Stanford Synchrotron Radiation Laboratory, Stanford University, Stanford, CA 94309

Introduction

Several crucial elements of the photographic system including spectral sensitizing dyes and chemical sensitization centers contain sulfur and chlorine atoms incorporated in species on the surface of the photoactive silver halide microcrystals. These centers are involved in surface electron and energy transfer processes and are, therefore, of general interest for their photophysical properties.

We have previously measured sulfur K-edge x-ray absorption spectra on a wide variety of merocyanine and cyanine dye nuclei as well as on structurally characterized Ag-S and Au-S compounds [1]. These experiments revealed sharp absorption features which are highly dependent on the local geometry around and oxidation state of the absorbing atom. Oriented single-crystal spectra of a merocyanine dye nucleus showed that these features are polarized along specific molecular bonds and can therefore be used to determine the orientation of dye molecules of this class in well-characterized systems. The spectra of metal sulfides and other metal/sulfur complexes are dramatically different from the non-metal-complexed ligands, allowing a direct determination of the extent of interaction between sulfur in photographic materials and the silver halide surface by x-ray absorption spectroscopy.

To complete our preliminary studies, we have measured the sulfur K-edge x-ray absorption spectra of an oriented single-crystal cyanine dye nucleus. In addition, we have measured the chlorine K-edge x-ray absorption spectra of a wide variety of cyanine and merocyanine dye molecules including an oriented single-crystal. We have also begun an investigation of the feasibility of measuring surface XAS of dye molecules and chemical sensitization centers on silver halide surfaces using a glancing angle configuration.

Experimental

Spectra were measured at room temperature and detected as excitation fluorescence using a Stern/Heald/Lytle detector [2]. The data were collected using Si(111) double-crystal monochromators on un-focussed beamline 4-1 and focussed beamline 6-2 at SSRL, and on unfocussed beamline X19A and focussed beamline X10C at NSLS. Operating conditions at SSRL were 3.3 GeV and 40 - 90 mA, and at NSLS, 2.5 GeV and 90 - 200 mA. Harmonic rejection was achieved by de-tuning the monochromator on beamlines 4-1, 6-2, and X19A 60% at 3000 eV, 30% at3000 eV, and 80% at 2740 eV, respectively. The post monochromator mirror rejected higher harmonics on beamline X10C.

Pre-oriented single crystal data were measured using a sample holder with χ fixed at 180° and full ϕ rotation. Solid samples weremeasured as powders on mylar tape. The silver sulfide surface sample was prepared by sputtering Ag on a quartz plate and treating the plate with hydrogen sulfide. The sample was mounted on a manipulator stage permitting rotation about the axes in the sample surface plane. The sample was aligned with the surface plane parallel to the incident radiation polarization vector at an incidence angle of 10-20 mrad, and the fluorescence detector was mounted perpen-dicular to the surface sample plane. The beamsize was defined by a pair of tantalum slits to a size of 6 mm wide by 1 mm high.

Results and Discussion

Oriented single-crystal spectra of bis(N-ethyl--thiazoline-2-yl)-trimethine-cyanine iodide, a typical cyanine dye nucleus, are compared to its powder spectrum in Figure 1. The in-plane polarization was defined to be in the plane of the molecule, parallel to the sulfur-sulfur vector. The polarization properties of the absorption spectra are not strong, however, the white line feature is more in-plane polarized than out-of-plane. We have also measured oriented single-crystal spectra of 3,3'-diethylthiacyanine bromide, another cyanine dye molecule and have found the same polarization dependent properties of the S K-edge spectral features.

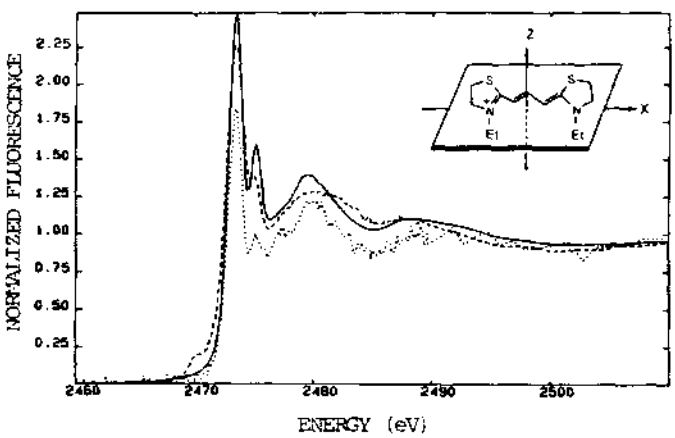

Figure 1. The powder spectrum (——) of bis(N-ethyl-thiazoline-2-yl)-trimethine-cyanine iodide compared to the single-crystal spectra corresponding to polarization along the average X (– – –) and Z (·····) molecular axes.

Chlorine is a common substituent on cyanine and merocyanine dye molecules and serves to facilitate aggregation of the dye molecules.The Cl K-edge absorption spectra of various cyanine and merocyanine dye molecules, shown in Figure 2, are independent of the position of the Cl substituent on the dye molecules studied thus far, however the dominant white line feature does show orientation dependence. Single-crystal oriented spectra of 9,10-dichloroanthracene are compared to its powder spectrum in Figure 3. The white line feature is clearly in-plane rather than out-of-plane polarized, and more strongly polarized along the X molecular axis (parallel to the C-Cl bond and in the plane of the molecule)

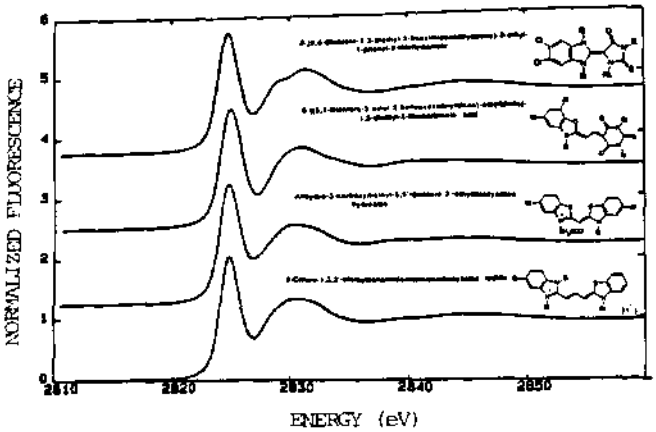

Figure 2. Cl K-edge spectra of various cyanine and merocyanine dye molecules.

than along the Y molecular axis (perpendicular to the C-Cl bond and in the plane of the molecule). These results suggest that polarized surface Cl K-edge x-ray absorption spectra will be another way to obtain information about the orientation of dye molecules on the silver halide surface.

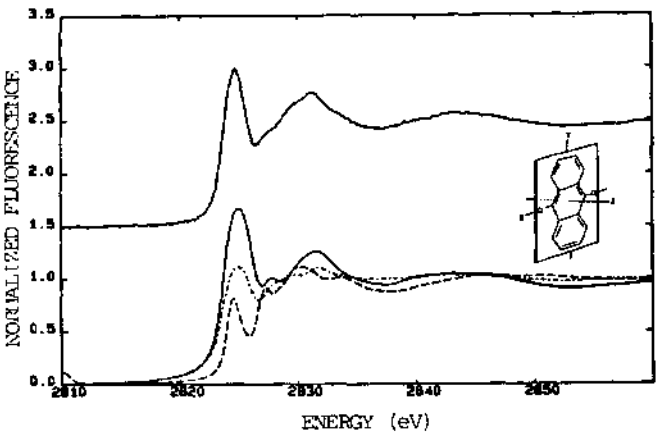

Figure 3. The powder spectrum (top) of 9,10-dichloroanthracene compared to the single-crystal spectra (bottom) corresponding to polarization along the average X (———), Y (-·-·-·) and Z (– – – –) molecular axes.

In addition to our model work with powder samples and oriented single crystals, we have recently demonstrated the feasibility of measuring low levels of sulfur on surfaces at grazing incidence angles. The excellent data confirms that surface XAS experiments on dilute photographic materials will be possible.

Conclusions

The polarization of the sulfur and chlorine K-edge features in these compounds taken together with the high polarization and sensitivity of the S K-edge spectra of the compounds previously studied [1] suggest that XAS will be a useful probe for determining the orientation of molecules on surfaces and detecting their direct interaction with the silver halide surface. The preliminary surface study confirms that we will be able to obtain surface spectra of dilute photographic samples at the sulfur K-edge using a glancing angle configuration.

Acknowledgment

This work is supported by research funds from Eastman Kodak Company. The data were measured at the Stanford Synchrotron Radiation Laboratory and the National Synchrotron Light Source, Brookhaven National Laboratory, which are supported by the Department of Energy, Division of Materials Sciences and Division of Chemical Sciences. SSRL is also supported by the National Institutes of Health, Biomedical Resource Technology Program, Division of Research Resources.

References

1. DeWitt, J. G.; Smith, T. A.; Hedman, B.; Hodgson, K. O. *Stanford Synchrotron Radiation Laboratory Activity Report*, **1989**, 60.

2. (a) Stern, E.; Heald, S. *Rev. Sci., Instrum.*, **1979**, *50*, 1579. (b) Lytle, F.W.; Greegor, R.B.; Sandstrom, D. R.; Marques, E.C.; Wong, J.; Spiro, C.L.; Huffman, G.P.; Huggins, F.E. *Nucl. Instr. and Meth.*, **1984**, *226*, 542.

GRAZING INCIDENCE X-RAY DIFFRACTION STUDIES OF POLYMER FILMS

B. J. Factor
Department of Applied Physics
Stanford University

T. P. Russell
M. F. Toney
IBM Almaden Research Center

INTRODUCTION

The behavior of polymer molecules at the air/polymer interface is of both scientific and technological importance. The presence of an interface places restrictions on the conformations of the molecules near the interface, and, consequently, the structure of the polymers near the interface can be substantially altered [1]. To enable the investigation of polymer structure as a function of distance from the air/polymer interface, the technique of grazing incidence x-ray diffraction (GIXD) has been employed. The goal of this study is to examine the near surface structure of several types of polymers and compare the surface structure with that found in the bulk.

In this report, we discuss measurements on films of an aromatic polyimide, PMDA-ODA, made from pyromellitic dianhydried and oxydianiline (shown below). The films have been prepared with different film thicknesses and annealing treatments. This polymer has received considerable attention in the microelectronics industry as a polymeric insulator. From the fundamental point of view, PMDA-ODA represents an interesting class of polymer which exists as a flexible coil in solution, but is ordered in the solid state.

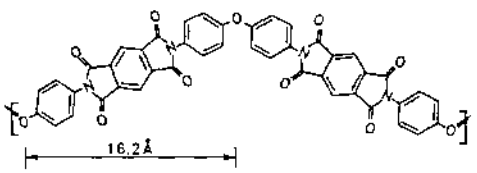

In GIXD, the x-ray beam impinges on the sample at angles close to the angle for total external reflection, typically 3-4mrad for polymers using $\lambda = 1.77$Å. By varying the incidence angle of the x-rays, the x-ray penetration depth can be varied from 50Å to microns[2,3]. For the penetration depth to be well defined, the divergence of the incident x-ray beam must be small, typically 1*mrad* or less. This requirement along with the small scattering volume and the low scattering power of hydrocarbon polymers necessitates the use of synchrotron radiation.

EXPERIMENTAL

Films of the diethylester precursor of PMDA-ODA of molecular weight 23,000 were spin coated onto polished silicon substrate from a solution in N-methylpyrrolidone. They were heated gradually to temperatures of 300°C and 420°C, and annealed at these temperatures for 1 hr. and 1/2 hr., respectively. The resulting films were shown by ellispometry and x-ray reflectivity measurements to be approximately 2600Å in thickness with an RMS roughness of less than 8Å. Thin films 100Å in thickness, with annealing treatment at 300°C and 420°C, were also prepared.

GIXD measurements were performed in on beam line X20C at the National Synchrotron Light Source at the Brookhaven National Laboratory. A pair of W/Si multilayers with a d-spacing of 23Å was used to monochromate the incident x-rays at a wavelength of $\lambda = 1.77$Å with a 1% bandwidth. The divergence of the collimated incident beam was 1*mrad* horizontally and 0.5*mrad* vertically, and the acceptance of the scattered beam at the detector was 8*mrad* horizontally and 2*mrad* vertically. GIXD was performed with a four circle goniometer (with standard θ, 2θ, χ and ϕ motions) in a geometry where the scattering vector was parallel to the surface. The sample was mounted nearly vertically, and the angle of incidence, α, was selected by appropriate motion of χ and θ angles according to the relation $\sin\alpha = \sin\chi \sin\theta$. In the measurements, scans in $q(=(4\pi/\lambda)\sin[(2\theta)/2])$ were made at constant α. The sample was blanketed in a helium atmosphere to prevent oxidation, and minimize background. For the data analysis, the appropriate corrections for background and scattering area were made.

RESULTS AND DISCUSSION

The diffraction from bulk of the 2600Å film annealed at 300°C was measured with $\alpha = 0.22°$. The profile, shown in figure 1a, has a strong reflection at 0.43Å^{-1} with width of 0.1Å^{-1} at FWHM as well as a broad diffuse reflection centered about 1.3Å^{-1}. The 0.43Å^{-1} reflection corresponds to a d-spacing of 14.5Å, the projected length of one segment onto the chain axis, while the 1.3Å^{-1} reflection is due to short range order among neighboring chains. The profile is consistent with *liquid crystalline* ordering of the molecules[4].

The surface sensitive diffraction profile, measured with $\alpha = 0.17°$ with a corresponding penetration depth of 65Å, ex-

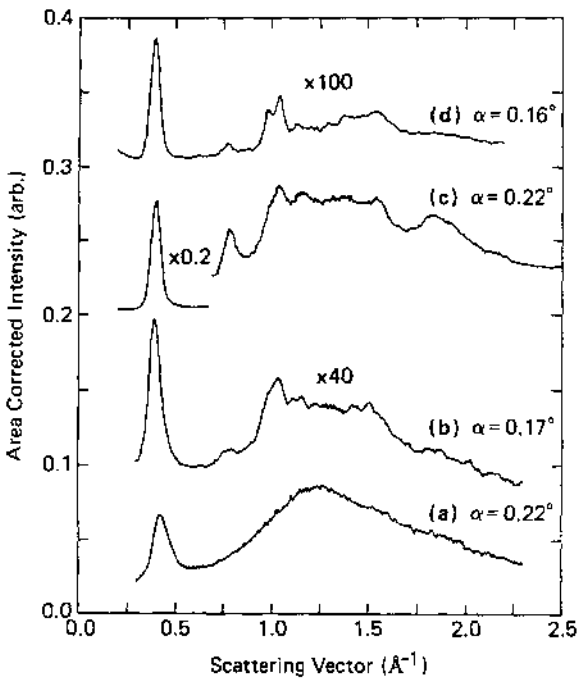

FIGURE 1: Diffraction profile for 2600Å thick PMDA-ODA films: (a) annealed at 300°C, $\alpha = 0.22°$ (bulk); (b) annealed at 300°C, $\alpha = 0.17°$ (d = 75Å); (c) annealed at 420°C, $\alpha = 0.22°$ (bulk); (d) annealed at 420°C, $\alpha = 0.16°$ (d = 65Å).

hibited a much different structure. The profile, shown in figure 1b, has several reflections, starting with a strong peak at 0.397Å^{-1} with a width of 0.055Å^{-1}, with many weaker reflections at larger q. The profile is consistent with a *crystalline* ordering of molecules which occurs above 350°C (see below), and the positions of the reflection are consistent with an orthorhombic unit cell structure previously measured[5].

The integrated intensity of the first reflection was modeled as a superposition of the reflections from the two phases. Consequently, the relative intensity of the two reflections varies as a function of α. Since the reflections occur at different q, the integrated intensities can be determined by fitting scans in q at constant α, assuming the first reflections from the two phases occur at 0.398Å^{-1} and 0.434Å^{-1}. The calculated intensities were then fit to a model where the crystalline phase persists a finite distance into the bulk, after which only the liquid crystalline ordering exists (figure 2). According to this model the thickness of the crystalline surface layer is 65Å ± 10Å.

Differences in the surface and bulk diffraction were also observed for the 2600Å film which was annealed at 420°C. The profiles, taken at $\alpha = 0.22°$ (figure 1c) for the bulk and $\alpha = 0.16°$ for the surface (figure 1d), are consistent with a crystalline ordering. The differences between surface and bulk are evident in the shift of the first reflection from 0.402Å^{-1} in the bulk to 0.394Å^{-1} at the surface, without a noticeable change in peak width from 0.055Å^{-1}. With increased surface sensitivity, the reflections at 0.98Å^{-1} and 1.04Å^{-1} decreased in width from 0.06Å^{-1} to 0.04Å^{-1}, but increased in integrated intensity relative to the *first reflection*. This an indication that the crystalline ordering at the film surface consists of crystallites which are both larger and more ordered. Based on the position of the first peak as a function of penetration depth, the enhanced ordering propagates approximately 80 ± 10Å from the surface.

PMDA-ODA films 100Å in thickness annealed at 300°C and 420°C were also examined. Their diffraction profiles were qualitatively equivalent to the bulk of the 420°C, and surface of the 300°C thick films, implying that both thin films are crystalline.

In summary, our measurements demonstrate that the air/polymer interface has a dramatic effect on the structure of neighboring polymers. For the 2600Å PMDA-ODA films, the surface is more ordered than the bulk independent of the annealing temperature. For the ultrathin 100Å films, the confined geometry results in a crystalline phase, a further demonstration of surface ordering effects.

REFERENCES

[1]Kumar, S.K.; Vacatello, M.; Yoon, D.Y. *J. Chem. Phys.*, *89*, 5206 (1988).

[2]Toney, M.F.; Huang, T.C.; Brennan, S.; Rek, Z., *J. Mater. Res.*, *3*, 351 (1988).

[3]Dosch, H.; Batterman, B.W.; Wack, D.C., *Phys.Rev.Let.*, *56*, 1144 (1986). Dosch, H., *Phys.Rev.B*, *35*, 2137 (1987).

[4]Takahashi, J.; Yoon, D.Y.; Parrish, W. *Macromolecules*, *17*, 2583 (1984).

[5]Kazaryan, L.G.; Tsvankin, D.Ya; Ginzburg, B.M.; Thuichiev, Sh.; Korzhaven, L.N.; Frenkel, S.Ya., *Vysokomol. soyed. A14*, 1199 (1972) (*Polymer.Sci. USSR (Engl. Transl.).21*, 1644 (1979)).

ACKNOWLEDGEMENTS

This research is supported by the Department of Energy through the Office of Basic Energy Sciences (DOE-BES), and IBM. B.J.F. acknowledges support from the DOE-BES, Division of Materials Science through SSRL.

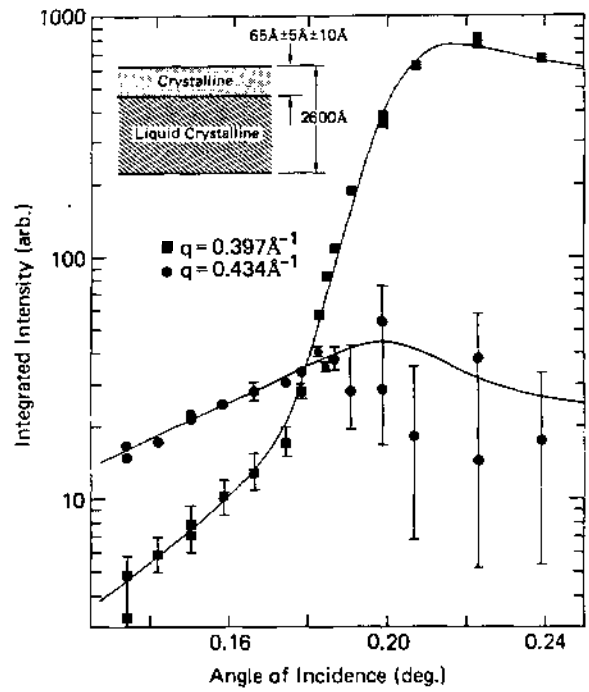

FIGURE 2: Integrated intensity vs. x-ray incidence angle for 2600Å thick film annealed at 300°C for the 0.434Å^{-1} (Δ), and 0.398Å^{-1} (•) reflections, representative of liquid crystalline and crystalline ordering, respectively. The lines are the model predictions for a 65Å thick crystalline surface layer.

STRUCTURAL STUDIES OF AMORPHOUS TERBIUM-IRON ALLOYS

Robert D. Lorentz
Applied Technology Laboratory, 201-1N-34
3M Center, St. Paul, MN 55144

and

Marybeth Rice
Department of Electrical Engineering
Stanford University, Stanford, CA 94305

INTRODUCTION

Amorphous terbium-iron ($a\text{-}Tb_xFe_{100-x}$) can be considered to be a model system representing a broad group of materials that are used as the active layer in magneto-optic recording media. These materials often consist of a combination of rare-earth and transition metals and are usually prepared by vacuum deposition methods as amorphous thin films. Hence, a better understanding of the structural characteristics of these systems will be useful.

EXPERIMENT

All of the $a\text{-}Tb_xFe_{100-x}$ samples used in this study were prepared as thin films by ion beam deposition. Amorphous films approximately 0.5 μm thick were deposited onto Kapton substrates over the composition

The absorption data collected in these experiments were used to extract both EXAFS (Extended X-ray Absorption Fine Structure) and XANES (X-ray Absorption Near Edge Structure) data for each sample. The EXAFS experiments are complicated by the small energy differences between the Fe K, Tb L_{III} and Tb L_{II} absorption edges, which result in small k-ranges for the data and in possible interference to the Tb L_{III} EXAFS signal from the lower energy Fe K absorption edge. Due to the disorder in the materials, however, this interference is small, and modeling of the data appears possible. The EXAFS data have been analyzed and modeling to obtain Tb-Tb, Tb-Fe, and Fe-Fe interatomic distances over the composition range studied is in progress. Several amorphous samples have been prepared with compositions similar to those of the crystal compounds occurring in the equilibrium Tb-Fe system. The 11 atomic % Tb sample studied here has the same composition as the lowest terbium concentration crystalline (c~) phase, $c\text{-}Tb_2Fe_{17}$. The other crystalline compositions are $c\text{-}Tb_6Fe_{23}$, $c\text{-}TbFe_3$, and $c\text{-}TbFe_2$. The amorphous samples studied here include several close to these in composition: x = 19, 23, and 36. The structural information obtained from the amorphous samples will be compared to the known structure of these compounds.

The scaled XANES data were generated from the absorption data by determining the imaginary part of the anomalous scattering factor, f", with use of the optical theorem. This way the XANES data from each sample can be compared. Interpretation of the changes seen in the XANES data as a function of composition is

Kapton substrate scattering. As expected the Kapton peak does not change with energy, indicating that the changes with energy for the other peak are real and represent composition fluctuations. The small changes in background signal level are due to changes in fluorescence. Efforts to identify the phases in the etched sample are continuing.

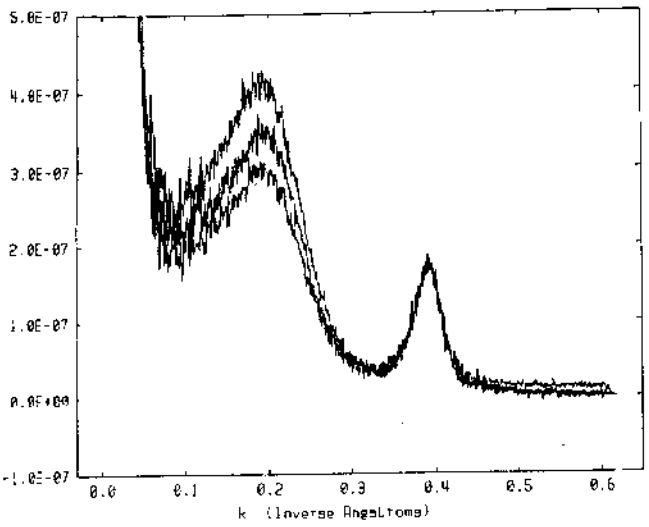

Figure 1. ASAXS below the Fe edge of the etched $a\text{-}Tb_{25}Fe_{75}$ film.

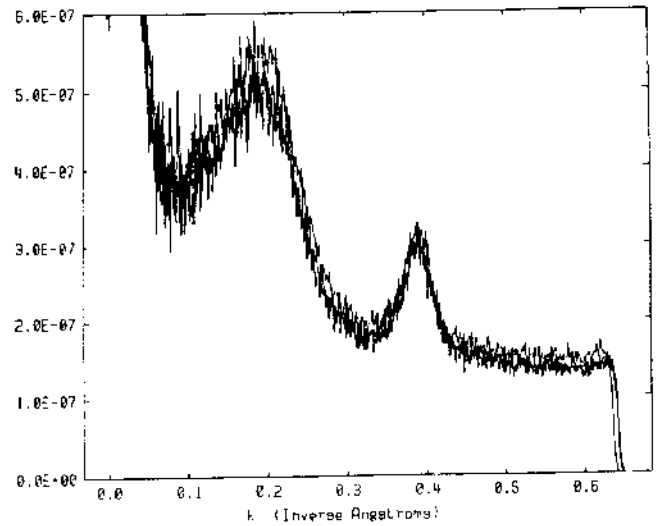

Figure 2. ASXAS below the Tb edge of the etched a-Tb25Fe75 film.

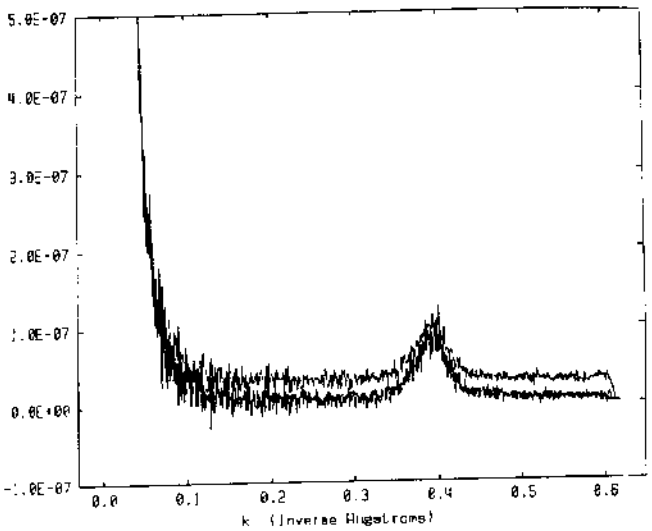

Figure 3. ASAXS below the Fe edge of the non-etched $a\text{-}Tb_{25}Fe_{75}$ film.

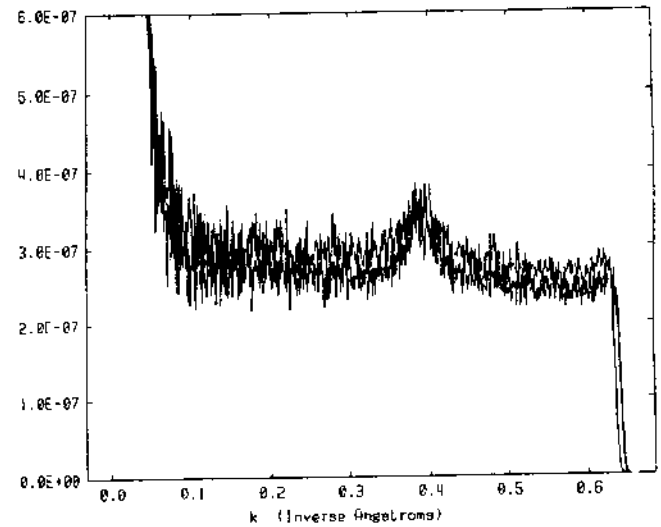

Figure 4. ASAXS below the Fe edge of the non-etched $a\text{-}Tb_{25}Fe_{75}$ film.

Surface EXAFS and Scanning Tunneling Microscopy of the Si(001) 2x1-Sb Interface

PROPOSAL NO. 2089M

M. Richter[1], J. C. Woicik[2], J. Nogami[3], P. Pianetta[1], K. E. Miyano[4], A. A. Baski[3], T. Kendelewicz[4], C. E. Bouldin[2], W. E. Spicer[4], C. F. Quate[3], and I. Lindau[1]

1) Stanford Synchrotron Radiation Laboratory, Stanford Ca. 94309
2) National Institute of Standards and Technology, Gaithersburg, Md. 20899
3) Edward L. Ginzton Laboratory, Stanford, Ca. 94305
4) Stanford Electronics Laboratory, Stanford, Ca. 94305

Figure 1

This is an image of the unoccupied states of the Sb/Si(001) surface annealed at 540° C. The image is 50Å by 50Å. The Sb dimers can clearly be seen. The bright areas are Sb dimers on the second Sb layer. The dark regions corresponds to the bare Si. Anti-site domain boundaries can also be seen. The image was obtained in constant-current mode.

Scanning tunneling microscopy (STM) has been combined with surface extended x-ray adsorption fine structure (SEXAFS) to determine both the local and long range bonding properties of the Si(001) 2x1-Sb surface. The coverage of Sb which remains after annealing thick layers at 375° C, previously reported to be one monolayer (ML), is found in this work to form a disordered overlayer with three dimensional Sb clusters. This finding is concluded from the Sb L3 absorption spectra which are similar for this coverage to that of bulk Sb. After a 550° C anneal, Auger electron spectroscopy (AES), and scanning tunneling microscopy (STM) show that about one ML of Sb remains. Phase and amplitude analysis of the Sb L3 edge SEXAFS shows that the Sb atoms occupy a modified bridge site and form dimers on the Si(001) surface with a Sb-Sb near neighbor distance of 2.88±0.04 Å. Each Sb atom of the dimer is bonded to two Si atoms with a Sb-Si bond length of 2.63±0.04 Å. STM resolves the dimer structure and provides the long range periodicity of the surface. Low energy electron diffraction of vicinal Si(001) shows that the Sb dimer chains run perpendicular to the Si dimer chains.

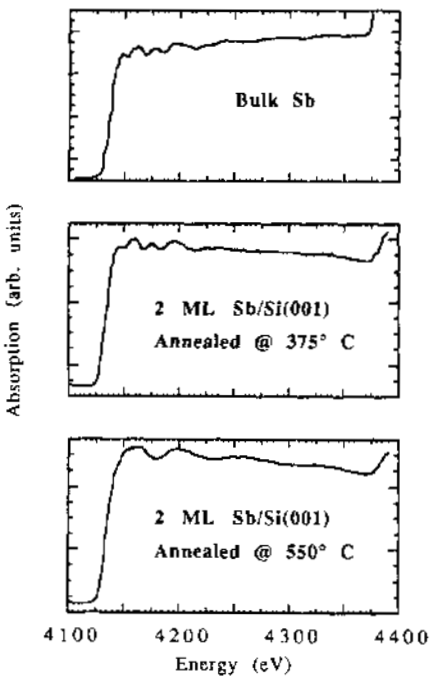

Figure 2

The L_3 adsorption spectra from bulk Sb, and the magic angle spectra for both annealing temperatures are shown. The bulk Sb spectrum and the spectrum obtained from the 375° C anneal are identical. This shows that this suface is covered with Sb clusters. The L_3 adsorption spectrum obtaine from the sample after annealing at 550° C is shown for comparison.

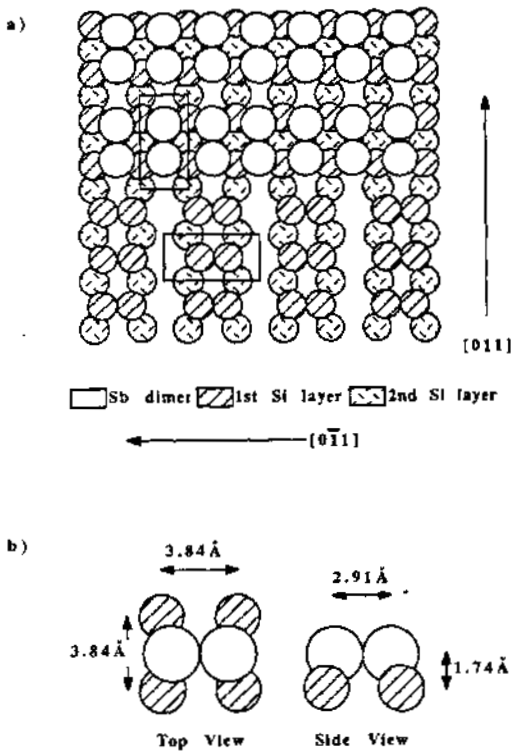

Figure 3

Fig. 3a shows the structure of a single Sb dimer. The atoms are drawn to scale with the radius of each atom taken to be the covalent radius in bulk Sb and Si. These radii would imply a Sb-Si bond length of 2.63 Å, in agreement with the experimentally determined value. Fig. 3b shows the registry of the Sb dimers relative to the clean, relaxed Si(001) 2x1 surface. The Sb dimers are aligned along the [011] direction forming rows that run in the [011] direction. The rectangles show the surface unit cell. The dimensions of the rectangles are 3.84Å x 7.68Å.

CHARACTERIZATION OF YB_{66} FOR USE AS A NEW SOFT X-RAY MONOCHROMATOR FOR SYNCHROTRON RADIATION

PROPOSAL NO. 8103M

Joe Wong*, Z. Rek**, T. Tanaka ***, G. Shimkaveg*, M. Eckart*

* Lawrence Livermore National Laboratory, P.O.Box 808, Livermore, CA 94551
** SSRL, P.O. Box 4349, Stanford, CA 94309
*** National Institute for Research in Inorganic Materials, Namiki 1-1, Tsukuba, Ibaraki 305, Japan

YB_{66}, a complex binary semiconducting compound with a cubic crystal structure and a cell parameter of 23.44 A, has been singled out as a potentially useful soft x-ray monochromator for dispersing synchrotron radiation. There is no intrinsic absorption by the constituent elements in the region 1~2 keV. Using the known structure factors for the (400) and (222) reflections, their rocking curves have been calculated and are shown[1] to be comparable to or better than that of beryl (1010). In terms of vacuum compatibility, resistance to radiation damage, and thermal and mechanical stability, YB_{66} satisfies all the material requirements for use as a monochromator for synchrotron radiation in the soft x-ray region.

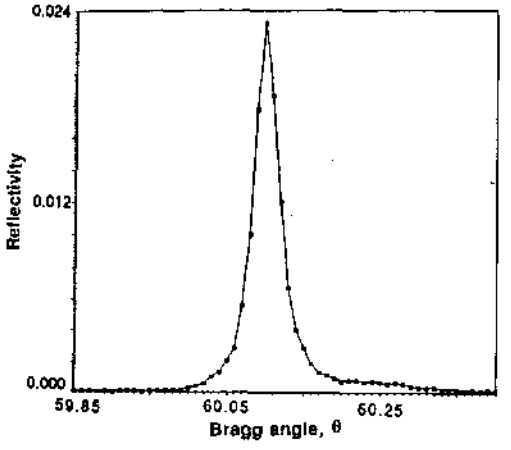

Fig.1. (400) double-crystal rocking curve of seed end area taken with beryl (1010) reference crystal and E=1.25 keV radiation from conventional Mg source. FWHM of this curve equals to 6.7×10^{-4} rad, what corresponds to 0.47eV energy resolution.

Fig.2. Synchrotron radiation white beam reflection topograph of YB_{66} crystal cut along [100] growth direction.

A floating zone method using indirect heating was applied to grow YB_{66} single-crystals [2]. Crystals as large as 50 mm long and 10 mm in diameter with growth directions along [100] and [110] were obtained. Double-zone passes and reduced temperature gradient at the crystal-liquid interface were applied to reduce sub-grain structure in the crystals. Rocking curve measurements, etch pit density, and x-ray white beam topography are used to characterize the quality of these crystals as a function of some critical growth parameters such as pulling rate and thermal gradient. YB66 crystals grown to date exhibit subgrain structure throughout the entire crystal or just part of crystal. The largest angular lattice misorientations measured were of the order of 800 arc seconds and not more than 300 arc seconds for higher quality crystals (Fig. 3B). Single grain areas of the crystal large enough to accept 1 mrad radiation are present. Rocking curves taken for these areas demonstrate their very good quality in terms of defect structure (Fig. 1 and 2A). The energy resolution obtained is very good. Both reflectivity and resolution, however, are lower than theoretically calculated. This indicates the existence of defects in the crystal. From these results, it is clear that control and retention of convexity of the crystal-liquid interface during growth is a key factor to achieve high crystal perfection. Further crystal growth in this direction is now underway.

[1] Joe Wong, G. Shimkaveg, W. Goldstein, M. Eckart, T. Tanaka, Z. Rek, H. Tompkins, Nucl. Instr. & Meth., A291,(1990), 243.
[2] T. Tanaka, S. Otani, Y. Ishizawa, J. Cryst. Growth, 73,(1985), 31.

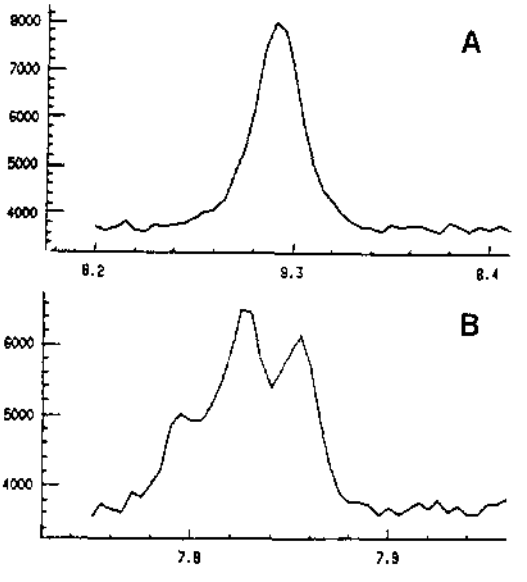

Fig.3. (400) double-crystal rocking curves taken with asymmetric (333) Si reference crystal and CuKα radiation. A) Seed end of the crystal. FWHM equals to 97 arc second (ca 50 times wider than theoretical one); B) Center part of the crystal. Maximum lattice misorientation is of the order of 300 arc seconds.

Quick-Scan EXAFS Study of Solid Combustions

R. Frahm*, Joe Wong, J.B. Holt, E.M. Larson, B. Rupp and P.A. Waide
Lawrence Livermore National Laboratory, University of California,
P.O. Box 808, Livermore, CA 94551

A new quick-scan EXAFS capability setup at SSRL Beamline 10-2 has been utilized to follow the time-resolved site specific chemical changes in a class of self-propagating solid combustion reactions at high temperature in the seconds time regime. The Ni K-edge XANES was used to monitor the combustion synthesis of NiAl from a equimolar mixture of Ni and Al in seconds time frame as well as constant energy scans in the 20 ms regime. In the WO_3 + Al -> W + Al_2O_3 reaction, the W L_3 white line was used to follow the reduction of tungsten oxide to the metal. Using a number of distinctive differential XANES features between the reactant and product, we have also carried out constant energy scan and monitor the transformation kinetics from reactant to the product in a time scale of 20 ms. Preliminary results for these two reaction systems are shown in the figures below. This time-resolved site-specific data will be useful to correlate with the corresponding time-resolved diffraction for these systems[1]. This work is supported under the auspices of DOE by the Lawrence Livermore National Laboratory under contract W-7405-ENG-48.

*On leave from HASYLAB at Deutsches Elektronen-Synchrotron (DESY), Hamburg, Germany.

1. Joe Wong, E.M. Larson, J.B. Holt, P.A.Waide, B. Rupp and R. Frahm, Science, 249,1406 (1990)

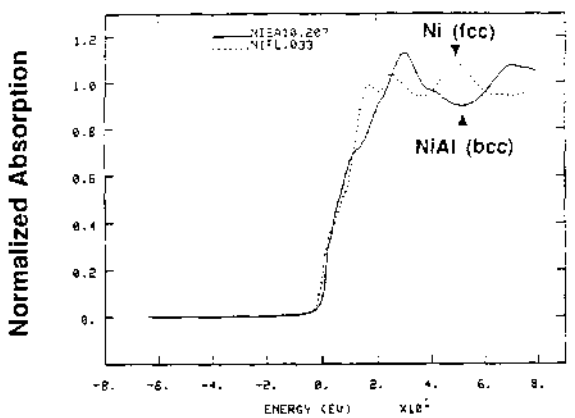

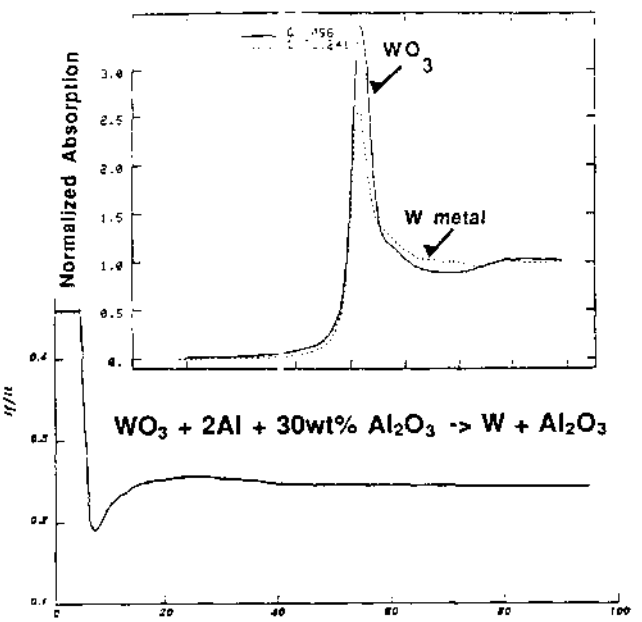

Constant Energy QEXAFS

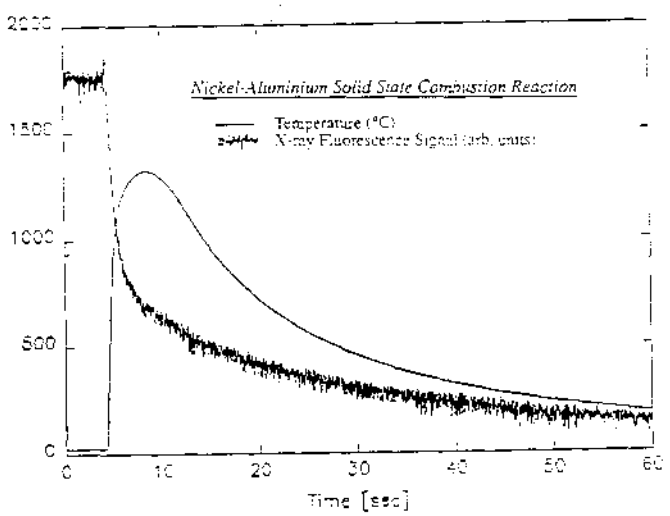

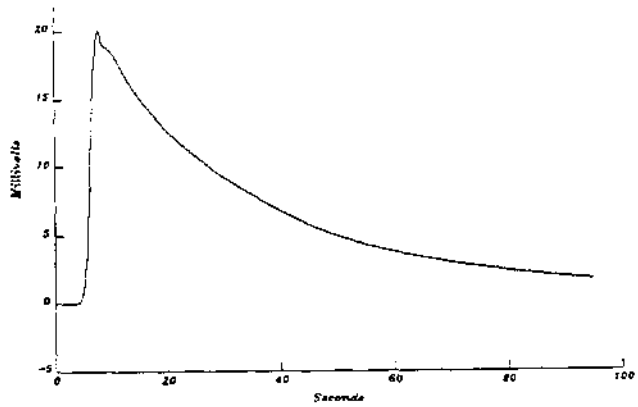

DISTORTED LOCAL ENVIRONMENT ABOUT Zn ON THE COPPER SITES IN $YBa_2Cu_3O_7$

F. BRIDGES and G. LI
Physics Department., University of California, Santa Cruz, CA 95064
J. B. BOYCE,
XEROX PARC, Palo Alto, CA 94304
T. CLAESON
Physics Department Chalmers University of Technology, Sweden.

We have investigated the local structure about Zn atoms in the high temperature superconductor $YBa_2Cu_3O_7$, using the x-ray absorption fine structure (XAFS) technique. This work is part of our continuing studies of the local environment about dopants in various superconductors. Zn is a particularly interesting defect in $YBa_2Cu_3O_7$, as Zn is non-magnetic and strongly suppresses the transition temperature T_c at low Zn concentrations. It is more effective than other transition elements such as Fe, Co, and Ni. There continues to be controversy as to the Cu site that is occupied, (the Cu(1) site or the Cu(2) site) and the details of the local structure out to the second and third neighbors have not previously been determined.

We have completed our analysis of the Zn and Cu edge XAFS on a series of samples from four sources. At the 10% Zn level, we find significant amounts of ZnO in many of the samples. The ZnO is identified by the strong Zn-Zn peak, characteristic of ZnO, that is observed in samples from three of our sources. Using x-ray diffraction, no significant amount of ZnO is detected. This indicates that the ZnO occurs as very tiny particles. Similar results were found earlier for Ni[1] substituted $YBa_2Cu_3O_7$.

A detailed analysis of the best samples (no significant amount of ZnO observed in the XAFS spectra) was carried out for several Zn concentrations. Our results indicate that the Zn substitutes primarily on the Cu(2) site, but the site is strongly distorted. The planar Zn-O(2) and Zn-O(3) distances are lengthened by 0.1 A and the Zn-O(4) c-axis bond is also lengthened. The large increase of the Zn-O(2) and Zn-O(3) bond lengths is inconsistent with the measured lattice parameter, if one assumes that there is little distortion of the site. In addition, the Zn-Y and Zn-Ba second neighbor distances also show distortions, which suggest that the Zn may be displaced along the c-axis.

The large distortion of the Zn(2) site may be an important factor in the strong suppression of T_c by Zn substitution. Fe and Co substitute primarily at the Cu(1) site, while the distortions at the Ni(2) site[1] are similar but smaller than for Zn(2).

This research is supported in part by the National Science Foundation, Grant No. DMR-9004325.

References

1. F. Bridges, J. B. Boyce, T. Claeson, T. H. Geballe, and J, M. Tarascon, Phys. Rev. B 42, 2137 (1990).

MINIMIZING "GLITCHES" IN XAFS DATA: A Model for Glitch Formation

FRANK BRIDGES and XUN WANG
Department of Physics, University of California, Santa Cruz, Santa Cruz, CA. 95064
J.B. BOYCE
Xerox PARC, Palo Alto, CA. 94304

In measurements of the x-ray absorption fine structure (XAFS), the x-ray absorption is obtained from the ratio, R, of the incident, I_o, to the transmitted, I_T, intensity. In such ratioed data, sharp spikes or "glitches" often occur at particular energies. Glitches are observed for all types of samples but are particularly bothersome for low concentration samples when large relative backgrounds must be subtracted, such as is the case for the substituted high T_c superconductors. This short investigation is part of our continuing effort to reduce the effects of glitches in our data.

Previous studies indicate that the orgin of most monochromator glitches is the loss of incident x-ray intensity when simultaneous diffractions occur at the same energy [1,2,3]. For the same angle of incidence relative to the monochromator crystal physical surface, several different sets of planes can diffract the same energy over a narrow range of angles.

Many authors state that for linear x-ray detectors such as gas ionization chambers, intensity variations of I_o caused by steps in beam current or by glitches, are *expected* to ratio out in the measurement of R[2,3]. However in practice, part of the glitch remains in the ratioed data and can be as large as the XAFS oscillations in low concentration samples. The problem is the assumption that the spatial distribution of the incident flux is constant; at a glitch, this assumption is not valid. We have examined the vertical, spatial intensity profile of I_o in the glitch region and found that the variation is strongly dependent on energy. The partial loss of flux when other reflections occurs has a spatial distribution that is related to the angular darwin width of the unwanted multiple scattering peak.

We have developed a model for glitch formation in XAFS data based on our experimental observations that the intensity profile is energy dependent at a glitch. We have shown that large glitches are expected for spatially non-uniform samples because variations in intensity do not ratio out in this case. One way to visualize this effect is in terms of an effective average sample thickness $\bar{t}_{eff}$. If the incident flux is higher at the thick side of the sample, $\bar{t}_{eff}$ is larger than the average sample thickness, $\bar{t}$. Conversely, if more of the incident flux passes through the thinner side of the sample the effective sample thickness is decreased. At a monochromator glitch, the spatial distribution of the flux changes considerably over a small range in energy.

Our model predicts that for a sample with a linear taper, the size of a glitch increases as the slit height squared. Consequently, glitches can be reduced by using smaller slits. The model also predicts both positive and negative lobes to a glitch and thus can explain either upward or downward glitches in real XAFS data for coarse steps in energy. We have also considered other ways to minimize glitches including the use of pixel array detectors for I_o and I_T.

References

1. Z.U. Rek, G.S. Brown and T. Troxel, "EXAFS and Near Edge Structure III." Ed. K.O. Hodgson, B. Hedman and J.E. Penner-Hahn. (Springer-Verlag, Proc. in Phys. 2 (1984)) p.511.

2. K.R. Bauchspiess and E.D. Crozier, ibid, p.514.

3. .G. Van Der Lann and B. T. Thole, Nuc. Instru. & Methods in Phys. Research **A263**, 515 (1988).

Static Structures of Associating Polymers via Small Angle X-Ray Scattering

Alice P. Gast, Kathleen Cogan, and Jennifer Raeder
Department of Chemical Engineering
Stanford University, Stanford, CA 94305 USA

Introduction

Block copolymers in a selective solvent can form associated structures due to their amphiphilic nature. They often assemble into spheres, with a compact core surrounded by a corona of soluble blocks. From light scattering studies (1) we have found that micelles from poly(ethylene oxide)/polystyrene (PEO/PS) can be extremely sensitive to the presence of trace amounts of water in cyclopentane. We can use this water sensitivity to vary the micellar aggregation number over an order of magnitude. Although water swells the micellar cores, the increase in size upon addition of water is dominated by the increase in aggregation number.

We compare the structures formed by block copolymers with those predicted for a multi-arm star polymer (2,3). We picture a homogeous core of PEO blocks and water surrounded by a semi-dilute solution of PS blocks. Each soluble block is represented by a succession of blobs with blob size,ξ, increasing from the center to the outside of the star. Within each blob the chains undergo a random walk of step 1 and the local concentration varies inversely with blob volume. This geometric model based on scaling concepts allows us to predict the density profile and overall size of the micelle given the aggregation number and physical parameters of the polymer/solvent system. We compare this with the radius of gyration and aggregation number obtained from static scattering at small scattering vectors, $R_g^{-1}<q<\xi^{-1}$. In the intermediate scattering regime,$\xi^{-1}<q<l^{-1}$we measure an average blob size as well as verify the random walk behavior expected within each blob.

Experimental

The polymers, described in Table 1, will be denoted by the number of repeat units in each block. We prepared solutions of PEO-PS block copolymers in cyclopentane with varying amounts of water as described before (1). At 23°C, polystyrene chains in cyclopentane are near theta conditions (3). Measurements were taken at SSRL station I-4 and at NSLS station X12B with the help of Malcolm Capel.

Table 1.

Polymer	M.W.	N_A/N_B	R_h(nm)		R_g(nm)
PEO/PS	11,140	65/80	19	(sat'd)	8
	187,500	170/1730	44	(sat'd)	31

Results

Micelles formed from PEO/PS=170/1730 are well described by the star-like micelle model. From light scattering of micelles saturated with water, we measure a radius of gyration of 31 nm compared to star-model predictions of 35 nm. Measured and predicted ratios of radius of gyration over hydrodynamic radius are 0.70 and 0.71, respectively; in comparison to values of 1.24 for single chains and 0.775 for solid spheres. In the intermediate scattering regime measured with x-rays, we find evidence of random walk behavior within the blobs. The decay of the scattered intensity for this sample as q^{-2} in Figure 1a represents correlations between monomers undergoing a random walk. Furthermore, the average blob size of 20.6 obtained from a Zimm analysis in this regime, shown in Figure 2, agrees well with the model prediction of 19.7 nm. Micelles composed of asymmetric block copolymers with large soluble blocks display the structure predicted by the star-like model on both small and large length scales.

The PEO/PS=65/80 micelles deviate from the star-like micelle predictions. Figures 1a and b display a decay of intensity as $q^{-1.5}$ in the intermediate scattering regime. We intrepret this as due to the extension of chains beyond a random coil as they are confined to the micellar corona. Since these chains are relatively short, the blob size never exceeds the minimum required space to execute a random walk. Thus, the chains appear stretched over a length scale longer than normally found for individual random coil polystyrene chains.

References

1. Cogan, K. A. and Gast, A. P., *Macromolecules*, **23**, 745 (1990).
2. Grest, G. S., Kremer, K. and Witten, T. A., *Macromolecules*, **20**, 1376 (1987).
3. Vagberg, L., Cogan, K. A. and Gast, A. P. *Macromolecules* , in press (1990).

Acknowledgements

This work was supported by du Pont Marshall Labs, the Exxon Educational Foundation and the NSF-MRL Program through the Center for Materials Research at Stanford University. We received grants through SSRL and NSLS to travel to NSLS at Brookhaven National Labs.

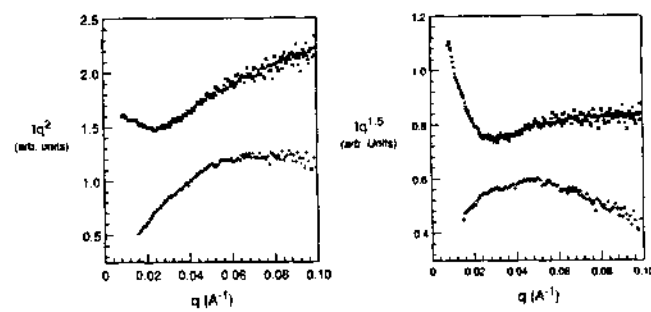

Figure 1 a) Kratky plot Iq^2 against q showing the q^{-2} scaling of the intensity at high q: (+) PEO/PS 170/1730, (x) PEO/PS 65/80.
b) Modified Kratky plot $Iq^{1.5}$ showing the $q^{-1.5}$ scaling of the intensity for PEO/PS 65/80.

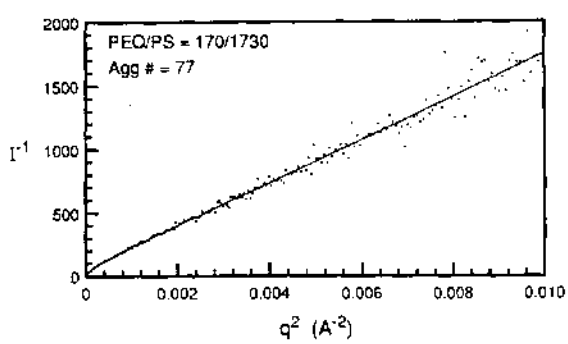

Figure 2 Zimm analysis of PEO/PS 170/1730 in the intermediate scattering regime.

Elastic Strains and Coherency Stresses in Mo/Ni Multilayers

J.A. Bain, L.J. Chyung and B.M. Clemens
Department of Materials Science and Engineering
Stanford, Ca. 94309
and
S. Brennan
Stanford Synchrotron Radiation Laboratory
Stanford Ca. 94309

Abstract

We have performed diffraction scans on symmetric, asymmetric and grazing incidence peaks on polycrystalline Mo/Ni multilayer samples and have determined the complete strain state of these multilayers. From these measurements and with the assumption of a Nishiyama-Wasserman epitaxial relationship, the stress state of both the Mo and Ni layers was determined. We conclude that the residual stress observed in these materials is due to an epitaxial relationship on a grain-by-grain basis between the Mo and Ni constituents and a compressive substrate interaction stress.[1]

Introduction

Several groups have observed that the average out-of-plane lattice parameter of metal multilayers increases with decreasing bi-layer spacing. A variety of mechanisms have been proposed to explain this behavior. Each of the proposed mechanisms can be distinguished if additional measurements are made, such as substrate curvature and non-symmetric Bragg x-ray scattering.

The first of these mechanisms is a compressive substrate interaction stress. This might be due to such effects as alloying, defect annihilation or differential thermal expansion. The compressive in-plane stress would result in an out-of-plane Poisson expansion. For a thin substrate there will be an observable convex bowing of the substrate associated with the compressive substrate interaction stress. The in-plane stress resulting from this would be equi-biaxial, i.e. it would have no variation with crystallographic orientation.[2]

The second proposed mechanism describes each interface between layers as a surface which adds energy to the system. Minimization of the surface energy would lead to an interfacial contraction force analogous to a surface tension. These forces would cause the observed out-of-plane expansion as the "bulk" of each layer is compressed in plane. The net effect of these forces on the substrate however would be a concave bowing. Again, the in-plane stress would be equi-biaxial.[3]

Coherency forces between layers arise from attempting to match the lattices of the two constituents within individual grains. In cases where the lattice mismatch is sufficiently large that interface misfit dislocations exist at all film thicknesses it has been shown that the thermodynamic equilibrium between strain energy and defect energy will result in coherency stresses which increase with decreasing layer thickness. The observed expansion of the atomic plane spacing in the growth direction will occur if the material in tension is elastically stiffer than the material in compression. Unlike the first two mechanisms, coherency forces should show a dependence on crystallographic direction.[4]

Experimental

We examined Mo/Ni multilayers deposited by magnetron sputtering onto Si(100) wafers with amorphous oxide caps of approximately 5000 Å. Bilayer periods vary from 10 Å to 200 Å with equal thicknesses of each constituent. The Ni (FCC) develops a strong (111) texture in the growth direction whereas the Mo (BCC) has a strong (110) texture in the growth direction. All layers are polycrystalline and exhibit no in-plane orientation relationship with the substrate. Symmetric reflection x-ray measurements were taken on using a fixed-target Cu source. Asymmetric measurements used a rotating anode Cu source. Grazing incidence measurements were performed on the beam line 7-2 4-circle diffractometer using 8210 eV radiation. Peak positions were extracted from the data by fitting to Gaussian peaks with linear or parabolic backgrounds.

Analysis

Our results show that the interfacial surface tension force cannot explain the data, because the bowing of the substrate is convex rather than concave. Additionally, we observe a non-equi-biaxial stress in these samples, so a compressive substrate interaction force is not sufficient to explain the data. When scattering x-rays from an FCC(111) textured film grown on a BCC(110) textured film there is an averaging which occurs between (h,k,l) and (h,k,$\bar{l}$) for the BCC reflections and among (h,k,l), (l,h,k) and (k,l,h) for the FCC reflections. The applied coherency stress will not be equal for these sets of reflections, so the measured strain cannot be related to a unique pair of principal stresses without an assumption of the epitaxial relationship between the two constituents. One such orientation is known as Nishiyama-Wasserman. In this arrangement the [001] (BCC) direction lines up with the [1$\bar{1}$0] (FCC) direction and the [1$\bar{1}$0] (BCC) lines up with the [11$\bar{2}$] (FCC). Given this epitaxial relationship we can determine the exact value of the two in-plane epitaxial coherency stresses which are equal and opposite for the Ni and Mo layers. Without this assumption we can still conclude that only non-equi-biaxial stresses will fit our data, but the magnitude of the stresses cannot be determined. In addition to the coherency stresses there is a equi-biaxial substrate interaction stress which can be determined without an assumption of epitaxial relationship. This stress agrees very closely with the substrate stress derived from the wafer curvature measurements.

References

1) J.A. Bain, L.J. Chyung, S. Brennan and B.M. Clemens, submitted to Phys. Rev. B.
2) S.P. Baker and W.D. Nix, M.R.S. Symp. Proc. Vol 188, 294, (1990).
3) R.C. Camarata and K. Sieradzki, Phys. Rev. Lett. **62**, 2005, (1989).
4) J.W. Matthews, in *Epitaxial Growth*, 559, Academic Press, N.Y, (1975).

PROPOSAL NO. 935Vp

ELECTRONIC STRUCTURE AND SCHOTTKY BARRIER FORMATION ON GaAs (100) SURFACES PREPARED BY THERMAL DESORPTION OF A PROTECTIVE ARSENIC COATING

C. J. Spindt, M. Yamada, P. L. Meissner, K. E. Miyano, A. Herrera, and W. E. Spicer
Stanford Electronics Laboratories, Stanford University, Stanford, CA 94305-4055

A. J. Arko
Los Alamos National Laboratory, Los Alamos, N.M.

J. M. Woodall and G. D. Pettit
IBM Thomas J. Watson Research Center, Yorktown Heights, N. Y. 10598

Soft x-ray photoemission spectroscopy has been used to characterize atomically clean MBE grown GaAs (100) surfaces which have been prepared by the thermal desorption of a protective As coating. The samples studied were grown and arsenic capped identically to those used in a previous study (Brillson, et al., J. Vac. Sci. Technol. B **6** 1263 (1988) which reported "unpinned" Schottky barrier formation, with barrier heights over a wide (0.75 eV) range. This is a striking result, as it was previously believed that all metals will pin in narrow range near midgap. This large range of barrier heights led to the suggestion that the (100) surface could become an insulating layer which could screen out MIGS. Motivated by this work, we have characterized the clean surface for the 580°C decapping anneal used in the earlier work, as well as for several other temperatures. The Ga 3*d* and As 3*d* spectra from the 580 °C anneal are deconvolved and separated into their surface and bulk components. It was found that the surface stoichiometry could be varied significantly with the desorption temperature. The As 3d was found to be the best indication of the surface stoichiometry after the anneal. The valence band spectra did not show any strong features due to the excess As which could be used to determine when the sample was completely decapped. The electronic structure of the surface layer was investigated experimentally, and it was found that there is no evidence for an insulating reconstruction. The 0.75 eV range of Schottky barriers reported earlier had Al and Au at the extremes. Because of this, we have studied the deposition of these two metals. We found that the barrier heights for Au and Al differ by 0.25 eV. In addition, we observe that the barrier measurements on the low doped samples are affected by photovoltaic effects, even at room temperature.

SCHOTTKY BARRIER FORMATION ON InP PASSIVATED WITH ONE MONOLAYER OF Sb

M. Yamada, A. K. Wahi, T. Kendelewicz, I. Lindau, and W. E. Spicer
Stanford Electronics Laboratories, Stanford University, Stanford, CA 94305

New procedures which give high Schottky barriers on n-InP have been established. The Schottky barrier heights (SBH) were measured by monitoring shifts in the binding energy of the bulk In 4d core level in surface sensitive photoemission spectra for clean cleaved n-InP (110) surfaces which were treated properly as is mentioned below. Obtained SBHs for n-InP are 0.82 eV for Au, 0.77 eV for Cu, 0.66 eV for Ag, 0.62 eV for Pd, 0.49 eV for Al, and 0.41 eV for In, whereas those reported at clean cleaved n-InP (110) surfaces are 0.45 eV for Au, 0.41 eV for Cu, 0.42 eV for Ag, 0.50 eV for Pd, 0.30 eV for Al, and 0.43 eV for In, including the experimental error of ±0.05 eV.

First of all, a clean InP (110) surface was obtained by cleaving in an ultra-high vacuum chamber (base pressure of 1×10^{-10} torr). Two monolayers (ML) of Sb were deposited on the surface and then annealed at 300°C to obtain just one monolayer of Sb evaporating any Sb not bound to the surface in the epitaxial first one monolayer. To make Schottky barriers on the surfaces, metals were evaporated from tungsten coils. The sample surfaces were kept at room temperature during the deposition. The band bending was monitored with surface sensitive photoemission spectroscopy.

The adsorption of one monolayer of Sb on InP gives a Fermi level pinning 0.35 eV below the conduction band minimum (CBM) for n-InP and that 0.85 eV above the valence band maximum (VBM) for p-InP. However, annealing above 200°C, but below 350°C, reduces the initial band bending at Sb (1 ML)/InP interfaces and recovers nearly the flat band condition with a residual band bending lower than 0.2 eV. The high Schottky barriers are obtained using n-InP (110) surfaces passivated with one monolayer of Sb and annealed at around 300°C. As for unpassivated surfaces, all metal/n-InP interfaces usually show a Fermi level pinning about 0.45 eV (<±0.1 eV) below the CBM. This seems to support the Unified Defect Model (UDM)[1] which explains the mechanism of the Schottky barrier formation, because the other model (Metal Induced Gap States[2]) predicts a different pinning level 0.59 eV below the CBM with experimental data. In this experiment, however, since the Fermi level position ranges over 0.4 eV (from an energy level of 0.41 eV to 0.82 eV below the CBM), an advanced UDM using surface defects, which energetically locate at around 0.4 eV and 0.85 eV below the CBM, seems to be effective in explaining the Fermi level positions observed on InP passivated with one monolayer of Sb, assuming that the effect of MIGS is reduced by inserting one monolayer of Sb between metals and InP as the interlayer which inhibits a tunneling of a wavefunction from a metal to InP.

REFERENCES

1. W. E. Spicer, I. Lindau, P. Skeath, C. Y. Su, and P. Chye, Phys. Rev. Lett. 44, 420 (1980).
2. J. Tersoff, Phys. Rev. B 30, 4874 (1984).

THE INFLUENCE OF THE PHOTOEMISSION PROCESS ON MEASUREMENTS OF SCHOTTKY BARRIER FORMATION: THE OVERSHOOT PHENOMENON

PROPOSAL NO. 935Vp

K. E. Miyano, R. Cao, T. Kendelewicz, I. Lindau, and W. E. Spicer

Stanford Electronics Labs, Stanford University, Stanford, CA 94305

In a recent paper[1] Hecht pointed out the influence of photovoltaic band flattening on photoemission measurements of Schottky barrier formation on low doped substrates; he further suggested that the overshoot observed on highly doped p-GaAs substrates (for an example, see Ref. 2) is due to photocurrent-induced charging of the sample surface upon lowering of the sample work function by the overlayer. While much recent experimental evidence has supported the photovoltaic band flattening, we now address the latter hypothesis. Specifically we present theoretical and experimental arguments against the overshoot being caused by the measurement process; instead we reemphasize an interpretation of this phenomenon in terms of adatom-based gap states. First of all, Ref. 1 does not account for hole-electron pairs produced by the light deep in the substrate (deeper than the depletion region). These electrons have long enough diffusion lengths and are of high enough concentration to null out any photocurrent-based surface charging. In addition the details of Hecht's hypothesis do not quantitatively agree with our LT p-GaAs data: for example the falloff of the band bending from the overshoot position to the final pinning position for Cs / p-GaAs occurs within a coverage regime in which the sample work function is still being lowered.[2] We observe that the overshoot band bending correlates with each adatom donating exactly one charge to the semiconductor depletion and is thus consistent with predictions that individual chemisorbed adatoms induce donor levels in the semiconductor gap.[3] Recent studies[4] on the In / p-GaAs (110) system, for which the overshoot returns at high In coverages when the sample is warmed to RT, can also best be explained in this framework. The falloff of the overshoot and the correlation of this falloff to the overlayer metallicity is key to testing various explanations of this overshoot. The metallicity criterion of emission at the Fermi level can be applied, and the effect photovoltaic band flattening on this criterion[5] is taken into account. The influence of the metallicity on low temperature band bending in general is evaluated in this context.

REFERENCES

1. M. H. Hecht, J. Vac. Sci. Technol. B **8**, 1018 (1990).
2. R. Cao, K. Miyano, T. Kendelewicz, I. Lindau, and W. E. Spicer, Phys. Rev. B **39**, 12655 (1989).
3. J. E. Klepeis and W. A. Harrison, J. Vac. Sci. Technol. B **7**, 964 (1989).
4. K. E. Miyano, R. Cao, T. Kendelewicz, I. Lindau, and W. E Spicer, J. Vac. Sci. Technol. A **7**, 731 (1989).
5. M. Alonso, R. Cimino, and K. Horn, Phys. Rev. Lett. **64**, 1947 (1990).

Photoelectron Spectroscopic Comparison of CO Adsorption on ZnO(10$\underline{1}$0) and CuCl(111)[1]

Jianyi Lin, Paul M. Jones, Jeffrey A. Guckert, Jennifer A. May, Edward I. Solomon*
Department of Chemistry, Stanford University,
Stanford, CA 94305

INTRODUCTION

ZnO serves as an industrially important catalyst in methanol synthesis from syngas. The same reaction, using the copper-promoted ZnO catalyst, exhibits an activation barrier nearly half that observed for pure ZnO; therefore, it is of considerable importance to elucidate the nature of CO bonding in these systems.

Previously, we have demonstrated that on ZnO single crystal surfaces CO binds to coordinatively unsaturated C_{3v} Zn(II) ions[2], while for (0001) and (10$\underline{1}$0) ZnO surfaces with submonolayers of copper CO binds to high-affinity, coordinatively unsaturated C_{3v} Cu(I) sites.[3] In the present study, we have used PES to define differences in bonding between CO adsorbed on Zn^{++} sites of ZnO(10$\underline{1}$0) and on Cu^{+} sites of CuCl(111), the latter serving as a model for the Cu/ZnO surface. Variable photon energy PES, core level PES, and constant initial state (CIS) resonance studies reveal that both the CO/ZnO(10$\underline{1}$0) and CO/CuCl(111) systems exhibit CO-metal bonding predominantly σ in nature; however, both CO 5σ-metal interactions and metal-to-ligand π back-bonding are found to be significantly stronger for CO on CuCl.

RESULTS AND DISCUSSION

Evidence of a stronger CO 5σ-Cu(I) bonding interaction is found in the energy shifts and intensities observed in the valence band PE spectra of the CO-covered ZnO(10$\underline{1}$0) and CuCl(111) surfaces. For the CO/CuCl system the CO 5σ photoemission peak is shifted relative to the gas phase CO value by 2.2 eV to deeper binding energy, whereas the corresponding shift for CO on ZnO is 1.3 eV. Part of this stabilization, however, can be attributed to the M $3d^{10}$-CO 5σ interaction, which does not contribute to the net bonding since both levels are completely filled. The fact that some $3d^{10}$ interaction contributes to the larger stabilization of the 5σ level in CuCl is demonstrated by the CO 5σ intensity-energy profiles in which the 3d delayed maximum is significantly weaker for CO/ZnO (Figure 1), indicating less mixing of the metal 3d orbitals with the ligand 5σ level. Alternatively, CIS resonance studies of the M 3d shake-up satellite collected at the respective metal 3p → 4s absorption edges, reveal a shift in the transition energy of 2.2 eV to higher photon energy in the CO/CuCl system compared to a much

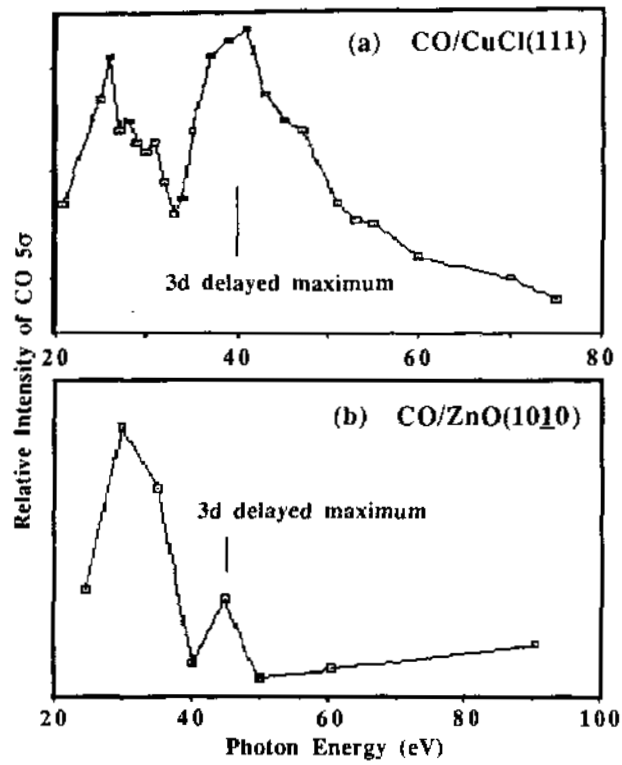

FIGURE 1. CO 5σ intensity-energy profiles for (a) CO/CuCl(111) and (b) CO/ZnO(10$\underline{1}$0).

smaller 0.8-eV shift for CO/ZnO (Figure 2). Thus, the net σ bonding which destabilizes the M 4s orbital is greater for CO chemisorbed to Cu(I). The relatively weak interactions between Zn 3d and CO 5σ likely derive from the higher effective nuclear charge on Zn(II), which lowers the ionization energy of, and contracts the Zn 3d orbitals, decreasing overlap with the CO 5σ orbital.

The virtual absence of π back-bonding in CO/ZnO(10$\underline{1}$0) is observed in the carbon core level PE spectra (Figure 3). Whereas prominent satellite structure in the CO/CuCl(111) carbon 1s spectrum indicates a fairly significant amount of of mixing between the CO $2\pi^*$ and Cu 3d orbitals, no such satellite structure appears in the CO-covered ZnO spectrum. This weak π back-bonding results from the fact that the filled Zn 3d band lies far below the Fermi level, also a result of the high effective nuclear charge of Zn(*II*).

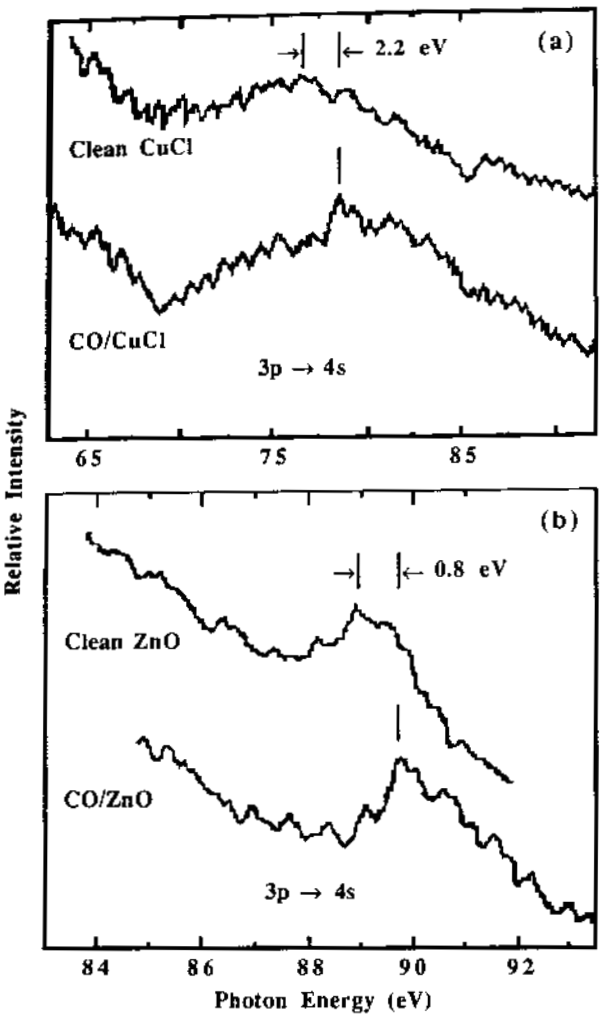

FIGURE 2. CIS intensity profiles of the metal 3p → 4s transition for the clean and CO-covered surfaces of (a) CuCl(111) and (b) ZnO(10$\underline{1}$0).

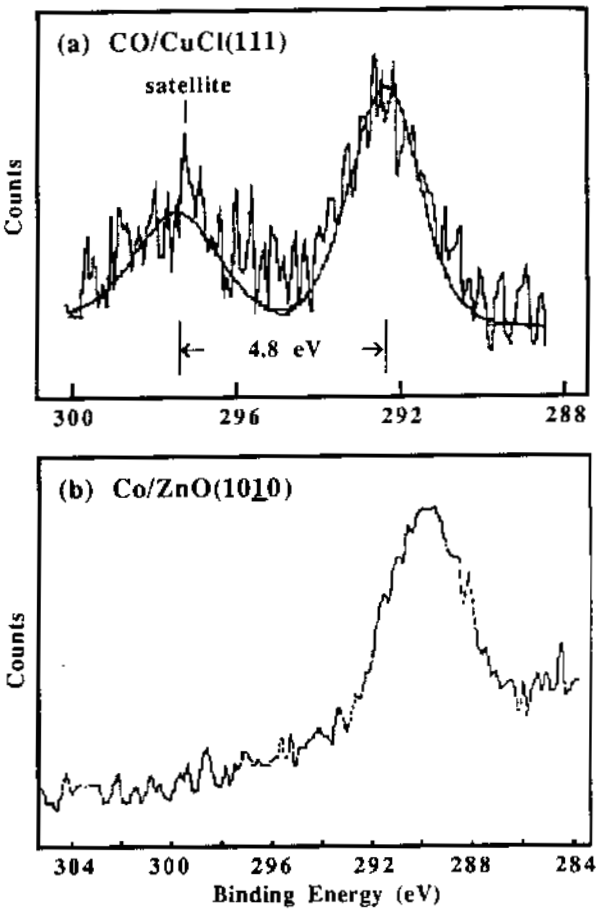

FIGURE 3. Carbon 1s PE spectra of (a) CO/CuCl(111) and (b) CO/ZnO(10$\underline{1}$0).

It is thus determined that by changing the d^{10} binding site on the substrate from Zn(II) to Cu(I) ions, the metal-CO ligand bonding scheme is greatly affected. The resulting effects on the physical properties of the chemisorbed CO molecule are directly relevant to the catalytic activity of these systems.[1]

ACKNOWLEDGEMENTS

Experiments were conducted on Beam Line III-1 at the Stanford Synchrotron Radiation Laboratory. Financial support and additional experimental facilities were provided by the Stanford Center for Materials Research, which is funded by the NSF Division of Materials Research.

REFERENCES

1. Lin, J.; Jones, P.M.; Guckert, J.A.; Solomon, E.I., submitted.
2. Gay, R.R.; Nodine, M.H.; Henrich, V.E.; Zeiger, H.J.; Solomon, E.I. *J. Am. Chem. Soc.* **102**, 6752 (1980).
3. Didziulis, S.V.; Butcher, K.D.; Cohen, S.L.; Solomon, E.I. *J. Am Chem. Soc.* **111**, 4150 (1989).

Synchrotron Based Studies of X-Ray Induced Photoconductivity

L. S. Pan, P. Pianetta
Stanford Synchrotron Radiation Laboratory
P. O. Box 4349, Bin 99
Stanford, CA 94309

D. R. Kania
Lawrence Livermore National Laboratory
M. S. 473, P. O. Box 5508
Livermore, CA 94550

I. Introduction

In recent years interest in the electronic properties of diamond has increased dramatically, motivated by the ability to deposit thin films of diamond on a number of substrates. Diamond is potentially unmatched for certain electronic applications, due to its high thermal conductivity, high dielectric breakdown strength, and large electron and hole mobilities. Properties such as carrier mobility and lifetime, however, are difficult to measure because the material is highly insulating. One technique which can be used is transient photoconductivity. With this method, the carrier concentration, normally low, is enhanced by photoexcitation to a measurable level and can be calculated, knowing the incident power. We have applied this technique to a number of different forms of diamond, including natural IIa diamonds, bulk synthetic diamonds formed by the high pressure-high temperature technique, and synthetic thin films of polycrystalline diamond. Synchrotron-induced photoconductivity has been used in conjunction with laser-based measurements to develop an understanding of the electronic properties of this material.

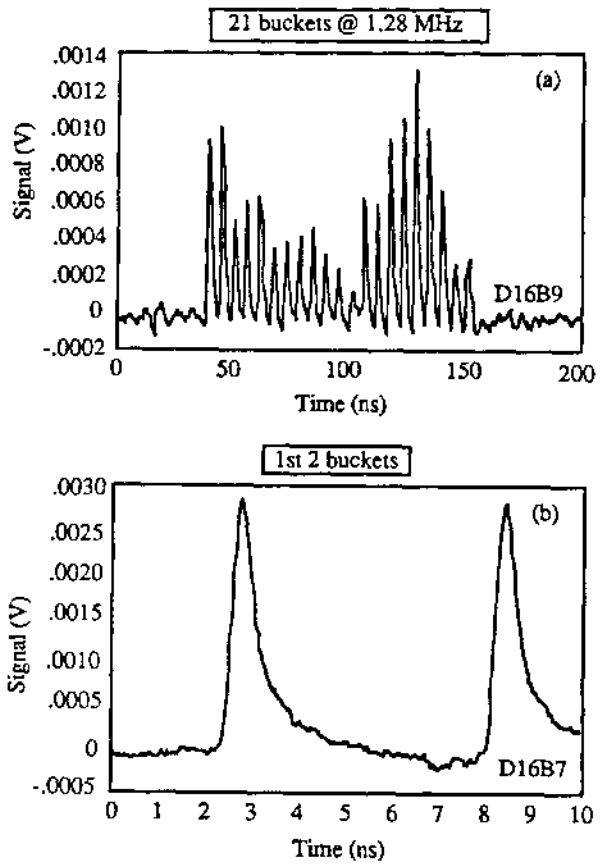

Fig. 1. Signals measured with a type IIa diamond, excited by the beam from BL III-4, with a 5 μm filter inserted. (a) Signals from a group of 21 buckets moving around the ring at 1.28 MHz. (b) Higher resolution of the first 2 buckets.

II. Experimental Setup and Analysis

A bias voltage is applied across the photoexcited volume of material, and the change in conductivity due to the induced carriers is measured. We take advantage of the repetitive, pulsed nature of the synchrotron to measure very low intensity photoconductivity in the material. Very fast signals can be measured with our sampling system (rise time ~30 ps), and a signal averager greatly improves the signal-to-noise ratio. Fig. Ia shows a typical signal measured with a type IIa natural diamond and illustrates the pulsed nature of the synchrotron. Fig. Ib shows a pulse under higher time resolution.

A deconvolution of the measured signal is performed with a gaussian of FWHM 350 ps, which removes the contribution from the x-ray pulse. The resulting decay is a measure of the lifetime of the free carriers in the material. The magnitude of the signal gives us the carrier mobility.

III. Results

Carrier mobilities in the natural IIa diamonds varied from 2000 to 4000 $cm^2/V\text{-}s$. The variation was due to different amounts of impurities and defects in the samples. Lifetimes varied between 200 and 600 ps. Shown in Fig. 2 is the mobility as a function of excited carrier density in sample D36. The points for densities less than $10^{14}/cm^3$ were taken with the synchrotron. The points at higher densities were taken using a UV laser [1]. The curve is a model taking into account the effects of scattering between electrons and holes at higher densities [2].

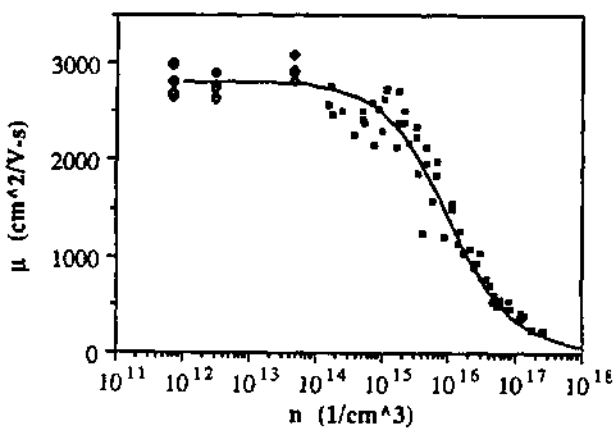

Fig. 2. Mobility as a function of excited carrier density in a natural diamond. The decrease at higher densities is due to scattering between electrons and holes. The solid curve is a model describing this effect [2].

Similar measurements were performed on synthetic samples formed by applying high temperatures and high pressures to graphite. The main difference between these samples and the natural IIa diamonds was that the nitrogen concentration is lower in the synthetic samples. Nitrogen is the main impurity in these single-crystal samples and acts as a recombination center for the excited electrons and holes [2]. The

lower concentration leads to a much longer lifetime, as illustrated in Fig. 3, where a slowly decaying component is seen in the pulses. The fast decaying component is a function of the penetration depth of the radiation, and is believed to be due to surface recombination and photoemission from the surface.

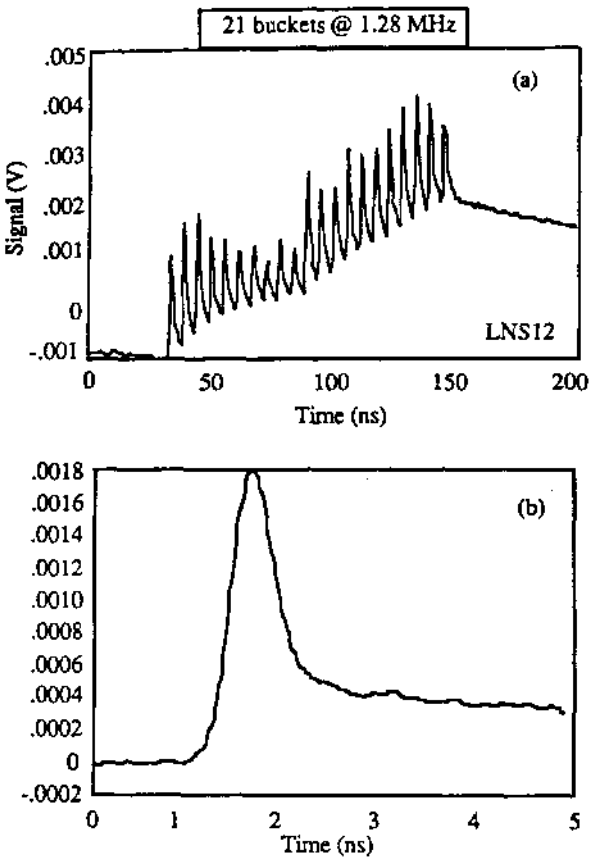

Fig. 3. Signals from a low nitrogen, synthetic sample. There are two components observed in the signals, the slow decay perhaps representative of the bulk lifetime, and the fast decay due to surface recombination and photoemission.

Because of the more complicated, two-component decay, it is more difficult to analyze the signal for a mobility. The fast decay is around 350 ps, following deconvolution, while the slow decay lasts many 100's ns. Work is being done presently with the laser system to try to determine the mobility and the lifetimes.

The final set of diamond samples that we examined with x-ray photoexcitation was polycrystalline films of chemical vapor deposited diamond on silicon. The films were 3 to 6 μm thick with grain sizes around 1 μm. The silicon substrate was etched off during sample preparation, leaving a free-standing film, which was epoxied to an alumina substrate. A gold transmission line was patterned across the sample, and a gap of 1 mm in the line defined the active region.

Photoconductivity in the films was much more difficult to measure for a number of reasons. First the mobility was lower, which meant the signals were smaller. Second photoemissive effects due to the x-rays hitting the gold or the non-active region of the diamond were significant. Only by carefully positioning the beam exactly in the gap were photoconductive signals measured.

From the limited number of such measurements, we extracted a mobility of around 50 to 60 $cm^2/V\text{-}s$ for these films. This is in good agreement again with laser based measurements, which again provided complimentary data at higher densities. Fig. 4 shows the mobility as a function of density in a microwave film. Lifetimes were measured to be between 300 and 400 ps.

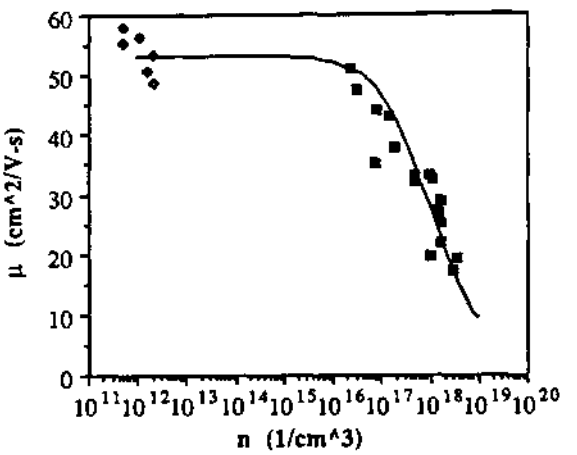

Fig. 4. Mobility as a function of excited carrier density in a natural diamond. Again the decrease at higher densities is due to scattering between electrons and holes.

IV. Conclusion

X-ray induced photoconductivity is a powerful technique for measuring the mobility and lifetimes in insulating materials, as illustrated by our work with diamond. The pulsed repetitive nature of the synchrotron allows measurements which are complimentary to those taken with an ultraviolet laser. In the future films of improved quality will be examined. Also future experiments will take advantage of the wide spectrum of radiation from the synchrotron and its tunability with filters or monochromators by examining photoconductivity as a function of photon energy.

References

[1] D. R. Kania, L. S. Pan, P. Bell, O. L. Landen, H. Kornblum, P. Pianetta, and M. D. Perry, J. Appl. Phys., 68 (1), 124 (1990).

[2] L. S. Pan, D. R. Kania, P. Pianetta, and O. L. Landen, Appl. Phys. Lett., 57 (6), 623 (1990).

SYNCHROTRON-BASED IMAGING WITH A MAGNETIC PROJECTION PHOTOELECTRON MICROSCOPE

P.L. King, A. Borg*, C. Kim, S. Yoshikawa, P. Pianetta and I. Lindau

Stanford Synchrotron Radiation Laboratory, Stanford, CA 94309, USA
**University of Trondheim, Trondheim N-7034, Norway*

Innovative instrumentation is currently being developed that brings photoelectron and photoabsorption analysis to the sub-micron arena. The synchrotron-based techniques are categorized into two classes [1]. In the "microprobe approach", state of the art x-ray optics are used to focus x-rays down to a point while the specimen is mechanically scanned to form an image. Zone plates [2], ellipsoidal focussing mirrors [3], and Schwartzschild objectives utilizing multilayers [4] are at the heart of these developments. For example, Ade et al have recently reported on progress with a zone plate based microscope having a resolution of 0.3 um [2]. In the "selected area approach", electrostatic and magnetic lenses are used to directly image a surface without scanning. Tonner has recently presented photoabsorption (NEXAFS) spectra from areas as small as 10 um square using an electrostatic immersion lens [5]. That technique may be extended down to 0.1 um at present being limited largely by photon flux. With modification, many commercial imaging systems (e.g. the Balzers KE3 Metioscope [6], Scientia ESCA-300 [7], or VG ESCASCOPE [8]) and a variety of laboratory PEEMs [9,10] brought into the synchrotron environment, would contribute significantly to the field of high resolution emission microscopy with either photoelectron or photoabsorption spectroscopic capabilities.

Our group is continuing its studies using a selected area technique that combines high lateral resolution imaging with both photoelectron (XPS) and photoabsorption (NEXAFS) spectroscopic capabilities. We utilize a magnetic projection photoelectron microscope (a commercial design manufactured by Surface Science Instruments) that is based on a concept that originated in the Turner group at Oxford [11]. The instrument has been fully described in a previous publication [12]. This instrument relies on a diverging magnetic field to directly project electrons from the photoexcited surface to a two dimensional detector and performs imaging photoelectron and photoabsorption spectroscopy with a lateral resolution on the order of microns. The retarding field analyzer (high-pass filter) incorporated into the instrument allows us to energy-filter the electrons emitted from a surface and produce spectroscopically significant images that reflect the core and Auger electron yield by which we can identify and track surface species. Energy resolution of the retarding field analyzer has been demonstrated to be better than 1%.

Figures 1 and 2 provide recently collected examples of the imaging capabilities of this instrument. These images resolve a region on a 254 um (10 mil) diameter tungsten wire that was found to be contaminated with Ta. The images were taken at a photon energy of 170 eV with the retarding potentials set to 129 V and 137 V respectively. In the first image no contrast is seen between the clean W filament and the Ta contaminant. The brighter region at the center of the wire originates from inhomogeneities in the photon beam illuminating the wire and can be removed by normalization. In the second image the contrast between a bright Ta region and the rest of the wire is 3.5:1 and can be attributed to energy filtering that enhances the Ta 4f core level.

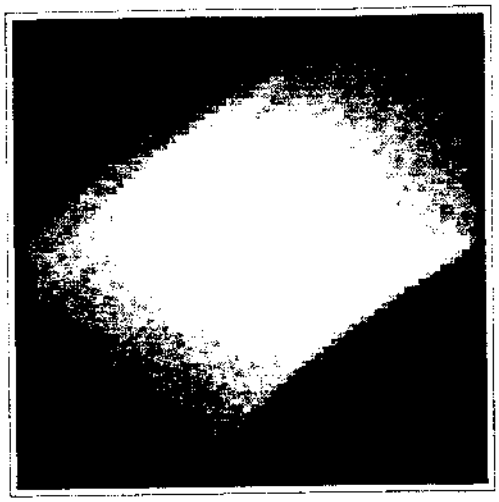

Figure 1. Photoelectron image of a 254 um (10 mil) W filament excited by 170 eV light. The bright spot at center originates from inhomogeneities in synchrotron beam. Electrons have been high-pass filtered such that only those electrons with energies over 129 eV are used to form the image.

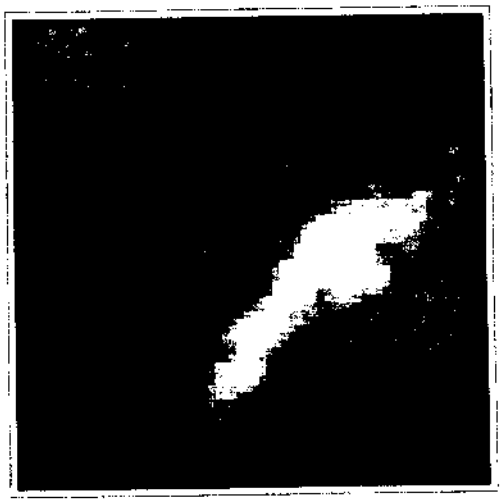

Figure 2. Same field of view and excitation energy as Figure 1. Retarding potential is set to 137 V to enhance the contribution to the image from Ta 4f core level electrons coming from a 1 monolayer Ta surface contaminant. See text for more details.

Figure 3 shows the integral N(E) spectra and contrast from the clean W and Ta contaminated regions. This is an excellent example of contrast that is purely core level derived. Contrast between these elements is high even though there are essentially no absorption cross section effects. The absorption cross section of the Ta 4f level is very similar to the W 4f at this photon energy . This is apparent in that the contrast below 130V and above 145V is equal to 1 i.e. there is no discernable contrast outside of the regions in which the core levels appear. The magnitude of the Ta core level and the reduction in the W emission in the contaminated region is consistent with the presence of a single monolayer of Ta.

The majority of the work carried out during the most recent (April 1990) synchrotron run involved observations of surface diffusion of metals-on-semiconductors. Figure 4 is an example of one of the many metal-on-semiconductor depositions used to examine this phenomena. This image is of a thin (1-3 monolayer) coverage of Al deposited through a 25um wide slit onto a MBE-grown GaAs wafer. The photon energy was 120eV and the retarding potential was set to 69 V to enhance the contribution of the Ga and As 3d core levels. Contrast between the metal and substrate is better than 2:1. This specimen was subsequently heated in order to promote surface diffusion of the deposited metal across the surface. In the case of thin metal coverages, we observed that the metals balled up locally, preferring island growth, rather than diffusing laterally over observable distances. Results of this and other experiments of this type are to be published in and upcoming issue of Ultramicroscopy.

REFERENCES

[1] J. Cazaux, Ultramicroscopy 17 (1984) 43
[2] H. Ade et al, Appl. Phys. Lett. 56 (1990) 1841
[3] R. Nyholm et al, Rev. Sci. Instrum. (1989) 2168.
[4] F. Cerrina et al, Nucl Instr and Methods A266 (1988) 303
[5] B.P. Tonner and G.R. Harp, J. Vac. Sci. Technol. A7 (1989) 1
[6] C. Hammond et al, Metallography 20 (1987) 199
[7] U. Gelius et al, J. Electron Spec., 52 (1990) 747
[8] P. Coxon et al J. Electron Spectr. and Related Phenomena., 52 (1990) 821
[9] G.F. Rempfer and O.H Griffith, Ultramicroscopy 27 (1989) 273
[10] E. Bauer, M. Mundschau, W. Swiech and W. Telieps, Ultramicroscopy 31 (1989) 49
[11] G. Beamson, H.Q. Porter, and D.W. Turner, J. Phys. E: Sci. Instrum. 13, 64 (1980).
[12] P. Pianetta et al , Rev. Sci. Instrum.60 (1989) 1686.

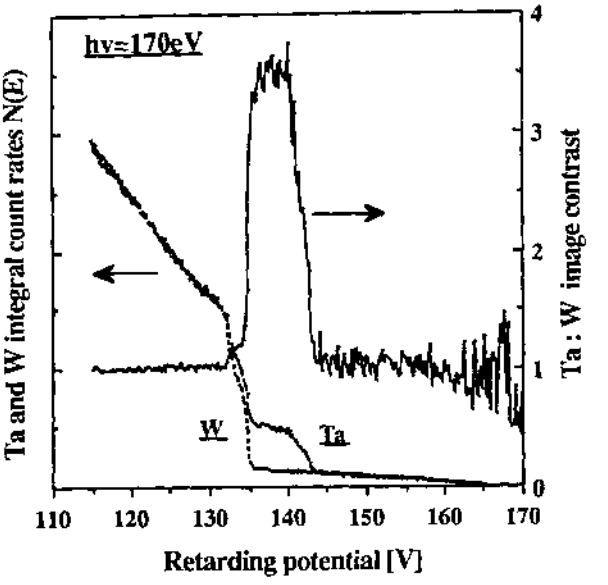

Figure 3. W and Ta integral count rates from the clean W and Ta contaminated regions seen in Figure 2. The observable image contrast which varies as the retarding potential is changed is shown using the scale on the right side.

Figure 4. Image of 25um wide line Al deposited through a mask onto an MBE-grown GaAs wafer. Photon energy is 120 eV and the retarding potential is set to 69 V to enhance the metal:substrate contrast by emphasizing Ga and As 3d core level emission.

Photoemission Studies of Band Structures in ULtrathin GaAs/AlAs Superlattices

Xiaoyu Yang and Piero Pianetta
Stanford Synchrotron Radiation Laboratory, Stanford University, CA 94305

Peng Cheng and James S. Harris, Jr.
Solid State Electronics Laboratory, Stanford University, CA 94305

R. Mariella, Jr.
Lawerence Livermore National Laboratory,Livermore, CA 94550

INTRODUCTION

Superlattice (SL) structures consisting of stacked AlAs/GaAs bilayers are being intensively studied because of potential application in novel devices. Band structures in ultrathin (GaAs)n(AlAs)n SL, when n is less than 8 monolayers, can not be predicted by Kronig-Penny model which treats the SL as sandwiched layers of bulk GaAs and AlAs[1]. There are many theoretical studies which calculate the band structures of ultrathin SL using either effective mass theory, tight-binding methods or self-consistent pseudopotential calculation. However, there have been no direct experimental measurements of the band structure except for the band gap measurements in the ultrathin SL's with n<8. The Valence band offset is a important property for heterojunctions. In this experiment, we use the photoemission method[2,3] to determine the nature valence band offset at the interface of AlAs/GaAs on ultrathin (GaAs)n(AlAs)n SL's as a function of layer thickness n.

METHOD and RESULTS

A series of (GaAs)n(AlAs)n ultrathin SL's were grown by Molecular Beam Epitaxy(MBE) with n=2,4. The arsenic capping technique had been used in order to eliminate any oxygen contamination of the MBE grown layers during the transfer from the growth to measurement system. This technique, which we had used in previous experiments, involves depositing an Arsenic layer on the top of the SL as soon as the growth has been completed[2]. The Arsenic cap was then removed by heating the sample to approximately 500°C in the measurement chamber. The photoemission data were taken using a (VG) ADES-400 angle-resolved spectrometer at beam line III-2. Fig 1 shows the photoemission spectra of Ga 3d for GaAs, $(GaAs)_2(AlAs)_2$ SL with the topmost layer as GaAs, $(GaAs)_4(AlAs)_4$ SL with the topmost layer as GaAs, $Al_{0.5}Ga_{0.5}As$ alloy. The energy positions of the core levels are referred to the valence band maximum(VBM). The alignment of VBM is shown in the right upper corner in Fig 1. The results show that the valence band alignment between GaAs layer and AlAs layer in ultrathin SL is different from that between bulk GaAs and AlAs in conventional heterojunctions. Fig. 2 shows the schematic diagram of VBM in the (GaAs)n(AlAs)n SL. The thin solid line shows the VBM alignment predicted by the Kronig-Penny model and the dark line shows the observed VBM in the (GaAs)n layer in SL and the dash line shows the VBM in the (AlAs)n layer. Δ is the difference between the bulk property and the thin layer property in SL for GaAs layer. The differences (Δ) are 0.1 and 0.04eV for n=2 and n=4, respectively. Δ is dependent on n--layer thickness. The natural valence band offset between GaAs and AlAs layer in ultrathin SL is also depend on the GaAs and AlAs layer thickness.

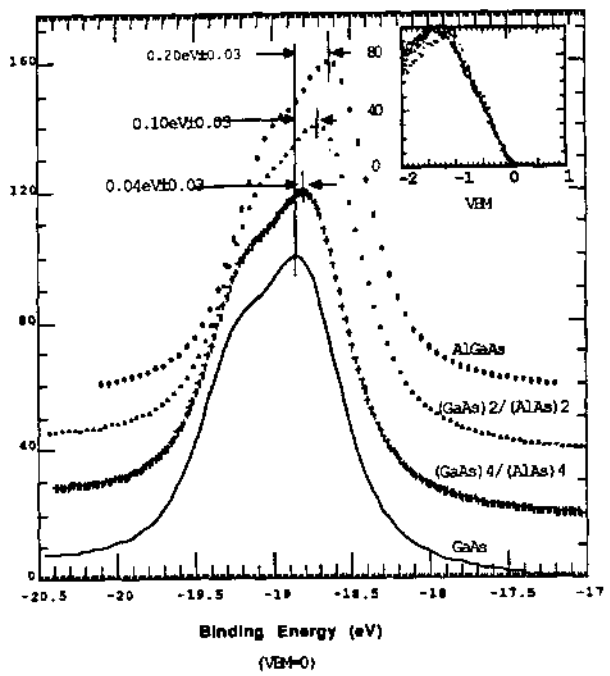

Fig 1: The Ga 3d core levels of GaAs, (GaAs)4/(AlAs)4, (GaAs)2/(AlAs)2 and AlGaAs alloy with the valence-band maxima taken as zero binding energy. (inset: Accuracy of alignment of VBM's)

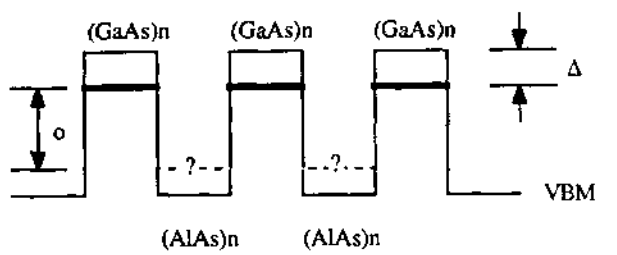

Fig.2 Schematic diagram of Valence Band Maximum in $(GaAs)_n(AlAs)_n$ SL. o is the natural band offset between GaAs and AlAs in the SL.

REFERENCE:
[1] A. Ishibashi, Y. Mori, M. Itabashi, and N. Watanabe, J. Appl. Phys. 58, 2691 (1985)
[2] J. Hwang, P. Pianetta, C. K. Shih, W. E. Spicer, Y.- C. Pao, and J. S. Harris, Jr., Appl. Phys. Lett. 51, 1632 (1987).
[3] C. K. Shih and W. E. Spicer, Phys. Rev. Lett. 58, 2594 (1987)

PHOTOELECTRON DIFFRACTION OF MAGNETIC ULTRATHIN FILMS: Fe/Cu(001)

PROPOSAL NO. 9901V

J. G. TOBIN,* M. K. WAGNER,** X.-Q. GUO,*** S. Y. TONG***, R. DALEY,**** and S. CHAUDHURY*****
*Lawrence Livermore National Laboratory, Livermore, California 94550
**Dept. of Chemistry, University of Wisconsin, Madison, WI 53706
***Dept. of Physics, University of Wisconsin, Milwaukee, WI 53211
****Sandia National Laboratory, Livermore, CA 94550
*****Dept. of Chemistry, University of California, Los Angeles, CA 90024

ABSTRACT

The preliminary results of an ongoing investigation of Fe/Cu(001) are presented here. Energy dependent photoelectron diffraction, *including* the spin-dependent variant using the multiplet split Fe 3s state, is being used to investigate the nanoscale structures formed by near-monolayer deposits of Fe onto Cu(001). Core-level photoemission from the Fe3p and Fe3s states has been generated using synchrotron *radiation as the tunable* excitation source. Tentatively, a comparison of the experimental Fe3p cross section measurements with multiple scattering calculations indicates that the Fe is in a fourfold hollow site with a spacing of 3.6Å between it and the atom directly beneath it, in the third layer. This is consistent with an FCC structure. The possibility of utilizing spin-dependent photoelectron diffraction to investigate magnetic ultrathin films will be demonstrated, using our preliminary spectra of the multiplet-split Fe3s of near-monolayer Fe/Cu(001).

INTRODUCTION

Photoelectron diffraction, both non-spin and spin-dependent, is being used *to investigate the magnetic ultrathin film system,* Fe/Cu(001). Fe/Cu(001) is the prototypical model system of magnetic ultrathin films, yet remains the subject of considerable controversy. For example, a theoretical study[1] predicts a large magnetic moment at a coverage of one monolayer, assuming perfect pseudomorphic growth. Nevertheless, surface magneto optic Kerr effect (SMOKE) measurements indicate an absence of such a magnetic moment, leading to the hypothesis of surface alloying [2]. Photoelectron diffraction has been shown to be a powerful probe of atomic geometric structure, particularly surface alloying [3]. We are performing a photoelectron diffraction study of Fe/Cu(001), using the Fe3p and Fe3s states and *including a full, multiple scattering analysis.* Moreover, a new variant, spin-dependent photoelectron diffraction[4] (SDPD) using the multiplet-split 3s state, will be discussed. SDPD promises to be a probe of both local geometric and magnetic structure, thus providing a nanoscale counterpart to SMOKE measurements.

DISCUSSION

Photoelectron diffraction is a probe that can be used to investigate the local (nanoscale, 10^{-9} m) geometric structure of surfaces and interfaces and which may be adaptable to determining local magnetic structure as well. Photoelectron diffraction can be thought of as an *angle-resolved surface-extended-x-ray-absorption-fine-structure* (SEXAFS) measurement. In our experiments, photoelectrons are ejected from core levels and can be involved with diffraction events caused by scattering off of nearby neighbors. From this, the local geometric structure can be determined to within ±0.05Å [5]. Our experiments are performed at low kinetic energy in order to maximize surface sensitivity [3] and the manifestation of magnetic effects. Thus it is essential that all analysis be performed within the framework of multiple-scattering calculations. The simplifications of single-scattering theory [4,6] are not appropriate except at higher kinetic energies. Moreover, the potential importance of surface alloying in the Fe/Cu(001) system militates against an *over-reliance on forward focussing measurements*, [6,7,8] which is a powerful probe of stacked or buried layers but is unable to distinguish an overlayer from a surface alloy [3, 9]. Finally, Sinkovik and Fadley [4] have pointed out the possibility of utilizing the multiplet split 3s peaks as a source of spin polarized electrons in these experiments. Recent spin-polarized photoemission investigations [10,11] of the Fe3s peak of bulk Fe have confirmed that these two peaks are in fact spin up and spin down *in magnetized samples.* Thus, we are beginning to use this intrinsic spin resolution in the investigation of magnetic ultrathin films, specifically Fe/Cu(001). It is not unreasonable to expect an approximately 10% effect, as is observed in spin polarized secondary electron spectroscopy [12]. Of course, a fully spin-parameterized, multiple scattering theory must and is being developed also.

Several technical details should be discussed before moving on to the results. The variability of the kinetic energy is obtained via the tunability of synchrotron radiation. Examples of the capabilities of the photoelectron spectrometer are published elsewhere [3,9]. Experiments and evaporations were performed under ultra-high vacuum conditions. Accurate coverage estimates are important to these studies. Low energy electron diffraction (LEED), Auger electron spectroscopy, valence band photoemission and a thickness analysis using a quartz crystal microbalance were all used to monitor deposition levels. Fe was evaporated from an effusive-beam thermal source and the Cu(001) sample was at or near room-temperature during deposition and the *photoelectron diffraction* measurements. An "elbow" was observed in the plot of the Auger ratio of Fe intensity divided by Cu intensity and we have assigned a deposition value of the equivalent of a "monolayer", i.e. $\Theta = 1$ at this point, based upon internal consistencies in this and the other measurements. Nevertheless, this *coverage estimate is limited* by the following caveats: (1) The actual geometric structure is unknown and possibly is not an epitaxial overlayer; (2) the meaning and possibly even the existence of the "elbow" is in doubt [13,14]; (3) the coverage estimate is probably fairly precise (reproducible) but in absolute terms (accuracy) only good to within a factor of two. Our strategy is thus to do a series of coverages and look for consistencies in the scattering.

The photoelectron diffraction experiment uses either the Fe3s or Fe3p levels as the internal and elementally specific source of electrons for the diffraction experiment. A simplified, atomistic view of the Fe *electronic structure is shown in figure 1 and examples* of photoelectron spectra of Fe/Cu(001) are presented in figure 2. The valence bands of the Fe will be strongly affected by neighboring atoms and this will include complications such as crystal field effects, spin-orbit splitting and delocalization. Nevertheless, it is reasonable to postulate some preferred alignment of spins in a magnetic system. It is the interaction of the remaining unbalanced spin in the Fe3s or Fe3p with the aligned 3d *spins*, after the photo-ionization, that causes the splitting of the Fe3s peak and asymmetry in the Fe3p peak [15] (see figures 1 and 2). While the Fe3s emission is the preferred mode for addressing magnetic questions, it is obvious from figure 2 that the Fe3p is a much better *candidate for the initial geometric-structural studies.*

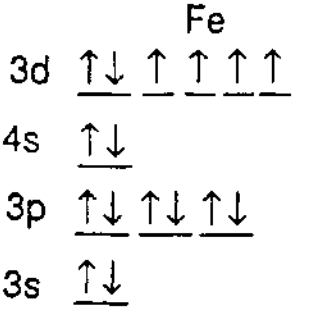

Figure 1. A simplified, atomistic view of the electronic structure of Fe is shown here, to illustrate the cause of the multiplet splitting. If a single 3s electron is removed, the remaining 3s electron will be either parallel or anti-parallel to the aligned 3d electrons. This type of spin-spin *interaction affects* the overall energetics of the photoemission process, thus producing the splitting in the 3s and the asymmetry in the 3p. This has been confirmed by spin-polarized photoelectron spectroscopy measurements [10, 11, 15].

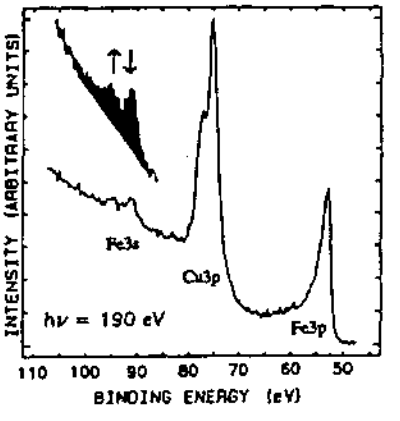

Figure 2. This figure shows normal emission angle-resolved photo-emission spectra of Fe/Cu(001), using hν = 190 eV and with $\Theta \approx 1$. The wide scan shows the Fe3p ($B^F \approx 53$ eV), Cu3p ($B^F \approx 75$, 77 eV) and the Fe3s ($B^F \approx 92$ eV). A narrower scan with better *statistics is also shown*, which more clearly illustrates the multiplet splitting of the Fe3s peaks. The spin has been assigned to the Fe3s peaks based upon the spin-polarized photoemission results [10, 11].

Preliminary results of the Fe3p photoelectron diffraction experiment suggest that the Fe is in a fourfold hollow site with a spacing between it and the underlying atom (in the third layer) of 3.6Å. This is consistent with a local FCC structure for the Fe. The calculations were performed using a multiple-scattering slab method and the photo-excitation matrix elements ($l_i \rightarrow l_{i+1}$) are explicitly calculated [16]. The geometric models used include a monolayer, a bilayer and a trilayer of Fe on top of Cu(001), with each successive layer of adsorbates in the fourfold hollow of the previous layer. The spacings d_{12} and d_{23} were varied independently. The result was that the curves in which $d_{13} = d_{12} + d_{23} = 3.6$Å, for the monolayer, bilayer and trilayer, were always in fairly good agreement with the experimental curve, regardless of the individual values of d_{12} and d_{23}. It is important to remember that while Cu is FCC with a = 3.61Å and Fe is BCC with a = 2.87Å at room temperature and pressure, an Fe FCC phase exists at higher temperatures and pressures (see figure 3 of ref. 17): Thus, for bulk Cu_{FCC}, $d_{13} = 3.6$Å; for bulk Fe_{BCC}, $d_{13} = 2.9$Å; and for Fe_{FCC}, $d_{13} = 3.6$Å (using the data of Table 1 in ref. 17). Hence, it is likely that the Fe is in a FCC site with $d_{13} = 3.6$Å, but it is not clear whether the Fe is surrounded by Fe, Cu or a mixture of both and whether the intermediate (second) layer is at the expected relaxed FCC position ($d_{12} = d_{23} = 1.8$Å). The sensitivity to d_{13} of the normal emission geometry is the result of the relatively large efficiency of 180° backscattering. To determine d_{12} and d_{23} and to lower the error estimate on d_{13}, it will be necessary for us to extend the data set to other angles (particularly 45°, along the [011] vectors of Cu(001)) and over a wider kinetic energy range. But to distinguish between Cu and Fe as possible nearest neighbors, it will probably be necessary to resort to spin-dependent photoelectron diffraction. That is because the non-spin scattering factors of Cu and Fe should be very similar, as is born out by the similarity of the monolayer, bilayer and trilayer calculations.

The plausibility of utilizing spin-dependent diffraction with this system is demonstrated by figure 3. Here, it is possible to see the two peak structure at fairly low coverages, without magnetizing the samples. It is of interest that the splitting between the peaks is 3.8eV, in distinct contrast with the bulk value of 4.4eV [18]. Additionally, we have collected data over a narrow range of photon energies (230eV $\leq h\nu \leq$ 260eV) for a sample with a coverage of $\Theta = 5/4$. Obviously, an order of magnitude increase in the data photon energy range is necessary. Nevertheless, if the spin-dependence can be properly incorporated into multiple scattering theory, a probe with nanoscale-magnetic sensitivity may be the result. Moreover, this probe could then be used to follow variations in the local magnetic environment as the sample was macroscopically magnetized.

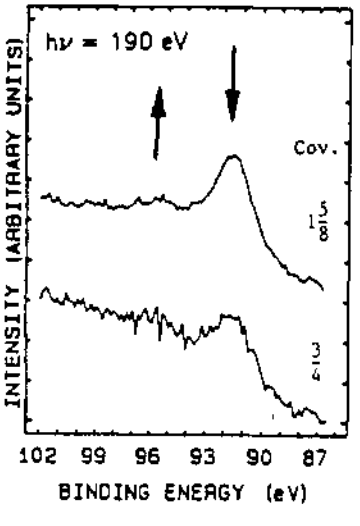

Figure 3. Narrow angle-resolved photoemission spectra of the Fe3s peaks of Fe/Cu(001) are shown here. The coverages were $\Theta = 3/4$ (lower) and $\Theta = 1$ 5/8 (upper). The splitting was approximately 3.8eV, significantly different than the bulk value of 4.4eV [18].

SUMMARY

Preliminary results of an investigation using photoelectron diffraction to investigate Fe/Cu(001) were presented. Tentatively, the Fe appears to be in a FCC site, with $d_{13} = 3.6$Å, which is consistent with earlier forward focussing experiments [6,14]. The plausibility of performing spin-dependent photoelectron diffraction on ultrathin magnetic films (sub- and near-monolayer coverages) with the multiplet-split Fe3s peak was also demonstrated.

ACKNOWLEDGEMENTS

Work performed under the auspices of the U.S. Department of Energy by the Lawrence Livermore National Laboratory under contract No. W-7405-ENG-48. S. Y. Tong acknowledges partial support by the Navy under grant no. ONR-00014-90-J-1749. Measurements were performed at the University of Wisconsin Synchrotron Radiation Center and at the Stanford Synchrotron Radiation Laboratory, on Beamline 8-2. S. Chaudhury pursuing a Ph.D. under the direction of R. S. Williams at UCLA. V. L. Colvin and A. P. Alivisatos aided in the collection of data at SSRL.

REFERENCES

1. C. L. Fu and A. J. Freeman, Phys. Rev. B35, 925 (1987).
2. C. Liu, E. R. Moog and S. D. Bader, Phys. Rev. Lett. 60, 2422 (1988).
3. J. C. Hansen, M. K. Wagner and J. G. Tobin, Solid State Commun. 72, 319 (1989); C. M. Wei, J. C. Hansen, M. K. Wagner, R. Machado, R. P. Harvey, J. G. Tobin, and S. Y. Tong, Bull. Am. Phys.Soc. 34, 446 (1989).
4. B. Sinkovic and C. S. Fadley, Phys. Rev. B 31, 4665 (1985).
5. J. G. Tobin, L. E. Klebanoff, D. H. Rosenblatt, R. F. Davis, E. Umbach, A. G. Baca, D. A. Shirley, Y. Huang, W. M. Kang and S. Y. Tong, Phys. Rev. B26, 7076 (1982). The principle results of this work were subsequently confirmed by SEXAFS measurements: U. Döbler, K. Baberschke, J. Stöhr and D. A. Outka, Phys. Rev. B31, 2532 (1985).
6. S. A. Chambers, T. J. Wagener and J. H. Weaver, Phys. Rev. B36, 8992 (1987).
7. W. F. Egelhoff, Jr., Phys. Rev. B 30, 1052 (1984).
8. H. C. Poon and S. Y. Tong, Phys. Rev. B30, 6211 (1984).
9. J. G. Tobin, J. C. Hansen and M. W. Wagner, J. Vac. Sci. Technol. A 8, 2494 (1990).
10. C. Carbone, T. Kachel, R. Rochow and W. Gudat, Z. Phys. B 79, 325 (1990).
11. F. U. Hillebrecht, R. Jungblut, and E. Kisker, Phys. Rev. Lett. 65, 2450 (1990).
12. D. P. Pappas, K.-P. Kämper and H. Hopster, Phys. Rev. Lett. 64, 3179 (1990).
13. D. Pescia, M. Stampanoni, G. L. Bona, A. Vaterlaus, F. Meier, G. Jennings and R. F. Willis, Phys. Rev. Lett. 60, 2559 (1988).
14. D. A. Steigerwald and W. F. Egelhoff, Jr., Phys. Rev. Lett. 60, 2558 (1988)
15. C. Carbone and E. Kisker, Solid State Commun. 65, 1107 (1988).
16. See for example, the review article by S. Y. Tong, Critical Reviews of Solid State Sciences, vol. 10, 209 (1981), CRC Press; C. H. Li, A. R. Lubinsky and S. Y. Tong, Phys. Rev. B 17, 3128 (1978).
17. L. N. Falicov, D. T. Pierce, S. D. Bader, R. Gronsky, K. B. Hathaway, H. J. Hopster, D. N. Lambeth, S. S. P. Parkin, G. Prinz, M. Salamon, I. K. Schuller, R. H. Victora, J. Mater. Res. 5, 1299 (1990).
18. C. S. Fadley, D. A. Shirley, A. J. Freeman, P. S. Bagus and J. V. Mallow, Phys. Rev. Lett. 23, 1397 (1969).

A PHOTOEMISSION INVESTIGATION OF COMPOUND SEMICONDUCTOR NANOCRYSTALS

J. G. TOBIN,*, V.L. COLVIN** and A.P. ALIVISATOS**
*Lawrence Livermore National Laboratory, Livermore, CA 94550
**University of California, Berkeley, CA 94720

Abstract

We have used synchrotron radiation photoemission to probe the valence and core level electronic structure of compound-semiconductor monodisperse clusters (nanocrystals). These clusters exhibited a 10% or less variation relative to the mean diameter and were attached to the metal substrates via alkane chains. Direct evidence of gap broadening due to size variation in CdS clusters was observed. The novel utilization of alkane chain attachment is the key to eliminating the otherwise debilitating problem of sample charging, as occurs with powders. The quality of sample preparation was confirmed by other methods such as transmission electron microscopy, Raman scattering and x-ray diffraction. This work provides a direct link between photoemission studies of expitaxial ultra-thin films of compound semiconductors, the photon-spectroscopy measurements of cluster powders and the existing theories of quantum confinement in reduced dimensionality structures.

Introduction:

Understanding the relationship between structures and properties on an atomic scale remains a crucial goal in the study of reduced dimensionality systems. One avenue of attack upon these important questions is the study of the size dependence of the electronic structure in compound semiconductor nanocrystals. In these monodisperse (single-size) clusters, the finite size (diameters of 2 to 20 nm, 10^2 to 10^5 atoms) and crystallinity may combine to create effects such as novel variations of their optical properties and catalytic capabilities. The thrust of the experiments described here is to probe the occupied valence electronic structure with synchrotron radiation photoemission, using a unique wet chemical method for growth and attachment of the nanocrystals to the metallic substrates.

Cluster Synthesis:

One of our goals is to prepare semiconductor clusters in the condensed phase with very narrow size distributions.[1] Clusters of CdS in the 2-20 nm size regime with diameter distributions of 3% to 10% are routinely synthesized in our laboratory. The chemical preparations rely on the fact that, in the very early stages of crystal growth in solution, small crystallites are formed which all grow in parallel, distributed uniformly in size. By terminating the crystal growth at this stage one is able to capture the crystallites. This can be done by reacting the crystallites with an organic terminating moiety. This organic group "caps" the cluster surface, preventing the clusters from aggregating or growing further. By appropriately choosing the organic group on the surface one can adjust the solubility of the clusters. Thus the clusters can be dissolved in polar or nonpolar solvents, or they can be dispersed in a polymer film; in addition, all solvent can be removed and one obtains a powder of coalesced clusters (these can subsequently be redissolved;) finally, the organic group can be bifunctional, so that the other end can be used to attach

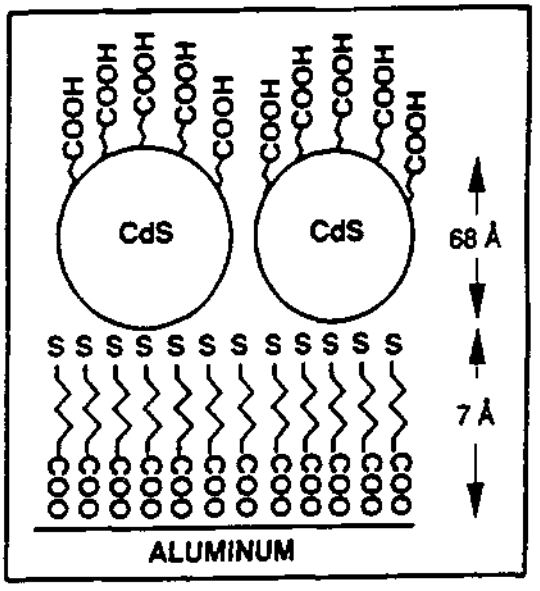

Figure 1. Schematic representation of the attachment of the CdS clusters to the aluminum substrate via alkane chains.

Figure 2. A Transmission electron micrograph of a 4nm GaAs noncrystal on a metal grid.

the clusters to a variety of substrates. We have developed a methods to attach the clusters to Au and Al surfaces using short chain alkanes as bridges. This is shown schematically in figure 1.

Cluster Characterization:

Once the clusters are made they are characterized by the following methods[1]:

1. Transmission Electron Microscopy is performed at the National Center for Electron Microscopy at LBL. These experiments allow us to determine particle size and shape. From the electron diffraction pattern one can determine the crystallinity of the samples. An example is shown in Figure 2.
2. X-ray powder diffraction is used to test the crystallinity of the samples. The width of the X-ray diffraction lines are consistent with the finite size of the clusters, and indicate that the material is highly crystalline.
3. Resonance Raman scattering is used to measure the vibrational spectra.
4. Optical absorption is measured to study quantum size effects.
5. X-ray fluorescence is used for elemental analysis.
6. In-house X-ray photoelectron spectroscopy (XPS).

Synchrotron Radiation Photoemission

The occupied electronic structure of the clusters was probed with photoemission,[2] using synchrotron radiation from the 4 meter NIM beamline on the 1GeV ring, Aladdin, at the University of Wisconsin Synchrotron Radiation Center and beamline 8-2 at the Stanford Synchrotron Radiation Laboratory. The novel use of the alkane chain attachment of the cluster to the metal substrate is essential for the avoidance of sample charging. As described above, the quality of the sample preparation was confirmed by several other methods and the distribution of cluster diameters is 10% or less of the mean diameter.

One of the most interesting properties of the clusters is the strong dependence of the valence band maximum on size. The crystallites we make are smaller than the bulk semiconductor exciton diameter, and consequently show quantum size effects. We have observed these effects in photoemission spectra which were obtained for CdS clusters ranging in size from approximately 2 to 7 nm in diameter.[3] The clearest result to emerge from these experiments is that the valence band collapses in the smaller clusters. That is, the valence band maximum moves to smaller binding energies as the nanocrystals increase in size. This shift is due to both a quantum confinement in the initial state and size-dependent final state charge solvation, as described in Ref. 3.

In the future, we expect that at sufficiently high resolution we may be able to observe a discrete series of states in the valence bands of the smallest clusters. Additionally, we recently have begun work using GaAs clusters[4] and have collected preliminary photoemission data of the GaAs clusters at the Stanford Synchrotron Radiation Laboratory,[5] shown in Figure 3.

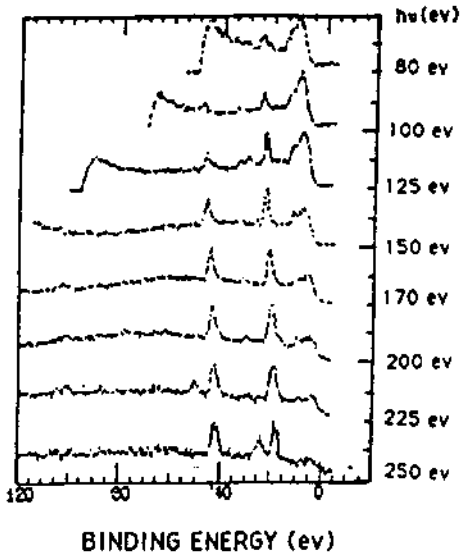

Figure 3. Photoemission spectra of 4nm radius GaAs clusters on a gold substrate. The photon energies are shown on the side. The binding energy is relative to the Fermi energy.

Acknowledgements:

A. P. Alivisatos and V. L. Colvin appreciate the support of the NSF through contract DMR-9057186. Work performed under the auspices of the U.S. Department of Energy by the Lawrence Livermore National Laboratory under contract No. W-7405-ENG-48. R. Daley of Sandia National Laboratory - Livermore and S. Chaudhury, who is pursuing a Ph.D. at UCLA under the direction of Prof. R. S. Williams, aided in the collection of this data at SSRL.

References:

1. V. L. Colvin, A. N. Goldstein and A. P. Alivisatos, to be submitted to J. Am. Chem. Soc., 1990.
2. B. J. Knapp, J. C. Hansen, M. K. Wagner, W. D. Clendening and J. G. Tobin, Phys. Rev. B40, 2814 (1989).
3. V. L. Colvin, A. P. Alivisatos and J. G. Tobin, submitted to Phys. Rev. Lett., 1990.
4. M. A. Olshavsky, A. N. Goldstein and A. P. Alivisatos, submitted to J. Amer. Chem. Soc., 1990.
5. J. G. Tobin, V. L. Colvin, A. P. Alivisatos, R. Daley and S. Chaudhury, 1990 Users Meeting of the Stanford Synchrotron Radiation Laboratory.

MICROCHANNEL-PLATE PHOTOCATHODE SPECTRAL RESPONSE

PROPOSAL NO. 9901V

K. Glenn Tirsell and M. R. Carter
University of California, Lawrence Livermore National Laboratory
P. O. Box 808, L-43, Livermore, California 94550

Introduction

During the 1990 SSRL spring run we continued our x-ray detector response studies using the spherical-grating monochromator

Measurements

Preliminary multi-strip MCP response measurements were

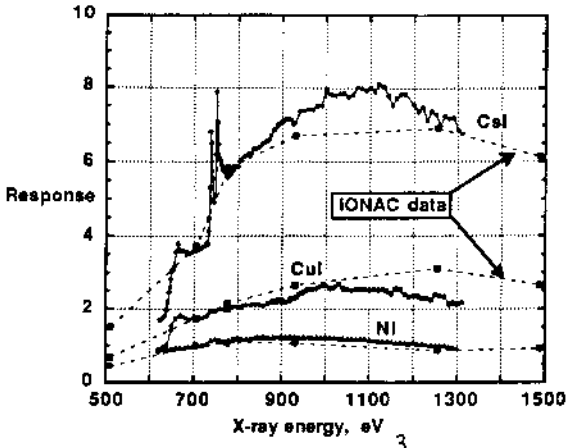

Fig. 3 CsI, CuI, and Ni photocathodes sensitivities measured using the single multi-strip MCP at SSRL BL-VIII-2 and at the LLNL IONAC line facility. The SSRL data are normalized to IONAC Fe-L line (705 eV) data.

Figure 4 shows the measured CuI MCP response compared to a simple Eμ(E) model of secondary electron emission, where E is the incident photon energy and μ(E) is the photoionization cross section. The magnitude of the jump of the Eμ(E) response has been reduced to fit the measured jump at the iodine edge. Figure 5 shows similar measured results for the Au strip compared to the Eμ(E) model. The increase in measured Au response at 730 eV suggests a possible CsI contamination due to migration or inadequate masking during the deposition.

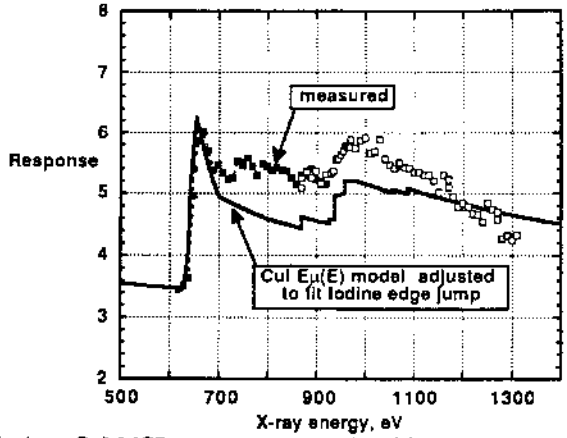

Fig.4 CuI MCP response measured at SSRL compared to an Eμ(E) model with edge jumps adjusted to fit the measured data.

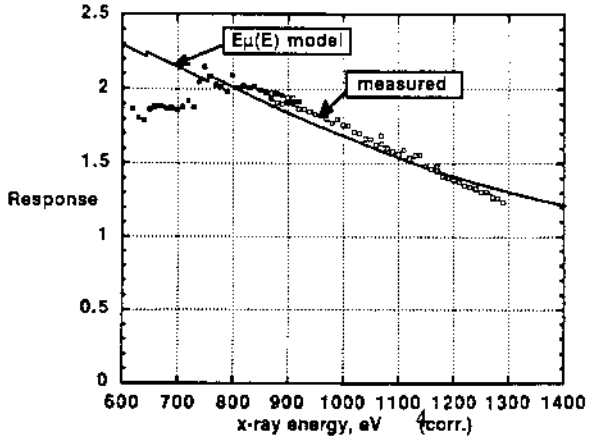

Fig. 5 Au MCP response measured at SSRL compared to an Eμ(E) model.

Our latest synchrotron radiation results indicate that by means of MCP deposition modifications, we have obtained a much more gradual change in output sensitivity with an increase in x-ray energy. Except near x-ray absorption edges, the results are somewhat closer to predictions based on a simple flat x-ray diode model that depends strongly on the photoelectric cross section of the respective photoconductive material used for the first interaction.

Acknowledgements The authors wish to thank C Bruns, R. Mazuch, J. Phillips, and T. Schaffer, LLNL, and D. Turley and C. Ashford, E.G.&G., Santa Barbara, for help on the measurements. We appreciate the help of M. Bowers, C. Bruns, P. Biltoft, G. Hattery, B. J. McKinley, R. Stewart, and B. Young, LLNL, in the MCP detector development.

This work was performed under the auspices of the U. S. Department of Energy by the Lawrence Livermore National Laboratory under Contract No. W-7405-Eng-48. Data were acquired at SSRL which is supported by the DOE's Office of Basic Energy Science.

SPIN DEPENDENT ELECTRON ATTENUATION IN FERROMAGNETIC FILMS

PROPOSAL NO. 9901V

D. P. Pappas, K.-P. Kämper, B. P. Miller, H. Hopster
Department of Physics, University of California, Irvine, CA 92717
D. E. Fowler, C. R. Brundle, A. C. Luntz
IBM Almaden Research Center, San Jose, CA 95120
Z.-X. Shen, Stanford Electronics Laboratory, Stanford University, Stanford, CA 94305

Introduction

The inelastic electron mean free path (IMFP) in solids is of fundamental importance in many aspects of electron spectroscopies. The energy dependence of the IMFP is often displayed as a "universal curve" with a large increase of the IMFP at low electron energies. Experimentally this behavior is not well established. The surface sensitivity of spin polarized secondary electron spectroscopy points to a probing depth of only 3 atomic layers in ferromagnetic 3d transition metals. In addition, in ferromagnetically aligned materials the IMFP can be expected to be spin dependent. This has been proposed as a possible cause for the observed spin polarization enhancement of secondary electrons from ferromagnetic surfaces.

The classical method of determining IMFPs (or more accurately, attenuation length) is the overlayer method where the attenuation of a substrate peak is measured as a function of overlayer thickness. We have, for the first time, employed a spin polarized version of the overlayer method by measuring the intensity attenuation and spin polarization of substrate electrons (originally unpolarized) as they pass through a ferromagnetic layer. Spin polarized photoemission spectra of the 3d states of Cu (100) with epitaxially grown overlayers of Fe were taken at various photon energies. The spectra at low photon energies show a substantial spin polarization. This allows the determination of spin dependent IMFPs in Fe.

Experimental

Ultra-thin Fe films are deposited on Cu (100) in a UHV chamber equipped for spin polarized electron spectroscopies. The apparatus consists of a 90° spherical electrostatic energy analyzer coupled to a medium-energy retarding field Mott detector that measures all three components of the spin polarization.

The structural and magnetic properties of the Fe films have been studied previously in the same system[1]. The films were evaporated at low substrate temperature to avoid intermixing and were then annealed to 300 K to improve the structural quality.

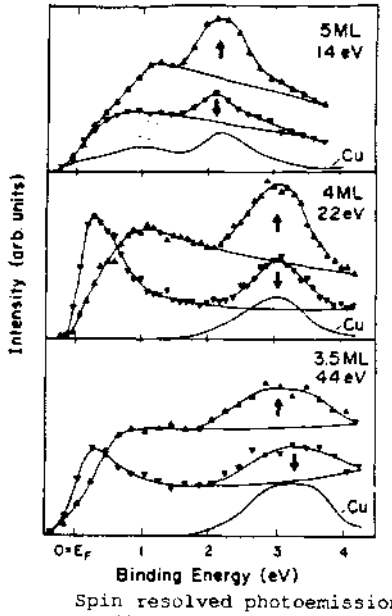

Fig. 1 Spin resolved photoemission spectra from Fe films on Cu (100)

Spin polarized photoemission spectra were recorded in the thickness range 3.5-5 ML at 14, 22, and 44 eV photon energy. In addition, spin-integrated photoemission spectra using a resonance lamp were used to determine the spin-averaged attenuation lengths.

Results

Fig. 1 shows a series of spin polarized photoemission spectra in normal emission. The Cu 3d features are clearly visible in the spectra (the bare Cu spectra are shown for comparison). A significant spin polarization of the Cu 3d intensity is obvious in the 14 eV and also to a somewhat lower extent in the 22 eV spectra while at 44 eV the spin polarization is very small. Net spin polarizations are obtained by integrating over the Cu intensity assuming a smooth background. From these polarization values and the absolute attenuation of the Cu intensity, which was determined in a non-spin polarized experiment one can arrive directly at the spin polarized attenuation

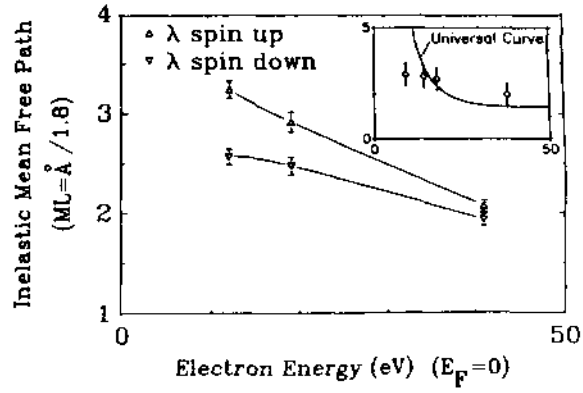

Fig. 2 Spin dependent electron attenuation length (inset shows the spin averaged data)

lengths by assuming that the spin resolved Cu intensities are attenuated according to

$$I_{+,-} \simeq I_o e^{-d/\lambda_{+,-}}$$

The results are shown in Fig. 2 for the three photon energies used. First, we note that the attenuation length remains small at low energies. A comparison to the universal curve is shown in the inset. Second, at low energies the mean free path becomes spin dependent with the spin-up IMFP being larger than for spin-down. This is consistent with spin polarized electron energy loss experiments on ferromagnetic 3d metal surfaces which show a higher energy loss rate for spin-down electrons compared to spin-up electrons. The spin dependent attenuation can therefore be expected to be a general feature in ferromagnetic transition metals.

The present results offer a consistent explanation of the spin polarization in secondary electron spectroscopy. The surface sensitivity is due to the small IMFP and the polarization enhancement is due to a spin filter effect. Spin-up electrons have a higher probability of being emitted due to their longer mean free path.

Work supported by NSF, DMR 8821293.

Ref. 1 D. P. Pappas, K.-P.Kämper, B. Hopster, Phys. Rev. Lett. 64, 3179 (1990).

EXAFS, WAXS AND DAS OF GOLD-BASED DRUGS USED TO TREAT RHEUMATOID ARTHRITIS

PROPOSAL NO. 922Bp

Richard C. Elder* and Katherine Tepperman
Departments of Chemistry and Biological Sciences
University of Cincinnati
Cincinnati, OH 45221-0172

Gold atoms show a relativistic interatomic attractive force, which, although weak, contributes in part to the molecular configurations and crystal packings found for the gold compounds.[1] Intramolecular gold interactions of this sort can be observed in the $[Au_2X_2(\mu\text{-dppm})_2]$, where X=Cl, Br, crystal structure[2] and in the EXAFS reportd by Elder et.al. in the SSRL 1989 activity report. Gold interactions are generally found to be at interatomic distances of 3.00 +/- 0.25 Å with the longer distance indicative of weak bonding between the atoms while the shorter distances are even less than that of the gold-gold interaction in metallic gold.[1] We are currently investigating several dinuclear gold species using EXAFS and X-ray crystallography to elucidate the structural properties and determine the influence of the gold-gold interaction on the structure of the molecule.

Both intramolecular and intermolecular interactions between gold atoms must be considered. However, it was unknown whether or not a weak intermolecular gold interaction could be observed using EXAFS. A classic example of this intermolecular gold-gold interaction is present in bis(thiosulfato)gold which has a gold-gold distance of 3.302 Å.[3] EXAFS data were measured on the solid form of sodium bis(thiosulfato)gold at the 10 K. The data were processed and a peak in the pseudo radial distribution function is present at 2.96 Å (figure 1) which was found to correspond to the intermolecular gold-gold interaction observed in the crystal structure data.

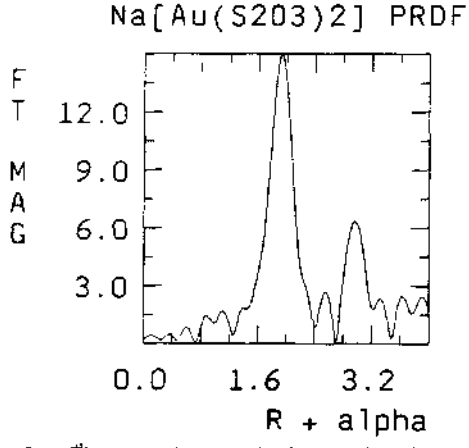

Figure 1: The psuedo radial distribution function for solid $Na_3[Au(S_2O_3)_2]$ showing peaks at 1.9 and 3.0Å.

Data were collected on two classes of compounds. Each class contains a bridging phosphine ligand with chain lengths of 2,3,4, and 5 carbons. The first class of compounds also has a methylthiocresol ligand bound to each gold atom while the second class of compounds has a bridging propane-dithiolate ligand (Figure 2). Data were measured at 10 K and gold-gold distances were calculated in Table 1.

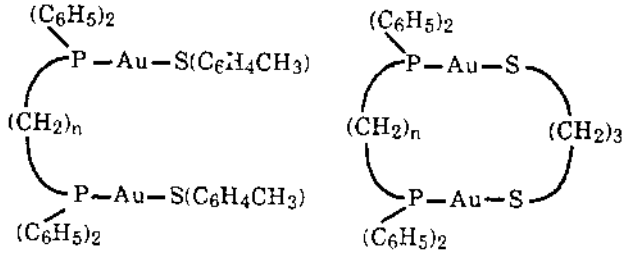

Figure 2: Dinuclear gold compounds containing a μ-phosphine of varying chain length and a sulfur containing ligand.

Table 1

Compound	Au-Au Distance Angstroms	Au-P/S Distance Angstroms
$Au_2(SC_6H_4CH_3)_2(\mu\text{-dppe})$	-	2.28
$Au_2(SC_6H_4CH_3)_2(\mu\text{-dppp})$	3.13	2.28
$Au_2(SC_6H_4CH_3)_2(\mu\text{-dppb})$	3.07	2.28
$Au_2(SC_6H_4CH_3)_2(\mu\text{-dpppe})$	3.10	2.29
$Au_2(S_2C_3H_6)(\mu\text{-dppe})$	2.96	2.28
$Au_2(S_2C_3H_6)(\mu\text{-dppp})$	2.93	2.29
$Au_2(S_2C_3H_6)(\mu\text{-dppb})$	-	2.28
$Au_2(S_2C_3H_6)(\mu\text{-dpppe})$	-	2.28

dppe=bis(diphenylphosphino)ethane
dppp=bis(dipheylphosphino)propane
dppb=bis(diphenylphosphino)butane

*For compounds with "-" as the bond distance, no interaction was observed.

We were able to determine the gold-gold distance of gold-μ-dppb-methanedithiocresol and gold-μ-dpppe-methanedithocresol by X-ray crystallography and found that the gold-ligand bond distance agrees very well with the EXAFS, this is also true for the gold-gold distance in the dppb compound. However, there seems to be a discrepancy between the gold distance for the dpppe copmound which is 3.20 angstroms in the crystal structure vs. 3.10 from the EXAFS which merits further study. Gold-gold calculations were performed with XFPAK from Professor Robert A. Scott of the University of Georgia. The plane-wave approach used in those calculations is known to be poor for second shell fitting. Further calculations will be performed using EXCURV from the Daresbury group. We hope to improve second shell fitting with the spherical-wave, multiple-scattering approach.

Weak metal-metal and metal-halide interactions are difficult to study due in part to the large degree of dynamic disorder inherent in this type of interaction. This disorder can be substantially reduced by performing experiments at low temperatures. To illustrate the utility of acquiring data at low temperature, data was measured on digold-bis(μ-dppp)dibromide at ambient, liquid nitrogen (77 K), and liquid helium (10 K) temperatures (Figure 3). The pseudo radial

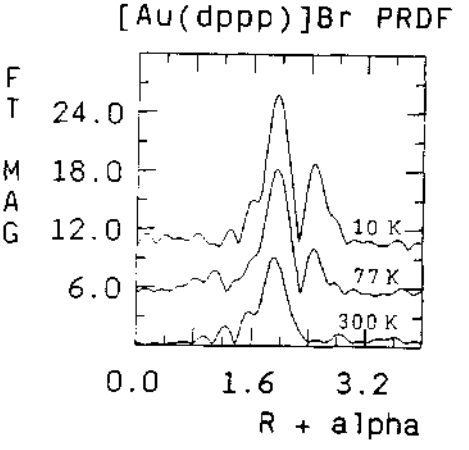

Figure 3: The pseudo radial distribution function of $[AuBr(\mu\text{-dppp})]_2$. Data collected at 10, 77, 300 degrees Kelvin in order from top to bottom. The peak at 1.9 angstroms is the Au-P bond, at 2.5 angstroms is the gold bromine bond.

function shows a peak for the gold-phosphorus bond that increases slightly in magnitude as the temperature is reduced. A more interesting fact is the total lack of a peak for the gold-bromine bond at ambient temperature and a relatively large peak for the same bond at liquid helium temperature. Further studies are planned at low temperatures to study the effects of gold-gold interactions on molecules.

Acknowledgements: The compounds studied here were prepared by Dr. Alice Bruce and her students at the University of Maine. The crystal structure determinations were performed by Dr. Douglas Ho at the University of Cincinnati. The work described in this report is largely that of Mr. W.B. Jones.

References

1. Schmidbaur, H.; Gold Bull. 1990, 23 (1) 11-21.

2. Fackler, J.P.; Shain, J.; Inorganic Chimica Acta, 1987, 131, 157-158.

3. Ruben, H.; Zalkin, A.; Faltens, M.O.; Templeton, D.H.; Inorganic Chemistry, 1974, 13 (8), 1836-39.

Phase Determination by Polarized Dispersion in Vanadyl Sulfate Pentahydrate

David H. Templeton and Lieselotte K. Templeton

Department of Chemistry, University of California, Berkeley, CA 94720

Introduction

A new way to get the phases of structure factors has been demonstrated in diffraction experiments at SSRL. It is based on the variation of X-ray dispersion with direction of polarization which occurs at absorption edges for some atoms when the symmetry of chemical bonding is low enough. When a crystal is turned around a diffraction vector this polarized dispersion causes the diffraction intensity to change in a manner which reveals phase information. This technique is like the multiwavelength anomalous dispersion ("MAD") method, but uses polarization as well as wavelength to change the atomic scattering factor.

Polarized dispersion in the vanadyl ion

The vanadyl ion VO^{2+} exhibits strong X-ray dichroism at a polarized pre-edge absorption line near the K edge.[1] We used crystals of its sulfate pentahydrate to obtain the vanadium anomalous scattering tensor (Fig. 1) at wavelengths near this line and to test the method of finding phases. The structure of these crystals is monoclinic and centrosymmetric.[2] The Enraf-Nonius CAD-4 diffractometer on Beam Line 1-5 was used as described elsewhere[3] to measure absorption spectra and diffraction intensities for different orientations with respect to the polarization of the beam.

Phase determination

The effects of polarized dispersion on diffraction intensities are intricate in the general case, but they can be included in the existing algebraic methods of the MAD method.[4] The present experiment shows that data for multiple azimuthal settings can add significant information to that method. A simplified approximate treatment is more direct for this centrosymmetric case in which all the vanadium tensors have nearly the same orientation. Then the structure factor is a linear function of $\cos^2\alpha$, where α is the angle between the polarization vector and the unique tensor axis:

$$F(\lambda\psi) = F_t + \frac{f'_\pi F_2}{f^0} + \frac{(f'_\sigma - f'_\pi) F_2}{f^0} \cos^2\alpha .$$

From this equation and the slope and intercept of a plot of $|F|$ *vs* $\cos^2\alpha$ (Fig. 3) one can find the magnitudes and phase difference of F_t and F_2, the structure factors for the whole structure and the vanadium atoms only, in each case free of the dispersion terms. One of the factors in the slope is the difference of σ and π principal values, a quantity which changes sign at the resonance line and adds power to the method. The reversal of slope with photon energy is evident in both plots.

Further details of the experiment, the theory, and the extension to noncentrosymmetric structures will be described elsewhere.[5]

We thank the many staff members of SSRL whose assistance made this work possible. We are particularly indebted to Dr. Michael Soltis. This research was supported by the National Science Foundation under Grant CHE-8821318.

References

1. D. H. Templeton & L. K. Templeton, *Acta Cryst.* A36, 237-241 (1980).
2. M. Tachez, F. Théobald, K. J. Watson & R. Mercier, *Acta Cryst.* B35, 1545-1550 (1979).
3. L. K. Templeton & D. H. Templeton, *Acta Cryst.* A44, 1045-1051 (1988).
4. E. Fanchon & W. A. Hendrickson, Acta Cryst., A46, 809-820 (1990).
5. D. H. Templeton & L. K. Templeton, *Acta Cryst.*, submitted for publication (1991).

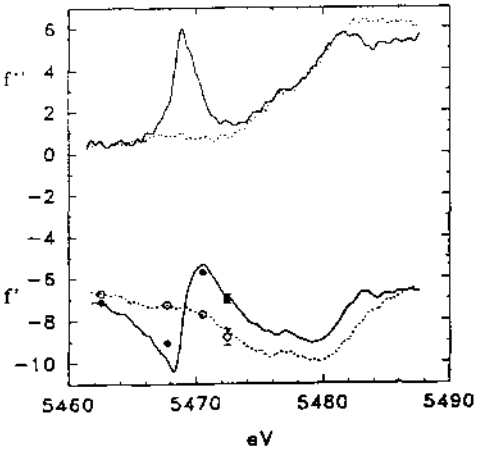

Figure 1. Principal values of f' and f'' tensors for vanadium derived from absorption data (curves) and diffraction data (points). Solid lines and circles are for σ polarization, broken lines and open circles for π.

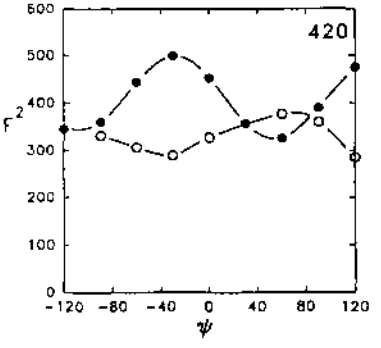

Figure 2. Change of diffraction intensity (F^2) with azimuthal angle ψ for reflection (420) at photon energies on each side of the absorption line: 5467.7 eV (open circles) and 5470.5 eV (solid circles).

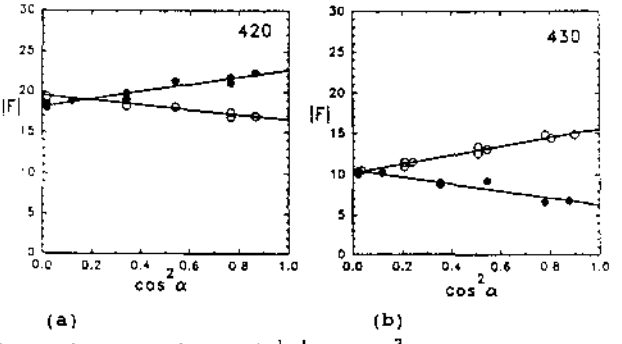

Figure 3. (a) Plots of $|F|$ *vs* $\cos^2\alpha$ for data of Fig. 2. The signs of the slopes show that $F(\lambda\psi)$ and F_2 have the same phase. (b) Similar plots for a reflection with opposite phases for $F(\lambda\psi)$ and F_2. A numerical analysis shows that F_t and F_2 have equal phases in each case.

Structure of the Mn Complex in Photosystem II of Plants and Cyanobacteria

Victoria J. DeRose, Matthew J. Latimer, Ishita Mukerji, Vittal K. Yachandra,
Kenneth Sauer and Melvin P. Klein.

Melvin Calvin Laboratory
Chemical Biodynamics Division
Lawrence Berkeley Laboratory
University of California, Berkeley, CA 94720.

Photosynthetic water oxidation and oxygen evolution in cyanobacteria and higher plants is catalyzed by a cluster of four Mn atoms. This oxygen evolving complex (OEC) cycles through a series of five states (S_0-S_4) by absorption of four successive photons. Although extensive studies have shown that Mn, Cl^- and Ca^{2+} are essential cofactors involved in this H_2O oxidation reaction, the structure of the Mn complex and the mechanism of the reaction is inadequately understood.

Previous work by our group has demonstrated that the minimal structure of the Mn cluster, in the O_2-evolving complex of photosystem II in higher plants and cyanobacteria, is a pair of di-μ-oxo-bridged binuclear structures with Mn-Mn distances of ~2.7 Å. We also showed that Mn is oxidized upon illumination during the S_0^* (NH_2OH induced S_0 state) to S_1 and S_1 to S_2 state transitions. The structures of the Mn cluster in the S_1, S_2 and S_3 states are essentially identical, consistent with two di-μ-oxo bridged binuclear structures containing Mn(III) and Mn(IV) predominantly, with a small increase in the spread of Mn-Mn distances in the S_3 state. The S_0^* state contains a Mn(II) which is not present in the other states and exhibits a more heterogeneous structure.

In the past year two improvements in our data collection methods have yielded spectra of S/N ratios much higher than had been previously obtained: 1) measurements at low temperatures, 10 K, and 2) the use of a multi-element solid state energy resolving Ge detector. EXAFS data were collected on beamlines X19A (in lieu of time at SSRL) and on X9A at NSLS using Si(111) crystals. Edge data were collected using a single element Si-Li solid state detector at SSRL on beamline IV-2 using Si(220) crystals in the unfocussed mode. Our XAS studies were performed using PS II preparations from spinach and PS II preparations from the cyanobacterium *Synechococcus*.

Item 1 mentioned above decreases the dynamic Debye-Waller factor that can broaden or smear EXAFS features. Item 2 permits an enhancement by a factor of 3 to 4 in signal/noise vs the single element Si-Li detector we used previously. These two items have enabled us to investigate structural changes in the Mn-OEC that were not possible previously in measurements at 170 K using a single-element detector. The Fourier transforms from the S_1 and S_2 states show three distinct peaks. The third peak was not obvious in data collected at 170 K, but is now clearly present in both the S_1 and S_2 states. Simulations show that the third Fourier peak fits to either Mn or C at ~3.3 Å, but the quality of the fit is better for the heavier atom. We have also obtained XANES and EXAFS dichroism data from oriented PS II membranes in the S_1 and S_2 states. The EXAFS results are consistent with a model of two di-μ-oxo bridged Mn binuclear structures with a Mn-Mn separation of 2.7 Å, which are linked by a mono-μ-oxo and mono- or di-μ-carboxylato bridges with a Mn-Mn distance of 3.3 Å. The dichroism results show that the 3.3 Å vector is perpendicular to the plane of the membrane and that the 2.7 Å vector is approximately in the plane of the membrane. There are also small changes in the structural parameters betweeen the S_1 and S_2 state, which were not detectable in our earlier data. The dichroism is also slightly different for the S_1 and S_2 states. The Mn-ligand and Mn-Mn distances change during this transition in a manner which is consistent with a change from a (III,III) di-μ-oxo bridged binuclear moiety to a (III,IV) moiety, a result which is consistent with the XANES results. The second derivative Mn K-edge spectra clearly show that not only is there a shift to higher energy in the S_1 and S_2 transition, but there is also a distinct change in *shape*. We have shown that the S_1 and S_2 state second derivatives can be simulated by a combination of Mn(III) and Mn(IV) model complexes, and that the most likely set of oxidation states of the four Mn atoms is (III_2,IV_2) in the S_1 state and (III,IV_3) in the S_2 state. Using oriented PS II membranes we have shown that the minima in the second derivatives which correspond to peaks or shoulders on the K-edge spectra show distinct dichroism and the dichroism is different in the S_1 and S_2 states. The K-edge dichroism spectra are dramatically different from those published earlier by George and coworkers (Science (1989) 243, 789-791) using chloroplast preparations. The EXAFS spectra and EXAFS dichroism spectra are also different in their intensities compared to those published by George and coworkers.

Cl^- is an essential cofactor for O_2 evolution. Cl^- can be replaced by Br^- with full retention in activity, but F^- is an inhibitor of O_2 evolution. The requirement of Cl^- or Br^- for activity has led to postulates that the halide ion is a ligand to one or more of the Mn atoms in the complex. Earlier EXAFS studies have been unable to resolve the question of halide ligation. Our new approach has been a comparative XAS study of PS II samples from *Synechococcus* which has been grown in either Cl^- or Br^- media; a method which permits the most extensive substitution of Br^- for Cl^-. The results from our recent experiments at 10 K preclude two halide ligands or a halide bridging ligand, but cannot exclude a single halide ligand in the OEC. Experiments with spinach samples treated

with F^- have successfully shown that F^- induces a change in the structure of at least one of the di-μ-oxo-bridged moities proposed to be present in the OEC. Ca^{2+} is another cofactor that is required for O_2 evolution. Experiments designed to determine whether Ca^{2+} is close to the Mn cluster have been based on reports that Ca^{2+} can be depleted from PS II membranes, and that restoration of O_2 evolution can be achieved upon repletion with Ca^{2+} or Sr^{2+}. The XANES and EXAFS of Ca-sufficient, Ca-depleted and Sr-repleted samples have been obtained. The EXAFS of the Sr-repleted samples exhibit a very large and wide feature that includes the 3.3 Å feature. Because Sr is a more effective backscatterer than Ca, its presence is highly visible. The XANES also changes quite dramatically on Ca depletion indicating a perturbation of the Mn cluster. The quantitation of the number of Sr(Ca) and distance(s) is underway.

Acknowledgments

This work was supported by the National Science Foundation, and by the Director, Division of Energy Biosciences, Office of Basic Energy Sciences, of the U.S. Department of Energy. *Synchrotron* radiation facilities were provided by SSRL and NSLS. We thank Prof. Britton Chance for the use of his Ge detector. We also thank Dr. Steve Cramer for the use of his Ge detector and liquid He cryostat. We thank Dr. Jean-Luc Zimmermann, Melissa Grush and Wenchuan Liang for help with data collection.

X-ray Absorption Spectroscopy of Diferrous and Diferric Protein A of Soluble Methane Monooxygenase from *Methylococcus capsulatus* (Bath)

Jane G. DeWitt,[1] James G. Bentsen,[2] Britt Hedman,[3] Amy Rosenzweig,[2] Jeffrey Green,[4] Simon Pilkington,[4] Keith O. Hodgson,[1] Stephen J. Lippard,[2] and Howard Dalton[4]

[1] Department of Chemistry, Stanford University, Stanford, CA 94305 USA.
[2] Department of Chemistry, Massachusetts Institute of Technology, Cambridge, MA 02139 USA.
[3] Stanford Synchrotron Radiation Laboratory, Stanford University, Stanford, CA 94309 USA.
[4] Department of Biological Sciences, University of Warwick, Coventry, CV4 7AL, England.

Introduction

Methane monooxygenase (MMO) is a non-heme binuclear iron oxygen activation protein that oxidizes methane to methanol in methanotrophic bacteria for growth. Soluble MMO from *Methylococcus capsulatus* (Bath) [1] is a non-specific enzyme that catalyses the oxidation of a wide variety of substrates [2]. The protein consists of three isolable subunits: protein A, the hydroxylase component (M_r 210,000) where substrate binding and oxidation occurs; protein C, an Fe-S flavoprotein (M_r 42,000) which is believed to mediate the transfer of electrons from NADH to protein A; and protein B, a small protein believed to couple electron transfer to substrate oxidation (M_r 15,700) [3].

Protein A of MMO, which contains the binuclear iron active site, is similar spectroscopically to the binuclear iron proteins oxyhemerythrin (oxyHr) and ribonucleotide reductase B2 (RR B2). X-ray absorption spectroscopy has proven to be a useful tool in the elucidation of the average environment around iron in the active site of these proteins, particularly in providing insight into the short Fe-O-Fe oxo bridge in their multiply bridged active sites [4] and in related models [5]. We have previously shown that the photoreduced semimet form of protein A of MMO from *M. capsulatus* (Bath) and *Methylosinus trichosporium* OB3b does not contain a short oxo bridge in its active site [6]. In this paper, we report preliminary results of Fe K EXAFS measurements of diferric and diferrous protein A of MMO from *M. capsulatus* (Bath).

Experimental

Earlier measurements of oxidized protein A of MMO from *M. capsulatus* (Bath) resulted in a 1 e^- photoreduction of the protein to its semimet state [6]. We were recently able to obtain Fe K EXAFS on an oxidized protein sample which did not photoreduce in the X-ray beam. The data were measured at 10 K on unfocussed beamline X-19A at NSLS (2.5 GeV, 180 mA) using a 13 element Ge solid state detector windowed on the iron Kα fluorescence signal. The diferric sample was measured twice, once with a Si(220) double crystal monochromator detuned 45% at 7375 eV, and once with a Si(111) double crystal monochromator detuned 50% at 7820 eV. The diferrous protein sample was measured using a Si(111) double crystal monochromator under the same experimental conditions.

Results and Discussion

The k^3 weighted EXAFS of diferric protein A of MMO, along with the Fourier transform (3.5-12.5 $Å^{-1}$) of the EXAFS data is shown in Figure 1. Results of fits to the data (fitting range 4-12 $Å^{-1}$) indicate a first shell coordination around iron of about 6 N/O at a distance of 2.04 Å,with an Fe-Fe distance of about 3.4 Å. We found no evidence that diferric protein A has a short μ-oxo bridge in its binuclear iron center. In Figure 2, the EXAFS of diferric protein A is compared to the EXAFS of an oxo-bridged and a hydroxo-bridged diferric model [7]. The protein EXAFS is quite similar to the hydroxo-bridged model EXAFS and different from the oxo-bridged model EXAFS, supporting our conclusion from fitting results that diferric protein A does not have an oxo bridge.

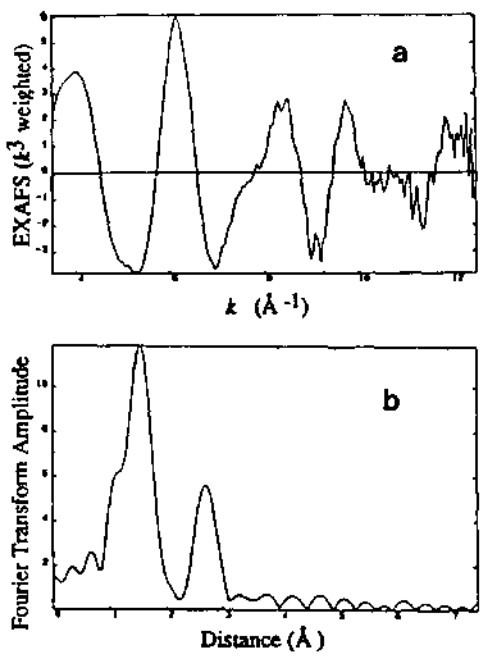

Figure 1. (a) k^3 weighted EXAFS of oxidised protein A. (b) The Fourier transform of the EXAFS data.

The data for the diferrous protein sample is presented in Figure 3. In agreement with an earlier experiment on diferrous protein A, fit results (fitting range 4-12 $Å^{-1}$) indicate that the coordination sphere around iron consists of about 5 N/O at 2.16 Å [6b]. There is no indication of Fe-Fe backscattering in the Fourier transform of the data and iron cannot be fit to the diferrous protein data. The lack of an Fe-Fe interaction could be due to the loss of a bridge between the iron atoms in the active site upon reduction resulting in uncorrelated motion of the iron atoms, or to low Z second shell backscattering destructively interfering with the Fe-Fe backscattering.

A manuscript giving a full description of XAS investigations of protein A of MMO, including these experiments, is currently being prepared.

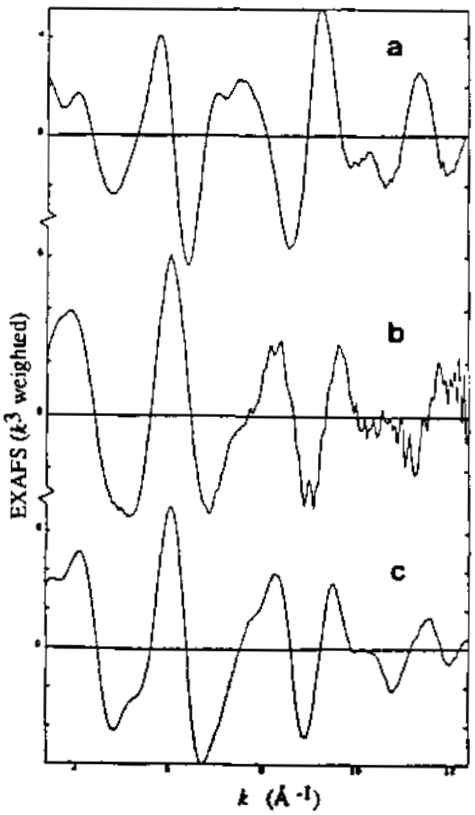

Figure 2. EXAFS of (a) $[Fe_2O(OAc)(HBpz_3)_2]$,

Acknowledgments

The measurements were performed on beam-time provided for SSRL users at the National Synchrotron Light Source, Brookhaven National Laboratory which is supported by the Department of Energy, Office of Basic Energy Sciences, Division of Materials Sciences and Division of Chemical Sciences. This work is supported by grants from the National Institutes of Health, Biomedical Resource Technology Program, Division of Research Resources, the National Science Foundation (CHE 88-17702 to KOH), the Gas Research Institute (5086-260-1209 to HD) and the National Institute of General Medical Sciences (GM 32134 to SJL).

References

1. (a) Colby, J.; Dalton, H. *Biochem. J.* **1976**, *157*, 495-497.
2. (a) Colby, J.; Stirling, D. I.; Dalton, H. *Biochem. J.* **1977**, *165*, 395-402.
3. (a) Green, J.; Dalton, H. *Biochem. J.* **1989**, *259*, 167-172. (b) Lund, J.; Woodland, M. P.; Dalton, H. *Eur. J. Biochem.* **1985**, *147*, 297-305.
4. (a) Elam, W. T.; Stern, E. A.; McCallum, J. D.; Sanders-Loehr, J. *J. Am. Chem. Soc.* **1982**, *104*, 6369-6373. (b) Scarrow, R. C.; Maroney, M. J.; Palmer, S. M.; Que, L. Jr.; Roe, A. L.; Salowe, S. P.; Stubbe, J. *J. Am. Chem. Soc.* **1987**, *109*, 7857-7864. (c) Bunker, G.; Petersson, L.; Sjoberg, B.-M., Sahlin, M.; Chance, M.; Chance, B.; Ehrenberg, A. *Biochemistry* **1987**, *26*, 4708-4716.
5. Hedman, B.; Co, M. S.; Armstrong, W. H.; Hodgson, K. O.; Lippard, S. J. *Inorg. Chem.* **1986**, *25*, 3708-3711.
6. (a) Ericson, A.; Hedman, B.; Hodgson, K. O.; Green, J.; Dalton, H.; Bentsen, J. G.; Beer, R. H.; Lippard, S. J. *J. Am. Chem. Soc.* **1988**, *110*, 2330-2332. (b) DeWitt, J.; Hedman, B.; Ericson, A.; Hodgson, K. O.; Bentsen, J.; Beer, R.;

PROPOSAL NO. 2101B

STRUCTURAL COMPARISON OF PURPLE AND BLUE FORMS OF BACTERIORHODOPSIN

S. Wakatsuki[1], Y. Kimura[2], N. Gillis[3], D. Eliezer[4], W. Stoeckenius[2], K. O. Hodgson[1], and S. Doniach[3]

1 Department of Chemistry, Stanford University Stanford, CA 94305.
2 Cardiovascular Research Institute, University of California, San Francisco, CA 94143.
3 Department of Applied Physics, Stanford University Stanford, CA 94305.
4 Department of Physics, Stanford University Stanford, CA 94305.

We have performed time-resolved x-ray diffraction studies on the blue and purple cell membranes containing the native and deionized forms of the protein Bacteriorhodopsin. Analysis of the data has yielded important insights into the role played by the bound cations in maintaining the structure and function of the native purple form of the membrane protein. Autocorrelation functions from x-ray diffraction data can elucidate many features of structural changes in real space: degree of crystallinity, size of the unit cell, change in correlation at a specific distance, etc.. Most of these are not readily seen in diffraction patterns. We have calculated successive radial autocorrelation functions for the time-resolved diffraction patterns obtained from blue membrane and purple membrane samples during drying of the samples (Fig. 1).

For blue membrane samples the position of the peak at 65.0 Å, which corresponds to the unit cell dimension, remains constant during the first 100 min, then it starts decreasing until it reaches 63.2 Å. The decrease results from a contraction of the 2D lattice during the latter half of the dehydration process. Purple membranes also show a decrease in lattice dimension by 1.0 Å from 64.6 Å to 63.6 Å. Interestingly, the peaks between 20 and 40 Ångstroms in the data from blue membranes show much smaller change in their positions, for example, from 30.5 Å to 30.2 Å. If the short range peaks would arise from correlations between helices in different trimers, shifts of their positions should be proportional to that of the peak at 65.0 Å; the position of the 30.5 Å peak should be shifted by 0.84 Å. Instead it shrank only by 0.3 Å, 36% of the expected change (Fig. 2). This is explained by the fact that the peak is a combination of intra-trimer (44%) and inter-trimer correlations (56%).

Contributions of intra- and inter- trimer correlations were calculated based on simple geometric considerations assuming a boundary for a trimer to be a hexagon with side centered on the origin. Inner helices 5, 6, and 7 see mostly other helices in the same trimer in the correlation at 30.5 Å, whereas outer helices, 1, 2, 3, and 4 have positive correlations in part with helices in the same trimer but also with those in the neighboring trimers.

While the lattice dimension decreases appreciably, the trimers apparently mostly maintain their structure during the dehydration. Thus the decrease in unit cell dimension should be attributed mainly to changes in the lipid region, between trimers. The contraction is about 200 $Å^2$ per unit cell, corresponding to areas of 3 to 4 lipids (area of a lipid in PM is 60 $Å^2$). This is a significant decrease. The lipid regions between trimers are about 5 to 10 Å wide (each lipid molecule can be modeled by an oval of 5 by 10 Å). Thus, the shrinkage of the lattice spacing introduces a significant constraint on the arrangement of lipids. Note, however, that the 110 $Å^2$ contraction, corresponding to the area of about 2 lipid molecules, does not produce lattice disorder in the case of the purple form. Therefore, an additional effect must be postulated to explain the larger shrinkage and disordering of the blue membrane lattice upon dehydration.

We report elsewhere that anomalous x-ray profile diffraction from Tb^{3+} bound to PM shows two binding regions for cations in the vicinity of membrane surfaces at the height of lipid head groups on both sides which are 42 Å apart (S. Wakatsuki, K. O. Hodgson, S. Doniach, manuscript in preparation). The cations may therefore stabilize the purple form of the membranes by shielding long range multipolar forces. On removal of the cations, carboxyl and lipid phosphate groups on the surfaces are unable to maintain salt bridges between lipids and proteins, which weakens the lattice. Removal of water will cause protonation of charged lipid groups and allow a rearrangement of the lipids with closer lateral packing. Zaccai et al. have shown that hydration occurs mainly in the lipid region (Rogan and Zaccai, 1981, Zaccai and Gilmore, 1979). Thus the lateral shrinkage of the lipid area could lead to the rotational disorder of the protein trimers in the lattice as a result of their long range competing attractive and repulsive interactions.

The rotation of trimers would move surrounding lipids until they find new stable positions. This rearrangement of the lipids is coupled with the lateral shrinkage of the lipid regions and should lead to relative displacements of the trimers, generating a translational disorder of the lattice, thus leading to broadening of the 2D Bragg peaks. It should be noted that a rotational disorder without displacement of trimers would not cause any broadening of the Bragg peaks; it would only change the x-ray diffraction intensities.

These results clearly show that hydration is indispensable for maintaining the 2D crystal structure of deionized PM while the presence of cations can sustain the lattice structure even upon dehydration. The demonstrated effects of dehydration with and without cations on screening of protein-protein interactions of blue membranes should be considered in crystallographic studies of other 2D protein-lipid membranes.

References

A. Blaurock and W. Stoeckenius. 1971. Structure of the purple membrane. Nature New Biol. 233:152-155.

Mikio Kataoka and Tatzuo Ueki. 1980. The significance of radial autocorrelation function for the interpretation of equatorial diffraction from biological membranes. Acta Cryst. A36:282-287.

P.K. Rogan and G. Zaccai. 1981. Hydration in purple membrane as a function of relative humidity. J. Mol. Biol. 145:281-284.

Giuseppe Zaccai and David Gilmore. 1979. Areas of hydration in the purple membrane of halobacterium halobium: a neutron diffraction study. J. Mol. Biol. 132:181-191.

Acknowledgements: This research was supported by NIH Grant RR 1209 and data were recorded at both SSRL and NSLS which are supported by the DOE's Office of Basic Energy Science. We are grateful to Drs. Gene Ice and Paul Zschack, Mr. Mark Engbretson and Ms. Marybeth Rice for experimental assistance during the data collection at NSLS.

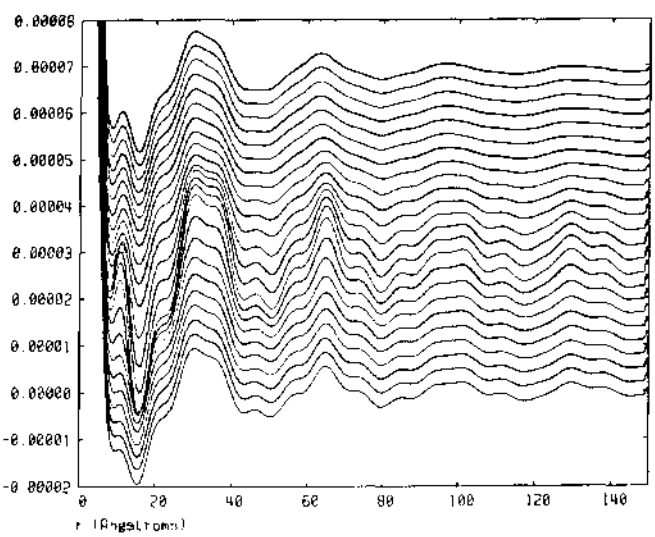

Fig. 1: Time-resolved radial autocorrelation functions during dehydration calculated from data in the S range between 0.029 -1 and 0.125 -1). The profiles are plotted with offset, the bottom being the first.

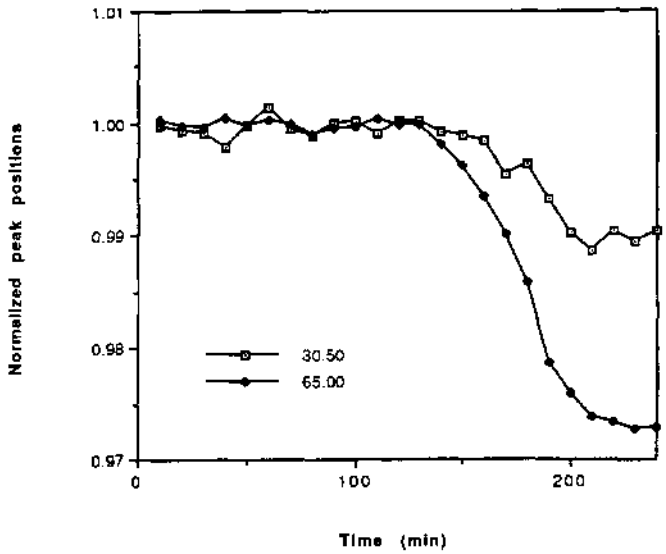

Fig. 2: Time changes of normalized peak positions at 30.5 and 65.0 of the autocorrelation functions. The peak at 30.5 is related to both intra- and inter- monomer helix-helix correlation whereas one at 65.0 arises from the unit cell repeat. Positions are normalized by those at the beginning of dehydration.

Kinetic Intermediates on the Pathway of Protein Folding

D.Eliezer[1], *K.O.Hodgson*[2], *S.Doniach*[3], *R.L.Baldwin*[4], *H.Kihara*[5]
Y.Amemiya[6], *A.Robertson*[4], *H.Tsuruta*[7]

1 Department of Physics, Stanford University, Stanford, CA 94305
2 Department of Chemistry, Stanford University, Stanford, CA 94305
3 Department of Applied Physics, Stanford University, Stanford, CA 94305
4 Department of Biochemistry, Stanford University, Stanford, CA 94305
5 Department of Physics, Jichi Medical School, Tochigi 329-04, Japan
6 Photon Factory, National Laboratory for High Energy Physics, Tsukuba, Ibaraki 305, Japan
7 Department of Materials Science, Hiroshima University, Hiroshima 730, Japan

Time resolved small angle X-ray scattering is a powerful tool for studying the kinetics of protein folding [1,2,3]. The most direct information provided is the radius of gyration (R_g) of the protein at various times during folding. It is increasingly probable that the "molten globule" state (see ref. 4 for a review) is a common intermediate in the refolding of small proteins, and that it is produced by a hydrophobic collapse. Such a collapse in a small protein is expected to be accompanied by a change in R_g of at least a few Angstroms. In this experiment we intend to observe such a change and determine when in the folding process it occurs.

We have chosen to study the folding of the small protein ribonuclease A (RNase A). This protein is available in large quantities and has been studied by many methods and in great detail, providing a wealth of information to assist in the interpretation of data. The protein was obtained from SIGMA corporation (grade XIIA) and was further purified chromatographically [5]. Samples for static experiments were made by dissolving the protein in a buffered solution at different concentrations of denaturant (GuHCL or Urea). For mixing experiments the protein is dissolved in a buffer containing a high concentration of denaturant and the resulting solution is then rapidly diluted into a buffer containing no denaturant, causing the protein to refold. The dilution step is completed on a time scale of tens of milliseconds, and is performed at a controlled temperature in the x-ray beam by a stopped flow rapid mixing device [6].

Preliminary static data were acquired in April of 1990 at SSRL on beamline 2-1, but a low beam intensity limited the number of samples which could be examined. A difference was observed between fully folded and fully unfolded protein samples (fig. 1), but the signal to noise ratio obtained was not sufficient to allow definite conclusions. No time resolved experiments were attempted. An experiment was also run at the Photon Factory in Japan in July of 1990. Static measurements indicated the presence of aggregation in the denatured protein solutions, but not in the folded protein solutions (fig 2). A mixing experiment was performed with an initial solution of 6mM RNase A, 4M GuHCl in buffer (40 mM NaFormate, pH 4) at a mixing ration of 3.5 - 1 (final conc. GuHCL 0.9M). No time dependent signal was observed.

Future efforts will include further static experiments to eliminate the presence of aggregation and determine the range of R_g between the folded an unfolded states, followed by mixing experiments using a higher mixing ratio to insure an unfolded initial state and a folded final state. In addition, calculations are in progress to demonstrate that these experiments can be performed using white light to achieve a far higher beam intensity.

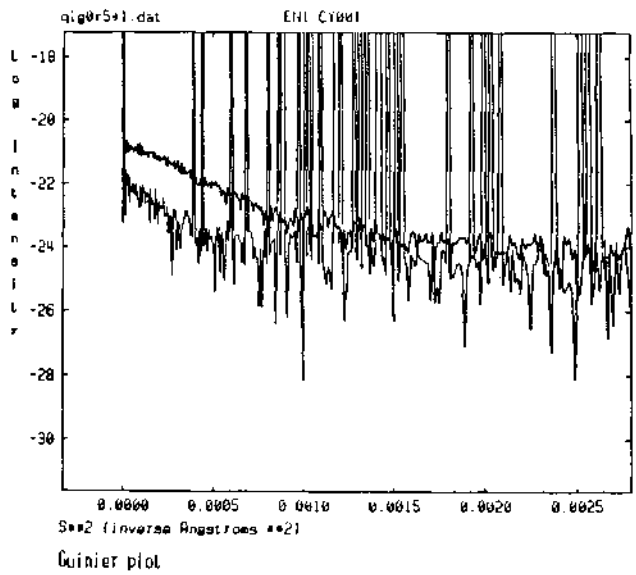

fig. 1 Guinier plots for folded RNase A and denatured RNase A (5M GuHCl), SSRL beamline 2-1.

References:

1. Phillips, J.C., LeGrand, A.D., Lehnert, W.F. Biophys. J. **53**, 461 (1988).
2. Moore, P.B. J. Appl. Cryst. **21**, 675 (1988).
3. Bordas, J., Mandelkow, E. *in* Structural Biological Applications of X-ray Absorption Scattering and Diffraction. Bartunik, H., Chance, B., eds. Academic Press Inc., 253 (1986).
4. Ptitsyn, O.B. J. Protein Chem. **6**, 273 (1987).
5. Garel, J. Eur. J. Biochem. **70**, 179 (1976).
6. Tsuruta, H. et. al. Rev. Sci. Instrum. **60** (7), 2356 (1989)

Acknowledgements:

This research was supported by NIH Grant RR 1209 and data were recorded at SSRL, which is supported by the DOE's Office of Basic Energy Science, and at the Photon Factory, National Laboratory for High Energy Physics, Japan.

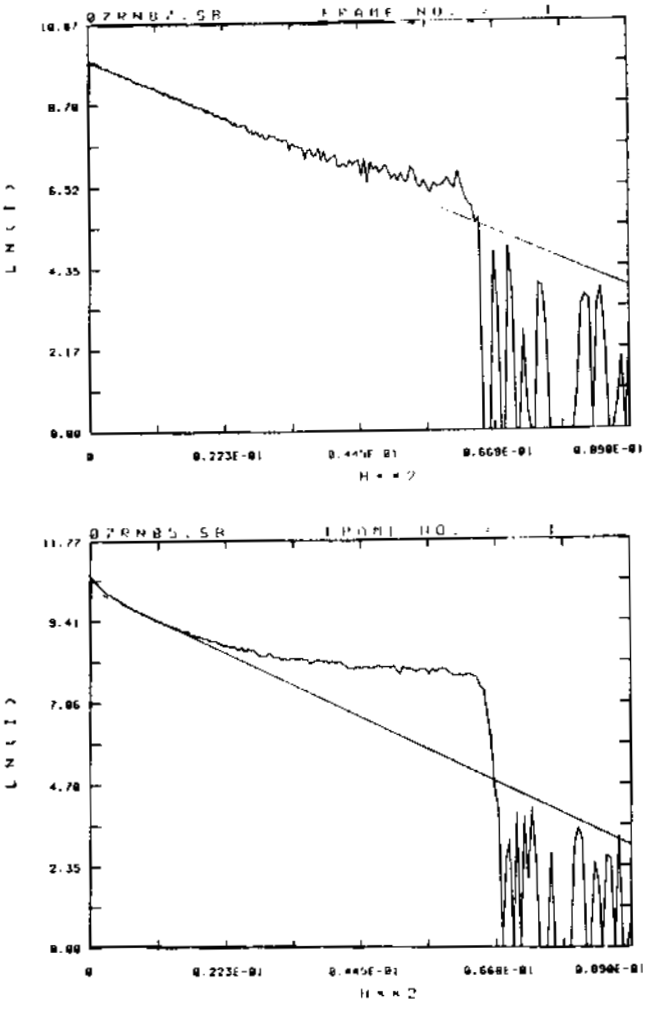

fig. 2 A) Guinier plot for folded RNase A. B) Guinier plot for denatured RNase A (4M GuHCl) showing aggregation. Photon Factory beamline 15-A.

X-RAY DIFFRACTION STUDIES OF MACROPHAGE-COLONY STIMULATING FACTOR

Jay PANDIT, Andrew BOHM and Sung-Hou KIM
Department of Chemistry, University of California, Berkeley, CA 94720

Introduction

Human Macrophage Colony Stimulating Factor 1 (M-CSF) is a growth factor that both stimulates monocytes and macrophages and induces the proliferation and differentiation of these cells from undifferentiated bone marrow stem cells. The binding of M-CSF to specific receptors on the surface of monocytes and macrophages has been linked to the release, by these cells, of gamma interferon, tumor necrosis factor, interleukin-1, E-series prostaglandins, and non-M-CSF colony stimulating factors. This is evidence for the role played by M-CSF in the complex regulation scheme that controls the response and development of the immune system.

M-CSF is produced in monocytes,macrophages,fibroblasts and endothelial cells as a membrane-bound, glycosylated dimer. It has been shown that an unglycosylated 155 residue sequence from the N-terminal domain of the protein is sufficient for stimulating the production of macrophage colonies from undifferentiated stem cells.

We are conducting X-ray crystallographic studies on recombinant human M-CSF (155 residue N-terminal fragment) in order to extend our biochemical understanding of this clinically important growth factor to include its three-dimensional structure.

Experimental

Crystals of M-CSF were grown by the vapor diffusion method. A 20 microliter droplet containing 20mg/ml protein,100mM $MgCl_2$, 50mM Tris.Cl pH 8.5 and 12% polyethylene glycol (PEG 4000) was equilibrated against a reservoir containing 24% PEG 4000, 200mM $MgCl_2$ and 100mM Tris. Chunky crystals measuring 0.4-0.8 mm appeared within one week. The crystals are orthorhombic, space group $P2_12_12_1$, with cell dimensions: a = 33.54, b = 65.26, c = 159.63 Å. Several potential heavy atom derivatives were obtained by soaking the crystals in different solutions of compounds of mercury and platinum. Native, and several derivative crystals were mounted in glass capillaries and transported to beamline 7-1 at SSRL. Intensity data were collected using X-ray film on an Arndt-Wonacott rotation camera installed at the beam line.

Results

A summary of the results of processing the film data is given below:

Crystal	No.of Reflections	Resolution(Å)	R_{merge}
Native	10284	2.5	8.2
$K_2Hg(SCN)_4$ soak	8008	2.7	8.5
$Pt((NH)_3)_2Cl_2$ soak	6861	2.7	9.6
Mersalyl acid soak	6198	3.0	7.8
Hg-Pt double soak	5205	3.1	8.3

MIR phases calculated from these data has yielded electron density maps in which the molecular outline and some secondary structural features are clearly identifiable. Further analysis is currently in progress to obtain an unambiguous tracing.

PROPOSAL NO. 8110B

Evidence from EXAFS for a Copper Cluster in the Metalloregulatory Protein CUP2 from Yeast.

Kent H. Nakagawa[1], Carla Inouye[2], Britt Hedman[3], Michael Karin[2], Thomas D. Tullius[4], and Keith O. Hodgson[1]

[1] Department of Chemistry, Stanford University, Stanford, California 94305-5080
[2] Department of Pharmacology, M-036, School of Medicine, University of California, San Diego, La Jolla, California 92093
[3] Stanford Synchrotron Radiation Laboratory, Stanford University, SLAC, Bin 69, P.O. Box 4349, Stanford, California 94309
[4] Department of Chemistry, The Johns Hopkins University, Baltimore, Maryland 21218

Introduction

Expression of yeast metallothionein, which binds copper specifically, is regulated by the protein CUP2 (a.k.a. ACE1).[1] CUP2 itself is activated for binding to DNA by copper(I).[2] Yeast metallothionein contains a cluster of eight copper(I) ions bridged by thiolate ligands that are likely provided by the 12 cysteines of the protein.[3] How copper is bound to CUP2 is unknown, however. Since stimulation by copper(I) of CUP2 binding to DNA is a cooperative process,[4] and the DNA binding domain of CUP2 contains 12 cysteines,[2,4] the presence of a copper cluster in CUP2 is also likely. We have undertaken a Cu K-edge EXAFS and edge study of Cu in CUP2.

Experimental

Cu K-edge x-ray absorption spectra were collected at the SSRL on BL 4-2 (unfocused) under dedicated ring conditions (3.0 GeV, 70-90 mA) using a Si(220) double-crystal monochromator. Protein data were collected at 10 K as Ni-filtered fluorescence excitation spectra. The EXAFS data obtained by normalization on spline background removal was analyzed using curve fitting techniques and empirical phases and amplitudes.

Results and Discussion

Single shell and wide shell fits (Figure 1; k^3 weighted data, 3.5-9.5 Å^{-1}) consistently showed that the first coordination shell is composed of two to three S at approximately 2.26 Å (Table 1) and the second shell of approximately 0.7-0.8 Cu atoms at 2.75-2.78 Å. Fits to this second shell with only a S wave were poor, as were wide shell fits with two S waves (at 2.26 Å and 2.75 Å). Fits were also done where the temperature factors were allowed to vary, with coordination numbers fixed and stepped at half-integer values. The best fits were obtained with coordination numbers of 3 for the short Cu-S and 1 for Cu-Cu. Distances showed no significant difference from those in Table 1.

Table 1. Summary of EXAFS Curve-Fitting Results *

Fourier region	Filter region Å	Inner S shell N	R, Å	Outer Cu shell N	R, Å	F*
first shell	0.90-2.35	2.34	2.27			0.72
second shell	2.10-3.25			0.80	2.78	0.45
wide shell	0.80-3.35	2.39	2.27			0.89
wide shell	0.80-3.35	2.44	2.27	0.66	2.75	0.75

* Errors in distances (± 0.03 Å) and coordination number (± 25%) are estimated from variance of fitting results between true values from models of known structure. $F = [\Sigma k^6(\text{data-fit})^2/(\text{no. of points})]^{1/2}$.

The Cu K x-ray absorption edge spectrum of CUP2 is shown in Figure 2 together with those of *Neurospora crassa* metallothionein,[5] of a Cu_4S_6 cubane-type cluster, which contains Cu in a distorted trigonal coordination, and of $[Cu_2(EDTB)](ClO_4)_2$, a two-coordinate linear Cu(I) complex. Each spectrum shows a transition on the rising portion of the edge at 8984 eV, which has been assigned to a 1s 4p-based electronic transition which is very sensitive to the coordination geometry of the Cu(I). The edge feature of the protein shows the closest resemblance to the Cu_4S_6 cluster and thus to a trigonal 3-coordinate environment. The CUP2 spectrum also closely resembles that of the Cu(I) cluster in *N. crassa* metallothionein as well as the *S. cerevisiae* yeast metallothionein itself.[3] The edge energy position, along with the absence of a 1s 3d transition further establishes that it is indeed a Cu(I), and not a Cu(II) cluster.

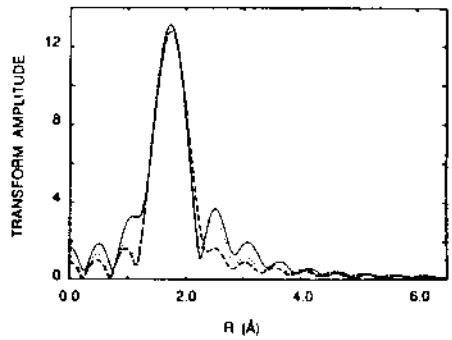

Figure 1. Comparison of the Fourier transform of filtered EXAFS data (R = 0.80 to 3.35 Å, k range of 3.0-10.0 Å^{-1}) from CUP2 (solid line) with transforms of a one-shell fit containing S (dashed line) and a two-shell fit containing S and Cu (dotted line). Notice the excellent agreement between the fit and data for the first shell in both cases. However, while the second peak is not reproduced by a single S shell, it is well reproduced with the presence of a second shell of Cu.

Taken together, the results thus show that CUP2 contains Cu atoms arranged in a cluster bridged by S atoms, presumably donated by protein cysteines. It is thus remarkable that the CUP2 copper cluster seems to resemble that of the very yeast metallothionein protein[3] that it regulates. What is the functional advantage for CUP2 to be activated by formation of a copper cluster, instead of a a simple mononuclear copper center? A possibility is that the metalloregulatory protein CUP2 is evolutionarily related to the protein whose synthesis it controls. The structural similarity of the copper(I) clusters in yeast metallothionein[3] and CUP2, as we have demonstrated in this paper, makes this an attractive prospect.

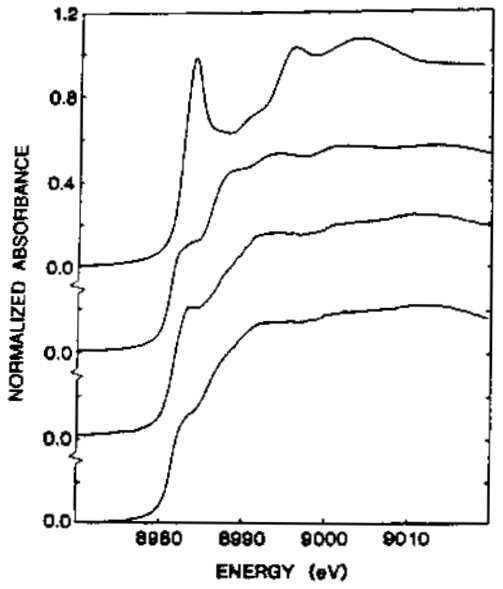

Figure 2. Comparison of the x-ray absorption Cu-K edge spectra. From top to bottom, a two-coordinate linear Cu(I) complex, a three-coordinate Cu_4S_6 model cluster compound, a Cu-metallothionein protein, and the CUP2 protein. Notice the strong similarities in the features of the lower three edges, and the distinct difference between the CUP2 and the two-coordinate Cu(I) complex edges.

Acknowledgements.

The data were collected at SSRL, which is supported by the DOE, Office of Basic Energy Sciences, Division of Chemical Sciences and Division of Materials Sciences and by the NIH, Biomedical Resource Technology Program, Division of Research Resources. Grant support was provided from the NIH (GM 40894) to T.D.T., the EPA (R-815580) to M.K., and the NSF (CHE 88-17702) to K.O.H.

References

(1) Thiele, D. J. *Mol. Cell. Biol.* **1988**, *8*, 2745; Welch, J.; Fogel, S.; Buchman, C.; Karin, M. *EMBO J.* **1989**, *8*, 255.

(2) Buchman, C.; Skroch, P.; Welch, J.; Fogel, S.; Karin, M. *Mol. Cell. Biol.* **1989**, *9*, 4091.

(3) George, G. N.; Byrd, J.; Winge, D. R. *J. Biol. Chem.* **1988**, *263*, 8199.

(4) Fürst, P.; Hamer, D. *Proc. Natl. Acad. Sci. USA* **1989**, *86*, 5267; Fürst, P.; Hu, S.; Hackett, R.; Hamer, D. *Cell* **1988**, *55*, 705.

(5) Smith, T. A.; Lerch, K.; Hodgson, K. O. *Inorg. Chem.* **1986**, *25*, 4677.

PROPOSAL NO. 8110B

WHOLE CELL XANES: SULFUR IN A. ceratodes BLOOD CELLS

Patrick Frank[1], Britt Hedman[1,2], Robert M.K. Carlson[3], Trevor Tyson[4], and Keith O. Hodgson[1]

1 Department of Chemistry, Stanford University, Stanford CA 94305, USA
2 Stanford Synchrotron Radiation Laboratory, SLAC, Bin 69, P.O. Box 4349, Stanford CA, 94305, USA
3 Chevron Oil Field Research Co., P.O. Box 1627, Richmond CA, 94802-0627, USA
4 Department of Applied Physics, Stanford University, Stanford CA, 94305, USA

Introduction

Application of XAS to whole cells is still a rare event, principally because of the difficulty in discerning one among the potentially numerous chemical species under observation, each of which is typically at low concentration. The blood cells of the tunicate, Ascidia ceratodes lend themselves to such study, however, since they are known to contain both vanadium and sulfur in high concentration (1-3).

Most recently, we have focussed on elucidating the chemical types of sulfur present in these cells (3-6). XANES sulfur-K spectra are very sensitive to both the chemical environment and oxidation state of sulfur atoms. We have found a shift of 1.6±0.2 eV per unit oxidation state change, over a range of 13 eV, in sulfur traversing the nominal valence states -2 to +6 (4,5).

In this report, we show XANES spectra for three batches of A. ceratodes blood cells collected over a span of 18 months, and describe methods to determine the nature of various sulfur types which may be present.

Experimental

Specimens of Ascidia ceratodes were collected from the Monterey Yacht Harbor; blood cell samples and inorganic model solutions were prepared as described (7). XANES spectra of blood cell samples and inorganic model solutions were measured on beamlines VI-2 or IV-2. Data were acquired in fluorescence mode using an N_2-filled Lytle detector. Fitting experiments were performed on a VAXstation 3500 using the program FITCUR, provided by professor James Penner-Hahn (Department of Chemistry, University of Michigan), and modified locally. Numerical addition spectra were constructed using the program ADDFIL running on a VAXstation 3500.

Results and Discussion

In Figure 1 we show a set of sulfur-K XANES spectra from three whole blood cell preparations of Ascidia ceratodes. Examination of the spectra immediately reveals that at least two types of sulfur are present: low-valent S near 2473 eV, and high-valent S near 2482 eV. The spectra have been normalized at 2488 eV, the sulfate edge-jump (8), so as to display the same apparent total sulfur concentration. It is therefore evident that the relative amounts of low valent sulfur varies from sample to sample. Comparison with solution models indicates that this sulfur is most similar to that found in the amino acid cysteine, having a C-SH, or sulfhydryl, grouping.

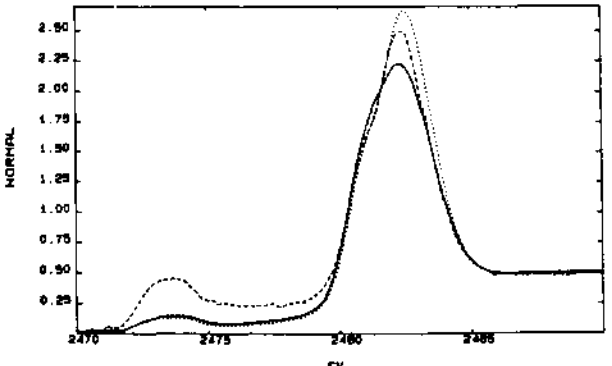

Figure 1. XANES spectra of three preparations of whole blood from Ascidia ceratodes: (full line) S85; (dash) S86; (dot) W87, where S = summer and W = winter.

Additional variations include the high valent S region, where differences in intensity, in line width, and in the prominence and definition of the low-eV shoulder are observed. In particular, samples S86 and W87 (see Legend to Figure 1 for nomenclature) exhibit a pronounced shoulder near 2480.5 eV whereas sample S85 only shows a broad absorption with the hint of an inflection at the maximum.

These features are resolved more readily as the two major minima in the second derivative spectra shown in Figure 2, which imply that at least two types of sulfur are present. However the disparities in lineshape pointed out above for the absorbance spectra are again evident both in the shape of the second derivative spectra in the triple inflection region around 2481.5 eV, and in the intensities and widths of the respective features.

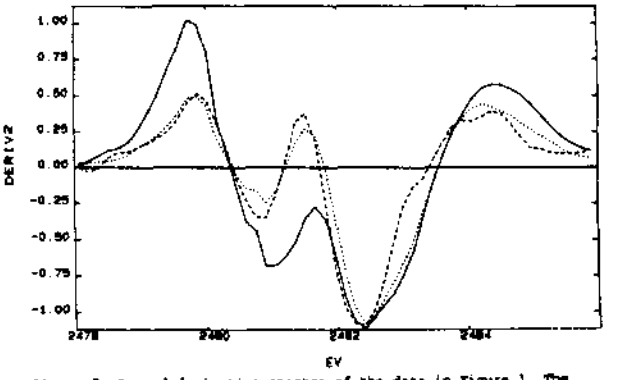

Figure 2. Second derivative spectra of the data in Figure 1. The spectra have been scaled to equal intensity at 2482.4 eV.

Earlier work on the S85 data (5) showed that two sulfur components were present: S(+5) represented by an aliphatic sulfonic acid of partial structure $C\text{-}SO_3(-)$, and S(+6) represented by sulfate $SO_4(2-)$. The broadening of the sulfate features at 2482.4 eV in the S85 and W87 second derivative spectra of Figure 2 additionally imply an interaction between intracellular sulfate and vanadium(III) ion, which is also known to be present in some cells. This aspect of tunicate biological chemistry, though novel, will not be further discussed here.

Two approaches were then taken in order to more fully resolve the portions of these spectra reflecting high valent sulfur components. The first was a curve fitting approach, using Gaussian functions to fit both the major valence level absorption features, and the Rydberg envelope incorporating lines at higher energy (9,10). The choice of Gaussian linewidth and position was made by preliminary fitting experiments carried out on model solutions containing both sulfonic acid and sulfate having varying component ratios and in varying chemical environments. The second derivatives of the model fits were further required to freely duplicate the structured region (2480-2484 eV) of the second derivatives of the model spectral data.

Figure 3 shows the data for, and the fit to, the S85 blood cell sample. The fit is seen to be very good, and the second derivative of the fit was a close match to that of the data (not shown). By way of caution, we have found that some fits to the data, judged good both visually and by difference statistics, yielded obviously incorrect second derivative spectra, strongly suggestive of an underlying problem with the component lineshapes.

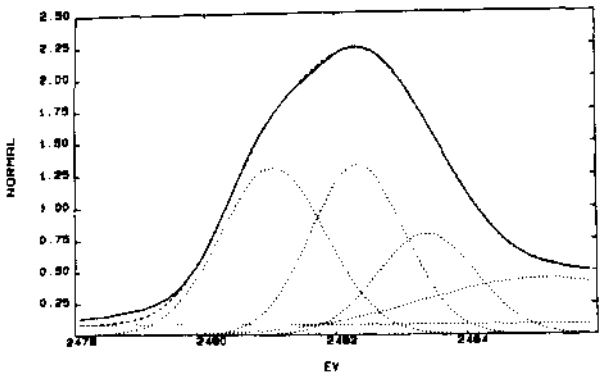

Figure 3. Gaussian fit to the S85 data set: (full line) S85 data; (dash) fit; (dot) Gaussian components and the constant linear offset, needed to account for the contribution of low-valent S at 2473 eV.

From the Figure 3 fit, the ratio of C-SO_3(-) to SO_4(2-) was determined to be 0.90 to 1.0. This compares to a ratio of 0.92 to 1.0 found previously by a numerical subtraction method (5). The ratio of low valent to high valent sulfur in this sample, 1.0 to 5.2, was determined directly from the respective edge jumps.

The deconvolution of the S86 and W87 samples in terms of constituent sulfur has proved more difficult. In particular, a third type of high valent sulfur was found to be present, when the fitting parameters derived from sulfonate/sulfate model solutions were found to be inadequate for these spectra. The new type of sulfur present is believed to be C-O-SO_3(-); that is, an ester of sulfuric acid. Figure 4 shows a spectrum of a normalized 1:0.55:0.25 mixture of sulfate methane sulfonate and inositol hexasulfate (containing six sulfate esters per molecule), numerically generated. This spectrum is seen to reproduce the distinct shape of the shoulder seen in the spectra for samples S86 and W87.

The inset to Figure 4 shows a spectrum of inositol hexasulfate in dilute solution. The single absorption feature of sulfate is seen to be strongly split. This is because the Td symmetry of sulfate is lowered to C3v in the sulfate ester, lifting the three-fold T degeneracy to A1 and E final states. The lower intensity A1 transition at 2481 eV overlaps almost perfectly the single transition due to C-SO_3(-) sulfur.

Experiments to fully resolve the components of these biological mixtures are currently in progress. These experiments are complicated by the fact that sulfonic acid is also present, and so the mixtures are ternary, rather than binary. In addition two of the spectra (S85 and W87) reflect an association with vanadium(III) ion, (present in some of the blood cells, as mentioned above) which broadens the sulfate line.

A best current estimate, based on incomplete numerical addition experiments, is that the ratio of sulfate to sulfate ester in samples S86 and W87 is about 1 to 0.3-0.5. In addition, the ratio of high to low valent sulfur is, for S86 1.0 to 1.0; and for W87 is 6.1 to 1.0, as obtained directly from the respective edge jumps.

In conclusion, XAS measurements have allowed us to determine the presence of exotic types of biological sulfur directly within living cells, and to gain some understanding both of their discrete chemical nature

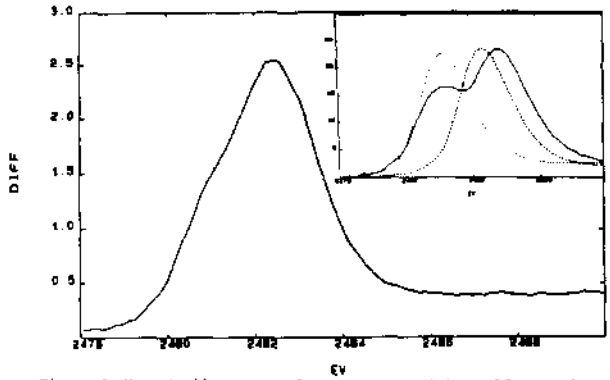

Figure 4. Numerically generated spectrum containing sulfate, sulfate ester and sulfonate in the ratio 1.0:0.55:0.25 (see text). Inset: Comparative overlay of sulfate ester (full line); sulfate (dash); and sulfonate (dot).

and their respective amounts. With regard to A. ceratodes, it is clear that a rich sulfur metabolism exists in these animals, and a potential oxidative pathway from low valent to high valent sulfur has been found.

Acknowledgments. This work was supported by the NSF, Grant number CHE88-17702 to KOH. The measurements were performed at SSRL, which is supported by the US DoE, Office of Basic Energy Sciences, Divisions of Chemical and Material Science, and by the NIH, Biomedical Resource Technology Program, Division of Research Resources.

References

1. Carlson, R.M.K. (1975) Proc. Natl. Acad. Sci. U.S.A. 72, 2217.
2. Tullius, T.D., Carlson,R.M.K., Gillum, W.O. and Hodgson, K.O. (1980) J. Am. Chem. Soc. 102, 5670.
3. Frank, P., Carlson, R.M.K. and Hodgson, K.O. (1986) Inorg. Chem. 25, 470.
4. Hedman, B., Frank,P., Penner-Hahn, J.E. Roe, A.L., Hodgson, K.O., Carlson, R.M.K., Brown, J., Cerino, J., Troxel, T., Winick, H. and Yang, J. (1986) Nucl. Instr. Meth. A246, 797.
5. Frank, P., Hedman, B., Carlson, R.M.K., Tyson, T.A., Roe, A.L. and Hodgson, K.O. (1987) Biochemistry 26, 4795.
6. Frank, P., Carlson, R.M.K. and Hodgson, K.O. (1988) Inorg. Chem. 27, 118.
7. Frank, P., Hedman, B., Carlson, R.M.K, Tyson, T.A. and Hodgson, K.O. (1891), in preparation.
8. Tyson, T.A., Roe, A.L., Frank, P. and Hodgson, K.O. Phys. Rev B. 39, 6305.
9. Lytle, F.W., Greegor, R.B., Sandstrom, D.R., Marques, E.C., Wong, J., Spiro, C.L., Huffman, G.P. and Huggins, F.E. (1984) Nucl. Instr. Meth. 226, 542.
10. Agarwal, B.K. "X-Ray Spectroscopy" Springer Verlag, Berlin, 1979, p 276ff.

Multielectron Photoexcitation: Measurement and Interpretation of the Sulfur KL_{23}-edge of SO_4^{2-}

T. A. Tyson[1], A. Filipponi[2], B. Hedman[1,3] and K. O. Hodgson[1]

[1]Department of Chemistry, Stanford University, Stanford, California 94305
[2]Departimento di Fisica Universita' degli studi dell'Aquila, 67010 Coppitio, L'Aquila, Italia
[3]Stanford Synchrotron Radiation Laboratory, SLAC, Bin 69, P. O. Box 4349, Stanford, California 94309

I. Introduction

The Problem of multielectron transitions involves taking into account the response of the full charge distribution to the stimulus which in this case is the time-dependent electromagnetic field.[1, 2] The standard approach to the true many-electron problem is to decompose the total charge density with respect to a set of single particle orbitals whose Slater determinant[3-5] minimizes the total energy. This is the well known Hartree-Fock method.[4-6] The set of orbitals which minimize the Hamiltonian is not unique. Starting from an arbitrary set of orbitals any unitary transformation of the set yields the same total energy.[5, 7] In general the single particle orbitals should be thought of as just basis sets (a convenience to facilitate computations) and should not be attributed any physical significance.

Typically transition rates are computed with wavefunctions calculated within the Hartree-Fock scheme (although theory is fully rigorous only for the ground state[1]). In many photoabsorption processes it is found that the dominant contribution comes from hydrogen atom like matrix elements. These processes are termed single-electron processes although it must be kept in mind that the full charge density and hence all of the electrons participate. In the discussion below when a given number of electrons ("active electrons") are said to be involved in a transition we mean that, with respect to the basis of single particle orbitals which we are using, the dominant contribution to the absorption cross section corresponds to so many interacting electrons.

Here we are interested in understanding multielectron processes induced by single photon absorption. Specifically, we are investigating KL_{23} near threshold (or edge) spectra. By KL_{23} we mean the transitions:

$$1s,2p \rightarrow nl, n'l'$$

involving the K and L_{23} (L_2 and L_3) shells. Examples are:

$$1s,2p \rightarrow np,n'p \qquad (I)$$

$$1s,2p \rightarrow ns,n's \qquad (II)$$

$$1s,2p \rightarrow ns,n'd \qquad (III)$$

In section II we outline a model developed to interpret both the multiplet energy splittings and the multiplet cross sections. In section III this model is applied to the KL_{23} spectrum of the sulfate anion.

II. Multiplet Energy Splitting and Cross Section

We focus on the splitting or the change in energy of a set of eigenstates due to the perturbation

$$H_e' = \frac{1}{2}\sum_{i,j=1}^{N}{}' \frac{e^2}{|\vec{r}_i - \vec{r}_j|} - \sum_{i=1}^{N} V(r_i) = V_{coul} - \sum_{i=1}^{N} V(r_i) \qquad (1)$$

The change in energy of a state $\Psi_{LmS\mu}$ due this perturbation is given by[8, 9]

$$E'_{LS} = \langle \Psi_{LmS\mu} | H_e' | \Psi_{LmS\mu} \rangle$$

The energy spacing between different multiplet states is determined by the difference between the matrix elements of the Coulomb interaction potential V_{coul} since the matrix element of the mean potential $V(r)$ is the same for all states $\Psi_{LmS\mu}$.[10, 11] We need only focus on the difference between multiplet energies

$$\Delta E'(L'S',LS) = \langle \Psi_{L'm'S'\mu'} | V_{coul} | \Psi_{L'm'S'\mu'} \rangle - \langle \Psi_{LmS\mu} | V_{coul} | \Psi_{LmS\mu} \rangle \qquad (2)$$

for the case when there are two or more particles and additionally

$$\Delta E'(LS,\{l', l'', s', s''\}',\{l', l'', s', s''\})$$

$$= \langle \Psi_{LmS\mu}(\{l', l'', s', s''\}') | V_{coul} | \Psi_{LmS\mu}(\{l', l'', s', s''\}') \rangle$$

$$- \langle \Psi_{LmS\mu}(\{l', l'', s', s''\}) | V_{coul} | \Psi_{LmS\mu}(\{l', l'', s', s''\}) \rangle \qquad (3)$$

for the case when there is more than one state with the same multiplet symbol. Each such state being designated by intermediate quantum numbers {1', 1", s', s"}. In general the latter case forces one to apply the methods of degenerate perturbation theory[8, 9] to determine the energy spacings between the states of a given multiplet and simultaneously the proper linear combination of multiplet states which diagonalize H in the subspace of the multiplet. However we found that for the case of KL_{23} edges in sulfur that H was diagonal with respect to the recessively determined functions $\Psi_{LmS\mu}$.

By coupling the particle and hole states (core states) in the lowest order transition amplitude we obtained for a process of the type mentioned above the cross section

$$\sigma^{\varepsilon}(\hbar\omega,\ 1',1'',\ s',\ s'',L,\ S) = 4\pi^2\,\alpha\,\hbar\omega \sum_{m\,\mu} \Big| \sum_{\substack{m1 m2 m3 m4 \\ \mu1\,\mu2\,\mu3\,\mu4}} \sum_{mg} \Big\{ \Big[(-1)^{m3+m4}\,(-1)^{\mu3+\mu4}$$

$$\langle 11\ m1\ 12\ m2 | 11\ 12\ 1'\ m' \rangle \langle 1/2\ \mu1\ 1/2\ \mu2 | 1/2\ 1/2\ s'\ \mu' \rangle$$

$$\langle 1'\ m'\ 13\ -m3 | 1'\ 13\ 1''\ m'' \rangle \langle s'\ \mu'\ 1/2\ -\mu3 | s'\ 1/2\ s''\ \mu'' \rangle$$

$$\langle 1''\ m''\ 14\ -m4 | 1''\ 14\ L\ m \rangle \langle s''\ \mu''\ 1/2\ -\mu4 | S''\ 1/2\ S\ \mu \rangle$$

$$a^{\varepsilon}_{mg}\ C(11,m1,1,mg,13,-m3)\ \delta_{\mu1,\,-\mu3}\delta_{m2,\,-m4}\delta_{\mu2,\,-\mu4}$$

$$\frac{(\varepsilon_1 - \varepsilon_3)}{\hbar\omega} M_{n_1 l_1\ n_3 l_3}\,\overline{M}_{n_2 l_2\ n_4 l_4} \Big] - [\text{Exchange Term}]\ \Big\} \Big|^2\ \delta(E_f - E_i - \hbar\omega) \qquad (4)$$

where the ordering of the states is

$$1 = n1,\ 2 = n'1',\ 3 = 1s \text{ and } 4 = 2p$$

with α being the fine structure constant, the parameter a^{l}_{mg} given by

$$a^{x}_{mg} = \begin{cases} -\sqrt{\frac{2\pi}{3}} & mg = 1 \\ 0 & mg = 0 \\ \sqrt{\frac{2\pi}{3}} & mg = -1 \end{cases}$$

$$a^{y}_{mg} = \begin{cases} i\sqrt{\frac{2\pi}{3}} & mg = 1 \\ 0 & mg = 0 \\ i\sqrt{\frac{2\pi}{3}} & mg = -1 \end{cases}$$

$$a^{z}_{mg} = \begin{cases} 0 & mg = 1 \\ \sqrt{\frac{4\pi}{3}} & mg = 0 \\ 0 & mg = -1 \end{cases}$$

C representing the Gaunt coefficient and with M and $\overline{M}$ being radial dipole and monopole matrix elements, respectively. It is understood that states 1 and 2 are valence states while 3 and 4 correspond to hole states. The exchange term comes into effect if either the pair of initial or final single-particle states have the *same* l-value and n-values. The unpolarized cross section is obtained by averaging over the x, y and z components.

III. Measurements and Interpretation

The KL_{23}-edge of the SO_4^{2-} anion in the compound $CuSO_4 \cdot 5H_2O$ prepared as a fine powder on mylar tape was measured according to experimental methods previously published[12] and the spectrum can be seen in Fig. 1. It was found (by looking at transitions of type (I) through (III) in atomic models) that the most intense peaks resulted from transitions of type (I) in which both final valence states were identical. That is to say from transitions of the form

$$1s,2p \rightarrow np^2$$

Consequently, the p-component of the relaxed t2 wavefunction on the sulfur site and the ground state 1s and 2p core functions were used in Eqs. (3) and (4) to determine the energy spacings and relative intensities using the MS-Xα model mentioned in reference 12. That is to say, the lowest energy transition of the type

$$1s,2p \rightarrow t2^2$$

was looked at. The results are presented in Table I. Three ^1P multiplet states are found for the transition and it is expected that these three peaks should dominate the experimental spectrum as was found in Fig. 1. The spacing between feature A and C can be predicted quite well but that between feature B and C are off by 1.7 eV. It is not clear why this deviation is so large. Good agreement of intensities (in general) is seldom found using the MS-Xα model but due to the fact that we have a high symmetry "closed cluster" here the agreement is quite close.[12] To recap, we have found that it is possible to construct multiplet wave functions and used them to determine the gross features (energy spacings as well as relative intensities) in KL_{23}-edges of closed clusters . That is to say, the peaks in the edge spectra can be labeled according to multiplet terms and their intermediate quantum numbers.

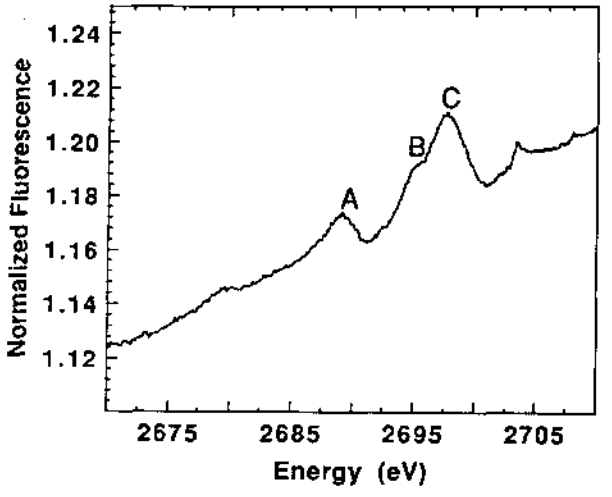

Fig. 1: Measured KL_{23}-edge of the SO_4^{2-} anion with peaks labeled A, B and C representing the dominant multiplet lines.

Table I. KL_{23} Multiplet Energy Splittings and Intensities[1]

Int. quan. no.[2]	ΔE	Expt. ΔE	σ/σ2	Expt. σ/σ2[3]
l'=1, s'=1 (^3P) l"=1, s"=1/2 (^2P)	-8.7	-8.7 (A)	1/2	0.5
l'=0, s'=0 (^1S) l"=0, s"=1/2 (^2S)	0.0	0.0 (C)	1	1
l'=2, s'=0 (^1D) l"=2, s"=1/2 (^2D)	-0.3	-2.0 (B)	1/2	0.6

[1]Int. quan. no. are intermediate quantum numbers, ΔE signifies energy difference between second (C in Fig. 1) and given multiplet and σ/σ2 is the ratio of the peak intensity to that of the second multiplet peak (again C). Expt. stands for the corresponding experimental values.

[2]These entries define the three ^1P multiplets in terms of their intermediate quantum numbers.

[3]Intensity ratios are with respect to the smooth EXAFS background.

References

[1]Z. Crljen and G. Wendin, Phys. Scr. 32, 359 (1985).

[2]R. L. Martin and D. A. Shirley, in *Electron Spectroscopy: Theory, Techniques and Applicatons*, edited by C. R. Brundle and A. D. Baker (Academic Press, London, 1977).

[3]R. E. Christoffersen, *Basic Principles and Techniques of Molecular Quantum Mechanics* (Springer-Verlag, New York, 1989).

[4]H. A. Bethe and R. W. Jackiw, *Intermediate Quantum Mechanics* (Benjamin/Cummings Publishing Company, Menlo Park, 1986).

[5]A. Szabo and N. S. Ostlund, *Modern Quantum Chemistry* (McMillan Publishing Co., New York, 1982).

[6]T.-Y. Wu, *Quantum Mechanics* (World Scientific, Singapore, 1986).

[7]E. Steiner, *The Determination and Interpretation of Molecular Wave Functions* (Cambridge University Press, London, 1976).

[8]L. I. Schiff, *Quantum Mechanics* (McGraw-Hill Book Company, New York, 1968).

[9]E. Merzbacher, *Quantum Mechanics* (John Wiley and Sons, New York, 1970).

[10]J. A. Sordo and L. Pueyo, J. Chem. Ed. 62, 468 (1985).

[11]M. Weissbluth, *Atoms and Molecules* (Academic Press, New York, 1978).

[12]T. A. Tyson, A. L. Roe, P. Frank, B. Hedman and K. O. Hodgson, Phys. Rev. B 39, 6305 (1989).

Acknowledgements

We are indebted to Dr. P. Frank (Stanford Univ. Chem. Dept.) for assistance in our experiments and for helpful discussions. This research was supported by National Science Foundation grant CHE 88-17702. The experiments were carried out at SSRL which is supported by the Department of Energy's Office of Basic Energy Science and the NIH's Division of Research Resources, Biotechnology Resource Program.

XAS EDGE STUDIES OF LIGANDS BOUND TO OPEN SHELL METAL IONS

Susan Shadle, Keith O. Hodgson, and Edward I. Solomon
Department of Chemistry, Stanford University, Stanford, CA 94305

Britt Hedman
Stanford Synchrotron Radiation Laboratory, Stanford, CA 94309

INTRODUCTION

X-ray absorption edge structure is an effective tool for probing electronic structure of a metal center. In most applications this has been done at the metal K- or L-edges. We have focused on probing the metal center electronic structure by examining the edge structure of its bound ligands (1). In particular, we have studied the K-edges of ligands such as sulfur and chlorine bound to open shell metal atoms. The K-edges of these ligands fall in the 2-3 KeV range, where features are well resolved compared to those at higher energy (2). Initially, the studies have focused on structurally known model systems. Knowledge acquired from these model systems is then used to understand ligand binding, both endogenous and exogenous, at metalloprotein active sites.

EXPERIMENTAL

Chlorine K-edge XAS data were measured at SSRL using the 54-pole wiggler beam line 6-2 at low magnetic fields (5 kG), using a Si(111) double crystal monochromator and a Pt-coated focusing mirror. The entire experimental beam path was in He atmosphere. Measurements were made in flourescence detection mode, using a N_2 filled Lytle detector. Model compounds were run as very thin powders on mylar tape to avoid self-absorption. Water sensitive compounds were prepared in an inert-atmosphere glove box and were protected from air by a polypropylene window.

RESULTS AND DISCUSSION

The XAS spectrum of a copper dimer, with chloride in both bridging and terminal positions and a distorted tetrahedral copper geometry, shows a split preedge feature (Fig. 1). The spectrum of a model in which chloride is present only in the bridging position (dashed spectrum) shows a decrease in intensity of the lower energy feature upon removal of the terminal chloride. (Note, this model cannot be made pure and there is therefore some intensity due to presence of terminal chloride). These spectra allow us to assign the lower energy feature at 2819.9 eV as a transition from the terminal chloride and the higher energy feature at 2821.0 eV as a transition from the bridging chloride. Our results thus show that it is possible to differentiate between inequivalent ligands in the same system, specifically bridging and terminal chlorides. This provides valuable insight into electronic structure differences in metal-ligand bonds.

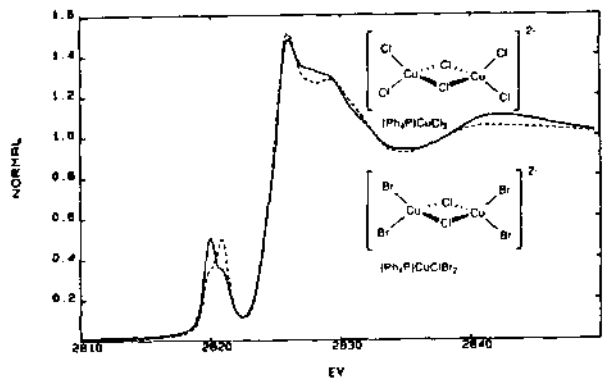

Figure 1. Chlorine K-edges of $(Ph_4P)CuCl_3$ (——) and $(Ph_4P)CuClBr_2$, impure (----).

A comparison of monomeric systems shows that a distorted tetrahedral $CuCl_4^{2-}$ complex exhibits a preedge feature at 2820.2 eV, while a square planar $CuCl_4^{2-}$ complex has this feature at 2820.6 eV, ~0.4 eV higher. (Fig. 2)

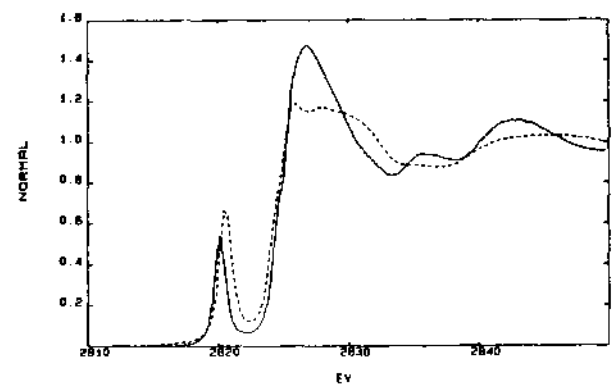

Figure 2. Chlorine K-edges of Cs_2CuCl_4, distorted tetrahedron (——) and $(Creatininium)_2CuCl_4$, square planar (----).

Data from a second dimer system which contains only one bridging chloride coordinated to tetragonal coppers exhibits a feature at 2821.4 eV (Fig. 3). This is, as expected, ~0.4 eV higher than the bridging chloride feature in the distorted tetrahedral dimer.

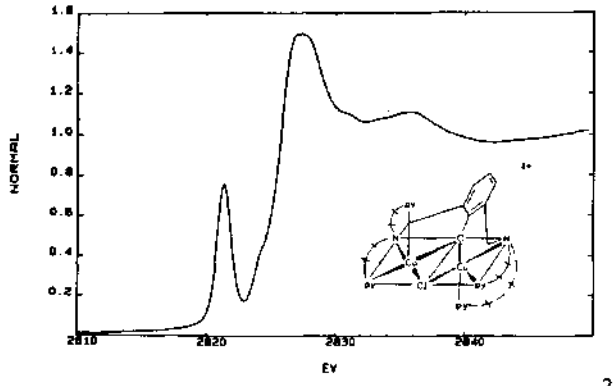

Figure 3. Chlorine K-edge of $[Cu_2(L\text{-}O\text{-})Cl]^{2+}$

The preedge transitions of these models illustrate the two primary variables which govern the energy position of these features. First, the amount of charge on the chloride ligand can shift its 1s orbital energy level. In the first model system, the bridging chloride shares electron density with two copper ions. It has a less negative charge than the terminal chloride, causing its 1s orbital to be at deeper binding energy. Consequently, transitions from a bridging chloride occur at higher energy by about 1 eV. Second, there is a shift in the energy level of the accepting $d_{x^2-y^2}$-type orbital with a change in geometry. This is because of differences in the repulsive interaction of the $d_{x^2-y^2}$-type orbital with the surrounding ligands.[2] The models show that the increased repulsion in tetragonal systems shifts transition energies about 0.4 eV higher than in a distorted tetrahedron.

The utility of this chloride K-edge XAS approach to the study of metal-ligand interaction will be important in studies planned for defining the nature of exo- genous ligand binding at active sites in metalloproteins.

ACKNOWLEDGEMENTS

Grant support was provided by NSF (CHE88-17702, KOH), (CHE89-19687, EIS). The measurements were performed at SSRL, which is supported by the US DOE, Office of Basic Energy Sciences, Divisions of Chemical and Material Science, and by the NIH, Biomedical Resource Technology Program, Division of Research Resources.

REFERENCES

1. Hedman, B., Hodgson, K.O., Solomon, E.I. J. Am. Chem. Soc. 112, 1643 (1990).
2. The high energy resolution is due to both reduced core hole life time (Krause, M.O., Oliver, J.H. J. Phys. Chem. Ref. Data 8, 329 (1979)) and improved monochomator resolution.

VII. ACTIVE PROPOSALS

As of January 1, 1991 there were 133 active SSRL proposals. Proposals remain active for two years after their initial rating by the Proposal Review Panel. Since October 1974 SSRL has received a total of 2133 proposals. The Spokesperson for each proposal is listed first and their institution shown in parentheses. The letter suffix appended to the proposal number indicates the sub-panel of the Proposal Review Panel to which the proposal is assigned: Materials (M), Biology (B) or Vacuum Ultra-Violet (V). The small p denotes a program proposal. The date is the original date of receipt.

922Bp 9/06/84 **Gold-Based Antiarthritis and Anticancer Drugs and Metabolites: XAS, WAXS, DAS**
Richard C Elder
Katherine Tepperman
(UNIVERSITY OF CINCINNATI)

935Vp 9/20/84 **Electronic Structure, Chemistry, and the Fermi Level at Semiconductor Surfaces and Interfaces**
Ingolf Lindau
Dan Dessau
Tom Kendelewicz
Paul Meissner
Ken Miyano
Z X Shen
William E Spicer
Chris Spindt
Anita Wahi
Barrett Wells
(SSRL)

943Vp 9/06/84 **Electron Spectroscopy of Gases, Solids, and Surfaces**
David A Shirley
Philip A Heimann
Zheng-qing Huang
Tony Huff
Zahid Hussain
Laura Medhurst
Eddie Moler
Li-quing Wang
Alexis Schach V Wittenau
(LAWRENCE BERKELEY LABORATORY)

956Mp 2/27/85 **Applications of EXAFS Spectroscopy in the Steel and Coal Industries**
G P Huffman
Naresh Shah
(UNIVERSITY OF KENTUCKY)

957Bp 2/28/85 **Anomalous Scattering of X-rays**
David H Templeton
L K Templeton
(LAWRENCE BERKELEY LABORATORY)

969Bp 3/14/85 **X-ray Absorption Spectroscopic Studies of Nickel-Containing Metalloenzymes**
Robert A Scott
Mitchell C Brenner
Robert Kertayasa
(UNIVERSITY OF GEORGIA)

995Mp 9/06/85 **XAS Study of Cation Adsorption at Aqueous/Oxide Interface**
Gordon E Brown, Jr
Kim F Hayes
Keith O Hodgson
James O Leckie
George A Parks
Glenn A Waychunas
(STANFORD UNIVERSITY)

999Mp 9/10/85 **EXAFS Study of Trace Element Environments in Quenched Silicate Melts of Geochemical Interest**
Gordon E Brown, Jr
W A Jackson
C W Ponader
S Rothfus
Glenn A Waychunas
(STANFORD UNIVERSITY)

1018Mp 3/03/86 **Diffusion in Ternary Multilayer Thin Films**
D De Fontaine
Jeff J Hoyt
Sarath Menon
S Spooner
(UNIVERSITY OF CALIFORNIA)

1019B 3/03/86 **Crystallographic Study of Amicyanin by Anomalous Scattering Using Synchrotron Radiation**
F Scott Mathews
Rosemary Durley
Ethan A Merritt
R. Paul Phizackerley
(WASHINGTON UNIVERSITY)

1021Mp 3/03/86 **Synchrotron X-ray Polycrystalline Diffractometry**
William Parrish
Maurizio Bellotto
Curt Erickson
Michael Hart
Ting C Huang
George Will
(IBM RESEARCH LABORATORY)

1022Vp 3/03/86 **UPS Studies of the Coordination Chemistry of Metal Oxides, Chlorides and Sulfides**
Edward I Solomon
Kristine Butcher
Jian-yi Lin
(STANFORD UNIVERSITY)

1030Bp 3/17/86 **Soft X-ray Spectrocopy of Molybdenum Enzymes, Cofactors and Model Compounds**
Stephen P Cramer
M W Adams
J H Enemark
Graham N George
V Minak
L S Solmonson
Edward I Stiefel
(BROOKHAVEN NATIONAL LABORATORY)

1041B 9/03/86 **Measurement of Metal-Metal Distances in Proteins by X-ray Anomalous Scattering**
Robert A Scott
Marly Eidsness
(UNIVERSITY OF GEORGIA)

1042B	9/03/86	**Studies of Intermediates in the Mechanism of Carboxypeptidase-a** Britton Chance David Auld Mark Chance Barton Holmquist Linda S Powers James Riordan B Vallee *(UNIVERSITY OF PENNSYLVANIA)*
1043B	9/03/86	**X-Ray Absorption Spectroscopy of Iron-Iron Interactions: Ribonucleotide Reductase** Britton Chance Grant Bunker S M Khalid Ali Naqui Peter Reichard Britt-marie Sjoberg Guang Zhang *(UNIVERSITY OF PENNSYLVANIA)*
1046Bp	9/03/86	**Iodine Dichromography with Monochromatic X-ray Beams for Angiography** Edward Rubenstein George S Brown Donald C Harrison Robert Kernoff John Otis W Thomlinson Albert C Thompson Herbert D Zeman *(STANFORD UNIVERSITY)*
1047M	9/03/86	**High Pressure Transition Mechanisms via EXAFS** Robert L Ingalls Daryl Crozier J Freund *(UNIVERSITY OF WASHINGTON)*
1048Mp	9/11/86	**High Resolution Compton Profiles of Iron and Silicon** Caroline Stahle Arthur Bienenstock Sean Brennan Douglas Osheroff *(STANFORD UNIVERSITY)*
1051M	9/11/86	**Crystal and Aqueous Chemistry of Germanium in Geochemically Important Systems** Glenn A Waychunas James A Davis Brigid A Rea *(STANFORD UNIVERSITY)*
1053B	9/15/86	**Copper EXAFS Spectroscopy of Non-Blue Copper Proteins. Amine Oxidases** Robert A Scott David M Dooley Robert Kertayasa *(UNIVERSITY OF GEORGIA)*
1055B	9/15/86	**XAS of Iron-Molybdenum Cofactor of Nitrogenase under Electrochemical Control** Keith O Hodgson Britt Hedman B J Feldman P Frank *(SSRL)*

1059M	9/16/86	**In Situ High P-T Equation-of-State, Phase Transformations and Kinetics Studies on Mantle Mineral Phases using Synchrotron Radiation** Murli H Manghnani Russell J Hemley H K Mao L C Ming J A Xu *(UNIVERSITY OF HAWAII)*
1064M	3/03/87	**Static High Pressure and High Temperature X-Ray Diffraction Studies of Some Rare-Earth Elements Using Diamond-Anvil Apparatus** J Akella L C Ming Choong Shik G S Smith S T Weir *(LAWRENCE LIVERMORE NATIONAL LABORATORY)*
1066Mp	3/01/87	**X-Ray Spectroscopy of Electrochemically Generated Species** Richard C Elder William R Heineman *(UNIVERSITY OF CINCINNATI)*
1067Bp	3/01/87	**Active Site Structures of Cytochrome c Oxidase** Robert A Scott Mitchell C Brenner Sunney I Chan Robert Kertayasa *(UNIVERSITY OF GEORGIA)*
1078M	3/01/87	**X-Ray Absorption Studies of Metal Ion Absorption at Semiconductor Surfaces** N S Lewis Keith O Hodgson *(CALIFORNIA INSTITUTE OF TECHNOLOGY)*
1080Vp	3/01/87	**Adsorption Structure of Heteroatom-Containing Molecules on Transition Metal Surfaces** Robert J Madix B Factor C M Friend A C Liu J T Roberts J Solomon *(STANFORD UNIVERSITY)*
1081M	3/01/87	**A Study of Creep Damage Using Microradiography** David P Pope John E Benci *(UNIVERSITY OF PENNSYLVANIA)*
1084Bp	3/01/87	**Polarized X-Ray Spectroscopy of the Oriented Chloroplast Water-Oxidizing Complex** Graham N George Stephen P Cramer Roger C Prince *(EXXON RESEARCH & ENGINEERING)*

1085Bp 3/01/87 **X-Ray Absorption Spectroscopic Characterization of the Manganese in Biological Systems**
James E Penner-hahn
W D Frasch
D Ghanotakis
J T Groves
V L Pecoraro
M Stern
Him-Tai Tsang
C F Yocum
(UNIVERSITY OF MICHIGAN)

1088M 3/01/87 **Polarized X-Ray Absorption Near Edge Structure**
James E Penner-hahn
Geoffrey Waldo
Shengke Wang
Glenn A Waychunas
(UNIVERSITY OF MICHIGAN)

1093Mp 8/07/87 **Structure of Superconducting Thin Films**
Stephen Laderman
Malcolm Beasley
Alice Fischer-Colbrie
Theodore H Geballe
R D Jacowitz
Aharon Kapitulnik
J Moll
R Smith
(HEWLETT PACKARD LABORATORIES)

1095Mp 8/07/87 **EXAFS and NEXAFS Investigation of OMPVE Growth of II-VI Compounds**
Paul H Fuoss
Sean Brennan
D W Kisker
(AT&T BELL LABORATORIES)

1096Mp 8/20/87 **In-Situ X-Ray Scattering Studies of OMVPE Growth of II-VI Compounds**
Paul H Fuoss
Sean Brennan
J Kahn
D W Kisker
(AT&T BELL LABORATORIES)

1097Mp 8/20/87 **Anti-Site Disorder in High T_c Superconductors**
Farrel W Lytle
Robert B Greegor
(BOEING COMPANY)

2010Bp 9/17/87 **X-Ray Spectroscopy of Manganese and Iron in Chloroplasts**
Melvin P Klein
Melissa Grush
Matthew Latimer
Wenchan Liang
Vittal K Yachandra
J L Zimmerman
(LAWRENCE BERKELEY LABORATORY)

2023Mp 9/21/87 **High T_c Superconducting Materials: Their Structural and Electronic Characterization by XAS**
Steve D Conradson
Zachary Fisk
Ian D Raistrick
Antonio Redondo
(LOS ALAMOS NATIONAL LABORATORY)

2029Bp 9/29/87 **Mo and Se XAS Studies of Small-Molecule Binding to Nitrogenase**
Keith O Hodgson
Barbara K Burgess
Britt Hedman
C Stanfel
(SSRL)

2030Bp 9/29/87 **XAS Structural Characterization of the Binuclear Iron-Center in Methane Monooxygenase**
Keith O Hodgson
Jane Dewitt
Britt Hedman
Stephen J Lippard
Amy Rosenzweig
(SSRL)

2031Bp 9/29/87 **X-Ray Absorption Studies of Coupled Binuclear Copper Sites in Proteins**
Keith O Hodgson
Britt Hedman
Kent Nakagawa
Edward I Solomon
Grace Tan
(SSRL)

2032Bp 9/29/87 **XAS Studies of Heme-Iron Enzymes: Cytochrome P-450 and Peroxidases**
Keith O Hodgson
John H Dawson
Britt Hedman
Masanori Sono
(SSRL)

2033Mp 9/29/87 **Sulfur K Edge XAS Studies of Photographic Sensitizing Centers**
Teresa A Smith
Britt Hedman
Keith O Hodgson
(EASTMAN KODAK COMPANY)

2044Mp 11/05/87 **Direct Scattering Studies of Surface Premelting**
J Kahn
Arthur Bienenstock
Sean Brennan
Paul H Fuoss
Frank Lamelas
Laura Norton
(STANFORD UNIVERSITY)

2048B 11/16/87 **X-Ray Absorption Spectroscopy of Galactose Oxidase**
James E Penner-hahn
Robert Kertayasa
James W Whittaker
(UNIVERSITY OF MICHIGAN)

2049Mp 3/01/88 **Catalyst Characterization by X-ray Absorption Spectroscopy**
Farrel W Lytle
Robert B Greegor
Edward C Marques
(BOEING COMPANY)

2050B 3/01/88 **Laue Diffraction Trials with Protein Crystals on PEP**
R Paul Phizackerley
Janos Hajdu
Michael Soltis
(SSRL)

2051Bp 3/01/88 **X-Ray Absorption of Vanadium and Tungsten Nitrogenases and Storage Proteins**
Brian J Hales
Cathy Coyle
Stephen P Cramer
Graham N George
(LOUISIANA STATE UNIVERSITY)

2053Mp 3/10/88 **Physical and Electronic Structure of Support Bimetallic Catalysts**
G Meitzner
Farrel W Lytle
John H Sinfelt
Grayson H Via
(EXXON RESEARCH & ENGINEERING)

2055Mp 3/15/88 **Shallow and Deep Donors in $Ga_{1-x}Al_xAs$ Semiconducting Alloys**
T M Hayes
P Gibart
D L Williamson
(RENSSELAER POLYTECHNIC INST.)

2056Mp 3/15/88 **Measurements in the Terapascal Range and Hydrogen Metallization**
H K Mao
Russell J Hemley
A P Jephcoat
Albert C Thompson
J H Underwood
Y Wu
(CARNEGIE INSTITUTE)

2059M 3/15/88 **X-Ray Scattering of Amorphous and Hydrogenated Amorphous Carbon Thin Films**
Mike Toney
Sean Brennan
Paul H Fuoss
(IBM RESEARCH LABORATORY)

2060Bp 3/15/88 **Structure-Function Studies of the Active Site of Lignases, Peroxidases, and Models**
Linda S Powers
S Aust
J Li
M Tien
(UTAH STATE UNIVERSITY)

2061M 3/17/88 **Electrochemically Deposited Metal Monolayers: Structure, Compressibility and Growth**
Owen Melroy
Mike Toney
(IBM RESEARCH LABORATORY)

2062Mp 3/17/88 **Structural Improvements in Multilayers for Instrumentation Applications**
William K Warburton
Edward Franco
Jonathan Kerner
(X-RAY INSTRUMENTATION ASSOCIATES)

2063Mp 3/17/88 **Characterization of Electrochemical Processes by X-Ray Absorption Spectroscopy**
Howard D Dewald
(OHIO UNIVERSITY)

2064M 3/21/88 **X-Ray Absorption Studies of Bimetallic Electrocatalysts for C_1 Oxidation**
Ian D Raistrick
Steve D Conradson
Antonio Redondo
(LOS ALAMOS NATIONAL LABORATORY)

2065M 3/24/88 **Elemental X-Ray Imaging with PEP Using an X-Ray Microscope**
Albert C Thompson
Robert D Giauque
J H Underwood
Y Wu
(LAWRENCE BERKELEY LABORATORY)

2067M 4/21/88 **X-Ray Absorption Spectroscopy of Transformation-Toughened Zirconia Ceramics**
James E Penner-Hahn
I-Wei Chen
T Y Tien
(UNIVERSITY OF MICHIGAN)

2068Bp 5/07/88 **X-Ray Absorption Spectroscopy of Phthalate Dioxygenase and Soybean Lipoxygenase**
James E Penner-Hahn
David P Ballou
Christopher J Batie
Dimitri Coucouvanis
Max O Funk
Him-tai Tsang
(UNIVERSITY OF MICHIGAN)

2069Mp 5/07/88 **XAS of Metal-Sulfur Clusters Supported on Metal Oxide Surfaces**
James E Penner-Hahn
M David Curtis
(UNIVERSITY OF MICHIGAN)

2074Vp 9/13/88 **Electronic and Geometric Properties of Impurities ON/IN Carbon**
Brad Pate
Ingolf Lindau
William E Spicer
J Wu
(WASHINGTON STATE UNIVERSITY)

2076Mp 9/13/88 **Investigation of Short Range Order in Mineralogical Solid Solutions**
Glenn A Waychunas
Wayne A Dollase
Richard J Reeder
Charles R Ross
(STANFORD UNIVERSITY)

2077M 2/01/89 **SEXAFS and Surface X-Ray Diffraction Study of Self-Assembled Monolayers on Gold Surfaces**
M Samant
Gary Borges
Charles A Brown
Joseph G Gordon
(IBM RESEARCH LABORATORY)

2078V 3/01/89 **X-Ray Induction of Charge Trapping Defects in Amorphous SiO_2**
David B Kerwin
Frank L Galeener
(COLORADO STATE UNIVERSITY)

2079Bp 3/01/89 **XAS Structural Characterization of the Active Center in the Rhodospirillum rubrum Carbon Monooxide Dehydrogenase Enzyme**
Keith O Hodgson
Scott Ensign
Britt Hedman
Paul W Ludden
Marie-Claire McKenna
Philip J Stephens
(SSRL)

2080M	3/01/89	**In-Situ EXAFS Transition Metal Macrocycles Adsorbed on Electrode Surface** Daniel A Scherson Philip N Ross *(CASE WESTERN RESERVE UNIVERSITY)*
2081Mp	3/07/89	**Glancing Angle Diffraction Studies on Polymer Films** B Factor Thomas P Russell *(STANFORD UNIVERSITY)*
2082Vp	3/07/89	**Dynamics of Atomic Inner-Shell Processes** Bernd Crasemann George S Brown Roger Carr A F Kodre J Ruscheinski S J Schaphorst *(UNIVERSITY OF OREGON)*
2083M	3/07/89	**Rare Gas Clusters** G Faraci S La Rosa A Terrasi *(UNIVERSITA DI CATANIA)*
2084M	3/07/89	**Small Angle X-Ray Studies of Phase Separation During Bulk Copolymerization** Tony Ryan Jeff T Korberstein Chris Macosko *(UNIVERSITY OF MINNESOTA)*
2085M	3/14/89	**Glancing Angle Diffraction Studies on Liquid Crystalline Polymers** Thomas P Russell B Factor *(IBM RESEARCH LABORATORY)*
2086Mp	3/15/89	**Diffraction Studies of Organic Monolayers on Water (Langmuir Films)** Pulak Dutta Tom Bohanon Binhua Lin Mingchih Shih *(NORTHWESTERN UNIVERSITY)*
2088M	3/15/89	**Anomalous Small Angle X-Ray Scattering Study of AmorphouMetal-Germanium** Marybeth Rice Arthur Bienenstock S Wakatsuki *(STANFORD UNIVERSITY)*
2089Mp	3/15/89	**Surface EXAFS of Epitaxial Semiconductor Interfaces** Tom Kendelewicz Ingolf Lindau Piero Pianetta William E Spicer Joe Woicik *(STANFORD UNIVERSITY)*
2090Mp	3/15/89	**Fluorescence EXAFS Applied to the Study of Impurity Site Location in Heavily-Doped III-V Compounds** Kin Man-Yu J Jaklevic Wladyslaw Walukiewicz *(LAWRENCE BERKELEY LABORATORY)*

2091Mp	3/15/89	**Strain Mapping and Crystal Characterization Using Synchrotron Radiation Polychromatic Topography** S R Stock Y H Chung T S Gross A B Lee J D Plummer Zophia U Rek *(GEORGIA INSTITUTE OF TECHNOLOGY)*
2092B	3/15/89	**Structure <-> Function Studies of RNA Polymerase from *E. coli*** Linda S Powers F. Y.-H. Wu *(UTAH STATE UNIVERSITY)*
2094V	3/15/89	**Photoelectron Microscopy** Piero Pianetta Anne Borg Paul King Gordon Knapp (SSRL)
2095V	3/15/89	**Synchrotron Radiation Studying Ultrathin Superlattice Band Structures** Piero Pianetta X Yang *(SSRL)*
2096B	3/30/89	**Measurement of Multiwavelength Diffraction Data from Glutamine PRPP Amidotransferase Crystals** Janet L Smith *(PURDUE UNIVERSITY)*
2097B	9/10/89	**Structural Investigation of Terbium Chelates in Aqueous Solution by X-Ray Absorption Spectroscopy** Cong-Yuan Guo *(UNIVERSITY OF MISSOURI)*
2098B	9/10/89	**Mo K and L Edge Spectroscopy of Cyandie Inhibited Sulfite Oxidase and Model Compounds** J H Enemark M D Carducci Stephen P Cramer *(UNIVERSITY OF ARIZONA)*
2099M	9/10/89	**Study of Framework Demetallation of COAPO and FAPO Molecular Sieves by X-Ray Absorption Spectroscopy, X-Ray Diffractio and Diffuse Reflectance Spectroscopy** Guang Zhang Gary S Mondo *(CHEVRON RESEARCH COMPANY)*
2100Mp	9/10/89	**X-Ray Absorption Investigation of Metal Binging Sites in Crude Oil and Petroleum Products** Guang Zhang Gary S Mondo *(CHEVRON RESEARCH COMPANY)*
2101B	9/10/89	**Structural Studies of the Blue Form of the Purple Membranes** Sebastian Doniach D Eliezer N Gillis Keith O Hodgson S Wakatsuki *(STANFORD UNIVERSITY)*

2102B	9/10/89	**Anomalous Dispersion Scattering Studies of Metal Clusters in Biological Systems** Keith O Hodgson Sebastian Doniach D Eliezer N Gillis S Wakatsuki *(SSRL)*
2103Vp	9/10/89	**Photoemission Study of High T_c Superconductors and Related Materials** Z X Shen Ingolf Lindau William E Spicer *(STANFORD UNIVERSITY)*
2104Bp	9/10/89	**XAS Structural Characterization of Vanadium Bromoperoxidase** Ulrich Kuesthardt Britt Hedman Keith O Hodgson Hans Vilter *(TU MUNCHEN)*
2105Mp	9/19/89	**Damage and Crack Closure in Composite and Monolithic Materials** S R Stock S D Antolovich T M Breunig Zophia U Rek *(GEORGIA INSTITUTE OF TECHNOLOGY)*
2106B	9/19/89	**Measurement of Nitrogenase Multiwavelength Anomalous Diffraction Data** Jeffrey T Bolin Nino Campobasso Wladek Minor R Paul Phizackerley *(PURDUE UNIVERSITY)*
2107M	9/28/89	**In-Situ EXAFS Transition Metal Macrocycles Adsorbed on Electrode Surfaces** Daniel A Scherson Philip N Ross *(CASE WESTERN RESERVE UNIVERSITY)*
2108B	3/01/90	**X-Ray Tomographic Microscopy of Human Dentin** John H Kinney Ulrich Bonse Greyson W Marshall Sally J Marshall Monte Nichols *(LAWRENCE LIVERMORE NATIONAL LABORATORY)*
2109M	3/01/90	**Structural Investigation of Metal Contaminants in Fluid Catalytic Cracking Catalysts using X-Ray Absorption Spectroscopy** Guang Zhang Gary S Mondo *(CHEVRON RESEARCH COMPANY)*
2110B	3/01/90	**XAS Structural Characterization of a Novel Molybdenum Site in 2-Hydroxycarboxylate Viologen Oxidoreductase** Ulrich Kuesthardt Britt Hedman Keith O Hodgson *(TU MUNCHEN)*

2111Vp 3/01/90 **Structural Studies of Thiols and Alcohols on Mo and Rh Surfaces**
C M Friend
Joachim Stohr
Benjamin C Wiegand
Xueping Xu
(HARVARD UNIVERSITY)

2112M 3/01/90 **Development of an 8 keV Synchrotron Microscope**
Richard M Bionta
Ken Skulina
(LAWRENCE LIVERMORE NATIONAL LABORATORY)

2113B 3/01/90 **Static Structures of Associating Polymers via Small Angle X-Ray Scattering**
Alice P Gast
Cathy Cogan
Robert Ju
Jenni Raeder
(STANFORD UNIVERSITY)

2114Bp 3/01/90 **Structural Interactions in Respiratory Proteins**
James O Alben
Craig F Hemann
John Hill
Kimerly A Powell
Jianhong Pu
Zhouhong Shi
(OHIO STATE UNIVERSITY)

2115Mp 3/21/90 **In-Situ Determination of Surface and Interface Structure of Sputter Deposited Films**
Bruce M Clemens
Sean Brennan
(STANFORD UNIVERSITY)

2116M 3/21/90 **Solution Structures of Lanthanide-CMPO Complexes in Organic Solvents by SAXS and ASAXS Techniques**
P Thiyagarajan
H Diamond
J E Epperson
Keith O Hodgson
E P Horwitz
(ARGONNE NATIONAL LABORATORY)

2117Bp 3/21/90 **Kinetic Intermediates on the Pathway of Protein Folding: SAXS Studies**
Keith O Hodgson
R L Baldwin
Sebastian Doniach
D Eliezer
A Robertson
(SSRL)

2118Mp 3/21/90 **Anomalous X-Ray Diffraction Studies of Crystal Structure and Valence Ordering**
George Kwei
Joyce A Goldstone
Jon M Lawrence
Andrew C Lawson
Robert B Von Dreele
(LOS ALAMOS NATIONAL LABORATORY)

2119M 8/11/90 **EXAFS Investigations of Metal Multilayers**
Geraldine M Lamble
Bruce M Clemens
Steve M Heald
(BROOKHAVEN NATIONAL LABORATORY)

2120M	8/28/90	**Local Atomic Structure of High T_c Superconductors** Frank Bridges James B Boyce Tord Claeson Theodore H Geballe Guoguang Li *(UNIVERSITY OF CALIFORNIA)*
2121Vp	8/28/90	**Spin Polarized Photoemission Studies of Magnetic Surfaces and Ultra-Thin Films** Herbert Hopster C R Brundle D E Fowler A C Luntz D P Pappas Z X Shen *(UNIVERSITY OF CALIFORNIA)*
2122V	8/31/90	**Investigation of UV-Induced Degradation of Space Optics** Mira Bakshi Mike Brinkman Dave Deacon *(DEACON RESEARCH)*
2123Vp	9/04/90	**Growth, Structure & Electrical Properties of Large Bandgap Materials** Don Kania Lawrence Pan Brad Pate Piero Pianetta *(LAWRENCE LIVERMORE NATIONAL LABORATORY)*
2124M	9/04/90	**Structural and Charge-transfer High Pressure Transitions in Perrhenates** Robert L Ingalls Daryl Crozier L Huang *(UNIVERSITY OF WASHINGTON)*
2125M	9/05/90	**Determination of the Strain Distribution in Aluminum Thi Films Using GIXS** John C Bravman Sean Brennan *(STANFORD UNIVERSITY)*
2126M	9/05/90	**X-Ray Absorption Studies of Perovskites as a Function of Pressure** Robert L Ingalls B Houser *(UNIVERSITY OF WASHINGTON)*
2127V	9/10/90	**Heteroepitaxial Interface Formation Between Insulators and Metals** Marjorie Olmstead Jonathan Denlinger Eli Rotenberg Gerard Wong (UNIVERSITY OF CALIFORNIA)
2128Bp	9/11/90	**Technetium and Rhenium Imaging Agents and Therapeutic Radiopharmaceuticals** Richard C Elder Edward A Deutsch *(UNIVERSITY OF CINCINNATI)*
2129Bp	9/14/90	**Synchrotron Radiation Detector Development Program** William K Warburton J S Iwanczyk S R Russell *(X-RAY INSTRUMENTATION ASSOCIATES)*

2130V 9/14/90 **The Role of Fluorine in Fluoride/Silicon Interface Formation**
Marjorie Olmstead
Jonathan Denlinger
Eli Rotenberg
Gerard Wong
(UNIVERSITY OF CALIFORNIA)

2131M 9/17/90 **Off-center Displacement of Cu^+ in KC_1**
Frank Bridges
James B Boyce
Guoguang Li
Xun Wang
(UNIVERSITY OF CALIFORNIA)

2132M 9/17/90 **"Glitch" Formation in XAFS Spectra**
Frank Bridges
James B Boyce
Guoguang Li
Xun Wang
(UNIVERSITY OF CALIFORNIA)

2133Mp 9/19/90 **Determination of Local Epitaxy and Strain in Sputter-Deposited Films**
Bruce M Clemens
Sean Brennan
(STANFORD UNIVERSITY)

PRT PROPOSALS

The Spokesperson only is listed on the PRT Proposals.

1001M 1/01/86 **EXXON PRT Time - BL 6**
Graham N George
(EXXON RESEARCH & ENGINEERING)

9900M 1/01/85 **Lawrence Berkeley Laboratory PRT Time-BL 6**
Philip N Ross
(LAWRENCE BERKELEY LABORATORY)

9901V 1/01/85 **National Labs/University of California PRT Time-BL 8**
Marvin J Weber
(LAWRENCE LIVERMORE NATIONAL LABORATORY)

9902M 9/01/88 **National Labs/University of California PRT Time - BL 10**
Marvin J Weber
(LAWRENCE LIVERMORE NATIONAL LABORATORY)

ROTATION CAMERA PROPOSALS

Access to the rotation camera facility for protein crystallography is through the submittal of a brief application which is reviewed by the Biology Sub-panel of the PRP on a short turnaround basis. The presently active rotation camera proposals are listed below.

1A95B	3/01/89	**Structure of Crystalline Proteins** David Eisenberg Duilio Cascio Chris Hill Herman Schreuder *(UNIVERSITY OF CALIFORNIA)*
2A03B	3/12/90	**Data Collection for B-Hexosaminidase-B** W Bret Church Michael N G James *(UNIVERSITY OF ALBERTA)*
2A04B	3/12/90	**Non Watson-Crick Base Pairing in Human Telomeric DNAs** Chulhee Kang Martin Egli Christin Frederick Qu Gao Rheinhard Gessner Alexander Rich Loren Williams Xiaohua Zhang *(MASSACHUSETTS INSTITUTE OF TECHNOLOGY)*
2A05B	3/12/90	**Study of Ribosomes** Ada Yonath William Bennett Felix Frolow Harly Hansen Ilona Makowski Nils Volkmann *(WEIZMANN INSTITUTE)*
2A06B	3/12/90	**Succinyl-CoA Synthetase** William T Wolodko William A Bridger Michael N G James *(UNIVERSITY OF ALBERTA)*
2A07B	5/11/90	**Structure of Human Growth Hormone in (hGH): Its Receptor and Complexes** Bart De Vos Charles Eigenbrot Mike Randal Mark Ultsch *(GENENTECH, INC.)*
2A08B	8/11/90	**The Crystal Structure of Telomere** Chulhee Kang Alexander Rich Xiaohua Zhang *(MASSACHUSETTS INSTITUTE OF TECHNOLOGY)*
2A09B	8/11/90	**Structural Studies of Myosin Subfragment-1** Ivan Rayment Matthew Benning Hazel Holden *(UNIVERSITY OF WISCONSIN)*

2A10B	8/28/90	**To Continue Heavy Atom Derivative Scanning for Pilin** Hans E Parge K Andrews M Boissinot D Christensen Elizabeth D Getzoff T Hong C F Kuo Duncan E Mcree S Mylvaganam S Redford John A Tainer *(RESEARCH INSTITUTE OF SCRIPPS CLINIC)*
2A11B	9/14/90	**Crystal Structure of PhoE Porin** Thomas Earnest Ed Berry Bing Jap *(LAWRENCE BERKELEY LABORATORY)*
2A12B	12/17/90	**Crystal Structure of Colicin Ia** Robert M Stroud Partho Ghosh Stephanie Mei V Ramalingam Michael Shuster *(UNIVERSITY OF CALIFORNIA)*

VIII. SSRL EXPERIMENTERS AND PROPOSALS BY INSTITUTION

As of January 1, 1991 there were 374 experimenters from 92 institutions officially involved with active proposals at SSRL. In addition, over a 100 others (graduate students, etc.) participated in work at the laboratory in collaboration with these scientists. The 75 United States institutions included 49 universities, 15 corporations and 11 government laboratories.

U.S. CORPORATIONS

ARACOR, AT&T Bell Laboratories, Becton Dickinson & Company Research Center, Boeing Company, Chevron Research Company, Deacon Research, Eastman Kodak Company, EXXON Research & Engineering, Genentech, Inc., Hewlett Packard Laboratories, IBM Research Laboratory, Surface Science Instruments, X-ray Instrumentation Associates, XEROX, Xsirius, Inc.

U.S. LABORATORIES

Argonne National Laboratory, Brookhaven National Laboratory, Lawrence Berkeley Laboratory, Lawrence Livermore National Laboratory, Los Alamos National Laboratory, Naval Air Development Center, National Institute of Standards and Technology, Oak Ridge National Laboratory, Sandia National Laboratories, Stanford Synchrotron Radiation Laboratory, US Geological Survey Water Resources Division

U.S. UNIVERSITIES

Amherst College, California Institute of Technology, Carnegie Institute, Carnegie Mellon University, Case Western Reserve University, Colorado School of Mines, Colorado State University, Georgetown University, Georgia Institute of Technology, Harvard Medical School, Harvard University, Louisiana State University, Massachusetts Institute of Technology, Northwestern University, Ohio State University, Ohio University, Pennsylvania State University, Princeton University, Purdue University, Rensselaer Polytechnic Institute, Research Institute of Scripps Clinic, Stanford University, State University-New York, University City Science Center, University of Arizona, University of California, University of Chicago, University of Cincinnati, University of Connecticut, University of Georgia, University of Hawaii, University of Illinois, University of Kentucky, University of Michigan, University of Minnesota, University of Missouri, University of New Hampshire, University of Notre Dame, University of Oregon, University of Pennsylvania, University of South Carolina, University of South Florida, University of Southern California, University of Toledo, University of Washington, University of Wisconsin, Utah State University, Washington State University, Washington University

FOREIGN INSTITUTIONS

Academia Sinica (People's Republic of China), Chalmers Institute of Technology (Sweden), Centre National de la Recherche Scientifique (France), Fudan University (Peoples Republic of China), Karolinska Institute (Sweden), Max Planck Institute (Germany), Medical Nobel Institute (Sweden), Simon Fraser University (Canada), The University Manchester (England), TU Munchen (Germany), Universita di Brescia (Italy), Universita di Catania (Italy), Universitat Bayreuth (Germany), Universitat Bonn (Germany), Universitat Dortmund (Germany), University of Alberta (Canada), University of Oxford (England), Weizmann Institute (Israel)

AMERICAN CORPORATIONS

ARACOR

Edward Franco	2062
Jonathan Kerner	2062

AT&T BELL LABORATORIES

Paul H Fuoss	1095, 1096, 2044, 2059
Frank Lamelas	2044
Laura Norton	2044

BECTON DICKINSON & CO. RESEARCH CTR.

Ali Naqui	1043

BOEING COMPANY

Robert B Greegor	1097, 2049
Farrel W Lytle	1097, 2049, 2053
Edward C Marques	2049

CHEVRON RESEARCH COMPANY

Gary S Mondo	2099, 2100, 2109
Guang Zhang	1043, 2099, 2100, 2109

DEACON RESEARCH

Mira Bakshi	2122
Mike Brinkman	2122
Dave Deacon	2122

EASTMAN KODAK COMPANY

Teresa A Smith	2033

EXXON RESEARCH & ENGINEERING

M W W Adams	1030
Cathy Coyle	2051
Graham N George	1001, 1030, 1084, 2051
G Meitzner	2053
V Minak	1030
Roger C Prince	1084
John H Sinfelt	2053
Edward I Stiefel	1030
Grayson H Via	2053

GENENTECH, INC.

Bart De Vos	2A07
Charles Eigenbrot	2A07
Mike Randal	2A07
Mark Ultsch	2A07

HEWLETT PACKARD LABORATORIES

Alice Fischer-Colbrie	1093
R D Jacowitz	1093
Stephen Laderman	1093
J Moll	1093
R Smith	1093

IBM RESEARCH LABORATORY

Gary Borges	2077
Charles A Brown	2077
C R Brundle	2121
Curt Erickson	1021
D E Fowler	2121
Joseph G Gordon	2077
Ting C Huang	1021
D W Kisker	1095, 1096
A C Luntz	2121
Owen Melroy	2061
D P Pappas	2121
William Parrish	1021
Thomas P Russell	2081, 2085
M Samant	2077
Joachim Stohr	2111
Mike Toney	2059, 2061

SURFACE SCIENCE INSTRUMENTS

Gordon Knapp	2094

X-RAY INSTRUMENTATION ASSOCIATES

S R Russell	2129
William K Warburton	2062, 2129

XEROX

James B Boyce	2120, 2131, 2132

XSIRIUS, INC.

J S Iwanczyk	2129

AMERICAN LABORATORIES

ARGONNE NATIONAL LABORATORY

H Diamond	2116
J E Epperson	2116
E P Horwitz	2116
P Thiyagarajan	2116

BROOKHAVEN NATIONAL LABORATORY

Stephen P Cramer	1030, 1084, 2051, 2098
Steve M Heald	2119
S M Khalid	1043
Geraldine M Lamble	2119
W Thomlinson	1046

LAWRENCE BERKELEY LABORATORY

Thomas Earnest	2A11
Robert D Giauque	2065
Melissa Grush	2010
Philip A Heimann	943
Tony Huff	943
Zahid Hussain	943
J Jaklevic	2090
Bing Jap	2A11

AMERICAN UNIVERSITIES

FOREIGN INSTITUTIONS

UNIVERSITY OF ALBERTA

William A Bridger	2A06
W Bret Church	2A03
Michael N G James	2A03, 2A06
William T Wolodko	2A06

UNIVERSITY OF OXFORD

A P Jephcoat	2056
S Wakatsuki	2088, 2101, 2102

WEIZMANN INSTITUTE

Felix Frolow	2A05
Ilona Makowski	2A05
Ada Yonath	2A05

IX. PUBLICATIONS BASED ON WORK AT SSRL

JOURNAL ARTICLES

J.W. Allen et al., *Electron Spectroscopy of Heavy-Fermion Materials*: accepted by Physica Scripta

J.W. Allen, M.B. Maple, J.-S. Kang, K.N. Yang, M.S. Torikachvili, Y. Lassailly, W.P. Ellis, B.B. Pate and I. Lindau, *Density-of-States-Driven Transition from Superconductivity to Ferromagnetism in $Ce(Ru_{1-x}Rh_x)_3 B_2$ Scenario for an Exchange Split Kondo Resonance:* Phys. Rev. B 41, 9013 (1990)

J. Arthur, D.E. Brown, S.L. Ruby, G.S. Brown and G.K. Shenoy, *Studying Hyperfine Fields with Resonant Nuclear Diffraction of X-Rays:* J. Appl. Phys. 67, 5704 (1990)

J.A. Bain, L.J. Chyung, S. Brennan and B.M. Clemens, *Elastic Strains and Coherency Stresses in Mo/Ni Multilayers:* submitted to Phys. Rev. B

T.W. Barbee, Jr., J.C. Rife, W.R. Hunter, R.G. Cruddace and P. Pianetta, *Multilayer Diffraction Gratings: Application to Synchrotron Radiation:* Optical Engineering 29, 738 (1990)

A.Q.R. Baron, T.W. Barbee, Jr. and G.S. Brown, *A Multilayer Monochromator for Synchrotron Radiation Angiography*: submitted to SPIE

J.B. Boyce, F.G. Bridges, T. Claeson, T.H. Geballe and J.M. Remeika, *X-ray Absorption of $BaBiO_3$ and Superconducting $BaBi_{0.25} Pb_{0.75} O_3$* : Phys. Rev. B 41, 6306 (1990)

L. Braicovich, E. Puppin, I. Lindau, A. Iandelli, G.L. Olcese and A. Palenzona, *Valence Photoelectron Spectroscopy of Gd Silicides:* Phys. Rev. B 41, 3123 (1990)

S. Brennan, P.H. Fuoss, J.L. Kahn and D.W. Kisker, *Experimental Considerations for In-Situ X-ray Scattering Analysis of OMVPE Growth:* Nucl. Instrum. & Methods A 291, 86 (1990)

F. Bridges, J.B. Boyce, T. Claeson, T.H. Geballe and J.M. Tarason, *Local Structure about Ni Atoms in Ni-substituted $YBa_2Cu_3O_{7-\delta}$* : Phys. Rev. B 42, 2137 (1990)

A.T. Brunger, M.V. Milburn, L. Tong, A.M. deVos, J. Jancarik, Z. Yamaizumi, S. Nishimura, E. Ohtsuka and S.-H. Kim, *Crystal Structure of an Active Form of ras Protein, a Complex of a GTP Analog and the Hras p21 Catalytic Domain:* Proc. Natl. Acad. Sci. U.S.A. 87, 4849 (1990)

K.D. Butcher, S.V. Didziulis, B. Briat and E.I. Solomon, *Variable-Photon-Energy Photoelectron Spectroscopic Studies of High-Spin d^6 Tetrahedral $FeCl_4^{2-}$ Electronic Relaxation Effects on Ionization:* Inorg. Chem. 29, 1626 (1990)

K.D. Butcher, M.S. Gebhard and E.I. Solomon, *Variable-Energy Photoelectron Spectroscopic Comparison of the Bonding in Ferric Sulfide and Ferric Chloride: An Alternative Description of the Near-IR-Visible Spin-Forbidden Transitions in High-Spin d^5 Complexes:* Inorg. Chem. 29, 2067 (1990)

K.D. Butcher, S.V. Didziulis, B. Briat and E.I. Solomon, *Variable Photon Energy Photoelectron Spectroscopy on $FeCl_4^-$ An Unusual Electronic Structure for High-Spin d^5 Complexes:* J. Amer. Chem. Soc. 112, 2231 (1990)

R. Cao, K. Miyano, I. Lindau and W.E. Spicer, *Investigation of In Contacts on Atomically Clean GaAs(110) Surfaces:* accepted by J. Vac. Sci. Tech.

R. Cao, K. Miyano, I. Lindau and W.E. Spicer, *Investigation of Interface States and Fermi Level Pinning Mechanisms with Metals on InP(110) Surfaces:* J. Elec. Spectros. Relat. Phenom. 51, 581 (1990)

R. Cao, K. Miyano, T. Kendelewicz, I. Lindau and W.E. Spicer, *On the Aspects of GaAs Initial Stage Band Bending:* accepted by Physica Scripta

R. Carr, *Adjustable Phase Insertion Devices as X-ray Sources:* accepted by Nucl. Instrum. & Methods

S. Caticha-Ellis, R. Boyce and H. Winick, *Conceptual Design of Instrumentation to Measure the Diffraction Profile of a Single Crystal at Bragg Angle Near π/2 by Using Synchrotron Radiation:* Nucl. Instrum. & Methods A 291, 132 (1990)

T.T. Childs and I. Lindau, *A High Yield LiF Monochromator System for Inverse Photoemission Spectroscopy:* J. Vac. Sci. Tech. A 8, 2521 (1990)

K. Clark, J.E. Penner-Hahn, M.M. Whittaker and J.W. Whittaker, *Oxidation-State Assignments for Galactose Oxidase Complexes from X-ray Absorption Spectroscopy. Evidence for Cu(II) in the Active Enzyme:* J. Amer. Chem. Soc. 112, 6433 (1990)

J.L. Cole, G.O. Tan, E.K. Yang, K.O. Hodgson and E.I. Solomon, *Reactivity of the Laccase Trinuclear Copper Active Site with Dioxygen: An X-ray Absorption Edge Study:* J. Amer. Chem. Soc. 112, 2243 (1990)

S.D. Conradson, I.D. Raistrick and A.R. Bishop, *Axial Oxygen-Centered Lattice Instabilities and High-Temperature Superconductivity:* Science 248, 1394 (1990)

D.S. Dessau, Z.-X. Shen, P.A.P. Lindberg, B.O. Wells, D.B. Mitzi, I. Lindau, W.E. Spicer and A. Kapitulnik, *The Electronic Structure of $Pb_2Sr_2CaCu_3O_8$ as Studied by Resonance Photoemission:* Physica C 162, 1373 (1990)

J. Freund, R. Ingalls and E.D. Crozier, *An Extended X-Ray Absorption Fine Structure Study of Amorphous Germanium Under High Pressure:* J. Phys. Chem. 49, 1087 (1990)

P.H. Fuoss and S. Brennan, *Surface Sensitive X-ray Scattering:* Annu. Rev. Mat. Sci. 20, 365 (1990)

G.N. George, W.E. Cleland, J.E. Enemark, B.E. Smith, C.A. Kipke, S.A. Roberts and S.P. Cramer, *L-Edge Spectroscopy of Molybenum Compounds and Enzymes:* J. Amer. Chem. Soc. 112, 2541 (1990)

R.D. Guiles, V.K. Yachandra, A.E. McDermott, J.L. Cole, S.L. Dexheimer, R.D. Britt, K. Sauer and M.P. Klein, *The S_0 State of Photosystem II Induced by Hydroxylamine: Differences between the Structure of the Manganese Complex in the S_0 and S_1 States Determined by X-Ray Absorption Spectroscopy:* Biochem. 29, 486 (1990)

R.D. Guiles, J.-L. Zimmermann, A.E. McDermott, V.K. Yachandra, J.L. Cole, S.L. Dexheimer, R.D. Britt, K. Wieghardt, U. Bossek, K. Sauer and M.P. Klein: *The S_3 State of Photosystem II: Differences between the Structure of the Manganese Complex in the S_2 and S_3 States Determined by X-ray Absorption Spectroscopy:* Biochem. 29, 471 (1990)

O. Gunnarsson et al., *Polarized Resonance Photoemission for Nd_2CuO_4* : Phys. Rev. B 41, 4811 (1990)

B. Hedman, K.O. Hodgson and E.I. Solomon, *X-ray Absorption Edge Spectroscopy of Ligands Bound to Open-Shell Metal Ions: Chlorine K-Edge Studies of Covalency in $CuCl_4^{2-}$* : J. Amer. Chem. Soc. 112, 1643 (1990)

P.A. Heimann et al., *High-Resolution Results from the LBL 55-Meter SGM at SSRL Near the K-Edge of Carbon and Nitrogen:* submitted to Physica Scripta

W.R. Heinemann and R.C. Elder, *EXAFS Spectroelectrochemistry:* Chem. Rev. 90, 705 (1990)

B. Hellquist, B. Holmberg, B. Hedman, I. Persson and L. Elding, *Structures of Solvated Cations of Palladium(II) and Platinum(II) in Dimethyl Sulfoxide, Acetonitrile and Aqueous Solution Studied by EXAFS and LAXS:* in press Acta. Chema. Scand.

T.C. Huang, W. Parrish, N. Masciocchi and P. Wang, *Derivation of d-Values from Digitized X-Ray and Synchrotron Diffraction Data:* Adv. X-Ray Anal. 33, 295 (1990)

G.P. Huffman, F.E. Huggins, N. Shah and A. Shah, *Behavior of Basic Elements During Coal Combustion:* Prog. in Energy & Com. Sci. 16, 243 (1990)

J.S. Iwanczyk, N. Dorri, M. Wang, M. Szawlowski, B.E. Patt, W.K. Warburton, B. Hedman and K.O. Hodgson, *The HgI_2 Energy Dispersive X-ray Array Detectors and Miniaturized Processing Electronics Project:* IEEE Trans. Nucl. Sci. 37, 198 (1990)

D.T. Jiang and E.D. Crozier, *A Gas-Flow Electron Yield Detector for Glancing-Incidence EXAFS:* Nucl. Instrum. & Methods A 294, 666 (1990)

D.R. Kania, L.S. Pan, H. Kornblum, P. Bell, O.L. Laden and P. Pianetta, *Soft X-ray Detection with Diamond Photoconductive Devices:* Rev. Sci. Instrum. 61, 2765 (1990)

D.R. Kania, L.S. Pan, P. Bell, O.L. Landen, H. Kornblum and P. Pianetta, *Absolute X-ray Power Measurements with Subnanosecond Time Resolution using Type IIa Diamond Photoconductors:* J. Appl. Phys. 68, 124 (1990)

R.M. Kettler, G.S. Waldo, J.E. Penner-Hahn, P.A. Meyers and S.E. Kesler, *Sulfidation of Organic Matter Associated with Gold Mineralization, Pueblo Viejo, Dominican Republic:* Appl. Geochem. 5, 237 (1990)

P.L. King, A. Borg, C. Kim, P. Pianetta, I. Lindau, G. Knapp and R. Browning, *From Small Area to Imaging Photoabsorption Spectroscopy:* Nucl. Instrum. & Methods A 291, 19 (1990)

P.L. King, A. Borg, C. Kim, P. Pianetta, I. Lindau, G. Knapp and M. Keenlyside, *Small Area Photoemission and Photoabsorption Measurements using a Photoelectron Microscope:* Physica Scripta 41, 413 (1990)
P.L. King, A. Borg, C. Kim, S.A. Yoshikawa, P. Pianetta and I. Lindau, *Synchrotron-Based Imaging with a Magnetic Projection Photoelectron Microscope:* accepted by Ultramicroscopy

J.H. Kinney, S.R. Stock, M.C. Nichols, U. Bonse, T.M. Breunig, R.A. Saroyan, R. Nusshardt, Q.C. Johnson, F. Busch and S.D. Antolovich, *Nondestructive Investigation of Damage in Composites Using X-ray Tomographic Microscopy (XTM):* J. Mater. Res. 5, 1123 (1990)

D.W. Kisker, P.H. Fuoss, K.L. Tokuda, G. Renaud, S. Brennan and J.L. Kahn, *An X-ray Analysis of GaAs Surface Reconstructions in H_2 and N_2 Atmospheres:* Appl. Phys. Lett. 56, 2025 (1990)

D.W. Kisker, P.H. Fuoss, S. Brennan, G. Renaud, K.L. Tokuda and J.L. Kahn, *In Situ Characterization of Organometallic Growth of ZnSe Using Grazing Incidence X-ray Scattering:* J. Cryst. Growth 101, 42 (1990)

G.H. Kwei, R.B. Von Dreele, A. Williams, J.A. Goldstone, A.C. Lawson and W.K. Warburton, *Structure and Valence from Complementary Anomalous X-ray and Neutron Powder Diffraction:* J. Mol. Struct. 223, 383 (1990)

E.M. Larson, F.W. Lytle, P.G. Eller, R.B. Greegor and M.P. Eastman, *XAS Study of Lanthanide Ion Speciation in Borosilicate Glass:* J. Non-Cryst. Solids 116, 57 (1990)

P.A.P. Lindberg, B.O. Wells, Z.-X. Shen, D.S. Dessau, I. Lindau, W.E. Spicer, D.B. Mitzi and A. Kapitulnik, *Interaction of Overlayers of Al and Rb with Single Crystalline Surfaces of $Bi_2Sr_2CaCu_2O_8$:* Appl. Phys. 67, 2667 (1990)

P.A.P. Lindberg, Z.-X. Shen, W.E. Spicer and I. Lindau, *Photoemission Studies of High-Temperature Superconductors:* Surf. Sci. Rep. 11, 1 (1990)

A.C. Liu, C.M. Friend and J. Stöhr, *The Orientation of Phenoxide on Oxygen Precovered Mo(110):* Surface Science 236, L349 (1990)

A.C. Liu, J. Stöhr, C.M. Friend and R.J. Madix, *A Critical Interpretation of the Near Edge X-Ray Absorption Fine Structure of Chemisorbed Benzene:* Surface Science 235, 107 (1990)

F.W. Lytle, G. van der Laan, R.B. Greegor, E.M. Larson, C.E. Violet and J. Wong, *Determination of the Valence of Pr, Gd, and Ho in $YBa_2Cu_3O_7$ by X-ray Absorption Spectroscopy:* Phys. Rev. B 41, 8955 (1990)

F.W. Lytle and R.B. Greegor, *Investigation of the "Join" Between the Near Edge and Extended X-ray Absorption Fine Structure:* Appl. Phys. Lett. 56, 192 (1990)

F.A. Marks, I. Lindau and R. Browning, *Characterization of the Pd/a-Al2O3 Supported Cluster System:* accepted by J. Vac. Sci. Technol.

M.V. Milburn, L. Tong, A.M. deVoss, A. Brunger, Z. Yamaizumi, S. Nishimura and S.-H. Kim, *Molecular Switch for Signal Transduction: Structural Differences Between Active and Inactive Forms of Protooncogenic ras Proteins:* Science 247, 939 (1990)

S. Mitra, F.E. Huggins, N. Shah and G.P. Huffman, *Investigation of Organic Sulfur Structure as a Function of Coal Rank:* ACS Div. Fuel Chem. Preprints 35, 364 (1990)

K. Miyano, R. Cao, T. Kendelewicz, A.K. Wahi, I. Lindau and W.E. Spicer, *Reaction and Barrier Formation at Metal/GaP(110) Interfaces:* Phys. Rev. B 41, 1076 (1990)

K. Miyano, R. Cao, T. Kendelewicz, A.K. Wahi, I. Lindau and W.E. Spicer, *Photoemission Spectroscopy of Ordered Overlayers on GaP(110):* accepted by Physica Scripta

J. Mustre de Leon, S.D. Conradson, I. Batistic and A.R. Bishop, *Evidence for an Axial Oxygen-Centered Lattice Fluctuation Associated with the Superconducting Transition in $YBa_2Cu_3O_7$:* Phys. Rev. Lett. 65, 1675 (1990)

L.S. Pan, D.R. Kania, P. Pianetta and O.L. Landen, *Carrier Density Dependent Photoconductivity in Diamond:* Appl. Phys. Lett. 58, 623 (1990)

J.E. Penner-Hahn, R.M. Fronko, V.L. Pecoraro, C.F. Yocum, S.D. Betts and N.R. Bowlby, *Structural Characterization of the Manganese Sites in the Photosynthetic Oxygen-Evolving Complex Using X-ray Absorption Spectroscopy:* J. Amer. Chem. Soc. 112, 2549 (1990)

P. Pianetta, I. Lindau, P.L. King, M. Keenlyside, G. Knapp and R. Browning, *Core Level Photoelectron Microscopy with Synchrotron Radiation:* J. Electron Spectros. Rel. Phen. 52, 797 (1990)

L. Powers, F.Y.-H. Wu, J.C. Phillips, W.-J. Huang and R.B. Sinclair, *Application of X-ray Absorption Spectroscopy and Anomalous Small Angle Scattering to RNA Polymerase:* Nucl. Instrum. & Methods A 291, 36 (1990)

E. Puppin, I. Abbati and I. Lindau, *Photoemission Core Levels in Gd Silicates:* accepted by Solid State Comm.

M. Rice, S. Wakatsuki and A. Bienenstock, *Anomalous Small Angle X-ray Scattering Studies of Metal-Germanium Alloys:* accepted by Mat. Res. Soc.

M. Rice, S. Wakatsuki and A. Bienenstock, *Composition Modulation in Amorphous Metal-Germanium Alloys Detected by Anomalous Small Angle X-ray Scattering:* accepted by J. Appl. Cryst.

M. Richter, J.C. Woicik, P. Pianetta, K.E. Miyano, T. Kendelewicz, C.E. Bouldin, W.E. Spicer and I. Lindau, *Surface Extended X-ray Absorption Fine Structure Studies of the Si(001) 2x1-Sb Interface:* accepted by J. Vac. Sci. Technol. A

M. Richter, J.C. Woicik, J. Nogami, P. Pianetta, K.E. Miyano, A.A. Baski, T. Kendelewicz, C.E. Bouldin, W.E. Spicer and C.F. Quate, *Surface EXAFS and Scanning Tunneling Microscopy of Si(001) 2x1-Sb:* Phys. Rev. Lett. 65, 3417 (1990)

M. Richter, J.C. Woicik, J. Nogami, K.E. Miyano, A.A. Baski, T. Kendelewicz, C.E. Bouldin, P. Pianetta, W.E. Spicer, C.F. Quate and I. Lindau, *A Combined Surface EXAFS/STM Study of the 1 ML Sb/Si(001) Interface:* accepted by J. Vac. Sci. Technol.

E. Rubenstein, J.C. Giacomini, H.J. Gordon, A.C. Thompson, G. Brown, R. Hofstadter, W. Thomlinson and H.D. Zeman, *Synchrotron Radiation Coronary Angiography with a Dual Beam, Dual Detector Imaging System:* Nucl. Instrum. & Methods A 291, 80 (1990)

M. Sancrotti, I. Abbati, E. Puppin, Z.-X. Shen, I. Lindau, R. Eggenhoffner, A. Iandelli and G.L. Olcese, *Yb Mean Valence in Chemically Compressed $Yb_{1-x}Se_{cx}A_{12}$ Pseudobinary Alloys: An X-ray Absorption Spectroscopy Investigation:* Solid State Comm. 74, 1131 (1990)

S. Sasaki, B. Youngman and H. Winick, *The Use of Single Wavelength Wiggler in PEP as Circular Polarized Hard X-ray Source:* Nucl. Instrum. & Methods A 291, 401 (1990)

R.A. Scott, P.A. Clark and D.E. Wilcox, *X-ray Absorption Spectroscopic Evidence for Binding of the Competitive Inhibitor 2-Mercaptoethanol to the Nickel Sites of Jack Bean Urease. A New Ni-Ni Interaction in the Inhibited Enzyme:* Inorg. Chem. 29, 579 (1990)

A. Shah, F.E. Huggins, N. Shah and G.P. Huffman, *The Form of Occurrence of Basic Elements in Coal and their Behavior During Combustion:* ACS Div. Fuel Chem. Preprints 35, 653 (1990)

N. Shah, R.A. Keogh, F.E. Huggins, G.P. Huffman, A. Shah, B. Ganguly and S. Mitra, *Coal Mineralogy, Forms-of-Sulfur and Iron, and Coal Liquefaction Properties for the Argonne Premium Coals and Nine Kentucky Coals:* ACS Div. Fuel Chem. Preprints 35, 784 (1990)

J.R. Shapley, W.S. Uchiyama and R.A. Scott, *Bimetallic Catalysts from Alumina-Supported Molybdenum-Iridium Clusters:* J. Phys. Chem. 94, 1190 (1990)

Z.-X. Shen, P.A.P. Lindberg, C.K. Shih, W.E. Spicer and I. Lindau, *Angle-resolved Photoemission Study of NiO and CoO:* Physica C 162, 1311 (1990)

Z.-X. Shen, C.K. Shih, O. Jepsen, W.E. Spicer, I. Lindau and J.W. Allen, *Aspects of the Correlation Effects, Antiferromagnetic Order, and Translational Symmetry of the Electronic Structure of NiO and CoO_4:* Phys. Rev. Lett. 64, 2442 (1990)

A.R. Siedle, W.B. Gleason, R.A. Newmark, R.P. Skarjune, P.A. Lyon, C.G. Markell, K.O. Hodgson and A.L. Roe, *Solid-State Chemistry of Molecular Metal Oxide Clusters. Bis(triphenylphosphine) rhodium(I) Carbonyl Derivatives:* Inorg. Chem. 29, 1667 (1990)

S.L. Sorenson, S.J. Schaphorst, S.B. Whitfield, B. Crasemann and R. Carr, *L-Shell Coster-Kronig Transition Probabilities in Ni, Cu, and Mo Measured with Synchrotron Radiation:* submitted to Phys. Rev. A

P.A. Stevens, R.J. Madix and J. Stöhr, *NEXAFS Study of HCOO/Ag(110): Evidence of Dynamic Bending:* Surface Science 230, 1 (1990)

L.K. Templeton and D.H. Templeton, *K-Edge Anomalous Scattering in Rubidium Hydrogen Tartate:* J. Appl. Cryst. 23, 18 (1990)

H. Toraya, N. Masciocchi and W. Parrish, *Rietveld Powder Structure Refinement of $Na_2Al_2Ti_6O_{16}$ Comparison of Synchrotron Radiation and Conventional X-Ray Tube Datasets:* J. Mat. Res. 5, 1538 (1990)

A.K. Wahi, K. Miyano, G.P. Carey, T.T. Chiang, I. Lindau and W.E. Spicer, *Band Bending at Al, In, Ag, and Pt Interfaces with CdTe and ZnTe(110):* J. Vac. Sci. Technol. A 8, 1926 (1990)

A.K. Wahi, G.P. Carey, K. Miyano, T.T. Chiang, I. Lindau and W.E. Spicer, *Interfacial Chemistry of Metals on CdTe and ZnTe(110):* J. Vac. Sci. Technol. A 8, 1152 (1990)

W.A. Warburton and P. Pianetta, *A Novel Differential Pump for Synchrotron Beamlines: Tests, Models and Applications:* Nucl. Instrum. & Methods A 291, 350 (1990)

W.K. Warburton, T.W. Barbee and Z.U. Rek, *Characterization Tests on Layered Synthetic Microstructures as X-ray Optical Elements:* Nucl. Instrum. & Methods A 291, 265 (1990)

G.A. Waychunas and G.E. Brown, Jr., *Polarized X-ray Absorption Spectroscopy of Metal Ions in Minerals:* accepted by Phys. Chem. Min.

G.A. Waychunas, W.A. Dollase and C.R. Ross, *Short Range Order (SRO) Measurements in MgO-FeO and MgO-$LiFeO_2$ Solid Solutions: EXAFS Analysis Assisted by DLS Computer Simulation and High Resolution Mössbauer Spectroscopy:* submitted to J. Mat. Sci.

B.O. Wells, P.A.P. Lindberg, Z.-X. Shen, D.S. Dessau, W.E. Spicer, I. Lindau, D.B. Mitzi and A. Kapitulnik, *Nature of the Valence Band States in $Bi_2(Ca, Sr, La)_3Cu_2O_8$:* accepted by J. Vac. Sci. Technol.

A. Williams, G.H. Kwei, A.T. Ortiz, M. Karnowski and W.K. Warburton, *Combined Neutron and X-ray Powder Diffraction Study of $Fe_{0.50}Co_{0.48}V_{0.02}$:* J. Mat. Res. 5, 1197 (1990)

H. Winick, *Overview of Synchrotron Radiation Facilities Outside the USA:* Nucl. Instrum. & Methods A 291, 487 (1990)

J.C. Woicik, T. Kendelewicz, K. Miyano, R. Cao, P. Pianetta, I. Lindau and W.E. Spicer, *Semiconductor Surface Core Level Shifts by Use of Selected Overlayers:* Phys. Scripta 41, 1034 (1990)

J.C. Woicik, T. Kendelewicz, K.E. Miyano, C.E. Bouldin, P. Pianetta and W.E. Spicer, *Local Bond Structure of Sb on Si(111) by Surface EXAFS and Photoemission:* accepted by Phys. Rev.

J. Wong, G. Shimkaveg, W. Goldstein, M. Eckert, T. Tanaka, Z.U. Rek and H. Tompkins, *YB_{66}: A New Soft X-ray Monochromator for Synchrotron Radiation:* Nucl. Instrum. & Methods A 291, 243 (1990)

J.G. Wright, H.-T. Tsang, J.E. Penner-Hahn and T.V. O'Halloran, *Coordination Chemistry of the Hg-MerR Metalloregulatory Protein: Evidence for a Novel Tridentate Hg-cysteine Receptor Site:* J. Amer. Chem. Soc. 112, 2434 (1990)

D. Yoon, N. Masciocchi, L. Depero, C. Viney and W. Parrish, *High-Temperature Structures of Poly(p-hydrobenzoic acid):* Macromolecules 23, 1793 (1990)

BOOKS AND CONFERENCE PROCEEDINGS

M.M. Baltay, W. Brunk, J. Cerino, R. Hettel, W. Leonard, J. Safranek, J. Voss, H. Wiedemann, K. Zuo, T. Sanchez and J. Jagger, *The Ring Magnets for a Dedicated Injector for SPEAR*, accepted by the 1991 Particle Accelerator Conference, San Francisco.

A. Bienenstock, R.D. Lorentz and M. Rice, *XANES, Anomalous Small-Angle Scattering and Fine Scale Composition Fluctuations in Amorphous Fe_xGe_{100-x} Films*, to be published in Proceedings of XAFS VI, 6th Interntl. Conf. on X-ray Absorption Fine Structure.

M. Borland, J.N. Weaver, M. Baltay, L. Emery, R. Hettel, H. Morales, J. Sebek, B. Youngman, R. Anderson, A.S. Fisher and R.H. Miller, *Design and Performance of the Traveling-Wave Beam Chopper for the SSRL Injector*, accepted by the 1991 Particle Accelerator Conference, San Francisco.

J.B. Boyce, F. Bridges and T. Claeson, *Local Structure and Distortions in Pure and Doped $YBa_2Cu_3O_{7-\delta}$: X-ray Absorption Studies*, in H.S. Kwok et al., eds., Superconductivity and Applications, (Plenum Press, NY, 1990) pp. 303-312.

S. Brennan, S. Baird, W. Lavender, H.-D. Nuhn, C. Wermelskirchen and J. Yang, *The Control and Operation of the Programmable Waveform Generator for the SSRL Injector*, accepted by the 1991 Particle Accelerator Conference, San Francisco.

J. Cerino, M. Baltay, R. Boyce, S. Harris, R. Hettel, M. Horton, and K. Zuo, *Extraction Septum Magnet for the SSRL Injector*, accepted by the 1991 Particle Accelerator Conference, San Francisco.

M. Cornacchia and H. Winick, *Technological Challenges of Third Generation Synchrotron Radiation Sources*, in Y. Kaneko, ed., Proceedings of Intl. Symposium on Advanced Nuclear Energy Research - Evolution by Accelerators, (January 24-26, 1990).

J.G. DeWitt, J.G. Bentsen, B. Hedman, A.C. Rosenzweig, J. Green, S. Pilkington, K.O. Hodgson, S.J. Lippard and H. Dalton, X-ray *Absorption Spectroscopy of Diferrous and Diferric Protein A of Soluble Methane Monooxygenase from Methylococcus capsulatus (Bath)*, to be published in the Proceedings of XAFS VI, 6th Interntl. Conf. on X-ray Absorption Fine Structure.

L. Emery, *Further Feasibility Studies on a Wiggler-Based Ultra-Low-Emittance Damping Ring Lattice*, accepted by the 1991 Particle Accelerator Conference, San Francisco.

L. Emery, *Energy Feedback System for the SSRL Injector Linac*, accepted by the 1991 Particle Accelerator Conference, San Francisco.

A. Fisher, S. Baird, H.-D. Nuhn, R. Tatchyn, H. Winick and C. Pellegrini, *A 40 Å FEL on PEP*, in Proceedings of the Workshop on the Prospects for a 1 Å Free Electron Laser, (Sag Harbor, NY, April 1990).

A. Fisher, S. Baird, H.-D. Nuhn, R. Tatchyn, H. Winick, C. Pellegrini, *Coherent X-rays from PEP*, accepted by the 1991 Particle Accelerator Conference, San Francisco.

R.D. Guiles, V.K. Yachandra, A.E. McDermott, V.J. Derose, J.-L. Zimmerman, K. Sauer and M.P. Klein, *Structures and Oxidation States of Mn in Several S-States of Photosystem II Determined by X-ray Absorption Spectroscopy*, in M. Baltscheffsky, ed., Current Research in Photosynthesis, (Kluwer Academic Publishers, 1990) pp. 789-792.

B. Hedman, P. Frank, B.J. Feldman, S.F. Gheller, F.A. Schultz, W.E. Newton and K.O. Hodgson, *Sulfur K and Molybdenum L Edge XAS of the Nitrogenase Iron-Molybdenum Cofactor under in-situ Electrochemical Control*, to be published in the Proceedings of XAFS VI, 6th Interntl. Conf. on X-ray Absorption Fine Structure.

B. Hedman, K.O. Hodgson and C.D. Garner, *Characterization of Mo and V Centres in Enzymes by X-ray Absorption Spectroscopy*, in S.S. Hasnain, ed., Synchrotron Radiation and Biophysics, (Ellis Horwood Ltd., Chichester, 1990) pp. 43-62.

R. Hettel, R. Averill, M. Baltay, S. Brennan, C. Harris, M. Horton, C. Jach, J. Sebek and J. Voss, *The 10 Hz Resonant Magnet Power Supply System for the SSRL 3 GeV Injector*, accepted by the 1991 Particle Accelerator Conference, San Francisco.

R.O. Hettel, D. Mostowfi, R. Ortiz and J. Sebek, *Triggers and Timing System for the SSRL 3 GeV Injector*, accepted by the 1991 Particle Accelerator Conference, San Francisco.

G.P. Huffman, F.E. Huggins and N. Shah, *XAFS Spectroscopy: A New Technique for Investigating Impurity Elements in Coal that Control Slagging and Fouling Behavior*, in R.W. Bryers, K.S. Vorres, eds., Mineral Matter and Ash Deposition from Coal, (Engineering Foundation, NY, 1990) pp. 63-74.

G.P. Huffman, F.E. Huggins, H.E. Francis, S. Mitra and N. Shah, *Structural Characterization of Sulfur in Bioprocessed Coal*, in R. Markuszewski, T.D. Wheelock, eds., Processing and Utilization of High Sulfur Coals III, (Elsevier, 1990) pp. 21-32.

F.E. Huggins, G.P. Huffman, N. Shah, S. Mitra, B. Ganguly, A. Shah, M.M. Taghiei and S. Vaidya, *Structural Characterization of Important Elements in Bioprocessed Coal*, in First Int'l Conf on Bioprocessing of Coal, May 1-3, 1990, Orlando, FL.

J.-S. Kang, J.W. Allen, B.-W. Lee, M.B. Maple, Z.-X. Shen, J.-J. Yeh, W.P. Ellis, W.E. Spicer and I. Lindau, *Electron Spectroscopy of High Temperature Superconductors:* $Y_{1-x}Pr_xBa_2Cu_3O_{7-\delta}$, in A. Bianconi, A. Marcelli, eds., High Tc Superconductors, Electronic Structure (Plenum Press, NY, 1990) pp. 225-236.

W. Lavender, S. Baird, M. Borland, S. Brennan, R. Hettel, H.-D. Nuhn, R. Ortiz, J. Safranek, J. Sebek, C. Wermelskirchen and J. Yang, *The SSRL Injector Beam Position Monitoring Systems*, accepted by the 1991 Particle Accelerator Conference, San Francisco.

I. Lindau, *Photoemission Cross Sections*, in R.Z. Bachrach, ed., Synchrotron Radiation Research: Advances in Surface Science (Plenum, New York, 1990): in press.

H. Morales, U. Cummings, N. Hower, W. Li, J. Safranek, J. Voss and H. Wiedemann, *Vacuum Chamber for the 3 GeV SPEAR Injector Synchrotron*, accepted by the 1991 Particle Accelerator Conference, San Francisco.

H.-D. Nuhn, R. Boyce, J. Cerino and T. Hostetler, *The SSRL Injector Kickers*, accepted by the 1991 Particle Accelerator Conference, San Francisco.

H.-D. Nuhn, Y. Sun, H. Winick, W. Xie, R. Yotam, H. Schwarz and P. Friedrichs, *A Longitudinal Multibunch Feedback System for PEP*, accepted by the 1991 Particle Accelerator Conference, San Francisco.

J.E. Penner-Hahn, R.M. Fronko, G.S. Waldo, C.F. Yocum, N.R. Bowlby and S.D. Betts, *X-ray Absorption Spectroscopy of the Photosynthetic Oxygen Evolving Complex*, in M. Baltscheffsky, ed., Current Research in Photosynthesis (Kluwer Academic Publishers, 1990) pp. 797-800.

P. Pianetta and P. King, *Photoelectron Spectroscopy of Solids*, in A. Craievich, ed., Synchrotron Light: Applications and Related Instrumentation II, (Singapore, World Scientific 1990) pp. 28-46.

P. Pianetta and L. Pan, *Design of a Synchrotron Radiation Lithography Station*, in A. Craievich et al., eds., Microlithography: High Integration in Microelectronics, (Singapore, World Scientific 1990) pp. 94-110.

J. Safranek and S. Baird, *Commissioning the SSRL Injector*, accepted by the 1991 Particle Accelerator Conference, San Francisco.

J. Safranek and H. Wiedemann, *Low-Emmittance in SPEAR*, accepted by the 1991 Particle Accelerator Conference, San Francisco.

K. Sauer, *Photosystem II and Water Oxidation*, in M. Baltscheffsky, ed., Current Research in Photosynthesis (Kluwer Academic Publishers, 1990) pp. 675-684.

J. Sebek, M. Baltay, M. Borland, J. Cerino, L. Emery, R. Hettel, H. Morales, D. Mostowfi, M. Rowen, J. Safranek, J. Voss, J. Weaver, H. Wiedemann, B. Youngman, J.-L. Pellegrin, V. Smith and Y.Yin, *Diagnostic Instrumentation for the SSRL 3 GeV Injector for SPEAR*, accepted by the 1991 Particle Accelerator Conference, San Francisco .

T.A. Smith, J.G. DeWitt, B. Hedman and K.O. Hodgson, *Sulfur K-edge XAS Studies of Photographic Materials*, to be published in the Proceedings of XAFS VI, 6th Interl. Conf. on X-ray Absorption Fine Structure.

G.O. Tan, J.L. Cole, E.K. Yang, K.O. Hodgson and E.I. Solomon, *Reactivity of the Laccase Trinuclear Copper Active Site with Dioxygen: An X-ray Absorption Edge Study*, to be published in the Proceedings of XAFS VI, 6th Interml. Conf. on X-ray Absorption Fine Structure.

L. Tong, A.M. deVoss, M.V. Milburn, J. Jancarik, S. Noguchi, S. Nishimura, K. Miura, E. Ohtsuka and S.-H. Kim, *Structural Differences of Transforming ras p21 (Val-12) from the Normal Protein* in Frontiers of NMR in Molecular Biology (Alan R. Liss, Inc., 1990) pp. 145-153.

T.A. Tyson, D.A. Case, B. Hedman and K.O. Hodgson, *On the Need to Account for Electron Spin when Interpreting Linearly Polarized XANES with Application to the Polarized Molybdenum L_2 and L_3 Absorption Edges of Single Crystal $MoS_2O_2^{2-}$*, in A. Balerna et al., eds., Proc. of the 2nd European Conference on Progress in X-ray Synchrotron Radiation, (SIF, Bologna 1990) pp. 247-250.

J.N. Weaver, S. Baird, M. Baltay, M. Borland, C. Chavis, L. Emery, R. Hettel, S.J. Mello, H. Morales, H.-D. Nuhn, J. Safranek, J. Sebek, J. Voss, D. Wang, H. Wiedemann, B. Youngman and R.H. Miller, *The Linac and Booster RF System for a Dedicated Injector for SPEAR*, accepted by the 1991 Particle Accelerator Conference, San Francisco.

C. Wermelskirchen, S. Brennan, T. Goetz, W. Lavender, R. Ortiz, M. Picard and J. Yang, *The SSRL Injector Control System*, accepted by the 1991 Particle Accelerator Conference, San Francisco.

H. Wiedemann, *3 GeV Injector Synchrotron for SPEAR* accepted by the 1991 Particle Accelerator Conference, San Francisco.

H. Wiedemann, *Sub-Picosecond Electron and Photon Pulses*, accepted by the 1991 Particle Accelerator Conference, San Francisco.

J. Woicik and P. Pianetta, *Studies of Si-Ge Interfaces with Surface EXAFS and Photoemission*, in R.Z. Bachrach, ed., Synchrotron Radiation Research: Advances in Surface and Interface Science (Plenum Press, NY, 1990), in press.

R. Yotam, J. Cerino, R. Garoutte, R. Hettel, M. Horton, J. Sebek, E. Benson, K. Crook, J. Fitch, N. Ipe, G. Nelson and H. Smith, *Personnel Protection and Beam Containment Systems for the SSRL 3 GeV Injector*, accepted by the 1991 Particle Accelerator Conference, San Francisco.

THESES BASED ON RESEARCH AT SSRL

The following is a list of Ph.D. theses completed in 1990 based on experimental research at SSRL. In total, 168 theses from 25 universities have been completed.

	TITLE/ADVISOR
K.R. Bauchspiess *Simon Fraser Univ.*	"A Study of the Pressure-Induced Mixed-Valence Transition in SmSe and SmS by X-ray Absorption" (Advisor - E.D. Crozier)
C.J. Chisholm-Brause *Stanford University*	"Sorption Mechanisms of Co(II) at Oxide/Water Interfaces" (Advisor - G.E. Brown, Jr.)
W.E. Jackson *Stanford University*	"X-Ray Absorption Analyses of Iron-Bearing Glasses and Melts: Implications for Glass-Melt Structural Differences and the Effect of Alkali and Alkaline-Earth Metals on Fe(II) Coordination" (Advisor - G.E. Brown, Jr.)
L.C. Wilson *Stanford University*	"Atomic Arrangements in Short Period Molybdenum/Germanium Multilayers" (Advisor - A. Bienenstock)
L. Emery *Stanford University*	"A Wiggler Based Ultra-Low Emittance Damping Ring and its Chromatic Correction" (Advisor - H. Wiedemann)
S. Wakatsuki *Stanford University*	"Structural Studies of Bacteriorhodopsin Using Synchrotron Small-Angle X-ray Diffraction" (Advisor - K.O. Hodgson)
V. DeRose *UC-Berkeley*	Studies of Manganese and Halide in the Photosystem II Oxygen Evolving Complex" (Advisor - M.P. Klein)